Maximiliano Puccio

Study of the production of nuclei and anti-nuclei at the LHC with the ALICE experiment

Ph.D. Thesis

Supervisor: Prof. Massimo Masera
Co–supervisor: Prof. Stefania Bufalino

Università degli studi di Torino
Scuola di Dottorato in Scienze della Natura e Tecnologie Innovative
Dipartimento di Fisica

2017, May

Abstract

In the ultra–relativistic lead–lead collisions at the CERN Large Hadron Collider (LHC), a state of matter called Quark Gluon Plasma (QGP) is created. A typical signature of a heavy ion collision (HIC) correlated to the production of the QGP is the large number of particles produced ($\mathrm{d}N_{\mathrm{ch}}/\mathrm{d}\eta$ up to 2000 in Pb–Pb collisions at $\sqrt{s_{\mathrm{NN}}}$ =5.02 TeV). This high multiplicity environment poses a tremendous experimental challenge on the experiments that have to cope with the high density of signals in their sensitive volume. A Large Ion Collider Experiment (ALICE) has been designed to deal with the harsh environment of a HIC and to study in details the characteristics of the QGP. Among the particles produced in a HIC, light nuclei and their anti–matter companions are of special interest since the production mechanism of such loosely bound states is not clear in high energy collisions. The production rate at the LHC for the lightest of these objects, the deuteron, is approximately one every ten Pb–Pb collisions with the highest charged particle density. Heavier nuclei, such as the ^{3}He, are even more rare.

The first goal of this work is to search with the ALICE experiment the haystack of particles produced in Pb–Pb collisions at $\sqrt{s_{\mathrm{NN}}}$ =2.76 TeV and $\sqrt{s_{\mathrm{NN}}}$ =5.02 TeV to find (anti–)deuterons and (anti–)^{3}He. It is possible to distinguish some of the leading features of the main models describing the (anti–)nuclei production, by studying the characteristics of their transverse momentum spectra, their evolution with the particle multiplicity and their relation to the measured yield of protons. It will be also evident that the detailed study of heavier nuclei is limited by the amount of data collected by the ALICE experiment. In its third run, starting in 2020, the LHC will deliver Pb–Pb collisions at the unprecedented interaction rate of 50 kHz. In order to fully profit from the high luminosity delivered by the LHC, the ALICE collaboration is now working on the upgrade of its experimental apparatus. In particular, a completely new silicon Inner Tracking System (ITS) and a new computing facility for the Online and Offline (O^2) data handling will be installed. With these upgrades the ALICE experiment will be able to collect the data of every single Pb–Pb interaction, enabling the detailed study of rare processes such as the formation of (anti–)nuclei. In this context, the second goal of this thesis is the development of a fast ITS tracking algorithm that is able to conjugate the timing requirements imposed by the online reconstruction of all the Pb–Pb events and the reconstruction efficiency requirements of the physics analysis. The result is a tracking algorithm based on the Cellular Automata that is able to reconstruct efficiently tracks of transverse momentum down to 100 MeV/c in the Pb–Pb events with the highest track density in less than 1 second.

Key words: ALICE experiment, ITS Upgrade, tracking algorithms, nuclei, anti–nuclei, statistical

hadronisation models, coalescence model

Sommario

Nelle collisioni ultrarelativistiche tra ioni di piombo al Large Hadron Collider (LHC) del CERN viene creato lo stato della materia chiamato Plasma di Quark e Gluoni (QGP). Una delle caratteristiche salienti delle collisioni tra ioni pesanti legata alla creazione del QGP è la abbondante produzione di particelle ($\mathrm{d}N_{\mathrm{ch}}/\mathrm{d}\eta$ fino a 2000 in collisioni Pb–Pb all'energia $\sqrt{s_{\mathrm{NN}}}$ =5.02 TeV). La rivelazione dell'elevato numero di particelle prodotte rappresenta una sfida per gli esperimenti che devono essere in grado di acquisire una grande densità di segnali nei loro rivelatori di particelle A Large Ion Collider Experiment (ALICE) è stato progettato per tollerare le condizioni estreme di una collisione tra ioni pesanti e per studiare in dettaglio le caratteristiche del QGP. Tra le particelle prodotte in una collisione, i nuclei leggeri e i loro corrispondenti anti–nuclei sono di particolare interesse poiché il meccanismo di produzione di questi stati debolmente legati in collisioni ad alta energia non è chiaro. Il rateo di produzione a LHC per il più leggero di questi stati, il deutone, è circa uno ogni 10 collisioni Pb–Pb centrali. I nuclei più pesanti, come ^{3}He, sono ancora più rari.

Il primo obiettivo di questo lavoro è identificare, nella moltitudine di particelle prodotte in collisioni Pb–Pb a $\sqrt{s_{\mathrm{NN}}}$ =2.76 TeV e $\sqrt{s_{\mathrm{NN}}}$ =5.02, (anti–)deutoni e (anti–)^{3}He usando l'esperimento ALICE. Alcune delle caratteristiche fondamentali dei principali modelli fenomenologici che descrivono la produzione di (anti–)nuclei possono essere studiate analizzando gli spettri di produzione degli (anti–)nuclei, la loro evoluzione con la molteplicità di particelle prodotte e la loro relazione con la produzione di protoni. Nella descrizione del lavoro svolto nella presente tesi si evidenzierà il fatto che la principale limitazione allo studio dettagliato della produzione di nuclei più pesanti è la quantità di dati raccolti dall'esperimento ALICE. Durante il suo terzo periodo di presa dati, che partirà nel 2020, LHC fornirà agli esperimenti collisioni Pb–Pb con la frequenza di interazione senza precedenti di 50 kHz. Per poter utilizzare al meglio l'alta luminosità fornita da LHC, la collaborazione ALICE sta lavorando sul rinnovamento del suo apparato sperimentale. In particolare verranno installati un nuovo tracciatore in silicio chiamato Inner Tracking System (ITS) e un nuovo centro di calcolo per l'elaborazione dei dati Online e Offline (O^2). Grazie a questo *upgrade* l'esperimento ALICE potrà raccogliere i dati relativi ad ogni singola collisione Pb–Pb consentendo così lo studio di processi rari come la formazione di (anti–)nuclei. In questo contesto, il secondo obiettivo di questo lavoro è lo sviluppo di un algoritmo veloce di ricostruzione delle tracce in ITS che sia in grado di coniugare le esigenze di velocità di computazione imposte dalla elaborazione *online* di tutti gli eventi Pb–Pb con le esigenze in termini di efficienza di ricostruzione delle tracce richiesti dalle analisi di fisica. Il risultato di questo sviluppo è un algoritmo di tracciamento basato

sugli automi cellulari (Cellular Automata, CA) che è in grado di ricostruire in modo efficiente le tracce di particelle con impulso trasverso fino a 100 MeV/c in meno di 1 secondo negli eventi Pb–Pb centrali.

Parole chiave: ALICE experiment, ITS Upgrade, algoritmi di tracciamento, nuclei, anti–nuclei, modelli di adronizzazione statistica, modelli di coalescenza

Contents

Abstract (English/Italian) **i**

1 High energy nuclear physics **1**
1.1 QCD: building the theory of the strong interaction . . . 1
1.2 States of hadronic matter . . . 4
1.3 Heavy Ion Collisions . . . 7
1.3.1 Smashing ions, colliding nucleons . . . 7
1.3.2 Space time evolution of Heavy Ion collisions . . . 10
1.4 Nuclei production in Heavy Ion collisions . . . 12
1.4.1 Statistical Hadronisation Models . . . 12
1.4.2 Coalescence Models . . . 15

2 Probing the Quark Gluon Plasma **19**
2.1 Soft probes . . . 19
2.1.1 Momentum spectra of hadrons . . . 19
2.1.2 Anisotropic flow . . . 21
2.2 Hard probes . . . 22
2.2.1 High momentum particles and heavy flavours . . . 22
2.2.2 Quarkonia . . . 26
2.3 Electroweak probes . . . 28

3 The ALICE experiment **31**
3.1 The Large Hadron Collider . . . 31
3.2 ALICE design . . . 34
3.2.1 Inner Tracking System . . . 37
3.2.2 Time Projection Chamber . . . 39
3.2.3 Time of Flight detector . . . 39
3.2.4 V0 . . . 40
3.2.5 T0 . . . 40
3.2.6 ZDC . . . 40
3.3 Trigger and Data Acquisition . . . 41
3.4 ALICE offline framework . . . 41
3.4.1 Monte Carlo simulations . . . 42
3.4.2 Event Reconstruction . . . 42

3.4.3 ALICE analysis framework . . . 45
3.5 Particle Identification . . . 47
3.5.1 ITS particle identification . . . 47
3.5.2 TPC particle identification . . . 47
3.5.3 TOF particle identification . . . 48
3.6 Centrality determination in Pb–Pb collisions . . . 50

4 Perspectives for the ITS reconstruction in Run 3 53
4.1 The upgraded ITS . . . 54
4.2 The Online–Offline systems upgrade . . . 56
4.3 Vertex finding and pile–up identification . . . 58
4.4 Track reconstruction . . . 59
4.4.1 The Cellular Automata algorithm . . . 61
4.4.2 Tracking performance . . . 64
4.5 Outlook . . . 72

5 Nuclei and anti–nuclei in Pb–Pb collisions: analysis technique 75
5.1 Data and Monte Carlo samples . . . 75
5.1.1 Event selection . . . 77
5.1.2 Track selection . . . 82
5.2 Raw spectra extraction . . . 83
5.2.1 Deuteron and ^{3}He identification using TPC . . . 83
5.2.2 Signal extraction for deuterons using TPC+TOF . . . 86
5.3 Corrections to the raw spectra . . . 90
5.3.1 Momentum shift correction . . . 90
5.3.2 Efficiency×Acceptance correction . . . 92
5.3.3 Secondary particle background rejection . . . 95
5.4 Systematic checks . . . 98

6 Final results 109
6.1 Production spectra . . . 109
6.2 Yield and mean p_{T} . . . 115
6.3 Comparisons to the theoretical expectations . . . 117
6.4 Nucleus over proton ratio . . . 121

7 Conclusions 123

A List of selections used in the CA tracker 127

B Ratios anti–nuclei over nuclei 133

Bibliography 141

Acknowledgements 143

1 High energy nuclear physics

In the current understanding, the energy density in the early universe was so high that the fundamental components of ordinary matter could not bind to form hadrons. The transition from this phase to the ordinary matter and the properties of the hot and dense nuclear matter is the main subject of study of High Energy Nuclear Physics.

Throughout this chapter the natural units are used, thus in the following $\hbar = c = k_B = 1$.

1.1 QCD: building the theory of the strong interaction

In the 1960's a large number of different hadronic states had been already discovered (e.g. Δ resonance, the kaons) and yet there was no theoretical framework able to explain the experimental observations of such a large zoo of particles. The first theoretical success in explaining the hadron spectroscopy was the prediction of the existence of the Ω baryon starting from the three flavour families classification, SU(3), of the hadrons [1, 2]. This classification evolved later into the static Quark Model that describes the hadron zoology in terms of constituent particles with fractional charge [3, 4].
Still, only the introduction of an additional quantum number the colour [5] could explain the existence of the double charged Δ^{++} baryon that could not be predicted in the framework of the Quark Model due to the Pauli exclusion principle.
The extended Quark Model with the colour degree of freedom predicts a modification in the ratio R between the interaction cross section of electron and positron going into hadrons and going into muon pair:

$$R(s) = \frac{\sigma(e^+e^- \rightarrow hadrons, s)}{\sigma(e^+e^- \rightarrow \mu^+\mu^-, s)} = n_c \sum_f Q_f$$

where n_c is the number of possible colour charges in the theory and Q_f is the electric charge for the quark with flavour f. The sum runs on the flavours accessible with the energy available in the centre of mass s. Many experimental results – summarised in [6] – verified this prediction (Figure 1.1) and found that the number of colours in the theory is 3. The formulation of

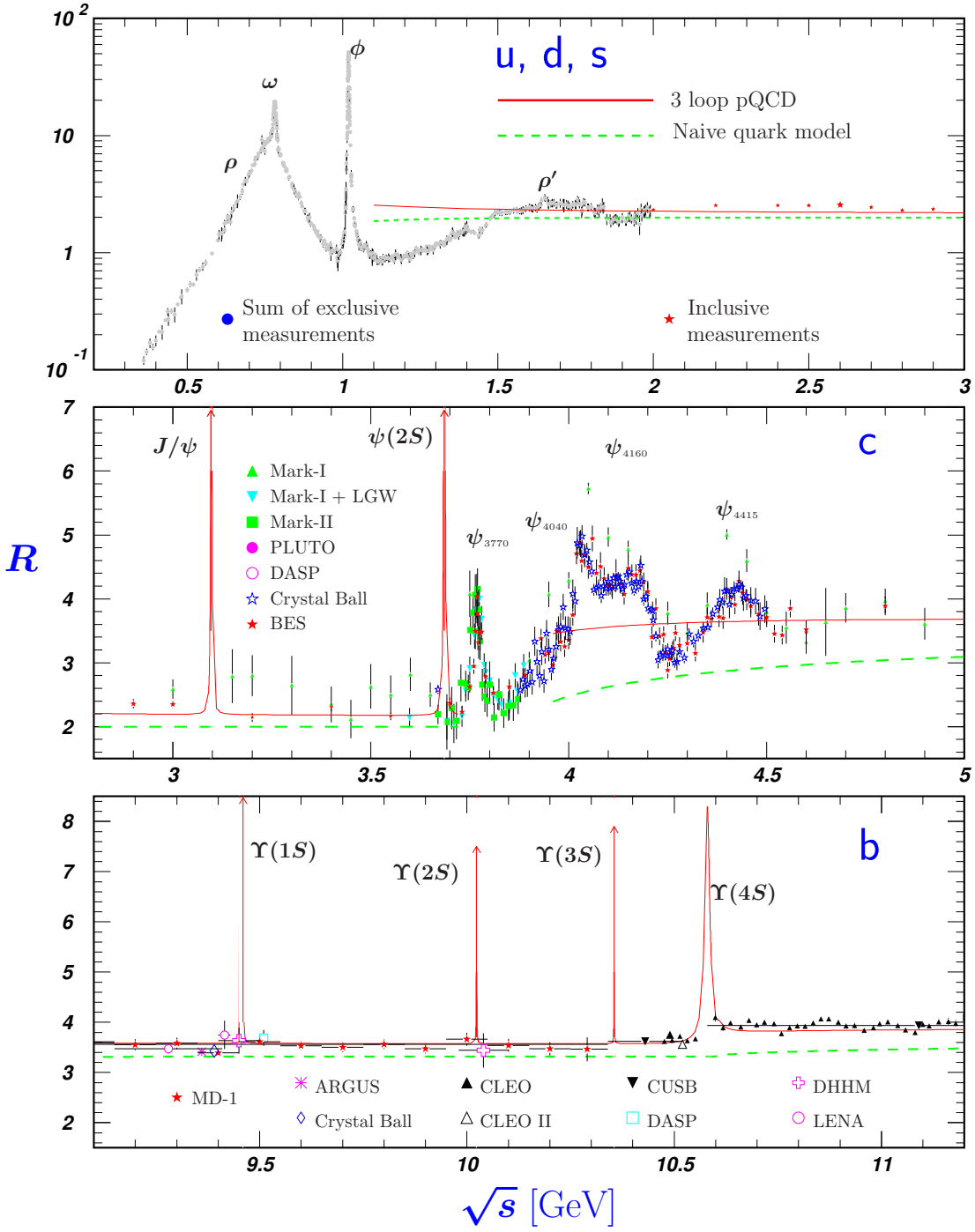

Figure 1.1: R ratio as a function of the $\sqrt{s}$ of the collision between electron and positron [6]. The three pads correspond to three different regions of $\sqrt{s}$: the top pad shows the region of the u,d and s quarks resonances, the middle one the region of the c quark resonances and the bottom one the region of the b quark resonances. It is possible to observe how the ratio changes value when new flavours are available. The observed ratio fits with the Quark Model expectations with 3 quarks (green line). The red line shows how the Quark Model predictions are refined taking into account loop corrections in perturbation theory.

the Quark Model with colour interaction mediated by massless coloured gauge bosons [7], also known as Quantum Chromodynamics (QCD), is currently the reference theory for the description of strong interaction and it is part of the framework of the Standard Model (*SM*) of the fundamental interaction. The Lagrangian of the theory has an explicit SU(3) local gauge invariance resulting in 8 massless mediator bosons:

$$\mathscr{L}_{QCD} = \mathscr{L}_{gluons} + \mathscr{L}_{quarks} = -\frac{1}{4} G^a_{\mu\nu} G^{\mu\nu}_a + + i \sum_f \bar{\Psi}_f (\gamma_\mu \partial^\mu - i g_s \frac{\lambda^a}{2} \gamma_\mu A^\mu_a) \Psi_f$$

where a is the group index, A^μ_a is the gluon field and f is the quark flavour. Due to the non-abelian nature of the symmetry group of the Lagrangian, the gluon tensor has an additional term with respect to the photon tensor in Quantum Electrodynamics (QED):

$$G^{\mu\nu}_a = \partial^\mu A^\nu_a - \partial^\nu A^\mu_a - g \sum_{b,c=1}^{8} f_{abc} A^{\mu b} A^{\nu c}$$

The additional term in the gluon tensor brings two self interaction vertices for the gluons (Figure 1.2) that are not present in QED at the tree level.

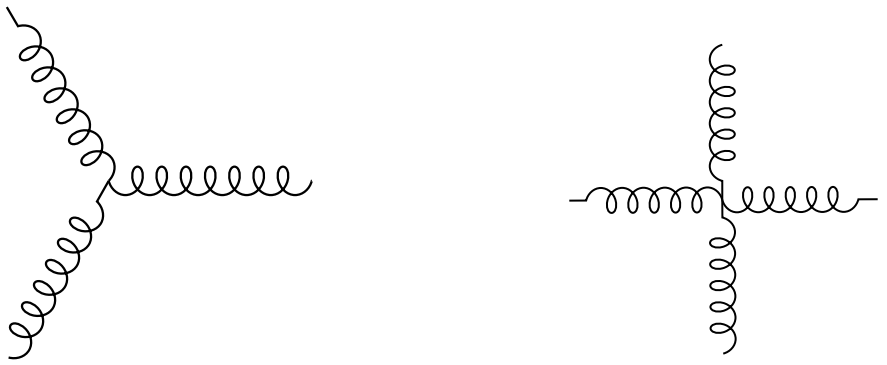

(a) $-\frac{g}{2} f_{abc} (\partial^\mu A^\nu_a - \partial_\nu A^\mu_a) A^b_\mu A^c_\nu$ (b) $-\frac{g^2}{4} f_{abc} f_{cde} A_{a\mu} A_{b\nu} A^\mu_c A^\nu_d$

Figure 1.2: Three and four gluon interaction vertices

The self interacting vertices in the gluon Lagrangian bring one loop corrections to the gluon propagator resulting in the so-called *anti-screening* in colour interaction. As a result, the QCD coupling constant α_s evolves with the transverse momentum as derived in [8, 9] and reported here:

$$\alpha_s(Q^2) = \frac{\alpha(\mu^2)}{1 + \frac{33-2n_f}{12\pi} \ln \frac{Q^2}{\mu^2}}$$

where n_f is the number of flavours and μ is the renormalization scale of the theory. For high Q^2 the QCD coupling goes to zero and the QCD becomes a free theory and this regime is called *asymptotic freedom*. At low transferred momenta quarks remain bound in the hadron phase: this is the so-called *confinement* regime. Over the years the experimental results, shown in

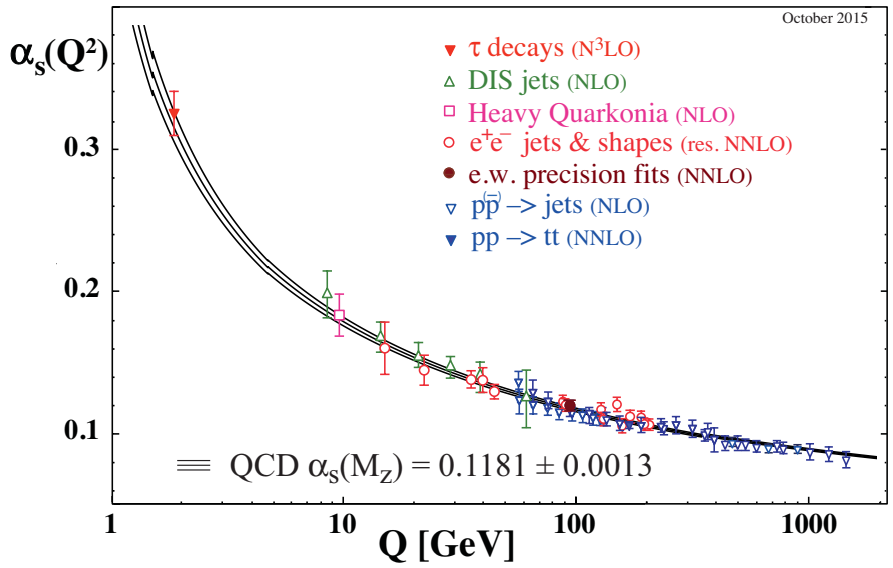

Figure 1.3: The experimental values found for the α_s coupling (courtesy of [6]) as a function of the process transferred momentum. The reference value at the energy scale of the Z boson mass $\alpha_s(M_z)$ has been evaluated using the χ^2 averaging method.

Figure 1.3, confirmed the trend of the coupling constant foreseen by the QCD.

The standard perturbative approach (pQCD) is able to calculate transition elements of the scattering matrices at $Q^2 \gg \mu^2$, thus $\alpha_s \ll 1$, while at low transferred momentum different kinds of approach are necessary to describe the colour interaction.

At low Q^2 it is still possible to solve gauge theories calculation starting from the evaluation of the Green's functions of the QCD Lagrangian on a space time lattice with spacing a. This method, called lattice regularised QCD or simply lattice QCD (LQCD), was illustrated for the first time in [10]. Extrapolating to the continuum ($a \to 0$) it is possible to get the results to be compared with the experiments. A remarkable recent success of LQCD in the description of the soft processes of the colour interaction is the determination of the proton mass with a precision of 2% [11].

1.2 States of hadronic matter

One important consequence of the running of α_s is the possibility of creating different states of the hadronic matter. Considering a system with finite dimensions composed by quarks and gluons, the state of the hadronic matter of the system depends on the mean transferred momentum in the interactions inside the medium. It is convenient to describe these hadronic systems using variables typical of thermodynamics like temperature (T) and chemical potential (μ) associated with the baryonic number. Figure 1.4 shows the phase diagram of the QCD matters predicted by the theory and the values of T and μ that are accessible experimentally in

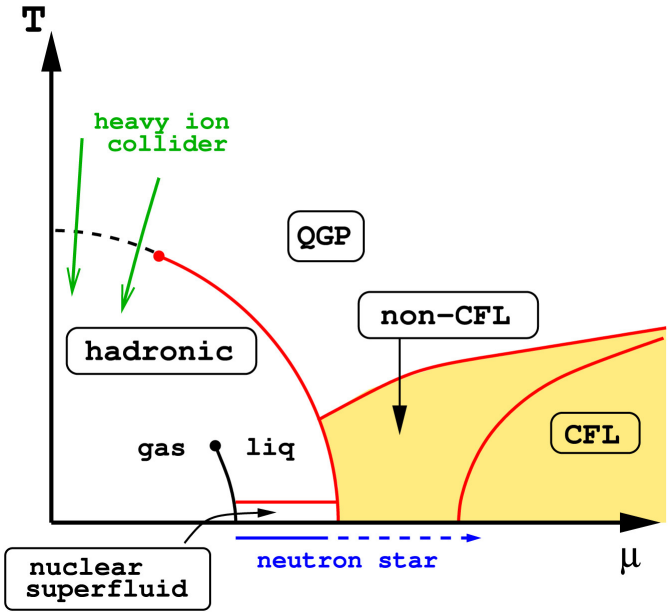

Figure 1.4: Schematic nuclear matter phase diagram from [12]. QGP refers to the Quark Gluon Plasma state, CFL (Colour-Flavour Locked) corresponds to the colour superconducting phase that is present in systems with high baryon chemical potential (e.g. core of neutron stars, from 5 to 10 times the baryon chemical potential of ordinary matter). The green arrows represent the phase space probed by collider experiments at the Relativistic Heavy Ion Collider (RHIC) and at the LHC.

high energy heavy ion collisions at colliders.

The origin of the phase diagram (T= μ = 0 GeV) corresponds to the QCD vacuum. At T= 0 GeV, μ is the energy required to create a baryonic state, thus ordinary QCD matter (proton, neutrons and nuclei) sits at almost zero temperature and $\mu \approx 1$ GeV. Moving further along the μ axis there is a phase transition to the deconfined state that has been hypothesised to be present in the core of neutron stars [13]. In a similar way when moving towards $T \gg \Lambda_{\mathrm{QCD}}$ and $\mu \approx 0$ the systems become similar to the primordial universe and undergoes a crossover transition to a deconfined state called Quark Gluon Plasma (QGP). As the temperature increases, the average momentum exchange between the constituents increases as well and the interaction becomes less and less strong. Quarks and gluons are no longer confined in colour singlets and they constitute a plasma of free coloured partons. The energy density ϵ and pressure p in this state of matter can be approximated using the equations of state of an ideal gas of massless particles confined in a bag of volume V [14]:

$$p = \frac{\pi^2}{90} n_{\mathrm{DOF}} T^4, \quad \epsilon = 3p \tag{1.1}$$

where n_{DOF} is the number of different particle states (degrees of freedom, DOF) populating the system. This simple approximation foresees a dramatic increase of pressure on the edge of the first order transition from a pion gas, with 3 DOF, to the QGP, containing $(16 + \frac{21}{2} n_{\mathrm{f}})$ DOF.

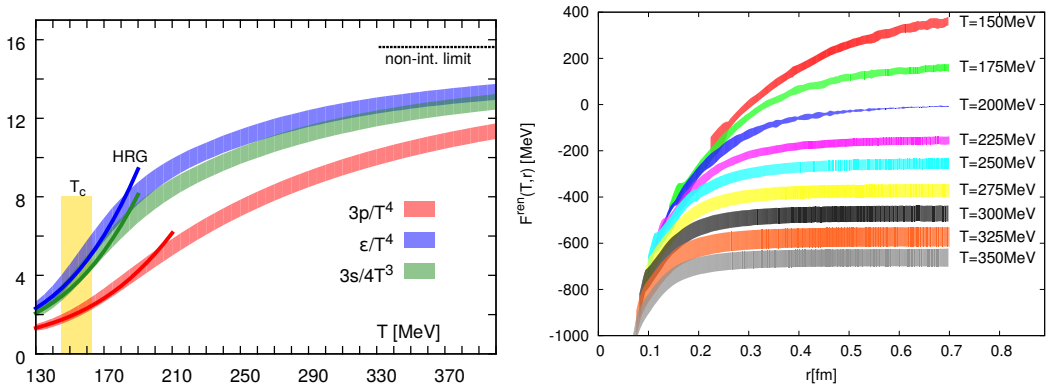

(a) (b)

Figure 1.5: On the left: QCD equation of state [16] as predicted by the Hadron Resonance Gas model and Lattice QCD calculations. On the right: free energy for heavy $q\bar{q}$ pair computed with continuum extrapolated Lattice QCD as a function of the distance and at different temperatures.

This prediction agrees qualitatively with the Hadron Resonance Gas model [15] and the Lattice QCD predictions (Figure 1.5a), that foresee an exponential increase of the energy density at increasing temperature in the crossover transition from hadronic gas to QGP.

At the same time, the interaction potential between two quarks, that in the vacuum is parametrised as a Cornell potential

$$V(r) = -\frac{\alpha(r)}{r} + kr, \tag{1.2}$$

where α is the strong coupling and k is the $q\bar{q}$ string tension induced by the gluon self interaction, is modified by the presence of the coloured medium of the deconfined phase that screens the interaction between quarks. Inside the medium the potential becomes:

$$V(r) = -\frac{\alpha(r)}{r} e^{-r/r_D}. \tag{1.3}$$

The potential is modulated by an exponential, driven by the attenuation length r_D that is called *Debye radius* such that hadrons with a radius larger than r_D cannot bind in the medium. The density of free colour charges in the plasma depends on the temperature ($\rho \propto T^3$), corresponding to the colour interaction attenuation with $r_D \sim 1/(gT)$where g is the coupling constant of the interaction in the medium[1]. Figure 1.5b shows the Lattice QCD prediction for the $q\bar{q}$ potential of heavy quarks [17]: with increasing temperature the evaluated potential flattens at large radii confirming the Debye screening expectations. While the Debye radius evolves with the temperature, the $q\bar{q}$ potentials at different temperatures converge at small

[1] g is tightly related to α_s by the relation $\alpha_s = \frac{g^2}{4\pi}$

distance. This is expected as the interactions at small radii (high transferred momenta) should not be affected by medium effects at finite temperature. Currently available QCD calculations [16, 18], at vanishing or finite μ, predict a cross over transition to the Quark Gluon Plasma at a critical temperature (T_c) around 150 MeV.

1.3 Heavy Ion Collisions

Currently the only known way to cross the phase boundary between ordinary hadronic matter and QGP in the laboratory is by colliding ultra–relativistic heavy ions. The first experiments on heavy ions collisions (HIC) was performed at the Bevalac accelerator, at the Lawrence Berkeley National Laboratory, probing collisions at the energy of ≈ 2 GeV/nucleon. Starting from then, many HIC experiments at higher and higher energies took place. Nowadays there are two main hadron colliders with an active HIC program: the *Relativistic Heavy Ion Collider* (RHIC) at the Brookhaven National Laboratory (BNL) and the *Large Hadron Collider* (LHC) at CERN. There are also two accelerators with experiments dedicated to the study of HIC at fixed target: the *Super Proton Syncrotron* (SPS) at CERN and the *Schwerionensynchrotron* (SIS) at the *Gesellschaft für Schwerionenforschung* (GSI).

1.3.1 Smashing ions, colliding nucleons

A collision between composite systems with finite dimensions, like the atomic nuclei colliding at the LHC, can be modelled starting from the constituents of the system. Indeed, it is natural to think about a HI collision as the sum of the interactions between the constituent nucleons of the two colliding nuclei. The relevant parameters in such a description are the number of nucleons participating in the interaction between the nuclei N_{part} and the number of binary collisions between two nucleons N_{coll}. These two parameters are correlated with the impact parameter of the collision $\vec{b}$. The impact parameter is defined as the vector connecting the centres of the colliding nuclei projected on the transverse plane to the nuclei momenta. Figure 1.6 shows a sketch of the colliding nuclei and it illustrates how the impact parameter is defined.[2]

The typical atomic nucleus radius is of the order of some femtometres and that is the maximum length of the impact parameter: a direct experimental measurement of $\vec{b}$ is then precluded. Similarly the direct measurements of N_{part} and N_{coll} are not possible. Nevertheless using phenomenological models of HIC it is possible to correlate these microscopic variables with measurable quantities such as the total number of particles produced in the collision.

Such a model for HIC is the Glauber Model[3]. Within this model nucleons are considered to be point like and independent inside the colliding nuclei, and only hadronic interactions are

[2] One of the two colliding nuclei is arbitrarily taken as the target and the impact parameter vector points towards the projectile centre, as shown in Figure 1.6

[3] A full description of the Glauber Model applied to HI collisions can be found in [19]

considered (i.e. there is no difference dealing with neutrons or protons) and each interaction does not deflect the trajectories of colliding nucleons. Moreover the model assumes a continuous nuclear density function $\rho(r)$ and that the interaction cross section of nucleons does not depend on the number of collisions they undergo. These assumptions, also known as *optical limit*, allow us to derive, for instance, an analytical expression for N_{coll}. Following the approach illustrated in [19], it is possible to define the nuclear overlap function for two colliding nuclei (A and B) as the probability of finding a nucleon in both the colliding nuclei inside the overlap region in the transverse plane. Following the notation introduced in Figure 1.6:

$$T_{AB}(\vec{b}) = \int T_A(\vec{s})\, T_B(\vec{s}-\vec{b})\mathrm{d}^2 s, \tag{1.4}$$

where $T_A(\vec{s})$ and $T_B(\vec{s})$ are called *thickness functions* for the nuclei A and B respectively and they represent the probability of finding a nucleon in the unit transverse area located at $\vec{s}$:

$$T(\vec{s}) = \int \rho(\vec{s}, z)\mathrm{d}z. \tag{1.5}$$

Starting from these quantities, the probability of observing an interaction between two nucleons sitting in the overlap region is defined as the product of the nuclear overlap function and the total inelastic cross section between two nucleons σ_{inel}. As outlined in the assumptions of the optical limit, each nucleon does not deflect its trajectory after the interaction with another nucleon thus each nucleon can participate in more than one binary collision. As a consequence it is possible to compute the probability of having n binary collisions between the nuclei A and B (having A and B nucleons respectively), out of the maximum number of collisions AB, using the binomial statistics:

$$P(n, \vec{b}) = \frac{(\mathrm{AB})!}{n!(\mathrm{AB}-n)!}\left[T_{AB}(\vec{b})\sigma_{\text{inel}}\right]^n \left[1 - T_{AB}(\vec{b})\sigma_{\text{inel}}\right]^{\mathrm{AB}-n}. \tag{1.6}$$

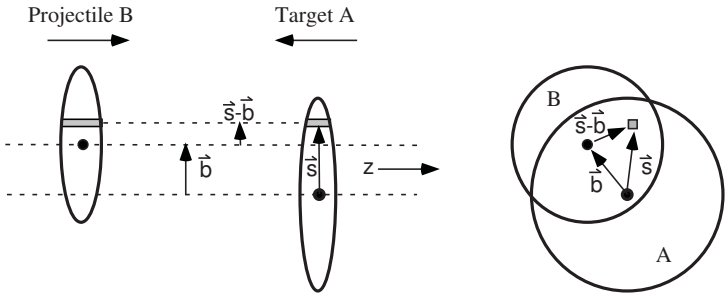

Figure 1.6: Sketch of the longitudinal view and transverse view of an HI collision taken from [19]. In the side view, the colliding nuclei are drawn as ellipses to represent the Lorentz boost contraction due to their momentum.

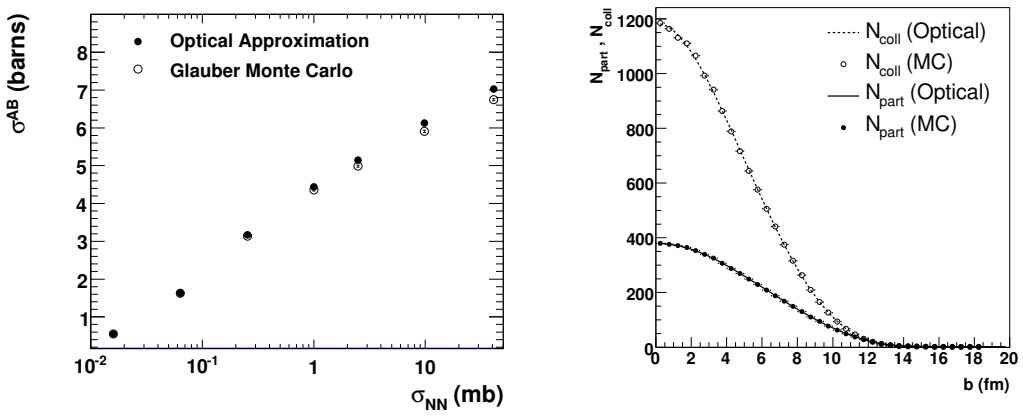

(a) (b)

Figure 1.7: Comparison between quantities computed with the optical Glauber Model and with the Glauber Model Monte Carlo taken from [19]. On the left the results for the total inelastic cross section for HI collision as a function of the input σ_{inel} are shown. On the right the results for N_{part} and N_{coll} as a function of the impact parameter are shown.

The N_{coll} expression as a function of the impact parameter is derived from this expression, summing all the possible numbers of collisions weighted by their own probability and using the definition of the mean of the binomial distribution:

$$N_{\text{coll}}(b) = \sum_{n=1}^{\text{AB}} nP(n,b) = \text{AB}\,T_{AB}(b)\sigma_{\text{inel}}. \tag{1.7}$$

In the last equation the impact parameter vector $\vec{b}$ has been replaced with its norm as the direction of the vector plays a role only for polarised nuclei. As a consequence the double differential interaction cross section for two colliding nuclei can be integrated to obtain the total inelastic cross section as a function of the impact parameter:

$$\begin{aligned} \frac{\mathrm{d}^2\sigma^{AB}_{\text{inel}}(\vec{b})}{\mathrm{d}b^2} &= \sum_{n=1}^{AB} P(n,\vec{b}) = 1 - \left[1 - T_{AB}(\vec{b})\sigma_{\text{inel}}\right]^{\text{AB}} \\ \Rightarrow \sigma^{AB}_{\text{inel}}(b) &= \int_0^{\infty} 2\pi b\mathrm{d}b \left\{1 - \left[1 - T_{AB}(\vec{b})\sigma_{\text{inel}}\right]^{\text{AB}}\right\}. \end{aligned} \tag{1.8}$$

As it has been shown, under the optical limit assumptions and with the input of the $\rho(\vec{s})$ and σ_{inel}, N_{coll} and N_{part} depend on the impact parameter $\vec{b}$. The main flaw in the approach of the optical limit calculations is the use of continuous density functions and integrals for quantities that are discrete in nature and that can fluctuate event by event. An alternative approach can be found in the Glauber Monte Carlo Model. In this approach the colliding nuclei geometry is generated by spawning their constituent nucleons in the space according to their nuclear density functions. The impact parameter is then generated according to the

relation $d\sigma/db = 2\pi b$ derived from 1.8. Once the impact parameter and nuclei geometry are generated, the collision between the nuclei is treated as the superposition of single binary collisions between the constituent nucleons. In these simulations a binary collision occurs when a particular condition on the distance d between two nucleons from A and B on the transverse plane is satisfied (e.g. $d \leq \sqrt{\sigma_{\text{inel}}/\pi}$). Within this method the number of N_{part} and N_{coll} can be easily computed by counting the number of wounded nucleons and the number of collisions in the simulation. Moreover, Monte Carlo Glauber simulation allows for simulation of the particles generated in the collision and can be used as input for impact parameter estimation in HI experiments, as it will be shown in the Chapter 3. The estimation of geometric quantities, such as N_{part} and N_{coll}, converges to the same values for the Glauber Monte Carlo and the Optical Glauber Model (Figure 1.7a). On the other hand Optical Glauber Model overshoots the estimated nucleus–nucleus inelastic cross section for high input σ_{inel} with respect to the Glauber Monte Carlo. The Optical Glauber Model gets the same $\sigma^{\text{AA}}_{\text{inel}}$ of the Glauber Monte Carlo when the input σ_{inel} is smaller and the approximation of point–like scattering centres is valid.

1.3.2 Space time evolution of Heavy Ion collisions

As already mentioned, a long lived and strongly interacting system is created when two ultrarelativistic atomic nuclei collide. The evolution of such a system, as well as the characterisation of its properties, is one of the subject of investigation of HI experiments. Figure 1.8 summarises in a space time plot the current view on the evolution of a HI collision [20]:

1. for $t < 0\,\text{fm}/c$: the two atomic nuclei travel in the beam line. At the relativistic energies reached at the modern accelerators, the nuclei are strongly Lorentz contracted in the laboratory reference frame (by a factor 100 and 2700 at the RHIC and at the LHC respectively);

2. at $t = 0\,\text{fm}/c$: collision time. The geometry of the collision can be described using the Glauber Model, as outlined in the previous section;

3. for $0 < t \lesssim \tau_0 \sim 1\,\text{fm}/c$: due to their nature and the fundamental quantum mechanics uncertainty relation between time and energy ($\Delta E \Delta t \geq 1/2$), hard processes (i.e. process with high transferred momentum) between the colliding partons occur at the very first instants of the collisions. In this phase, called *pre–equilibrium*, all the particles with high energy (either high momentum or/and high mass), are produced. The typical time scale for such processes is 0.1 fm/c. In high energy collisions, the nuclei momentum is such that, in the first instants of the collision, their constituent partons undergo several interactions, losing energy in the mid–rapidity[4] region ($y \approx 0$), and then they escape at forward rapidities ($|y| \gg 0$). The resulting system has a hot, interacting medium at mid–rapidity with vanishing baryonic chemical potential. The baryonic potential carried by

[4] The rapidity is defined, for a particle with momentum $p^\mu = (E, \vec{p})$, as $y = \frac{1}{2}\log\left(\frac{E+p_z}{E-p_z}\right)$, with z parallel to the beam direction.

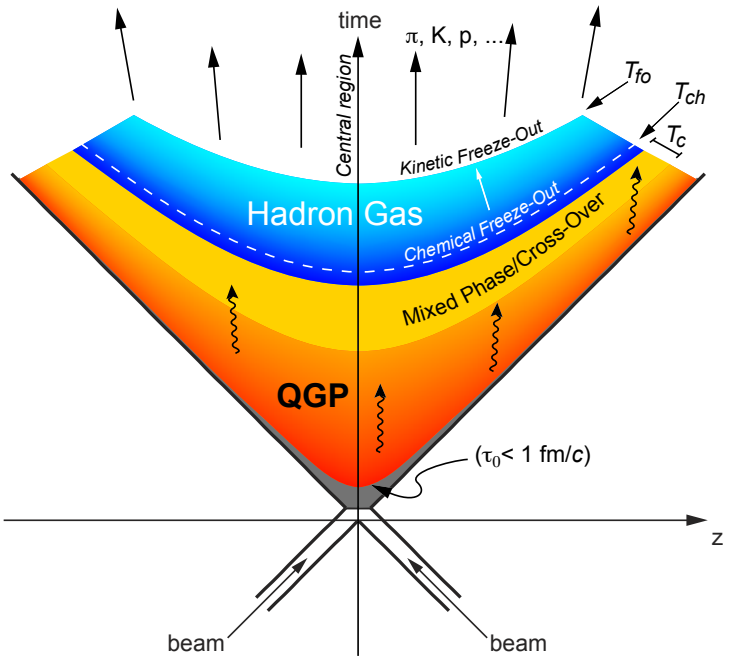

Figure 1.8: Evolution of a Heavy Ion collision represented in a space time diagram. The z direction is parallel to the beam line.

the colliding nuclei is brought at forward rapidity by the escaping valence quarks and by the nucleons that did not participate in the collision (often called *spectators*). In HI collisions at RHIC and at LHC, the energy density is such that a transition to the QGP state is expected. After a short strong parton rescattering phase, the obtained droplet of QGP matter reaches the equilibrium at his proper time τ_0;

4. for $1 \lesssim t \lesssim 10\,\mathrm{fm}/c$: the equilibrated QGP droplet rapidly expands under the push of the thermal pressure gradients generated at the system boundaries. This phase of rapid expansion of the QGP droplet is commonly modelled using relativistic hydrodynamics [21] which provide useful insights to interpret the experimental data, as shown in the following. With its expansion the system cools down, crossing eventually the phase boundary between Quark Gluon Plasma and ordinary hadronic matter;

5. for $10 \lesssim t \lesssim 15\,\mathrm{fm}/c$: when the critical temperature between the two phases is reached, the hadronisation starts and the system gradually evolve into an interacting *hadron resonance gas*. While expansion and contextual cooling of the systems continues in this phase, elastic and inelastic interactions among the hadrons within the system continue to occur. The instant in which the momentum exchange between hadron is not sufficient for inelastic interactions it is called *chemical freeze–out*. Since no other inelastic processes will take place, the relative abundances of different particle species are fixed after the chemical freeze–out. The second landmark in the evolution of the hadron gas is the *kinetic freeze–out*, when the hadrons stop interacting with each other

and the particle momenta are fixed;

6. for $t \gtrsim 15\,\mathrm{fm}/c$: hadrons created in the collision escape the interaction region with no further interaction. This regime is also known as *free hadron stream*.

The last step, not mentioned in the list, is of course the detection by the experimental apparata of the particles produced in the collisions: the technologies and methodologies implied in this last step will be presented in the Chapter 3. In the following it will be shown how properties of the systems and characteristics of its evolution can be inferred by the measurement of particle production spectra and particle correlations.

1.4 Nuclei production in Heavy Ion collisions

The observation of light nuclei and anti–nuclei production in Heavy Ion collisions leads to a major puzzle: how these loosely bound objects could bind at the temperature reached in HI collisions? While the experimental techniques used to measure the production spectra of light nuclei and anti–nuclei are the main subject of this thesis, the following two sections are dedicated to a brief description of the major two classes of models that try to explain such a strange phenomenon: the Statistical Hadronisation Models (SHMs) and the Coalescence model [22].

1.4.1 Statistical Hadronisation Models

The SHM was born from the necessity of describing the abundances of different particle species produced in the collision between particles. As outlined in [15], the first prototype of the model was pioneered by Enrico Fermi and evolved until the Hagedorn formulation that was able to describe successfully the production rate in proton–proton collisions.

The general idea behind these models (often called Thermal Models) is that the final state of the interaction is composed by all the particle states compatible with the conservation laws imposed by the underlying theory of interaction (in our case the Standard Model of particle physics). The relative abundance of different particle states is set by the maximisation of the total phase space filled by the system, to which each particle species contributes according to its partition function. These models are of particular interest in HI collisions as the presence of an expanding medium that eventually reaches the thermal equilibrium seems appropriate for the statistical hadronisation approach. As described in [12], the system created in a relativistic HIC is large enough to be modelled using the Grand Canonical ensemble. This formalism can be used as the experiments measure only the characteristics of a small portion of the system, like the central rapidity region in the case of the ALICE central detectors. This part of the phase space is in equilibrium with a thermal reservoir (the rest of the medium created in a HIC) and quantities like energy, baryon number, charge and isospin are conserved on average. Within the Grand Canonical formalism the parameters describing the equilibrium condition of a HIC

include the temperature T and the baryon chemical potential μ_B. The partition function of the system can be written as:

$$Z(T,V,\mu) = \mathrm{Tr}\left[e^{-\beta(H-\sum_i Q_i\mu_{Q_i})}\right] \quad \text{with } \mu = \sum_i Q_i\mu_{Q_i} \quad \text{and } \beta = \frac{1}{T} \tag{1.9}$$

where V is the volume of the system at equilibrium (also known as canonical volume) and μ_{Q_i} is the chemical potential associated to the conserved quantum number Q_i. For a strongly interacting medium created in relativistic HIC, the main conserved quantum numbers are the electric charge Q, the strangeness content of the system S and the baryon number B. The Hamiltonian H of a Hadron Resonance Gas is used as it is able to describe the interaction of a strongly interacting medium reproducing over a wide temperature range the equation of state obtained with LQCD (Figure 1.5a) before the transition to a deconfined state. The choice of the mesonic, baryonic and resonance states considered in the Hamiltonian is matter of the implementation of the model and it determines the maximum temperature that can be described accurately. The product of the partition functions Z_i of all the particle states in the Hadron Resonance Gas is equal to the total partition function of the system:

$$Z(T,V,\mu) = \prod_i Z_i(T,V,\mu_i) \quad \rightarrow \quad \log Z(T,V,\mu) = \sum_i \log Z_i(T,V,\mu_i). \tag{1.10}$$

The Z_i functions, defined as

$$\log Z_i(T,V,\mu_i) = \frac{Vg_i}{2\pi^2}\int_0^\infty \pm p^2 \mathrm{d}p \log\left(1 \pm \lambda_i(T,\mu_i)e^{-\beta\epsilon_i}\right), \tag{1.11}$$

are the Fermi–Dirac (+) and Bose–Einstein (-) partition functions for fermions and bosons respectively. The g_i constant is the number of spin and isospin degenerate state for the species i (spin-isospin degeneracy factor) and ϵ_i is the energy of one particle of the species with momentum p ($\epsilon_i = \sqrt{p^2 + m_i^2}$). The dependence on the chemical potentials is encoded within the *fugacity* λ_i:

$$\lambda_i(T,\mu_i) = e^{\beta(B_i\mu_B + S_i\mu_S + Q_i\mu_Q)} = e^{\beta\mu_i} \tag{1.12}$$

where B_i, S_i and Q_i are the baryon number, strangeness content and electric charge associated with the particle species and μ_B, μ_S and μ_Q are the respective chemical potentials. As illustrated in [23], doing a Taylor expansion of the logarithm and integrating over the momentum, the partition function for the species i becomes

$$\log Z_i(T,V,\mu_i) = \frac{VTg_i}{2\pi^2}\sum_{k=1}^{\infty}\frac{(\pm 1)^{k+1}}{k^2}\lambda_i^k m_i^2 K_2(\beta k m_i) \tag{1.13}$$

with the (+) for bosons and the (-) for fermions and with K_2 being the second modified Bessel function. For a system described by the Grand Canonical ensemble, the average number of

particle for the species i, $\langle N_i \rangle^{\text{th}}$, is defined as:

$$\langle N_i \rangle^{\text{th}}(T,V,\mu_i) = \frac{1}{\beta}\frac{\partial}{\partial \mu_i}\log Z_i(T,V,\mu_i) = \frac{VTg_i}{2\pi^2}\sum_{k=1}^{\infty}\frac{(\pm 1)^{k+1}}{k}\lambda_i^k m_i^2 K_2(\beta k m_i), \tag{1.14}$$

but it does not describe fully the particle production measured in a HIC. For the measured yields one should consider the feed–down contributions from all the other particle species (resonances) j in the thermal system that can decay strongly in a final state containing particles of the species i:

$$\langle N_i \rangle(T,V,\mu) = \langle N_i \rangle^{\text{th}}(T,V,\mu_i) + \sum_j \Gamma_{j\to i}\langle N_j \rangle^{\text{th}}(T,V,\mu_j). \tag{1.15}$$

This definition of particle yields holds in the limit of a low density system, where the repulsion interaction between the hadrons constituting the systems is negligible. While the treatment of these interactions, introducing an eigenvolume for each particle state in the system as described in [23], is still matter of active research (especially for light nuclei where it is difficult to neglect) [24], equation 1.15 already outlines the crucial dependencies of the observed particle yields on the temperature, volume and the three chemical potentials (μ_B, μ_Q and μ_S). Out of these five parameters, two are constrained from the HI collision conditions as no net strangeness is present in the colliding nuclei, thus $\mu_s = 0$, and μ_Q is fixed by the isospin asymmetry in the collision. One might think that also the baryon chemical potential is constrained in HI collisions, but this is not true as the "amount of baryonic number" transported in the equilibrium region varies with the energy of the collision. The dependence on the volume of the system can be removed looking at ratio between the yields of different particle species, which therefore depends only on the temperature of the system and on the baryon chemical potential.

Some extensions of this model can be formulated postulating the emission of some particle species (e.g. strange particle) out of the grand canonical equilibrium. Such models, for instance that described in [25], introduce some additional phase space occupancy factors that are useful to describe systems where the suppression of the production rate for some particle species (e.g. strange particles in small systems) is observed.

In the framework of the thermal models, light nuclei yields arise naturally when the chemical freeze–out temperature and the baryon chemical potential are set. A possible explanation on how the light nuclei can survive to the high temperature of the chemical freeze–out was pointed out in [26]: as the system expansion after the chemical freeze–out is supposed to conserve the entropy density, such conservation could be the steering mechanism for the nuclei production. Finally, from the fit of the particle abundances at lower energies, the authors of [26] predicted, using the thermal model, the yields of (hyper-)(anti-)nuclei at the LHC energy (Figure 1.9).

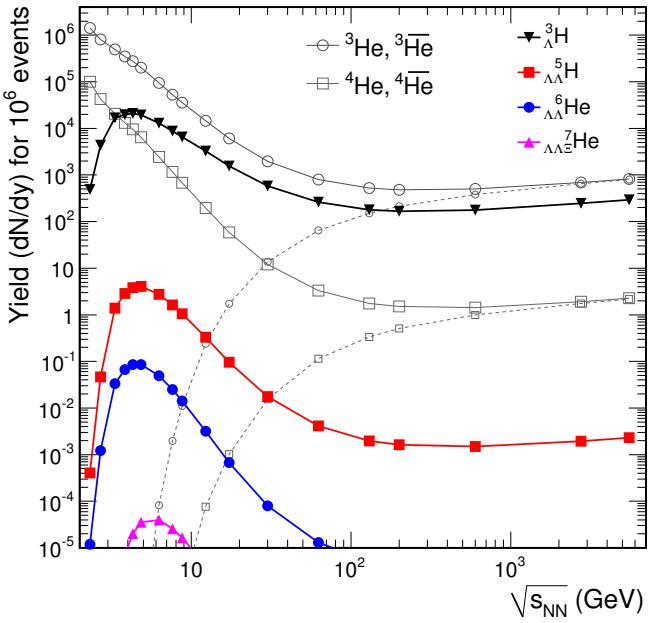

Figure 1.9: Thermal model predictions for the production of various nuclei, anti-nuclei and hyper–nuclei as a function of the ion collision energy taken from [26]. One striking feature of the thermal model predictions is the difference between matter and anti–matter: at low collision energy the baryon chemical potential differs significantly from zero and the $e^{\beta B_i \mu_B}$ term in the particle yield favours matter over anti–matter. As the energy increases, μ_B decreases and this difference vanishes.

1.4.2 Coalescence Models

Another theoretical approach that tries to explain the measured light nuclei production in HIC is represented by the hadron coalescence models [22]. In these *static* models the nuclei are created at the kinetic freeze–out and there is no attempt to give detailed description of the interactions that lead to their formation. The coalescence models make available a clear prediction about the momentum distribution of the produced light nuclei as a function of the production spectra of the constituent nucleons. The fundamental idea that enables this prediction is that if A constituent nucleons are close enough in phase space at the kinematic freeze-out they can bind to form a nucleus of the species i:

$$E_i \frac{\mathrm{d}^3 N_i}{\mathrm{d}p_i^3} = B_A \left(E_p \frac{\mathrm{d}^3 N_\mathrm{p}}{\mathrm{d}p_\mathrm{p}^3} \right)^A , \tag{1.16}$$

where the proton momentum spectrum is used as a proxy of the constituent neutron spectrum. These nucleon spectra are not those measured in the experiments, but the ones produced in the collision and not yet modified by the coalescence mechanism. Nevertheless, the amount of observed nuclei is so small with respect to the amount of protons and neutrons created that

this difference is often neglected in the practice. This is also the main reason why protons are used in the formula: they are easier to measure in an experiment. The goodness of this simplification can be tested experimentally by comparing the value of the coalescence parameter, B_A, of nuclei with the same A but different nucleon content (e.g. ^{3}H and ^{3}He): any deviation between the observed coalescence parameters would point to different momentum distributions of neutrons and protons. The simplest formulation of the coalescence models consider only the momentum space and not the space–time, thus the coalescence parameter can be expressed, neglecting the nucleon spin, as

$$B_A = \left(\frac{4}{3}\pi p_0^3\right)^{A-1} \frac{m_i}{m_p^A}. \tag{1.17}$$

where p_0 is maximum distance at which coalescence can happen. This is the only dependence of the coalescence parameter foreseen by this formulation of the model, that is the most commonly used for the comparison with the data. Other extensions of the models predict a dependence on the geometry of the system. For instance, if one assumes that neutrons and protons are emitted in thermal and chemical equilibrium [27], in the limit of high temperature their momentum spectra can be described by the Boltzmann–Gibbs distribution[5]:

$$E\frac{\mathrm{d}^3N}{\mathrm{d}p^3} = gV\frac{m_\mathrm{T}}{8\pi^3}e^{-\beta m_\mathrm{T}}, \tag{1.18}$$

where g is the spin–isospin degeneracy of the nucleon. Using this expression in the definition of the coalescence parameter a dependence from the volume V of the emitting source becomes explicit:

$$B_A = \frac{2J_i+1}{2^A}\left(\frac{8\pi^3}{V}\right)^{A-1} \frac{m_{i\mathrm{T}}}{m_\mathrm{T}^A}, \tag{1.19}$$

where J_A is the total angular momentum of the nucleus. This formulation of the model predicts a smaller coalescence parameter for central collisions (bigger volume) than in peripheral collisions (smaller volume). In a more sophisticated approach [28] the volume of the emitting system can be computed starting from femtoscopic measurements of the profile radii:

$$V_\mathrm{eff} = (2\pi)^{3/2} R_\mathrm{side}^2 R_\mathrm{long}, \tag{1.20}$$

Using this expression and a proper quantum mechanical approach to describe the nucleus structure, the expression for the coalescence parameter, for the deuteron in this case, becomes:

$$B_2 = \frac{3\pi^{3/2}\langle C_d\rangle}{2m_\mathrm{T}R_\mathrm{side}^2 R_\mathrm{long}}, \tag{1.21}$$

[5] In the expression of the Boltzmann–Gibbs distribution the transverse mass m_T is used. It is defined as $m_\mathrm{T} = \sqrt{m^2 + p_\mathrm{T}^2}$

where $\langle C_d \rangle$ is the quantum mechanical coefficient that keeps into account the internal structure of the deuteron. The underlying assumption of 1.21 is that the emitting source has a gaussian profile and it is modified by the assumption of the commonly used box profile:

$$B_2 = \frac{3\pi^{3/2}\langle C_d \rangle}{2m_{\mathrm{T}}R_{\mathrm{side}}^2 R_{\mathrm{long}}} e^{2(\beta_p - \beta_d)(m_{\mathrm{T}} - m)}, \tag{1.22}$$

where β_p and β_d are the thermal slopes for protons and deuterons. The latter formulation of the coalescence parameter predicts not only the dependence on the system volume but also from the transverse momentum of the produced nucleus.

2 Probing the Quark Gluon Plasma

This Chapter is devoted to the description of a few of the experimental results that shed light on the features of the hot and dense medium created in high energy HIC. The first Section contains the description of the global event properties that corroborated the evidence of the formation of the Quark Gluon Plasma in HIC. These observables are also called Soft Probes as they are related to the particles originated in the QGP phase. Conversely the second section is then dedicated to the description of the particles created in the very first instants of the collisions and that interact with the medium. The study of these observables, often called Hard Probes, gives important insights about the energy loss of partons in the medium. In the last section the description of the production of electroweak particles in HIC can be found. With these particles it is possible to study different aspects of the QGP: from the photon spectra it is possible to inquire into the temperature of the early stages of the medium while the production spectra of the $W^{\pm}$ and Z bosons show how the nucleus structure modify the parton distribution function of the nucleons.

2.1 Soft probes

2.1.1 Momentum spectra of hadrons

Low momentum hadrons, often called soft hadrons, represent the large majority ($\approx 99\%$) of the particles produced in a HI collision. The study of the momentum spectra of identified particle gives important insights about the condition of the medium at kinetic freeze–out. Assuming a Boltzmann–Gibbs distribution for the particle emission at kinetic freeze–out, the particle spectra for the species i can be modelled as:

$$\frac{1}{m_{\mathrm{T}}}\frac{\mathrm{d}^2 N_i}{\mathrm{d}m_{\mathrm{T}}\mathrm{d}y} \propto e^{-\beta m_{\mathrm{T}}}. \tag{2.1}$$

These formulation keeps into account only the thermal component of the spectra and predicts a common emission temperature (β) for all the particle species. The measured spectra in HI collisions defy this prediction showing a different slope (i.e. temperature) for different

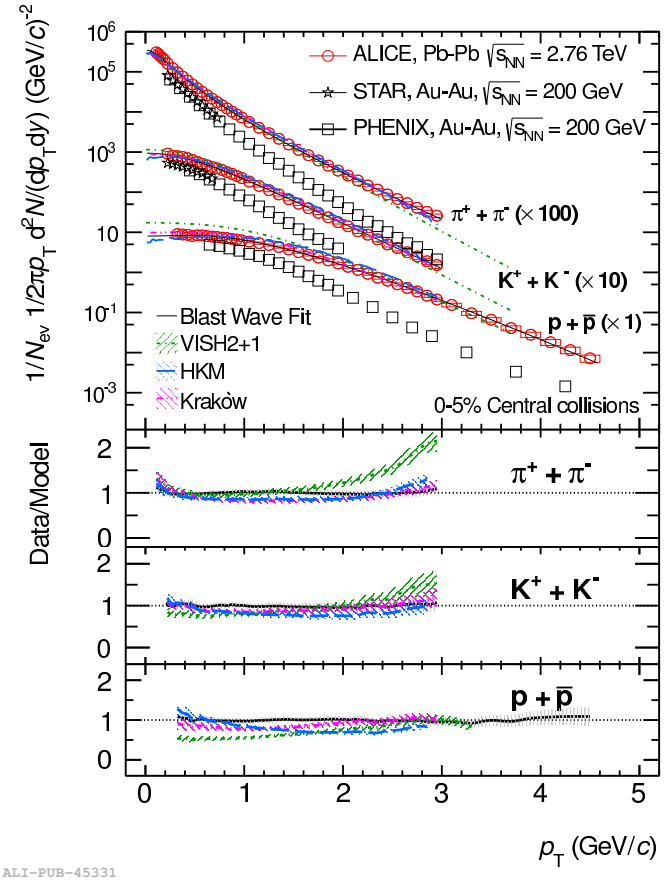

Figure 2.1: Pion, kaon and proton transverse momentum spectra in central (0-5%) Au–Au collisions at $\sqrt{s_{\rm NN}}$ = 200 GeV at the RHIC and in Pb–Pb collision at $\sqrt{s_{\rm NN}}$ = 2.76 TeV at the LHC (see [29] and references therein). The data are fitted with a Blast–Wave model (lines) and compared with three additional hydrodynamical models predictions (shaded areas).

particle species. This kind of behaviour can be interpreted adding a further component to the measured emission temperature for each particle species:

$$T_i = T_{\rm Kin} + \frac{1}{2} m_i \langle v_\perp \rangle^2, \tag{2.2}$$

where $T_{\rm Kin}$ is the temperature at kinetic freeze–out while the additional term keeps into account the mean kinetic energy acquired by the particles of the species i due to the hydrodynamical collective expansion along the transverse plane[1]. This phenomenon, called *radial flow*, modifies the production spectra pushing the mean transverse momentum of the emission at higher values the higher is the particle species mass. This can be also seen qualitatively from the particle spectra in Figure 2.1, where it is possible to see a steeper spectrum slope for pions (soft spectrum) while for protons the slope of the spectrum is reduced (hard

[1] $\langle v_\perp \rangle$ is the average transverse velocity acquired by the particles due to the hydrodynamical expansion.

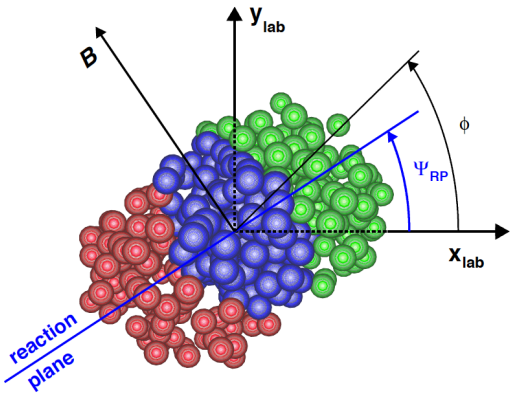

Figure 2.2: Sketch of the geometry of a HIC taken from [34]. The blue spheres represent the nucleons participating in the interaction, while the green and the red ones represent the spectators of the collision.

spectrum). Another interesting feature related to the radial flow is the evolution of the particle spectra shape with the collision energy: the production spectra measured at lower collision energy [30, 31] show a profile softer than the ones measured at the LHC energies [29]. This trend suggests the presence of a stronger radial flow in more energetic collisions and thus stronger pressure gradients driving the hydrodynamical expansion at the LHC. The radial flow interpretation of the slope modification of the production spectra is well captured by the comparison with the hydrodynamical calculations shown in Figure 2.1, yet either a full description of the hadronic phase following the hydrodynamical expansion (as implemented in the HKM model [32]) or some corrections due to the bulk viscosity at the freeze–out (as implemented in the Krakow model [33]) are required to obtain a proper description of the measured spectra over the full momentum range. Finally a simplified hydrodynamical model, corresponding to a Blast Wave description, is usually fitted simultaneously to the measured spectra of pions, kaons and protons in order to extract the temperature T_{Kin} and the mean radial velocity $\langle\beta_{\perp}\rangle$ of the particles at the kinetic freeze–out. From the results of these fits, the authors of [29] concludes that indeed both the radial flow velocity $\langle\beta_{\perp}\rangle$ and the kinetic freeze–out temperature T_{Kin} at the LHC energies are larger than those extracted at the RHIC collision energies.

2.1.2 Anisotropic flow

Another signature of the collective motions of particles created in HI collision is the presence of azimuthal anisotropies in the particle production spectra. In particular when considering the geometry of a collision between two nuclei overlapping only partially (Figure 2.2), a correlation between the emission angles of the particles and the impact parameter can be found. This

kind of azimuthal anisotropies can be measured by looking at the Fourier expansion in the azimuthal angle of the production spectra:

$$\frac{\mathrm{d}N}{\mathrm{d}\phi} \propto 1 + 2\sum_{n=1}^{\infty} v_n \cos[n(\phi - \Psi_n)], \tag{2.3}$$

where the magnitude of the anisotropy with respect to the symmetry plane at Ψ_n is quantified by the coefficients v_n. The typical almond shape of the overlap region between the colliding nuclei, when the impact parameter is large, creates a pressure gradient parallel to the plane defined by the beam direction and the impact parameter vector (the reaction plane). The reaction plane direction cannot be measured directly, instead the n^{th} order event planes[2] are used for the calculation of the Fourier expansion as shown in Equation 2.3. The flow of particles created by these pressure gradients is called *elliptic flow* and it contributes to the v_2 coefficient of Equation 2.3. Conversely the higher order Fourier coefficients are related to initial inhomogeneities of the colliding systems. The properties of the medium, such as the shear viscosity over entropy η/s, the bulk viscosity over entropy ζ/s and its lifetime, define how efficiently these initial geometric condition and inhomogeneities are translated in the v_n coefficients. For this reason, the detailed study and comparison of the experimentally measured v_n with the models permits to uncover the characteristics of the medium and the dynamics of its thermalisation. For instance, as discussed in [36], the v_n coefficients measured by the ALICE experiment in Pb–Pb collision at different collision energies (Figure 2.3) are compared with hydrodynamical calculations that combines the initial spatial anisotropy and the hydrodynamical response. From this comparison it is possible to inquire into the value of η/s and it is possible to state that the current v_n measurements favour a medium with small shear viscosity values.

2.2 Hard probes

2.2.1 High momentum particles and heavy flavours

High momentum quarks, as well as heavy flavour quarks (charm and beauty), can be created only at the very early stages of the collisions, when the processes at high transferred momentum occur. For this reason, the study of the hadrons with high momentum and/or containing heavy flavour quarks allows to inquire into the mechanisms driving the parton propagation and energy loss in the QGP. The processes that create such hard partons can be modelled with the perturbative QCD approach, thus if the collision between two nuclei is just the superposition of uncorrelated nucleon–nucleon collisions, the observed production cross section for hard particles when two heavy nuclei collide should be equal to the pp cross section scaled by the number of nucleon–nucleon collisions N_{coll}. In formulas: if a HIC is the incoherent sum of nucleon nucleon collisions, then the *nuclear modification factor*, defined

[2] An example of how the n^{th} order event plane direction can be computed is in [35]

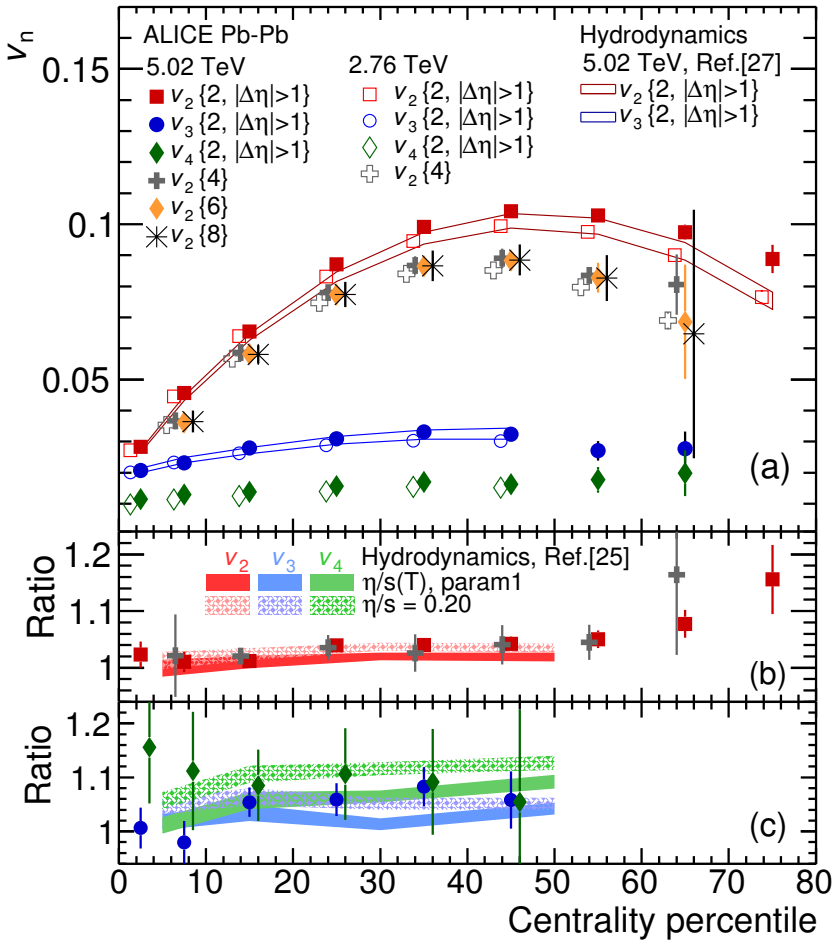

Figure 2.3: Panel (a): Fourier coefficients up to the fourth order measured by the ALICE experiment at different collision energies [36] as a function of the centrality percentile. The panels (b) and (c) show the ratio between the measurements at $\sqrt{s_{\rm NN}}$ =5.02 TeV and those at $\sqrt{s_{\rm NN}}$ =2.76 TeV. No striking difference between the two energies is seen, hinting that there is not a major change in the medium characteristics and thermalisation dynamics. The results are then compared with hydrodynamical models (see the references in [36]) showing a good agreement with the model using a small η/s value. Data points are shifted for visibility.

as

$$R_{\rm AA} = \frac{1}{\langle N_{\rm coll}\rangle}\frac{{\rm d}^2N_{\rm AA}/{\rm d}p_{\rm T}{\rm d}y}{{\rm d}^2N/{\rm d}p_{\rm T}{\rm d}y}, \tag{2.4}$$

should be equal to unity for hard processes. Studying the $p_{\rm T}$ dependence of the nuclear modification factor, other effects not related to the presence of a QGP can cause deviations of the $R_{\rm AA}$ from unity, for instance the Cronin enhancement [37] and the modification of the parton distribution functions of neutrons and protons inside the nuclei (mainly the nuclear

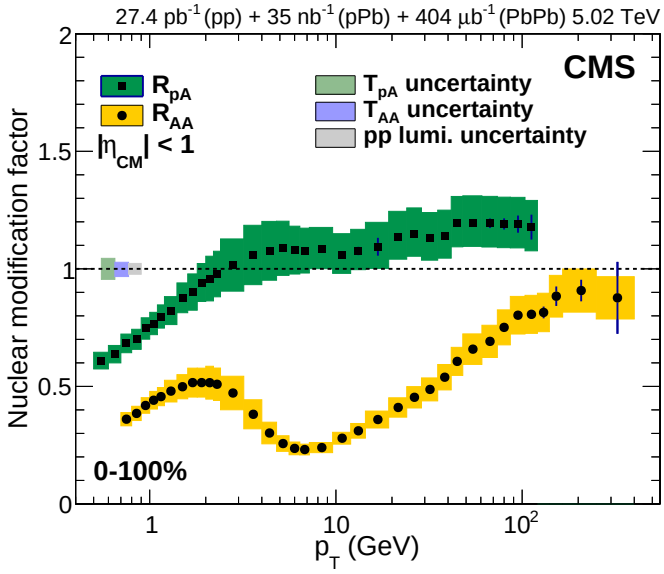

Figure 2.4: Nuclear modification factors of charged particles as a function of transverse momentum in p–Pb and Pb–Pb collisions at $\sqrt{s_{\mathrm{NN}}}$ =5.02 TeV measured by the CMS collaboration [38].The coloured boxes refer to the systematic uncertainties of the measurement while the vertical bars represent the statistical uncertainties.

shadowing). Nevertheless, it is possible to factorise these *cold nuclear matter* effects from the QGP induced effects by studying them separately in p–Pb collisions. Figure 2.4 shows the nuclear modification factors in p–Pb and Pb–Pb collisions measured by the CMS experiment. It is possible to see that the R_{pA} measured by CMS for hard particles ($p_{\mathrm{T}} \geq 3$ GeV/c) is close to one and it even overshoots one at very high transverse momenta. On the other hand, for $p_{\mathrm{T}} \geq 3$ GeV/c, the R_{AA} shows a clear suppression of the production of hard particles hinting for the presence of the energy loss of the partons in a hot and dense medium. At even higher transverse momentum the R_{AA} grows again to reach 1 ($p_{\mathrm{T}} \geq 100$ GeV/c): this trend is understood by the models reported in [38] and it can be naively interpreted as very fast partons that manage to escape the interaction region before the medium formation.[3]

The main difference between a generic high momentum particle and the study of heavy flavour is that while the parton from which the high momentum particle originates is unknown[4], heavy flavour hadrons allows to tag and study the energy loss of a specific heavy quark (either charm or bottom). Moreover the fragmentation functions of heavy quarks are such that a large fraction of the momentum carried by the original parton is transferred to the observed heavy flavour hadron. Thanks to this, it is possible to study in details the energy loss effects for heavy

[3] In this discussion the low momentum region of the nuclear modification factor has been neglected since the dominant processes for the production of such soft hadrons are expected to scale with the number of nucleons participating in the collision (N_{part}) and not with the number of binary collisions.

[4] According to QCD calculation light flavour particles with momentum ranging between 5 and 20 GeV/c originate from gluons while at higher momentum they are produced by the fragmentation of a light quark.

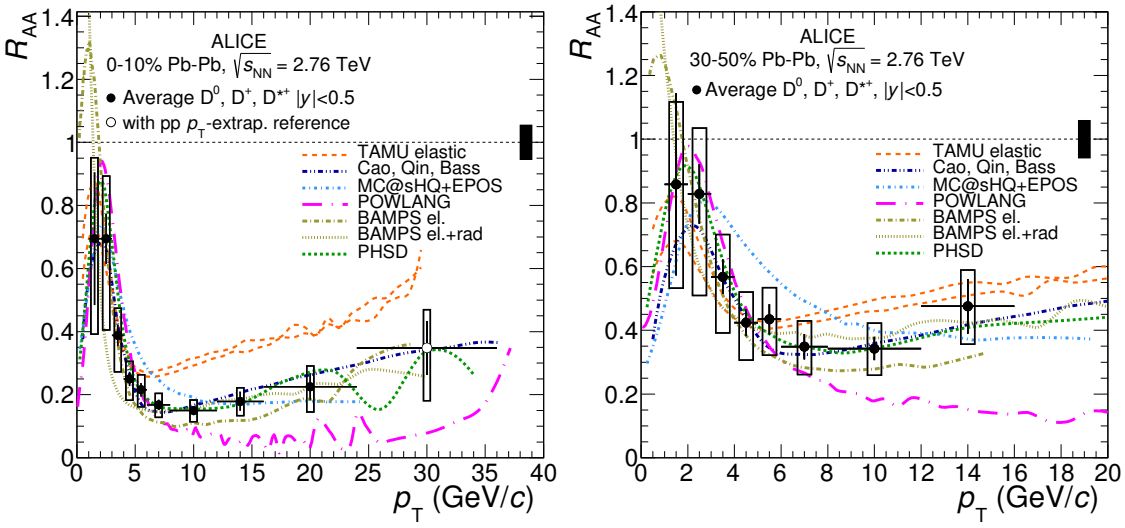

(a) Centrality 0-10%

(b) Centrality 30-50%

Figure 2.5: Nuclear modification factors of D mesons as a function of transverse momentum in Pb–Pb collisions at $\sqrt{s_{NN}}$ =2.76 TeV measured by the ALICE collaboration [39] in two centrality classes. The boxes refer to the systematic uncertainties of the measurement while the vertical bars represent the statistical uncertainties. The coloured lines correspond to different transport model predictions; see [39] for the detailed comparison and the reference therein for the descriptions of the models.

flavour quarks as a function of their momentum. There are two components contributing to the heavy flavour quark energy loss in the medium: the elastic scatterings with other partons (collisional energy loss) and the inelastic scatterings (radiative energy loss). The measurement of the R_{AA} of charmed mesons by the ALICE experiment compared with the transport models for heavy partons in the medium[5] (Figure 2.5), shows that the data favour those models including both collisional and radiative energy losses. Moreover in [39] the authors show that the ratio between the nuclear modification factor of D mesons and the one of charged particles is 1σ over the unity: this can be explained by the fact that the energy loss of gluons in the medium is larger than the energy loss of the charm quark because of the larger coupling of gluons with the coloured medium.

Finally, another interesting phenomenon related to hard processes in HI collisions is called *jet quenching*. In pp collisions, at the leading order (LO) in the vacuum (i.e. without any energy loss) dijets are physical objects consisting of two back-to-back jets of equal transverse momentum ($\Delta\phi_{\text{dijet}} \approx \pi$). If the two partons originating the dijet are created by a hard scattering in a HI collision, they interact with the medium losing part of their energy and changing their direction. As a consequence, depending on the length of the path followed inside the medium by each parton, the dijet structure is modified leaving a leading jet (the most energetic) and a subleading jet with less energy. In addition, the direction of the two jets might also show

[5]The details about the analyses and the comparison with the models can be found in [39] and references therein.

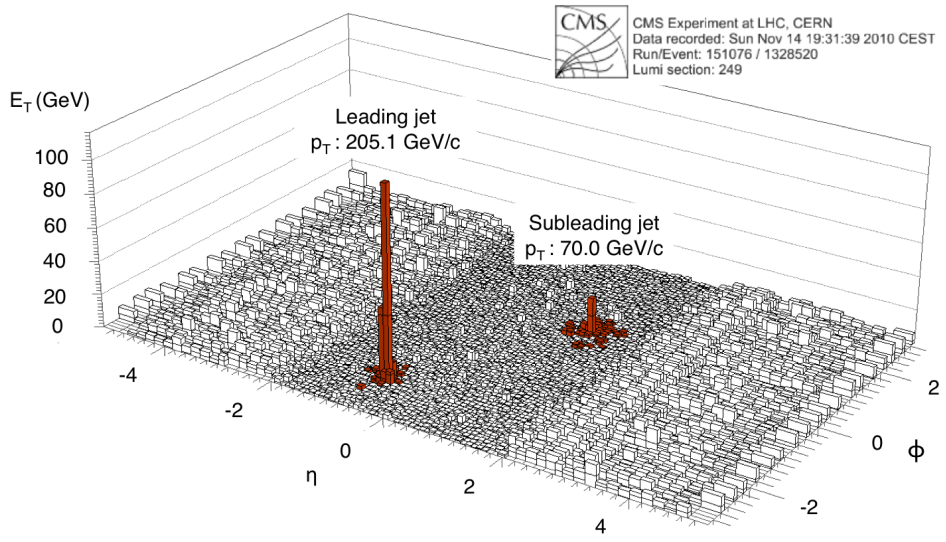

Figure 2.6: Event display of the sum of the energy deposit in the CMS electromagnetic and hadronic calorimeters as a function of the azimuthal angle ϕ and the pseudorapidity η for a Pb–Pb collision at $\sqrt{s_{\mathrm{NN}}}$ =2.76 TeV [40]. The leading and sub-leading jet structures are highlighted in red and labelled with their p_{T}.

large deviation from the $\Delta\phi_{\mathrm{dijet}} \approx \pi$ observed in pp collision. The measurements by the CMS experiment [40] (Figure 2.6 shows an example of dijet event in Pb–Pb collisions), show that the jet energy imbalance is present and significant for $120 \leq p_{\mathrm{T}} \leq 210$ GeV/c and that it is possible to recover this energy imbalance by keeping into account, in a wider cone around the subleading jet, the charged particles with transverse momentum down to 2 GeV/c. This observation indicates that the fragmentation functions for jets in the QGP favour the production of soft hadrons at large angles with respect to the leading parton direction.

2.2.2 Quarkonia

One of the most interesting features of a deconfined state of quark and gluons is the modification of the interaction potential between two quarks (see Section 1.2). As the Cornell potential describing the interaction between quarks in the vacuum becomes the Yukawa potential in the QGP, all the $q\bar{q}$ states whose radius is larger than the Debye length cannot bind as a consequence of the colour screening of the medium. As shown in Figure 1.5b, the Debye length decreases with increasing temperature suppressing more and more quarkonium states. If the $q\bar{q}$ pair cannot bind then they can either fragment (at high momentum) and form a hadron with light flavour content or they can pick another quark from the QGP and form an hadron with it. For this reason heavy flavour quarkonia states, $c\bar{c}$ and $b\bar{b}$ states, are good candidates to study the temperature of the QGP created in a HIC. The relative suppression in HIC with respect to pp collisions of a particular quarkonium state $q\bar{q}$ indicates that the temperature of the medium is such that the Debye length is smaller than the binding radius of

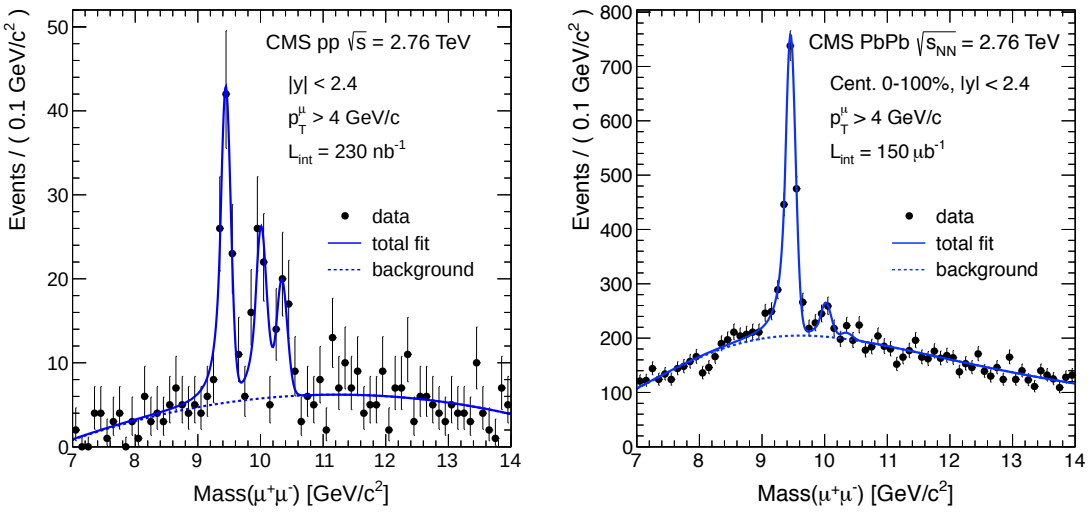

(a) pp collisions

(b) Pb–Pb collisions

Figure 2.7: Fit to the $\mu^+\mu^-$ invariant mass pairs in pp (on the left) and in Pb–Pb (on the right) collisions performed by the CMS experiment [41]. The three peaks corresponding to the $\Upsilon(1S)$,$\Upsilon(2S)$ and $\Upsilon(3S)$ states are clearly visible for pp collisions, whereas in Pb–Pb collisions a suppression is seen for the 2S and 3S states with respect to the 1S state.

the $q\bar{q}$ state under investigation.

Among the quarkonia states charmonia and bottomonia, which are $c\bar{c}$ and $b\bar{b}$ states respectively, are the most interesting: as charm and bottom quarks are heavy and thus produced rarely, the probability that a melted charmonium/bottomonium state recombines with another charm/bottom quark are low. ALICE collaboration results on the J/ψ nuclear modification factor in Pb–Pb collisions at $\sqrt{s_{\rm NN}}$ =2.76 TeV [42] show a smaller suppression for the J/ψ state with respect to what has been observed at lower energies. As highlighted in [43], these results suggest a late-stage formation of J/ψ states either by the recombination with other charm quarks in the medium [44] or during hadronisation, as suggested by some predictions done with the Statistical Hadronisation Model [45]. In the same collision system, the CMS collaboration measured the momentum and centrality integrated $R_{\rm AA}$ of 0.56 ± 0.08 (stat.) ± 0.07 (syst.), 0.12 ± 0.04 (stat.) ± 0.02 (syst.), and 0.03 ± 0.04 (stat.) ± 0.01 (syst.) for the $\Upsilon(1S)$, $\Upsilon(2S)$, and $\Upsilon(3S)$ states, respectively [41]. Since the nuclear modification factor for the $\Upsilon(3S)$ is compatible with the non–observation of the particle in Pb–Pb collisions, the CMS collaboration provided also an upper limit for the $R_{\rm AA}$, that is less than 0.10 at the 95% confidence level. Figure 2.7 shows an example of the fits to the invariant mass spectra of these three bottomonium states in pp and Pb–Pb collisions: already from a qualitative look at these mass spectra it is possible to see the relative suppression of the $\Upsilon(2S)$ and $\Upsilon(3S)$ states with respect to the $\Upsilon(1S)$ state in Pb–Pb compared to pp collisions. These results clearly show that the less the states are bound the more they are suppressed (sequential melting), as one would expect a priori from the modification of the $q\bar{q}$ potential in the QGP and confirm the leading

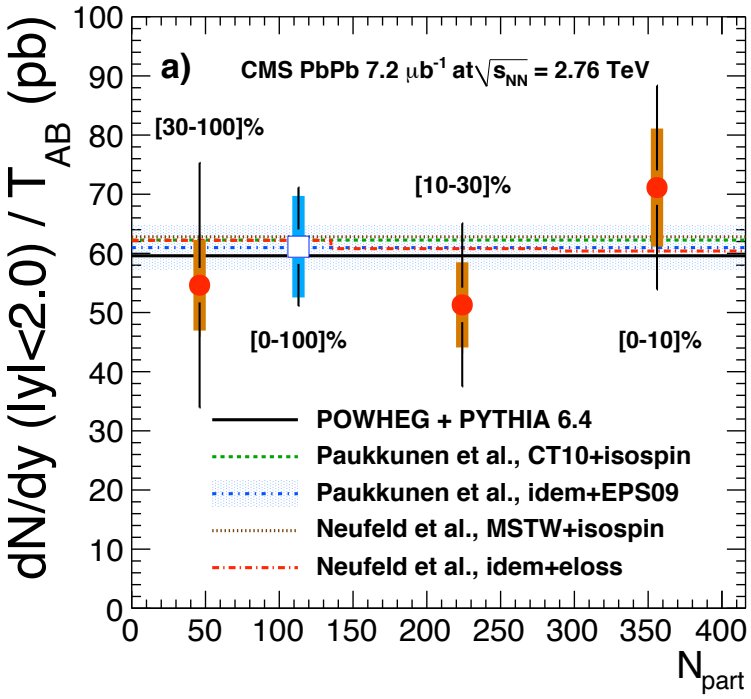

Figure 2.8: Yield of Z boson scaled on the nuclear overlap function measured by the CMS collaboration. As expected the yields are in agreement with the prediction of POWEG+PYTHIA for the pp collisions (see [46] for details).

role of the quarkonia study in the characterisation of the QGP state.

2.3 Electroweak probes

The study of electroweak probes is a useful instrument to cross check whether the medium created in HIC is indeed a droplet of QGP. Leptons, Z and $W^{\pm}$ bosons are *colour blind probes*, they do not interact in the Standard Model at the tree level with the QGP and they carry the information about the initial stages of the collisions without any modifications. For these reasons, no modification of the production spectra of these particles is foreseen in HI collisions, modulo the expected effects due to the modification of the nucleon parton distribution function in the nuclei and the scaling with the number of binary collisions N_{coll} (Figure 2.8). CMS Collaboration measured the nuclear modification factor for the Z boson and confirmed this expectation: the observed Z boson production nuclear modification factor in Pb–Pb collisions is compatible with unity [46].

Photons do not interact either at the tree level with the medium and those produced in the initial hard scatterings survive the QGP evolution unaffected. Nevertheless, the hot and dense medium created in a HIC emits itself thermal photons that cannot be distinguished by those

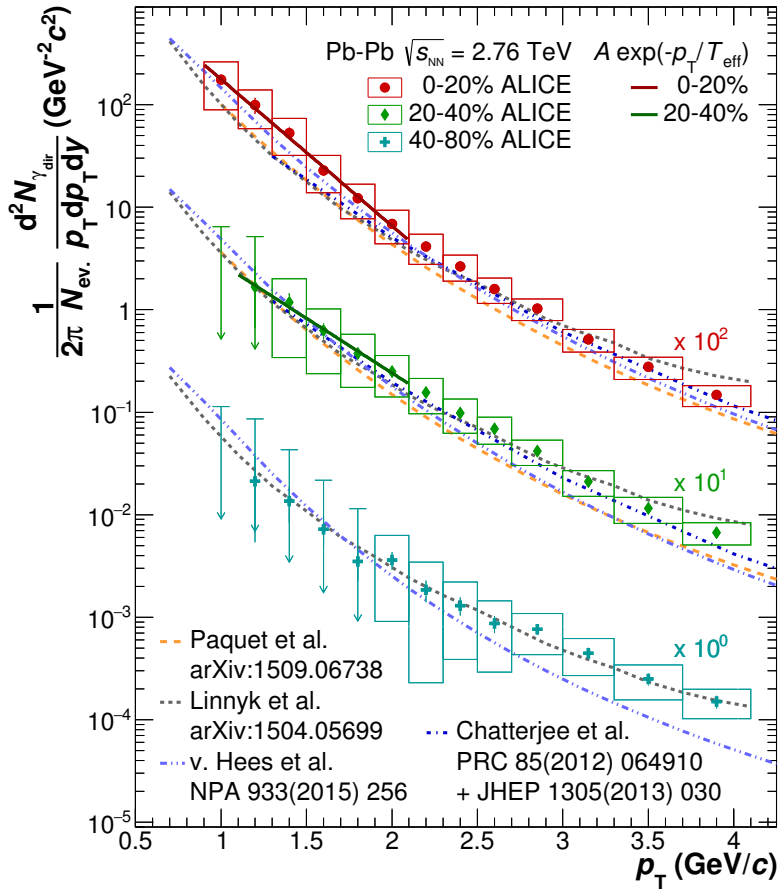

Figure 2.9: Direct photon spectra measured by the ALICE collaboration. The boxes represent the systematic uncertainties while the vertical lines represent the statistical one. The dashed lines correspond to the different models predicting the direct photon spectra (for details see [47])

produced in the initial stages of the collision and that carry the precious information about the effective temperature of the QGP droplet. For simplicity in the following all the photons that are not produced by hadron decays will be called *direct photons*. The ALICE collaboration provided the first measurement of the direct photons in Pb–Pb collisions [47] showing in its paper that the direct photon production spectra (Figure 2.9) follow the trend indicated by the models including effects of the QGP formation. For $p_T \geq 5$ GeV/c the photon spectra follow the pQCD calculation expectation for pp collisions scaled by N_{coll}, suggesting that the high p_T region of the spectra is dominated by the photons coming from hard scatterings.

3 The ALICE experiment

The most powerful particle collider in the world, the Large Hadron Collider (LHC), is able to produce the high energy density required to melt hadronic matter. Indeed, while most of the LHC uptime is dedicated to the proton–proton physics that led to the discovery of the Higgs Boson [48, 49] and of two charmed pentaquark states [50], a significant part of the physics programme at the LHC is dedicated to heavy-ion physics and the characterisation of the Quark Gluon Plasma. Among the four major collaborations running experiments at the LHC, A Large Ion Collider Experiment (ALICE) collaboration is focused on the investigation of the properties of the Quark Gluon Plasma.

3.1 The Large Hadron Collider

The Large Hadron Collider is the last component of the complex acceleration setup[1] installed at CERN (Figure 3.1). Each machine in the chain accelerates particles to increasingly higher energies. Protons and lead ions go through different acceleration chains.

Protons are extracted from a source consisting of ionised hydrogen and then they are accelerated up to 50 MeV by LINAC 2. The resulting beam is injected in the Proton Synchrotron Booster (PSB), which accelerates the protons to 1.4 GeV and provides the beam, now structured in bunches, to the Proton Synchrotron (PS). The Proton Synchrotron pushes protons at 25 GeV into the Super Proton Synchrotron (SPS) where they are accelerated to 450 GeV before their injection to the LHC.

Lead ions, instead, are produced ionising the gas obtained heating up a small isotopically pure ^{208}Pb sample. The obtained ions travel through the LINAC 3 that provides the ion beam at the energy of 4.5 MeV per nucleon to the Low Energy Ion Ring (LEIR) where the beam is split into 4 short bunches and it is further accelerated from 4.2 MeV to 72 MeV. From the LEIR, the ion beam is then transferred to the Proton Synchrotron and it follows the same path previously described for the proton beams.

[1] a brief wrap up about the CERN accelerator complex can be found in [51] and the web pages linked therein

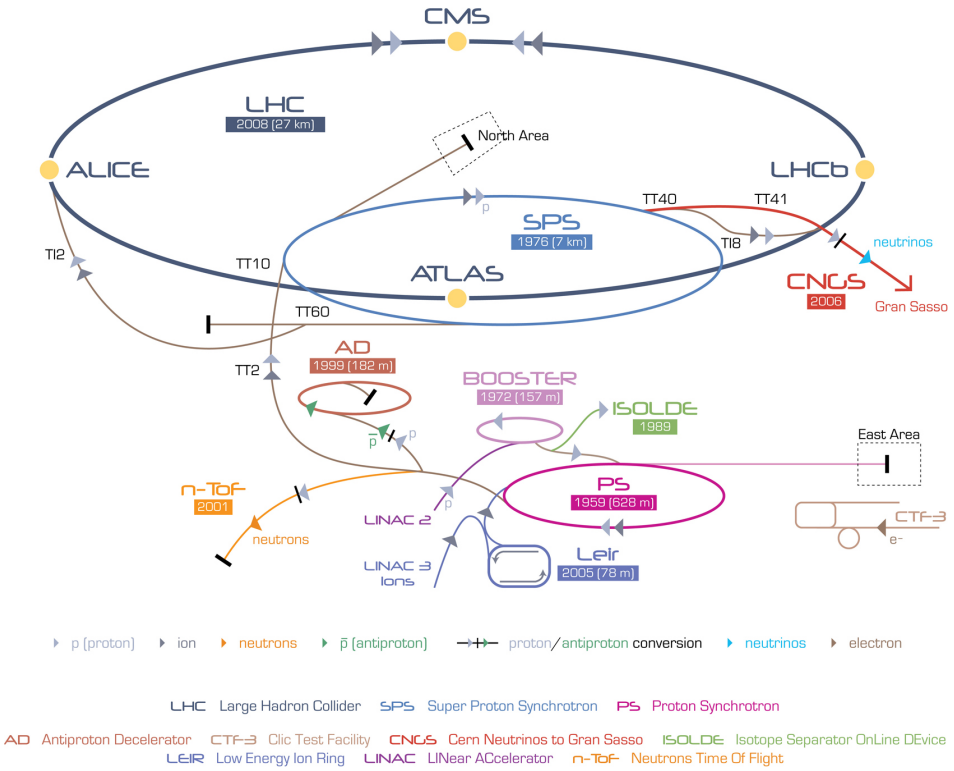

Figure 3.1: The accelerator complex at CERN [51].

In the LHC the counter–rotating beams circulate in separate vacuum–filled pipes and they are accelerated up to the energy of 6.5 TeV for protons. Finally the beams are brought into collision in the four interaction points corresponding to the major LHC experiments. The top centre–of–mass energy reached at the LHC in the collisions are 13 TeV and 5.02 TeV per nucleon pair for pp and Pb–Pb collisions respectively.

Along with the top energy, one of the most important parameters for the experiments at the LHC is the *luminosity* delivered by the collider. The reaction rate R for a process can be easily evaluated using the process cross section and the luminosity:

$$R = L\sigma_{\text{process}}.$$

The luminosity delivered by a hadron collider can be measured experimentally through a special procedure called van der Meer scan [53]. The instantaneous luminosity can be also defined as

$$L = \frac{N_b N^2 f_{rev} \gamma}{4\pi\epsilon_n \beta^*} F,$$

where N_b is the number of bunches in the collider ring, N is the number of charges in each bunch, f_{rev} is the revolution frequency of the beam, γ is the relativistic factor, ϵ_n is the

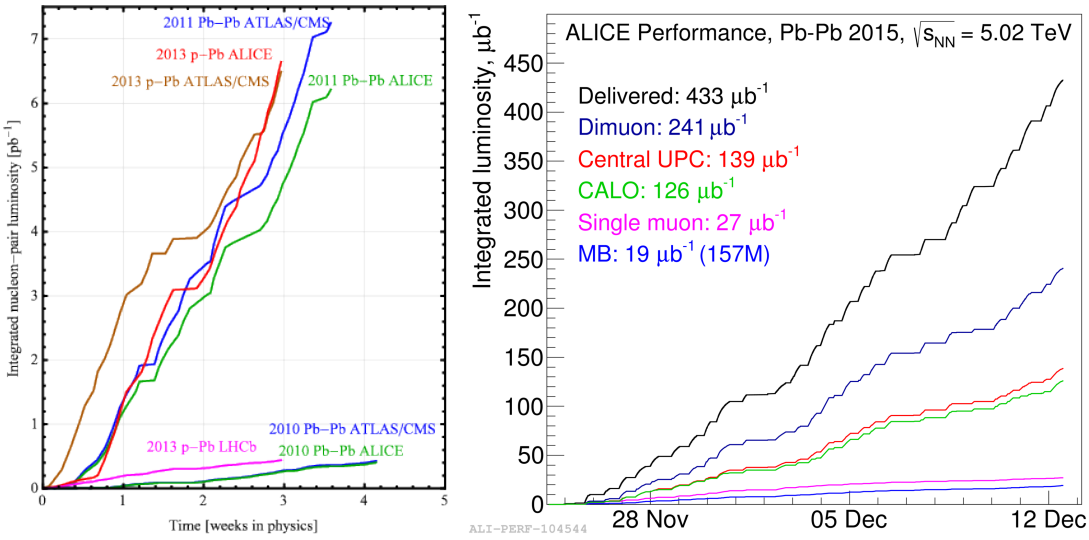

(a) (b)

Figure 3.2: Panel (a): luminosity delivered in heavy ion collisions to the experiments during LHC Run 1(from [52]). Panel (b): ALICE integrated luminosity during the first Pb–Pb period in Run 2.

normalised emittance[2], F is a geometrical factor and β^* is the value of the amplitude function[3] at the interaction point (IP) where the luminosity is estimated. In order to reduce the long range electromagnetic interaction between the two beams in the IP, the two beams are not perfectly parallel when they collide. The small angle (about 300 microradians at the LHC) between the two beams at the IP location is called crossing angle θ_c. While limiting the long range electromagnetic interaction, the non zero θ_c limits also the instantaneous luminosity of the collider and this is taken into account by the geometrical factor F:

$$F = \left[\sqrt{1+\left(\frac{\sigma_z}{2\sigma_T}\theta_c\right)^2}\right]^{-1},$$

where σ_T and σ_z are the root mean square (*rms*) of the transverse and longitudinal size of the beam respectively. In order to maximise the luminosity of the LHC, the option of a $p\bar{p}$ collider was ruled out since the production of anti–protons is much more complicated than the production of protons. The number of protons per bunch N at the LHC can be as high as $\sim 10^{11}$ and the ring can store up to 2808 bunches with 25 ns spacing [54–56]. The normalised emittance at the end of the acceleration is 3.75 μm rad while β^* depends on the IP. The peak luminosity requirement is $L = 10^{34}$ cm^{-2}s^{-1} for ATLAS and CMS and

[2] The normalised emittance is defined as $\epsilon_n = \beta\gamma\epsilon$, where β and γ are the usual relativistic factors. The emittance ϵ is the spread of beam particles in the position–momentum phase space.

[3] The $\beta(s)$ function, also known as the amplitude function, describes the amplitude of the trajectories of the particles in the beam. Together with the emittance it defines the transverse size of the beam: $\sigma_T(s) = \sqrt{\epsilon\beta(s)}$

$L = 10^{32}$ cm^{-2}s^{-1} for LHCb experiments in pp collisions. ALICE aims, instead, to a peak luminosity of $L = 10^{27}$ cm^{-2}s^{-1} in Pb–Pb collisions. Figure 3.2a shows the delivered luminosity to the experiments in the heavy ion periods during the LHC Run 1, while Figure 3.2b shows the delivered and integrated luminosity in the first Pb–Pb period of the LHC Run 2. Another important piece of information for the physics analyses at a collider experiment is the position where the collision between the two beams takes place, the so–called primary vertex. The nominal position of the primary vertex coincides with the origin of the reference coordinate frame of the experiment. Still, due to the finite size of the bunches the position of the primary vertex fluctuates around the nominal position. Being $\sigma^{\text{bunch}}_{x,y,z}$ the *rms* size of the bunch in the transverse and longitudinal direction, it can be shown that, assuming gaussian dispersion of the bunches, the *rms* of the vertex fluctuations is

$$\sigma^{\text{vertex}}_{x,y,z} = \frac{\sigma^{\text{bunch}}_{x,y,z}}{\sqrt{2}},$$

where the *rms* size of the bunch depends on the beam emittance and β^*:

$$\sigma^{\text{bunch}}_{x,y,z} = \sqrt{\frac{\epsilon_{x,y,z}\beta^*}{\sqrt{\pi}}}.$$

The typical values in pp collisions at the IP2, where ALICE apparatus is installed, are ~ 50 μm for $\sigma^{\text{vertex}}_{x,y}$ and ~ 5 cm for $\sigma^{\text{vertex}}_{z}$.

3.2 ALICE design

ALICE experiment has been specifically designed and optimised [57, 58] to be a general purpose heavy ion experiment. The main goal is studying the properties of the QGP and for that purpose it is necessary to track and to identify all the particles produced in heavy ion collisions. ALICE detectors were designed when the foreseen number of charged particles per pseudo–rapidity unit was ranging between 2000 and 8000 [57, 58], for this reason relatively slow detectors with high granularity and low material budget, such as the Time Projection Chamber and the Silicon Drift Detector, have been adopted. When using these two detectors in the data acquisition, the maximum readout rate for minimum bias events of the ALICE experiment is 1 kHz, regardless the colliding system.

The current setup of the ALICE experiment is shown in Figure 3.3 while Table 3.1 lists the position and some geometrical details of the ALICE detectors. In the apparatus two main parts can be distinguished: the *central barrel*, consisting of all the detectors located inside and outside the ALICE solenoid in the pseudo–rapidity region[4] $|\eta| < 0.9$, and the *muon arm*, sitting in the $-4 \leq \eta \leq -2.5$ region and consisting of an absorber with small atomic number Z, a spectrometer with a dipole magnet, five tracking stations and finally an iron absorber.

[4] here and in the following all the pseudo–rapidity acceptance intervals are referred to events with the primary vertex position along the beam direction z in the region $|V_z| < 5.3$ cm

The ALICE coordinate system, used also in Table 3.1, is a right-handed Cartesian system with the origin sitting at the nominal IP. The x axis of the reference frame is aligned with the accelerator plane and it points to the centre of the LHC while the y axis is perpendicular to the accelerator plan and it points upward. Finally the z axis is parallel to the beam line and its pointing is defined by the chirality of the coordinate system.

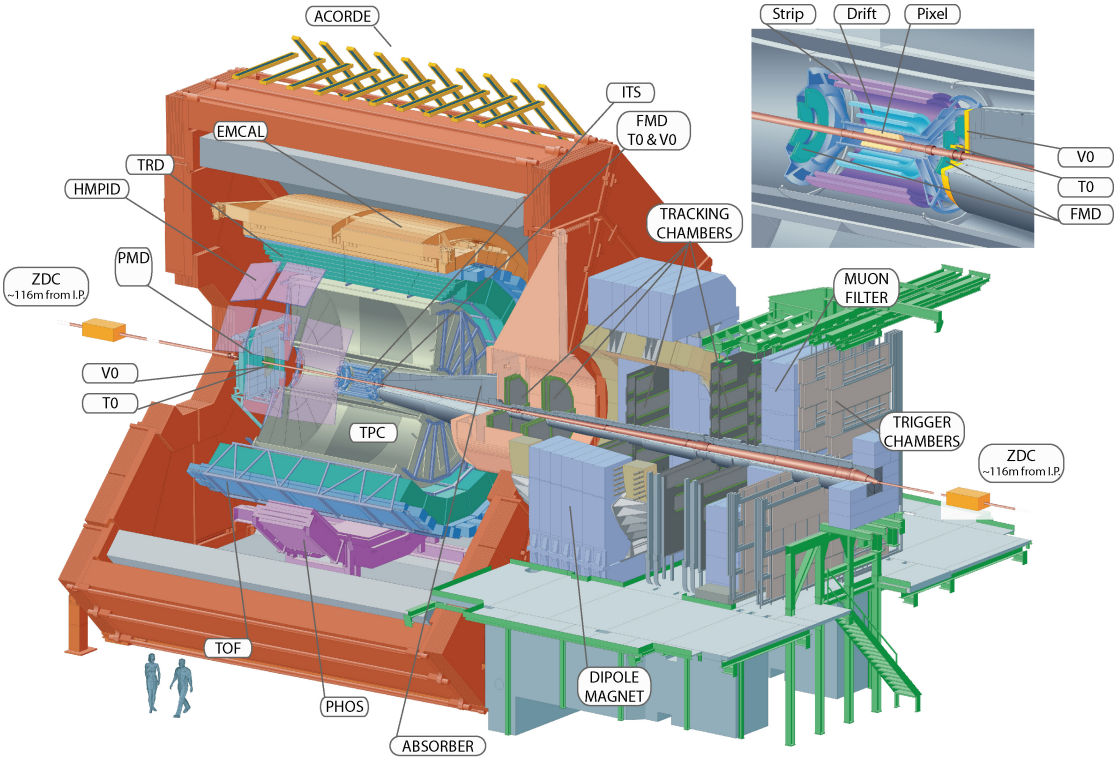

Figure 3.3: The ALICE experimental setup. The ALICE Diffractive (AD) scintillator detectors are not represented here. The top right inset shows a zoom on the V0, T0, FMD, ITS detectors.

The central barrel tracking detectors cover the full azimuthal acceptance and they include, going from the beam line outward: a silicon tracker (Inner Tracking System) made with three different technologies (Silicon Pixel Detector, Silicon Drift Detector and Silicon Strip Detector), a Time Projection Chamber and a Transition Radiation Detector.
In order to extend the transverse momentum reach of the experiment down to 80 MeV/c [60], a mild solenoidal magnetic field – with respect to the other LHC experiment – of 0.5 T has been adopted. ALICE is the only experiment at the LHC using a warm resistive magnet to measure the momentum of the charged particles, the same magnet used for the L3 experiment at LEP. As it will be shown in the following, the track reconstruction efficiency at low p_{T} strongly profited from the usage of tracking detectors with a very low material budget. The resolution on the momentum does not depend only on the magnetic field used, but also on the lever arm

Table 3.1: Geometrical details about the configuration of the ALICE detectors. This table has been adapted from the extensive description of the ALICE apparatus in [59]. When it is not specified, the azimuthal coverage for the detector is 2π. The position of the detector corresponds to the radial distance from the beam axis for the barrel detectors and to the distance along z for the others. When more than one position values are specified the detector is subdivided in two or several parts and those values are the minimum and maximum distances from the interaction point.

Detector	Acceptance (η,ϕ)	Position (m)	Surface (m^2)	Channels
ITS layer 1,2 (SPD)	±2,±1.4	0.039,0.076	0.21	9.8 M
ITS layer 3,4 (SDD)	±0.9,±0.9	0.150,0.239	1.31	133 K
ITS layer 5,6 (SSD)	±0.97,±0.97	0.380,0.430	5.00	2.6 M
TPC	±0.9 at r = 2.8 m ±1.5 at r = 1.4 m	0.848,2.466	Readout 32.5 m^2 Volume 90 m^3	557568
TRD	±0.84	2.90,3.68	716	1.2 M
TOF	±0.9	3.78	141	157248
HMPID	±0.6, $1.2 \leq \phi \leq 58.8$	5	11	161280
PHOS	±0.12, $220 \leq \phi \leq 320$	4.6	8.6	17920
EMCAL	±0.7, $80^\circ \leq \phi \leq 187^\circ$	4.36	44	12672
ACORDE	±1.3, $-60^\circ \leq \phi \leq 60^\circ$	8.5	43	120
Muon Tracking	$-2.5 \leq \eta \leq -4.0$	-14.22,-5.36	95	1.08 M
Muon Trigger	$-2.5 \leq \eta \leq -4.0$	-17.12,-16.12	138	21000
ZDC: ZN	$\lvert\eta\rvert \leq 8.8$	±116	2×0.0049	10
ZDC: ZP	$6.5 \leq \lvert\eta\rvert \leq 7.5$ $-9.7^\circ \leq \phi \leq 9.7^\circ$	±116	2×0.027	10
ZDC: ZEM	$4.8 \leq \eta \leq 5.7$, $-16^\circ \leq \phi \leq 16^\circ$ and $164^\circ \leq \phi \leq 196^\circ$	7.25	2×0.0049	2
PMD	$2.3 \leq \eta \leq 3.7$	3.64	2.59	221184
FMD disc 1	$3.62 \leq \eta \leq 5.03$	3.2		
FMD disc 2	$1.7 \leq \eta \leq 3.68$	0.752,0.834	0.266	51200
FMD disc 3	$-3.4 \leq \eta \leq -1.7$	-0.752,-0.628		
V0A	$2.8 \leq \eta \leq 5.1$	3.4	0.548	32
V0C	$-3.7 \leq \eta \leq -1.7$	-0.897	0.315	32
T0A	$4.61 \leq \eta \leq 4.92$	3.75	0.0038	12
T0C	$-3.28 \leq \eta \leq -2.97$	-0.727	0.0038	12

length of the tracking detectors L and on the resolution on the track sagitta measurement σ_s:

$$\frac{\sigma_p}{p} \propto p\frac{\sigma_s}{BL^2}.$$

Thanks to the large radial coverage ($0.039 \leq r \leq 3.680$ m), despite the mild solenoidal magnetic field, the ALICE apparatus is able to reconstruct tracks up to $p \sim 100\,\mathrm{GeV}/c$. The above mentioned tracking detectors are also among the detectors of ALICE providing particle identification (PID). The Time Of Flight detector is another key component of the PID systems in ALICE and it is fundamental for the analyses carried out in this thesis. In many analyses (e.g. identified particle spectra, charm decaying into hadrons and nuclei spectra) particle identification detectors play a crucial role. In the central barrel, for instance, protons can be identified up to $p_{\mathrm{T}} = 4\,\mathrm{GeV}/c$ in the full azimuth, as it is shown in [61], and in this thesis it will be shown how the identification of deuterons can go up to $p_{\mathrm{T}} = 6\,\mathrm{GeV}/c$. At higher momenta (e.g. up to 6 GeV/c for protons) the hadron PID can be performed only in the restricted range of η and ϕ, as reported in Table 3.1, covered by the High-Momentum Particle Identification Detector (HMPID), made of an array of ring-imaging Cherenkov counters.

There are, in addition, other detectors dedicated to the physics of high p_{T} photons and jets that do not cover the full azimuthal or pseudorapity acceptance of the central barrel region: the ElectroMagnetic Calorimeter (EMCal) and the Photon Spectrometer (PHOS). In the forward–backward pseudorapidity region there are the Forward Multiplicity Detector (FMD), made of silicon strips detectors, the Photon Multiplicity Detector (PMD) and the Zero Degree Calorimeters (ZDC) consisting of two hadronic calorimeters, for protons and neutrons, plus one electromagnetic calorimeter. Two trigger detectors are located on each side of the interaction point: the V0, made out of scintillator detectors, and the T0 composed by two arrays of Cherenkov counters. Finally, the ALICE collaboration is studying the high-energy cosmic air showers in the energy range $10^{15} \div 10^{17}$ eV to determine the nature of primary cosmic rays [62]. For this purpose an array of 60 large scintillators (ACORDE) was placed on top of the ALICE solenoid to trigger on cosmic rays for calibration and alignment purposes, as well as for cosmic ray physics.

In the next sections the detectors relevant for the analyses of this thesis are further described.

3.2.1 Inner Tracking System

The Inner Tracking System (ITS) is a cylindrical silicon tracker and it is the ALICE detector closest to the interaction point. It surrounds a 800 μm thick Beryllium beam pipe and it is composed of six layers of silicon detectors. It uses three different technologies: the two innermost layers are silicon pixel detectors (SPD), the third and the fourth ones are silicon drift detectors (SDD) and the last two layers are double sided silicon strip detectors (SSD) (Figure 3.4).

Thanks to its position close to the interaction point, the low material budget per layer and the

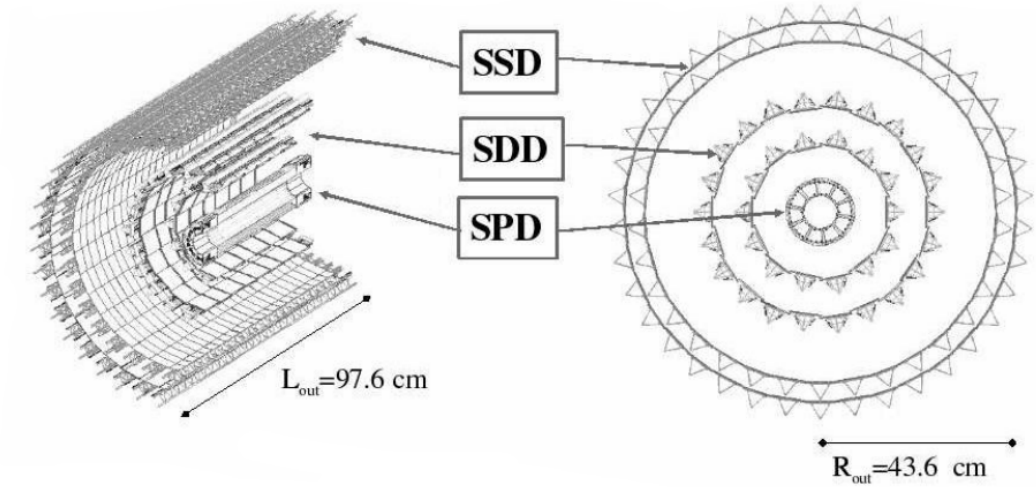

Figure 3.4: ITS schematic layout. The details about the geometry of the detector can be found in Table 3.1.

high spatial resolution of its subdetectors (Table 3.2), the ITS permits the reconstruction of primary and secondary vertices with a resolution better than 100 μm extending at the same time the tracking of low p_{T} particles down to $p_{\mathrm{T}} = 80$ MeV/c. Because of detector operation constraints, a set of thermal shields are in place between the different subdetectors increasing sensitively the material budget. The total material budget of the ITS, keeping into account the thermal shields and the support structures, is 7.18% X/X_0 (7.26% X/X_0 including air) for particles in the $y \approx 0$ region.

The SDD and SSD provide also information about the energy loss of particles in their sensitive volume, extending the ALICE PID capabilities in the p_{T} region below 200 MeV/c (see Section 3.5.1). In addition, the SPD contributes to the Level 0 trigger of the experiment providing local *Fast-OR* information and, as it will be shown in Section 3.4.2, it plays a fundamental role in the reconstruction of primary vertices.

Table 3.2: Details about the spacial resolution and material budget of the ITS subdetectors [59]. The material budget of each layer of the subdetectors is also reported.

Parameter	SPD	SDD	SSD
Material budget per layer (%X_0)	1.14 - 1.14	1.13 - 1.26	0.83 - 0.86
Spatial resolution $r\phi$ (μm)	12	35	20
Spatial resolution z (μm)	100	25	830
Two track resolution $r\phi$ (μm)	100	200	300
Two track resolution z (μm)	850	600	2400
Active cell size (μm^2)	50×425	202×294	95×40000

3.2.2 Time Projection Chamber

The Time Projection Chamber (TPC) is the main tracking detector of ALICE. The TPC is also one of the main PID detectors as it provides the information about the specific energy loss of the tracked particles in its volume. During the LHC Run 1, the TPC was filled with a gaseous mixture of Neon and CO_2, while during the LHC Run 2 it was changed to a mixture of Argon and CO_2.

The TPC, schematically depicted in Figure 3.5, is partitioned in 36 sectors: 18 azimuthal sections divided in 2 longitudinal halves by the central electrode. The central cathode and the end caps anodes produce two uniform electrical fields that push the electron clouds, generated by ionising particles traversing the TPC volume, towards the readout chambers in the end caps. The readout chambers are a system of multi-wire proportional chambers (MWPC) with cathode pad read-out. Each sector is segmented by pads organised in rows and the longitudinal coordinate is given by the drift time. In order to cope with the high multiplicity environment, the pads in the inner readout chambers (IROC) are smaller (4×7.5 mm^2) than the pads in the outer readout chambers (OROC) (6×15 mm^2). Thanks to this segmentation schema, charged particles can be tracked and identified with up to 159 3-dimensional space points including energy loss information. The TPC covers a pseudorapidity range of $|\eta| \leq 0.9$ while the radial coverage is $85 < r < 247$ cm. While the TPC structure covers the full azimuthal angle, the boundaries between different azimuthal sectors are inactive, bringing some dead zones in the detector acceptance.

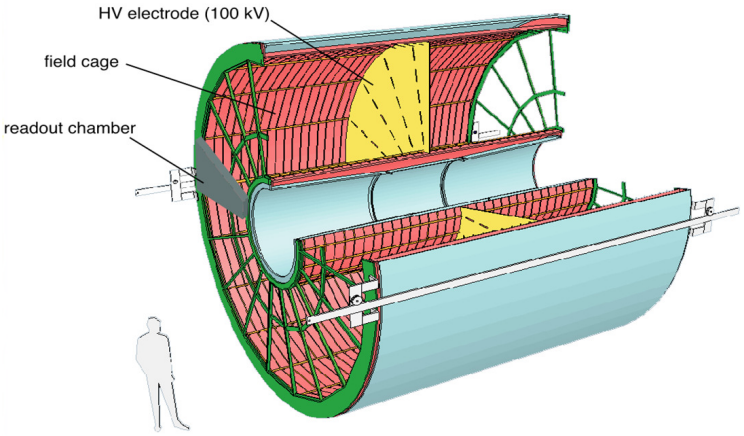

Figure 3.5: TPC schematic representation

3.2.3 Time of Flight detector

The Time of Flight detector (TOF) of ALICE is used to identify charged particles in the momentum range $0.2 \div 4$ GeV/c in the central pseudorapidity range ($|\eta| < 0.9$). Like the other central barrel detectors, the TOF has a cylindrical geometry and it is 3.8 m far from the interaction

region on average. It consists of 1593 Multi-gap Resistive Plate Chambers (MRPC), with a sensitive area of 7.4×120 cm^2 each and an intrinsic resolution of about ~ 40 ps [59].

The determination of the time when the beams collide, the so called event time t_0, is performed using the information from the T0 detector and the TOF detector as described in [63]. The time of flight of a particle is determined by measuring the elapsed time between the event time and the particle hitting the TOF. The information about the time of flight of the particle together with the momentum determined with the tracking detectors allows to compute the particle β and thus its mass.

3.2.4 V0

The V0 detector consists of two arrays (V0A and V0C) of 64 scintillator counters distributed in 8 rings and located at high pseudo-rapidity on both sides of the ALICE detector (Table 3.1). The logical *"or"* between the signals of V0A, V0C and SPD defines the minimum bias trigger selection in ALICE. The signals from V0 are also used to reject beam–gas interaction by measuring the time difference between the signals in V0A and V0C and to define the centrality in Pb–Pb and p–Pb collisions as it will be described in the following.

3.2.5 T0

The T0 detector is made of two arrays of Cherenkov radiators (Table 3.1). Its main purpose is to contribute to the determination of the event time [63] independently from the track and vertex reconstruction and with a time resolution below 50 ps. As of Run2 it is used as the primary online luminosity monitoring detector. Using the timing information from the T0 it is also possible to estimate the primary vertex position along the beam axis with a precision of about 1.5 cm.

3.2.6 ZDC

ALICE ZDC is made of three different types of calorimeters: two electromagnetic calorimeters, two proton calorimeters and two neutron calorimeters. Their position and geometrical details are summarised in Table 3.1. The closest to the interaction point are the electromagnetic calorimeters (ZEM). They are used to distinguish between central and peripheral Pb–Pb collisions by measuring the energy deposited by π_0s and photons produced at forward rapidity. The two sets of sampling hadronic calorimeters are installed 116 m away from the interaction region on both sides. On each side there is a neutron calorimeter (ZN), placed between the two beam pipes, and a proton calorimeter (ZP), placed outside the beam pipe on the side where positive particles are deviated by the LHC magnetic field. The ZDC is mainly used to veto on the parasitic beam–beam background interactions and to determine the centrality in Pb–Pb collisions by measuring the energy deposited by spectator nucleons [64]. They are also fundamental for the determination of the direct flow in Pb–Pb collisions [65].

3.3 Trigger and Data Acquisition

A 3–level trigger system has been deployed in ALICE to comply with the different readout times and trigger latencies of the large variety of detectors adopted to build the experimental apparatus. The 3-level trigger system of ALICE is managed by the Central Trigger Processor (CTP). The CTP catches the signals of the trigger detectors, combines them with the information on the LHC filling scheme and then it checks if any of the trigger conditions are satisfied. CTP receives the signal from fast detectors, such as SPD, V0, T0, the electromagnetic calorimeters and the Muon Trigger, and generates the Level 0 trigger decision in ~ 0.9 μs. The Level 1 decision is taken in ~ 6.5 μs for the events passing the L0 trigger selection. The Level 2 decision is then taken after 100 μs (the expected maximum drift time for electron clouds in the TPC volume) and all the events passing this selection are sent both to the Data Acquisition (DAQ) [66] machines and to the High Level Trigger (HLT) [67].

When the trigger signal arrives, the Local Data Concentrators (LDCs) get the raw data from the detectors through optical connections, the Detector Data Links (DDLs). Each LDC is a computer node connected to one subdetector of ALICE and each subdetector, depending on the size and the complexity of its raw data, may have more than one LDC. The raw data in the LDC are checked and processed to build a fragment of the full event. These fragments, called *subevents*, are then sent (with a data rate up to 20 GB/s) to the Global Data Collectors (GDCs) where they are composed, together with the HLT output, in the full event. In the HLT step a fast reconstruction of the data, including clusterisation and track reconstruction, is performed. On the output of this first reconstruction it is possible to apply further selections that are not possible in the hardware triggers. If the events pass the HLT selection, the TPC information, accounting for more than 90% of the total event data size, are compressed before sending the data stream to the GDCs. When the event building in the GDC is terminated, the data are buffered in a local disk pool waiting to be transferred to the CERN computing centre. During Run 1 and 2 of the LHC, this setup has been able to sustain a data rate up to 2 GB/s after the HLT compression.

3.4 ALICE offline framework

The routines of Monte–Carlo simulations and data reconstruction will be briefly introduced in this section. As a part of this thesis work is about the track reconstruction for the upgrade of the ALICE experiment, the attention will be focused on the track reconstruction algorithms currently employed. A comparison with the work done in this thesis for the track reconstruction in the ITS during the LHC Run3, especially with the performance of the current ITS standalone algorithm, will be shown in Chapter 4.

3.4.1 Monte Carlo simulations

The first step in the Monte Carlo simulation in ALICE is the event generation. The event generation consists of the simulation, in a parametrised way or from first principles, of the interaction between two particles from the LHC beams in the interaction region. The result of the event generation step is a set of kinematic parameters corresponding to the stable or weakly decaying particles that will be transported. Typically the strong decays of unstable particles is handled at the generation step. The generated kinematic parameters are then propagated through a precise geometrical description of the experiment, available in the ALICE software, using a transport framework. Within ALICE simulation framework it is possible to use three different transport codes: GEANT3, GEANT4 and FLUKA. These codes provide the information about the energy loss of the particle in the detector sensitive material, they steer the generation of secondary particles from material (e.g. the delta rays) and finally they handle the decays of the particles. The energy deposition and the spatial coordinates of the impact point of the particle on the sensitive areas of the detectors are stored and they are called *hits*. The hits are then processed by the simulation of each detector response to produce the corresponding signal in the electronics: the *digits*. The digits are then stored in the detector raw data format that is identical to the one used in the real data taking and reconstruction.

3.4.2 Event Reconstruction

The ALICE event reconstruction flow starting from the raw data either collected or generated via Monte Carlo is illustrated in Figure 3.6.

The first step in the event reconstruction is the local reconstruction, a set of algorithms reconstructing the information about the particles that crossed each sub-detectors. The typical outputs of the local reconstruction are the *recpoints* or *clusters*: the spacetime coordinates where the particle hit the subdetector active surface. Other information, like the energy lost by

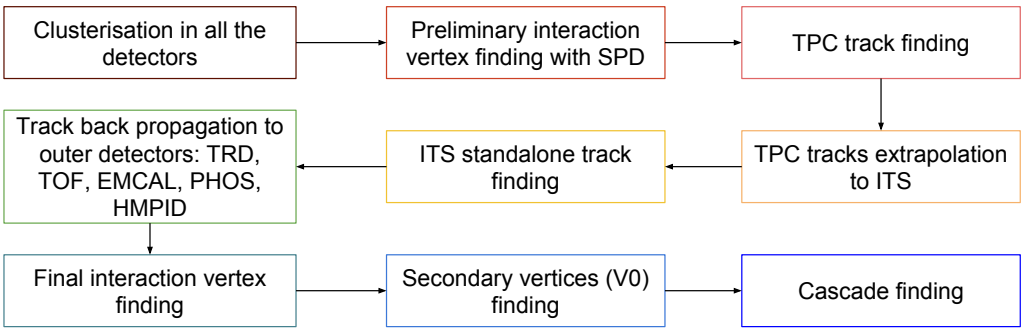

Figure 3.6: Sequence of the various steps in the reconstruction flow of the ALICE experiment.

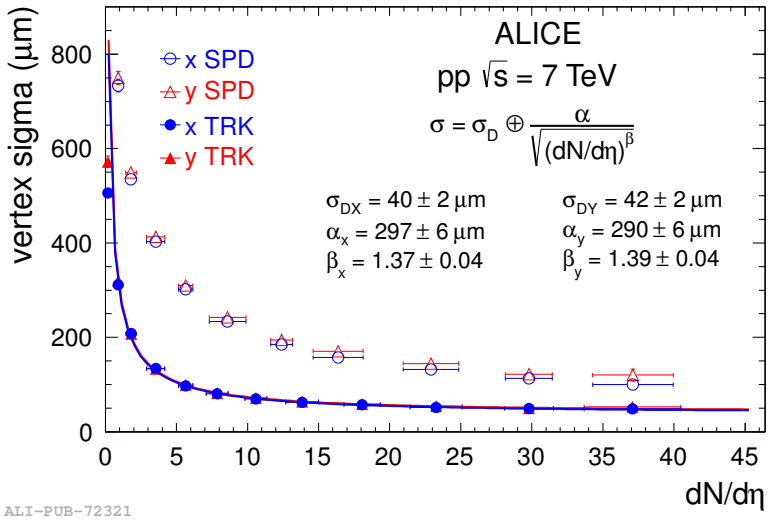

Figure 3.7: Resolution on the primary vertex position using the SPD and the track algorithms as a function of the charged particle multiplicity of the event in pp collisions at $\sqrt{s} = 7$ TeV [59].

the particle, the time of flight or the Cherenkov angle are attached to the clusters in the PID detectors allowing the identification of the tracked particle.

The second step in the reconstruction chain is the estimation of the position of the primary vertex of the event. The best estimation of the primary vertex can be obtained only by using the full track information. Nevertheless, as the primary vertex position is necessary for the tracking algorithm to speed-up the search of valid track candidates, a first estimation of its position can be obtained using only the first two layer of the ITS (SPD). The used algorithm builds a set of segments, called *tracklets*, connecting the clusters on the SPD Layer 0 with those on the SPD Layer 1 within an azimuthal acceptance window. A routine then computes the point in the space minimising the distance from all the tracklets and it removes the outliers. The resulting space point is the primary vertex estimation. The reconstruction of the 3D position of the primary vertex requires at least two tracklets. In pp collisions it is not unusual to get only one tracklet: in this case the z position of the primary vertex can be still computed using as a constraint the beam line position in the transverse plane. In Figure 3.7 the resolution on the primary vertex position obtained with this method in pp collisions at 7 TeV is shown.

Once that the position of the primary vertex has been estimated, the track reconstruction starts. In the following the techniques currently used in ALICE, extensively illustrated in [60], are summarised. The first step of the tracking algorithm is building track seeds in the outer part of the TPC. Track seeds consist of two clusters plus the vertex constraint in the first stage of the tracking procedure. In later stages, seeds are made of three clusters without any vertex constraint. Track seeds are then propagated inward and, whenever at one step of the propagation a compatible cluster is found, the track parameters are updated using a Kalman Filter. With this algorithm it is not uncommon that two or more track candidates share some clusters. If the fraction of shared clusters is above a predefined threshold (between 25% and

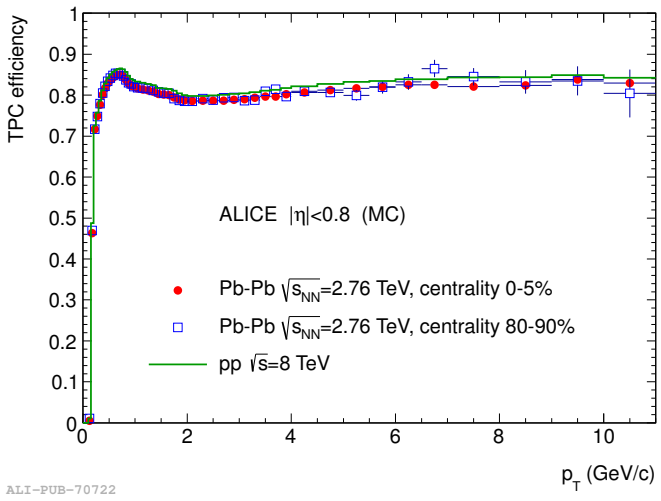

Figure 3.8: Track reconstruction efficiency for TPC tracks in Pb–Pb collisions at 2.76 TeV (red dots) and in pp collisions at 2.76 TeV (blue open square) for central and peripheral collisions, respectively [59]. It is possible to observe that the tracking efficiency is independent of the charged particle multiplicity of the events.

50%), the algorithm rejects the track candidates with the worse track parameters quality. Then all the track candidates with at least 20 clusters (out of a maximum of 159) and with a number of clusters over crossed rows ratio greater than 0.5 are accepted and propagated at the inner radius of the TPC. The reconstruction efficiency for TPC tracks at this stage is shown in Figure 3.8. The efficiency drops for $p_{\mathrm{T}} \leq 500$ MeV/c due to the energy loss in the material of the detector: the more the particle loses energy, the more its trajectory deviates from the helicoidal path of a charged track in a magnetic field. The observed shape of the efficiency at higher p_{T} is due to the loss of clusters in the dead zones of the TPC.

With the preliminary information about the momentum and the energy loss from the clusters attached to the tracks, it is already possible to assign a first hypothesis about the species of the particle being tracked. This first estimation is useful to determine correctly the energy loss of the particle in the material and to properly keep it into account when propagating the track to the outermost layer of the ITS. Starting from the outermost layer of SSD, the tracking in ITS proceeds similarly to what described for the TPC tracking: the track candidate is propagated to the next ITS layer and, if there is one or more clusters compatible with the expected track position on the layer according to a proximity cut, the track parameters are updated and stored as a new track seed. Whenever a seed in the extrapolation does not find a compatible cluster on an active zone of a layer, a penalty factor to its χ^2 is added. As a result of this algorithm, each TPC track produces a tree of track hypotheses in the ITS. Among the track candidates of each tree, the one with the highest quality is kept as a ITS+TPC track in the reconstructed event.

In order to reconstruct the trajectories of particles with $p_{\mathrm{T}} \leq 200$ MeV/c, an ITS standalone

algorithm is used to reconstruct the tracks using the remaining clusters from the previous step. The ITS standalone algorithm, as for the TPC one, is based on the Kalman Filter track following pattern recognition. Helicoidal seeds are built using two points from the three innermost layers of the ITS plus the primary vertex constraint and then they are propagated outward trying to attach all the compatible clusters according to a proximity cut. The procedure is repeated in few iterations with increasing tolerance of the proximity cut to improve the efficiency at low p_{T}.

The ITS standalone reconstruction can proceed in parallel with the backward refit of the ITS+TPC track using the Kalman Filter. During this step the integrated track length is computed, together with the expected time for different particle species, both necessary for a proper TOF PID (see Section 3.5). When the track is successfully refitted up to the outer radius of the TPC, it is further extrapolated to the TRD where the algorithm attempts to match the track with the TRD tracklets. When the algorithm succeeds, it updates the track parameters using the TRD tracklets information. Even when the TRD information is not available, an attempt to extrapolate the track and to match it to one of the TOF clusters is performed. The integrated track length and expected times are calculated until the TOF matching hit.

A further extrapolation is performed to match the track with the hits in the external detectors such as HMPID, EMCAL and PHOS. All the tracks are then propagated back to the innermost ITS layer in one last Kalman Filter refit pass, using the information of all the attached clusters and completing the three passes fit of the track parameters. In Figure 3.9 the resolution on $1/p_{\mathrm{T}}$ for tracks is shown, which is related to the resolution on the p_{T} by the simple formula:

$$\frac{\sigma_{p_{\mathrm{T}}}}{p_{\mathrm{T}}} = \frac{\sigma_{1/p_{\mathrm{T}}}}{1/p_{\mathrm{T}}}.$$

As it is shown in the figure, tracks can be reconstructed with a momentum resolution between 1% and 10% in the momentum range between 0.1 and 100 GeV/c.

The sample of reconstructed tracks is composed mainly by primary tracks, however secondary tracks are reconstructed releasing the constraint on the primary vertex at the seeding level and using a dedicated algorithm. Being mostly primary tracks these are used to perform the final measurement of the primary vertex position. All the tracks are propagated to the nominal beam line position and all the tracks too far ($O(100\ \mu m)$) from it are removed from the vertex computation. The point of closest approach to the selected set of tracks is the first estimate of the primary vertex that is refined through precise vertex fit as described in [68]. More information about the strategies adopted in case of pile-up are explained in [60].

3.4.3 ALICE analysis framework

The analysis framework is as important as any detector for a High Energy Physics experiment. The large amount of data collected during the last years, of the order of ten petabytes, requires a complete set of tools in order to process and analyse the reconstructed events. For the work

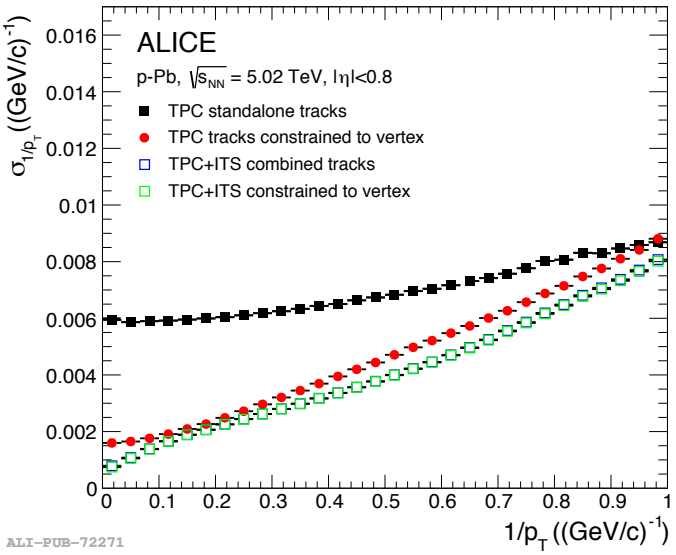

Figure 3.9: Resolution on the $1/p_T$ parameter as a function of $1/p_T$ in p–Pb collisions. The resolution is quoted for TPC tracks with (red dots) and without (black squares) vertex constraint and for ITS+TPC tracks with (green square) and without (blue square) vertex constraint. The resolution is quoted for $1/p_T$ because this can be extracted directly from the covariance matrix of the Kalman Filter fit.

presented in this thesis a total of approximately 2 PB of data, corresponding to the 2011 and 2015 Pb–Pb reconstructed data, are analysed. The reconstruction of the data, the analyses and the Monte Carlo simulations are performed using the Worldwide LHC Computing Grid (WLCG), a federation of computing centres whose aim is the processing of the data acquired by the LHC experiments. The computing centres in this federation are organised in 3 tiers. The first tier, labelled Tier 0 and constituted by the CERN computing centre and the computing centre at Wigner Research Centre for Physics in Budapest, hosts one replica of the raw data and it is responsible for the first reconstruction of the raw data. From the Tier 0 centres the raw data and the reconstructed data are distributed to the Tier 1 centres, where a second replica of these data is stored. Tier 1 centres are also involved in the re-processing of the data and in part of the reconstruction. Finally Tier 2 centres main tasks are the production of Monte Carlo simulations and the processing of analyses.

In the case of ALICE the data are stored in binary files using the ROOT framework data format. The ROOT framework is also used as the core of the ALICE software framework: *AliRoot*. A collection of the analysis related code is also part of the ALICE offline framework and denominated *AliPhysics*. The reconstructed events are stored in the Event Summary Data (ESD) format, that are mainly used for calibration and detector performance studies. The analysis code of the users are mainly run on the Analysis Object Data (AOD), a pruned version of the ESD data containing only the information relevant at the analysis level (e.g. only the track parameters computed at the primary vertex are stored and the intermediate track parameter estimations are dropped). In order to analyse the full datasets collected in ALICE,

the Alien (ALICE Environment) grid middleware is used. Using the Alien user interface it is possible to access the collected data and the simulated Monte Carlo available everywhere on the grid. Moreover it is also possible to launch analysis tasks on those data. When more users are interested in analysing the same sample of data, the access pattern to the sample is optimised by running the analysis tasks of these users together in the same jobs. This access pattern, called *analysis train*, defines a standard analysis flow for the users and ensures the reproducibility of the analysis steps required to obtain the final results.

3.5 Particle Identification

The four detectors used in the data analyses for the charged hadron PID are the ITS, the TPC, the TOF and the HMPID. The ITS and the TPC detectors provide the specific energy loss of the tracked charged particle, the TOF detector provides the time of flight while the HMPID gives the $\beta = v/c$ of the particle through the Cherenkov angle measurement. These kinds of information, together with the momentum of the track allow to identify the tracked particle in a wide momentum range. The ITS, TPC and TOF identification are described in some details in the following sections as they are used as PID detectors in this thesis.

3.5.1 ITS particle identification

The two SDD layers and the two SSD layers of the ITS provide a measurement of the specific energy loss of the charged particle traversing their 300 μm thick silicon sensors. From the measurement of the cluster charge and of the track path length in the sensor it is possible to obtain the ionisation energy loss for each layer. The $\mathrm{d}E/\mathrm{d}x$ of one track is then calculated using a truncated mean to keep into account properly the Landau tail of the energy loss. If four clusters are available, the average of the lowest two points is used. If only three points are available a weighted sum is used assigning a weight equal to unity to the lowest point and a weight of one half to the others. An example of the obtained ITS $\mathrm{d}E/\mathrm{d}x$ distribution as a function of track momentum is shown in Figure 3.10. For each particle, the expected detector response is parametrised with a polynomial shape for $\beta\gamma < 0.7$ to keep into account the non–linear detector response while at higher $\beta\gamma$ a Bethe–Bloch formula is used. The resolution on the measured $\mathrm{d}E/\mathrm{d}x$ goes from 5.2% in pp collisions to 6.5% in Pb–Pb [60].

3.5.2 TPC particle identification

The energy loss as a function of the particle momentum in the TPC (Figure 3.11) can be parametrised with splines or using a Bethe–Bloch parametrisation:

$$f(\beta\gamma) = \frac{P_1}{\beta^{P_4}}\left[P_2 - \beta^{P_4} - \ln\left(P_3 + \frac{1}{(\beta\gamma)^{P_5}}\right)\right]$$

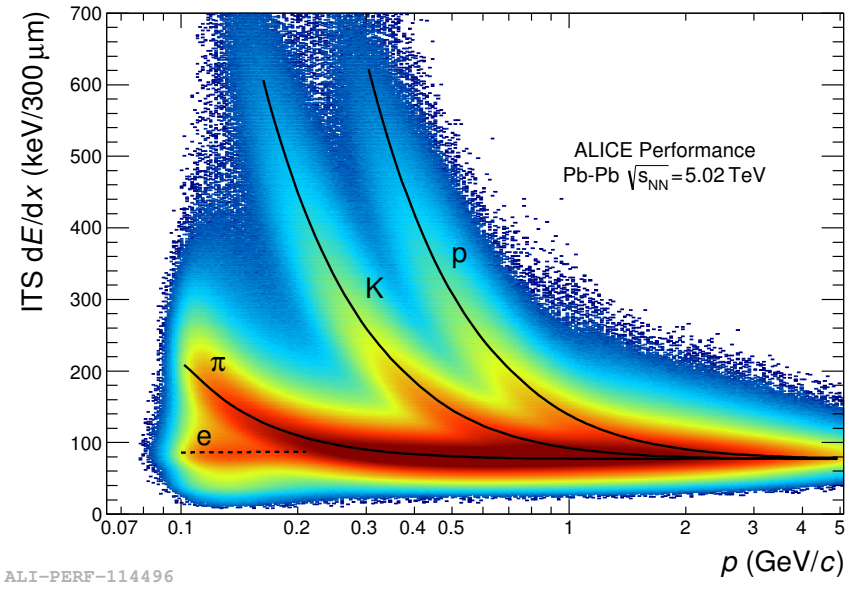

Figure 3.10: Specific energy loss of particles in the SDD and SSD layers of the ITS in Pb–Pb events at 5.02 TeV. The black solid lines represent the expected detector response for different particle species.

where β and γ are the relativistic factors, and P_{1-5} are free parameters. This parametrisation, derived by the ALEPH collaboration [69], can be fitted to the data. Alternatively, in Figure 3.11 the light hadrons response functions have been parametrised using splines. The parametrisation of these splines is provided by the central ALICE framework. At low momenta ($p \leq 1$ GeV/c), where the $1/\beta^2$ dependence of the dE/dx is more important, the particle identification can be performed on a track–by–track basis by performing a fiducial selection around the signal expected for the particle of interest. The amplitude of this fiducial selection is usually expressed in terms of number of σ, where σ is the expected dE/dx resolution for the analysed track. Thanks to the relative dE/dx resolution as good as 5.2% in pp collisions and 6% in the 0-5% centrality in Pb–Pb collisions, at higher momenta it is still possible to extract the relative contributions of different particle species through the statistical unfolding of the dE/dx distributions. This method can be also applied in the relativistic rise region, where the separation between the different particle species in the dE/dx versus momentum space is nearly constant over a wide momentum range. Using such a method, particle ratios were extracted up to $p = 20$ GeV/c [39]: the analyses are eventually limited by the available statistics and not by the method itself.

3.5.3 TOF particle identification

The ALICE TOF is able to measure in Pb–Pb collisions, in the centrality range 0-70%, with a resolution of 80 ps the time of flight of pions at $p \sim 1$ GeV/c. This resolution keeps into

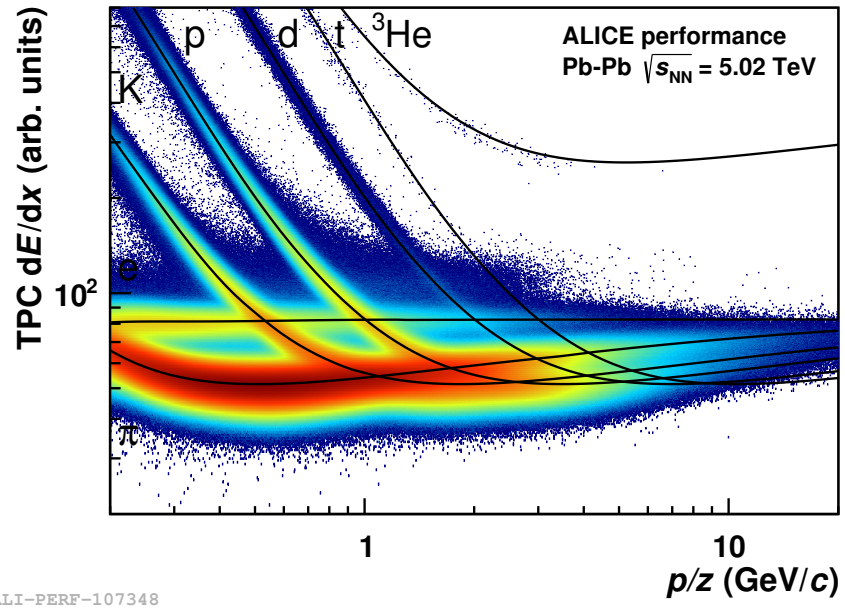

Figure 3.11: Specific energy loss of particles traversing the TPC volume as a function of their momentum in Pb–Pb collisions at $\sqrt{s_{\mathrm{NN}}} = 5.02$ TeV. The solid black lines represent the expected detector response for different particle species.

account the intrinsic detector resolution, the detector calibration, the momentum resolution and the resolution on the start time of the event. A complete review of the methods used to compute the event start time can be found in [63].

Thanks to the excellent resolution on the start time, the TOF detector can be used to identify protons up to 4 GeV/c and deuterons up to 6 GeV/c, as it will be shown in Chapter 5. Figure 3.12 shows the particle β as a function of the momentum estimated with the tracking procedure. It is possible to distinguish, on top of the mismatch background, the populations corresponding to the different particle species. Starting from the time of flight t_{TOF} and the track integrated length measured during the tracking, the particle β can be easily computed with the classical formula:

$$\beta c = \frac{t_{\mathrm{TOF}}}{L}.$$

As its name suggests, the mismatch background is due to the erroneous assignment of a TOF cluster to a track. As shown in [60], this background becomes more and more important as the TOF occupancy increases, being prominent in central Pb–Pb collision and almost negligible in pp collisions.

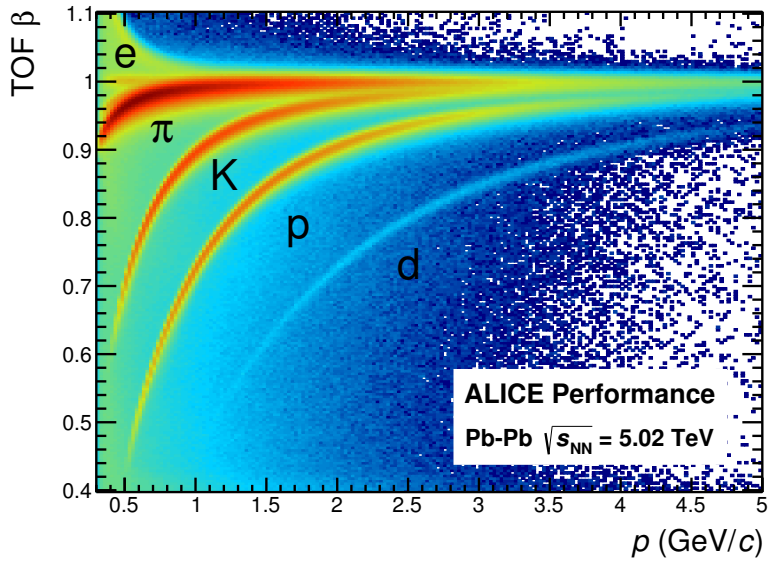

Figure 3.12: β of the particles in Pb–Pb events at $\sqrt{s_{\mathrm{NN}}}$ = 5.02 TeV computed using the time of flight information from the TOF detector as a function of the measured track momentum.

3.6 Centrality determination in Pb–Pb collisions

As already discussed in Section 1.3.1, the characterisation of a collision between two nuclei starts with the estimation of the impact parameter b. This quantity cannot be measured directly but using the Glauber Model (Section 1.3.1) they are correlated to experimental quantities, such as the energy deposited in the ZDCs or the charged particle multiplicity, with the value of the impact parameter. In the literature events are classified into centrality classes corresponding to percentiles of the total hadronic interaction cross section of the colliding nuclei:

$$c(b) = \frac{1}{\sigma_{AA}} \int_0^b \frac{\mathrm{d}\sigma}{\mathrm{d}b'} \mathrm{d}b' \quad \text{where} \quad \sigma_{AA} = \int_0^\infty \frac{\mathrm{d}\sigma}{\mathrm{d}b'} \mathrm{d}b'.$$

Under the assumption of monotonic dependence on the impact parameter of both the charged particle multiplicity and the energy deposit at zero degrees, the centrality is expressed as:

$$c \approx \frac{1}{\sigma_{AA}} \int_{N_{\mathrm{ch}}}^\infty \frac{\mathrm{d}\sigma}{\mathrm{d}N'_{\mathrm{ch}}} \mathrm{d}N'_{\mathrm{ch}} \approx \frac{1}{\sigma_{AA}} \int_0^{E_{\mathrm{ZDC}}} \frac{\mathrm{d}\sigma}{\mathrm{d}E_{\mathrm{ZDC}}} \mathrm{d}E_{\mathrm{ZDC}}.$$

Similarly, the hadronic cross section can be replaced by the number of events, corrected for the trigger efficiency and for the background:

$$c \approx \frac{1}{N_{\mathrm{ev}}} \int_{N_{\mathrm{ch}}}^\infty \frac{\mathrm{d}n}{\mathrm{d}N'_{\mathrm{ch}}} \mathrm{d}N'_{\mathrm{ch}} \approx \frac{1}{N_{\mathrm{ev}}} \int_0^{E_{\mathrm{ZDC}}} \frac{\mathrm{d}n}{\mathrm{d}E_{\mathrm{ZDC}}} \mathrm{d}E_{\mathrm{ZDC}}.$$

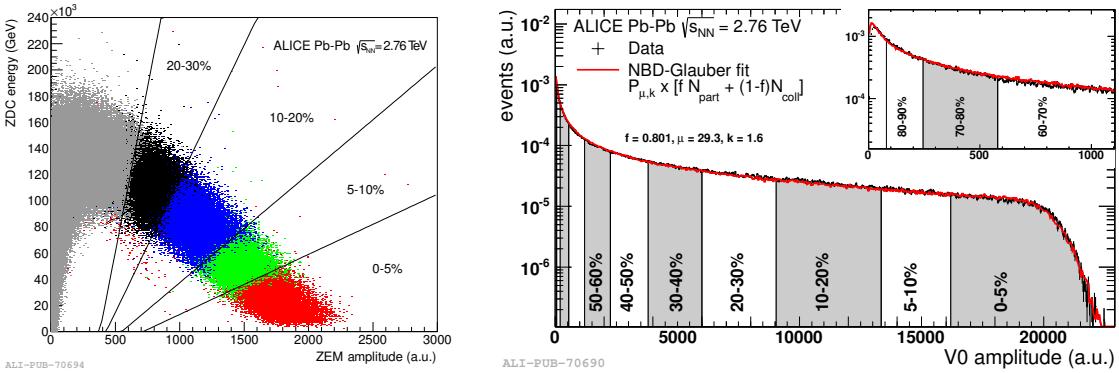

(a) (b)

Figure 3.13: Panel (a): distribution of the ZDC energy deposit as a function of the ZEM energy deposit. The solid lines represent the separation between the centrality classes determined with the ZDC while the coloured points represent the centrality classes determined with the V0. Panel (b): distribution of the V0A + V0C amplitude. The centrality intervals are determined integrating the distribution as described in the text. The red line is the fit with the Glauber–NBD model and the inset shows a zoom on the peripheral collisions.

The assumption of monotonic decrease of the energy deposit with increasing centrality in the ZDC breaks for $c > 50\%$ as in peripheral events some nuclear fragments can be deviated by LHC magnets outside the acceptance of the ZDC leading to a energy signature similar to the central collisions. This ambiguity can be solved by correlating the ZDC energy deposit with the energy deposit in the ZEM as shown in Figure 3.13a. Figure 3.13b shows how the centrality determination is performed using the V0 detector. The distribution of the sum of V0A and V0C amplitudes is fitted with a parametrisation based on a Glauber Monte Carlo and the Negative Binomial Distribution (NBD–Glauber fit) to connect this experimental quantity with the impact parameter of the collision. This parametrisation is obtained generating the number of participant nucleons N_{part} and the number of binary collisions N_{coll} with the Glauber model. The particle multiplicity per nucleon–nucleon collision is then parametrised with a NBD distribution with parameters μ and k:

$$P_{\mu,k}(n) = \frac{\Gamma(n+k)}{\Gamma(n+1)\Gamma(k)} \cdot \frac{(\mu/k)^n}{(\mu/k+1)^{n+k}}$$

The same fit can be performed on the distribution of the number clusters on the second layer of SPD or on the distribution of the number of TPC tracks. The resolution on the centrality determination has been evaluated in [64] and it has been shown that the resolution depends on the pseudo–rapidity coverage of the detector used. The best estimator is obtained when combining V0A and V0C detectors (Figure 3.13b) with a total pseudo–rapidity coverage of 4.3 units and a resolution ranging between 0.5% for central collisions and 2% for the peripheral ones.

Another method to determine the collision centrality is relating the ZDC energy deposit E_{ZDC} with N_{part}:

$$N_{\mathrm{part}} = 2A - E_{\mathrm{ZDC}}/E_A.$$

As mentioned above, the relation between N_{part} and E_{ZDC} is not monotonic due to the ambiguity between central and peripheral collisions. It is still possible to define centrality classes slicing with straight lines the ZDC energy deposit versus ZEM amplitude plane as shown in Figure 3.13a. As the slope of the lines increases with decreasing centrality, this method is trustworthy for $c < 30\%$ and, as Figure 3.13b shows, the centrality classes obtained with this method correspond to the classes defined with the V0 detectors.

4 Perspectives for the ITS reconstruction in Run 3

The ongoing LHC Run 2 will end in 2018 and it will be followed by the second long shut–down (LS2) of the collider that is scheduled for lasting two years. After the LS2, the Run 3 will be characterised by a higher luminosity of the collider. A major upgrade of the ALICE apparatus will take place during the LS2, in order to allow the experiment to exploit the new data taking conditions.

One of the main goals of the ALICE collaboration for the LHC Run 3 is to measure rare processes, like the production of Λ_c and Λ_b baryons in Pb–Pb collisions, down to very low momentum. For processes including low momentum particles it is very difficult to establish a reliable low level trigger. In order to collect enough events to study such processes, an experiment has either to run without hardware trigger (i.e. reading out and writing on tape all the events) or to rely on the High Level Trigger to select the events to store. To fully profit from the high luminosity that will be delivered by the LHC in the Run 3 (up to $L = 6 \times 10^{27} cm^{-2} s^{-1}$ in Pb–Pb), the ALICE collaboration designed and it is building, at the time of this thesis, an upgraded experimental apparatus that is able to cope with the foreseen Pb–Pb interaction rate of 50 kHz and that includes:

- a completely new ITS [70], based on a new layout and a new technology;
- a silicon telescope for tracking muons in the forward region (MFT) [71];
- a different readout chamber technology for the TPC [72];
- upgraded trigger and readout systems for several other detectors [73];
- a completely new Online–Offline infrastructure [74].

In the framework of two of the most important upgrades for ALICE (ITS and Online–Offline), the possibility of reconstructing online the tracks in the Upgraded Inner Tracking System offers on the one hand a tool required for the prompt calibration of the external detectors (i.e.

Table 4.1: Geometrical parameters of the upgraded ITS [70]

Parameters	L0	L1	L2	L3	L4	L5	L6
Radial position (min.) (mm)	22.4	30.1	37.8	194.4	243.9	342.3	391.8
Radial position (max.) (mm)	26.7	34.6	42.1	197.7	247.0	345.4	394.9
Length (mm)	271	271	271	843	843	1475	1475
Pseudorapidity coverage	±2.5	±2.3	±2.0	±1.5	±1.4	±1.4	±1.3
Nr. Pixel Chips	108	144	180	2688	3360	8232	9408

the Time Projection Chamber) and on the other a significant speed-up of the data analysis procedure.

In the next sections, after a brief introduction to the upgrade of the ITS and the online–offline system, the new track reconstruction program, developed in this thesis project, based on Cellular Automata, will be described. This task is particularly challenging because on the one hand the track reconstruction will be done online and, on the other hand, the experiment aims to reconstruct all the Pb–Pb collisions that will occur at a 50 kHz rate (to be compared to the 8 kHz of the present data taking).

4.1 The upgraded ITS

The measurement of the production of Λ_c and Λ_b baryons, of the low mass di-leptons resonances and a refinement and extension to higher masses of the current hyper–nuclei measurements are some of the flagship topics for the ALICE physics program during the LHC run 3. All of these measurements call for a better performance of the Inner Tracking System in terms of spatial resolution, tracking efficiency at low p_{T} and readout capabilities. In order to satisfy these strict requirements a complete new ITS will be installed (Figure 4.1) and the geometrical parameters of the new ITS [70] are reported in table 4.1.

The new ITS will feature:

- a first detection layer closer to the beam line (from r = 3.9 cm to r = 2.2 cm). This will be possible thanks to the installation of a new 0.8 mm thick beryllium beam pipe with a diameter of 19.2 mm. The reduction of the radius of the first detection layer improves the resolution on the impact parameters of tracks by a factor 3 and 5 in the $r\varphi$ and z directions respectively at p_{T} = 1 GeV/c. The hit density for the innermost layer will increase to ~ 19 hits/cm^2 per Pb–Pb minimum bias collision on average. Such a high hit density requires a very high granular detector to make track reconstruction feasible. Moreover the expected radiation load at the innermost layer is expected to be 700 krad

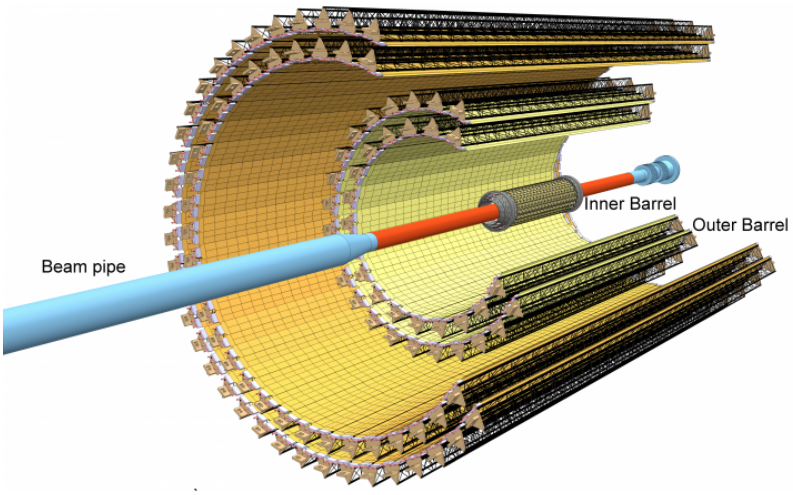

Figure 4.1: The layout of the upgraded ITS. In the Long Shutdown 2 a new beam pipe will be installed (blue cylinder) together with a completely new silicon tracker. The ITS Upgrade will have 7 layers of silicon pixel detectors organised in two groups: the inner barrel (the 3 innermost layers) and the outer barrel.

of Total Ionising Dose (TID) and 1×10^{13} 1 MeV n_{eq}/cm^2 of Non Ionising Energy Loss (NIEL) including a safety factor of ten.

- A new geometry and a finer segmentation: the ITS Upgrade geometry has been optimised in terms of tracking efficiency and impact parameter resolution as shown in [70]. It will feature seven layers grouped into an Inner Barrel, consisting of the three innermost layers, and an Outer Barrel corresponding to the other four layers. The radii of the layers are 22 mm, 31 mm and 39 mm and 194 mm, 247 mm, 353 mm and 405 mm, respectively. The total sensitive area will be about 10 m^2 containing about 12 billions pixels with binary readout. The seven layers and the use of the Monolithic Active Pixel Sensors with small pixel size of $O(30 \times 30\ \mu m^2)$, to be compared with the pixel size of SPD $50 \times 425\ \mu m^2$, will increase significantly the granularity of the ITS Upgrade compared with the current silicon tracker. The upgraded ITS will provide pseudorapidity coverage of $\eta \leq 1.3$. One of the design goals of the ITS Upgrade is to allow for easy removal and insertion during the Year End Technical Stops (YETS) of the LHC in order to replace, possibly, faulty components of the detector.

- A reduced material budget per layer: while posing a challenge to the mechanical and electrical design of the detector, the reduced material budget of the ITS Upgrade will bring substantial contribution to the aforementioned improvement of the track impact parameter resolution, especially for low momentum particles. Furthermore, the reduced multiple scattering in the detector material permits to track low momentum particles more efficiently. In order to meet such a stringent requirement in terms of material budget, the silicon sensors will be thinned down to 50 μm. The optimised power

Table 4.2: General pixel-chip requirements from the ALICE ITS Upgrade Technical Design Review [70] (second and third columns) and current performance of ALPIDE prototypes [75].

Parameter	Inner Barrel	Outer Barrel	ALPIDE
Chip dimensions $r\phi \times z$ (mm^2)	15×30		✓
Sensor thickness (μm)	50	100	✓
Spatial resolution (μm)	5	10	≈ 5 μm
Detection efficiency (%)	> 99		✓
Fake-hit-rate (event^{-1}pixel^{-1})	$< 10^{-6}$		$\ll 10^{-6}$
Event time resolution (μ s)	< 30		< 2
Power density (mW/cm^2)	< 300	< 100	≈ 40
TID radiation hardness (krad)	2700	100	tested at 350
NIEL radiation hardness (1 MeV n$_{eq}$/cm^2	1.7×10^{13}	1×10^{12}	✓

consumption of the front–end electronics allows for room temperature operation of the detector with a lightweight water cooling system that, together with the ultra light carbon fibre support structures, brings the total foreseen material budget to 0.3%X_0 for the innermost layers and around 1%X_0 for the outermost ones.

- Faster readout: compared with the 1 kHz limitation of the current silicon tracker, ITS Upgrade will be able to read Pb–Pb events at a peak rate of 50 kHz and pp collisions at 400 kHz. The ITS Upgrade will also feature the possibility of reading out data continuously.

The Monolithic Active Pixel Sensor (MAPS) technology meets all the design requirements of the ITS Upgrade project as it allows to incorporate in a high-resistivity 50 μm thick silicon epitaxial sensor a matrix of charge collection diodes (pixels) with a pitch of the order of 30 μm and the electronics that perform signal amplification, digitisation and zero-suppression (Figure 4.2). A ionising particle crossing the sensor creates some electron–hole pairs that are collected, via simple diffusion as the epitaxial layer is not depleted with a bias voltage, by the n–well collection diode. The MAPS technology will be implemented using the 0.18 μm CMOS technology of TowerJazz [70]. The main advantage of the proposed solution is the possibility of using both N–MOS and P–MOS transistors for the in–sensor electronics thanks to the integration of a deep p–well that screens the electronics from the charge induced in the epitaxial layer by ionising particles. At the time of this thesis the first samples of the production chip, the ALice PIxel DEtector (ALPIDE) [75], are available and Table 4.2 summarises how it compares with the Technical Design Report (TDR) requirements.

4.2 The Online–Offline systems upgrade

During the Run 3 of the LHC, the foreseen data throughput in ALICE can reach 1.1 TB/s (Table 4.3), most of which coming from the upgraded Time Projection Chamber [72]. The data rate values for MFT and ITS are still considering the pessimistic scenario, in terms of noise in

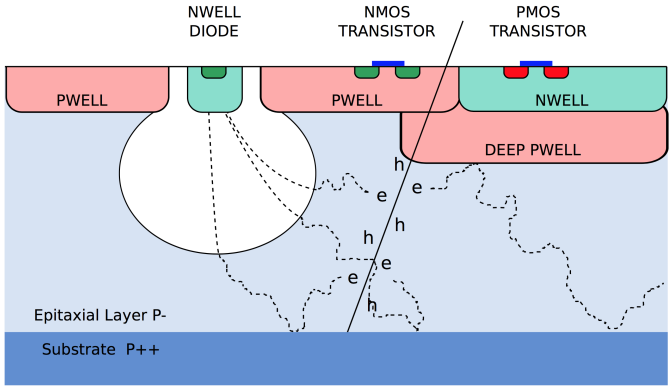

Figure 4.2: Sketch of the cross section of a MAPS detector used for the ITS Upgrade.

the sensors, presented in the respective TDRs [70, 71]. As shown in Table 4.2 that scenario is ruled out by the tests [75] on the latest sample of the ALPIDE chip, reducing contextually the data rate in ITS and MFT significantly. The data rate is anyway too large to be written on tape unprocessed and uncompressed. For this reason a new approach to the data acquisition and reconstruction will be adopted in ALICE: most of the Offline processing (i.e. detector calibrations and data reconstruction) will be moved Online in a dedicated facility. This upgrade project, called O^2 [74], aims to provide a fast turnaround time between the data taking and the data analysis providing event building, reconstruction, calibration and selection online or quasi–online.

Table 4.3: Data size per Pb–Pb event and data throughput foreseen for ALICE detectors during the LHC Run 3.

Detector	Event Size	Pb–Pb at 50 kHz
TPC	20.7 MB	1012 GB/s
ITS	0.8 MB	40 GB/s
TRD	0.5 MB	20 GB/s
MFT	0.2 MB	10 GB/s
Others	0.3 MB	12.2 GB/s

The continuous readout of some detectors, like the upgraded TPC, will change the read out of the data and the data handling paradigm. Instead of triggered events, data will be read out and processed – for some detectors – in Timeframes (TF), which are groups of read out cycles (snapshots) of the detectors. The detectors front-end electronics (FEE) send the data of a readout cycle (or of a triggered event for detectors not supporting the continuous readout) through approximately 8100 read-out links. The First Level Processors (FLP) computing nodes aggregate data from up to 48 optical links and execute the local reconstruction and calibration for the detectors. At the FLP level the TF structure for the local detector is built and it is

then shipped through a switching network to the Event Processing Nodes (EPN). On the EPNs the global reconstruction is performed: the local TF are composed and physical objects like tracks are reconstructed. The reconstructed TF, constituted of reconstructed tracks and compressed reconstructed hits, is then stored on tape. The O^2 infrastructure will be a High Performance Computing (HPC) facility hosting heterogeneous hardware, including 250 First Level Processor worker nodes equipped with Field Programmable Gate Arrays (FPGA) and 1500 Event Processing Nodes equipped with Graphics Processing Units (GPU).

As illustrated in [74], it is necessary to compress data before storage by about a factor of 20. This can be achieved through zero suppression of TPC data and online reconstruction of the TPC hits (compression factor 2.5), removing all the TPC hits not associated to particle tracks (compression factor 6) and using an optimised data format (compression factor 1.35). Therefore both ITS and TPC tracking will be required in order to reduce the data size. Moreover, the online tracking of the ITS Upgrade will be required to perform an online calibration of the space charge distortions of the TPC: a map of the distortions can be constructed using the track-point residuals between the ITS tracks and the TPC clusters, then it can be used to correct the cluster displacements. This method has been already developed and shown to be working offline during LHC Run2 [76], and there are developments ongoing within the ALICE collaboration to bring this calibration online.

4.3 Vertex finding and pile–up identification

The vertex reconstruction algorithm for the upgraded layout of the ITS – that we developed in a previous work [77] – is able to reconstruct the primary vertices in pp, p–Pb and Pb–Pb collisions using the hits in the three innermost layers of the ITS. The base objects for the calculation of the primary vertex coordinates are the *tracklets*, segments spanning between two clusters on subsequent layers. The tracklets are built associating to each cluster in the innermost layer (Layer 0) all the clusters on Layer 1 within a fiducial azimuthal window $\Delta\phi$. The formed tracklets are extrapolated to the third layer and are considered to be valid if a hit is found on layer 2 within a $\Delta z \times \Delta\phi$ rectangular window. The organisation of the algorithm are specified in Figure 4.3.

A set of "*tracklet clusters*" is defined using the validated tracklets. These are groups of tracklets that are closer than a predetermined distance (400 μm by default) to a common point: the centroid of the cluster. The tracklet clusters are built using tracklet pairs:

- a tracklet pair is formed when the DCA between two tracklets is less than 400 μm. The point minimising the distance between the two tracklets, here called "intersection" and corresponding to the midpoint of the DCA segment, of the pair is also found at this stage. If this point is located outside the beam pipe internal radius the pair is rejected;
- all the tracklets closer than 400 μm from the pair intersection are attached to the pair. When a new tracklet is attached, the centroid of the clusters is re-computed and the

tracklets are marked as used.

This procedure is repeated with all the tracklets still unused (unmarked) to find all the possible clusters. The tracklet clusters closer than 400 μm are joined and then the list of clusters is sorted by the number of tracklets contributing to tracklet clusters. The centroid of each cluster is considered to be a primary vertex candidate. False candidates might arise from the wrong association of fake tracklets with good tracklets or even from decay vertex of particles. To reduce the number of such false positives, if a vertex candidate is distant less than 8 mm from another candidate with more contributing tracklets, then it is rejected. Finally, if more than one candidate is remaining, all the clusters with 3 or less contributing tracklets are deleted. The remaining clusters are the reconstructed vertices for the current event.

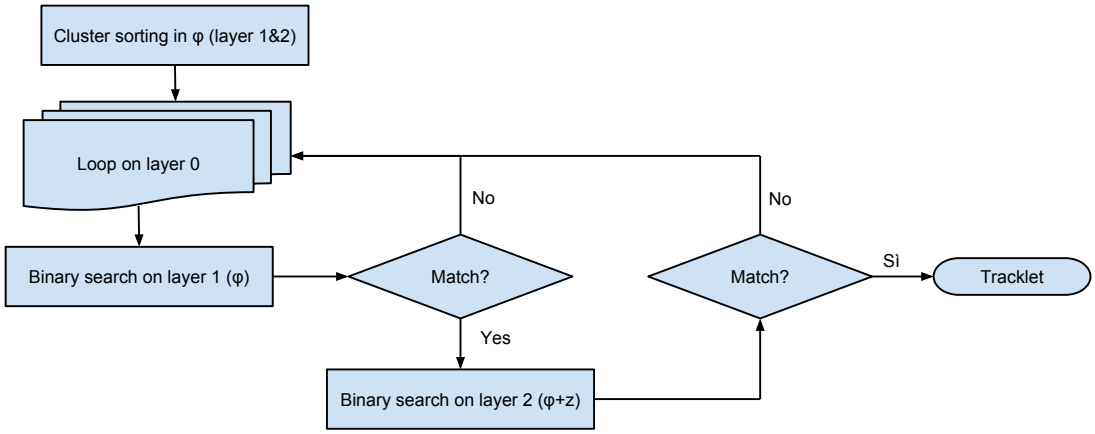

Figure 4.3: Workflow of the cluster matching and tracklet definition.

The vertex reconstruction starting from the tracklets is summarised in Figure 4.4 while Figure 4.5a shows the reconstruction efficiency in minimum bias pp collisions[1] as a function of the true z position of the primary vertex. As expected, when the z position of the vertex is at the limit of the detector coverage the reconstruction efficiency drops significantly. Figure 4.5b shows the resolution on the primary vertex on the transverse plane and on the longitudinal direction as a function of the number of reconstructed tracklets in the event. The obtained resolution in the transverse plane and on the longitudinal direction are compliant with the expectation for the ITS Upgrade and it allows to ease the primary track reconstruction.

4.4 Track reconstruction

The reconstruction flow for the ITS Upgrade will follow four main steps:

[1] The data sample used in this context is constituted by approximately 100 thousands pp events at $\sqrt{s}$=14 TeV simulated with the ALICE offline framework.

- first the position of the primary vertex is found by the fast algorithm illustrated in the previous section;
- a pattern recognition method is used to find track candidates;
- track candidates are fitted in three passes using the Kalman Filter: from the outermost layer inward, then outward and then refitted inward;
- in case of two or more candidates are sharing reconstructed hits, only the one with the best χ^2 is kept.

For the ITS Upgrade there are currently two different approaches to the pattern recognition: a Kalman Filter track-following algorithm, called Cooked Matrix (CM) tracker and similar[2] to the one explained in Section 3.4.2 for the current ITS, and a Cellular Automata based algorithm. The Cellular Automata algorithm has been developed as part of this thesis and the comparison between both algorithms will be shown when relevant.

[2]The name Cooked Matrix comes from a special treatment of the covariance matrix of the track seeds utilised for the track finding.

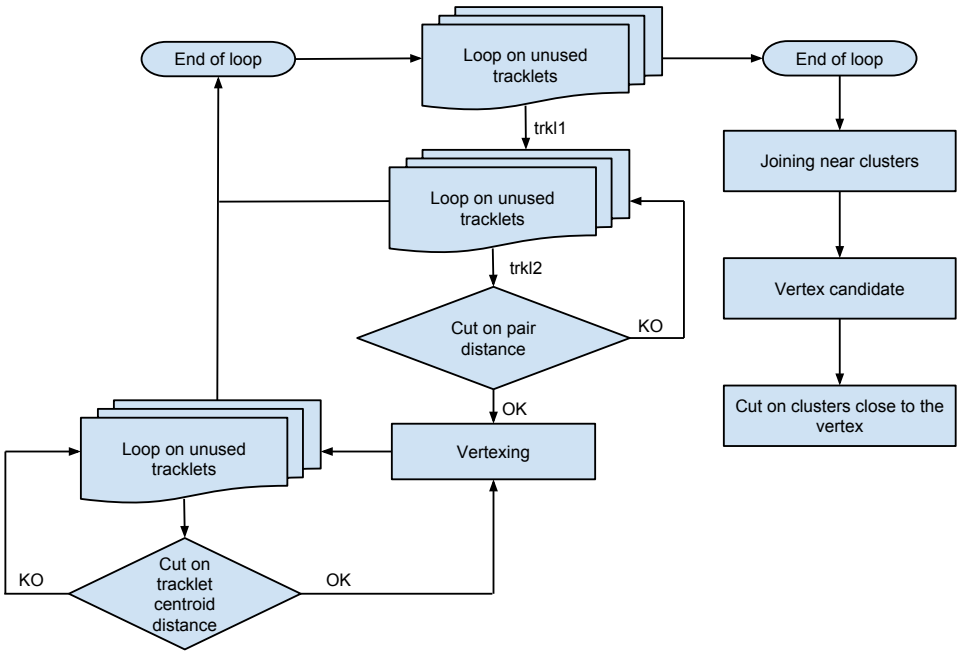

Figure 4.4: Algorithm flow chart for vertices reconstruction. This kind of algorithm features the pileup tagging and the reconstruction of multiple primary vertices.

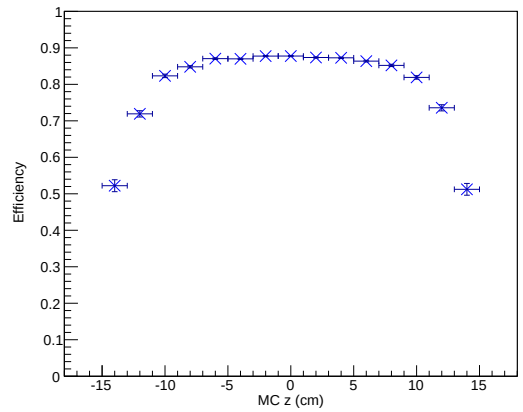

(a)

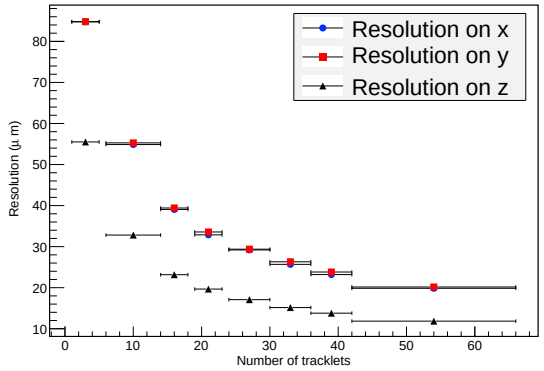

(b)

Figure 4.5: On the top: primary vertex reconstruction efficiency as a function of the z position of the primary pp collision is shown. The vertical lines represent the binomial error of the efficiency. The efficiency does not saturate to one as diffractive events are considered in the denominator. On the bottom the corresponding resolutions on the primary vertex position, evaluated with a gaussian fit to the residual distributions, are shown as a function of the number of reconstructed tracklets in the event. The vertical lines represent the error on the resolution estimated by the fit. These results are taken from [77].

4.4.1 The Cellular Automata algorithm

Connecting hits belonging to the same particle trajectory is a classical pattern recognition puzzle in particle physics. Among the many different pattern recognition algorithms, the Cellular Automata algorithm[3] offers the possibility of reconstructing the full tracks linking small track segments: the *cells* or, more traditionally in High Energy Physics, the *track seeds*. This kind of approach is computationally appealing because track seeds can be built in parallel and looking only at a small data portions in memory. A similar algorithm is already in use for

[3] for a description of the features of the algorithms, see http://web.stanford.edu/ cdebs/GameOfLife/

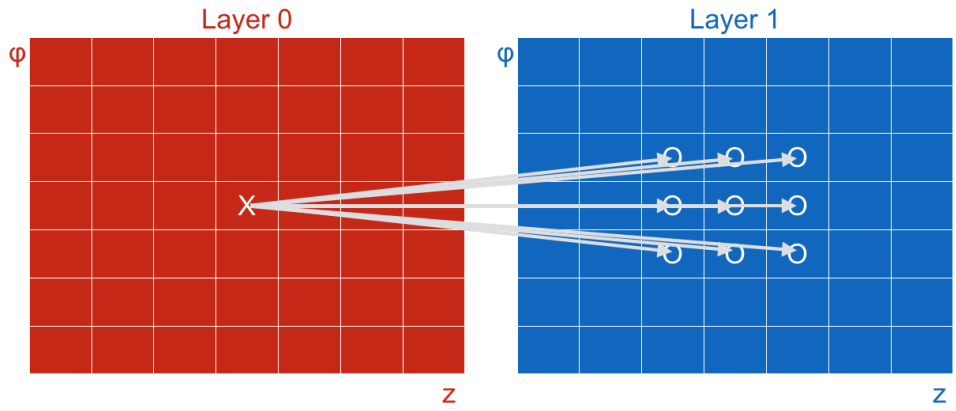

Figure 4.6: Example of the index tables used to organise the hits according to a 2 dimensional grid on Layer 0 and Layer 1. The hits are sorted according to their ϕ and z coordinates. Thanks to this organisation, for any cluster on Layer 0, it is possible to quickly look up the corresponding region of interest on Layer 1.

the ALICE TPC [78] and it has been developed for the CBM [79] and CMS experiments [80].

The information about the reconstructed hits, coming from the cluster reconstruction algorithm, have to be organised and skimmed in order to get only the relevant information for the tracking algorithm available in an ordered grid. The granularity of the grid can be tuned in order to get the best computing time performance and it does not influence the reconstruction efficiency of the algorithm. The skimmed reconstructed hits contains the information about the spatial position of the hits in cartesian and cylindrical coordinates referred to the ALICE reference frame ($\{x, y, z, r, \phi\}$). The information about the sensor on which the hit is located is also saved to rapidly get the information required to transform, when needed, the laboratory coordinates into the tracking coordinates. Figure 4.6 shows how these skimmed hits are distributed in the ordered grid and how the information is accessed in the first step of the Cellular Automata algorithm. An index table is compiled to rapidly access the hits in a region of interest of the detector.

In the first step of the Cellular automata algorithm (Figure 4.7a), for each cluster on each layer a two dimensional window (in azimuth and z) is opened, then the clusters are joined with those on the next layer within the window, building a set of tracklets. For each association within the acceptance window, two compatibility selection criteria are applied: the difference between the azimuthal angle of the two clusters is required to be smaller than $\Delta\phi_{\mathrm{MAX}}$ and the distance of closest approach to the primary vertex of the prolongation of the tracklet should be smaller than $\mathrm{DCA}_z^{\mathrm{MAX}}$. The applied selection requirements have been optimised looking at the distributions of these two variables for good tracklets (i.e. tracklets composed by two hits belonging to the same particle) and fake tracklets. The observed distributions in $\Delta\phi$ and Δz for the various cluster combinations are shown in Figure A.3 and Figure A.2 in the Appendix. While the $\Delta\phi$ distributions do not exhibit a strong dependence on the layers on which the

tracklet is spanning, the DCA_z does: for this reason, while a common $\Delta\phi$ window is used for all the combinations regardless the distance from the interaction region, the applied DCA_z^{MAX} selections are layer dependent. Here the z position of the primary vertex is extremely useful as the cut on the DCA_z of the tracklets discriminates well between good and fake tracklets.

If a tracklet is accepted two quantities related to its direction are stored: the segment inclination in the transverse plane (ϕ) and the inclination on rz:

$$\tan\lambda = \frac{\Delta z}{\Delta r}.$$

Here r and z do not define a proper plane because of the (small) change of the ϕ coordinate of the hits. Yet, the usage of $\tan\lambda$ as a discriminating quantity proves to be effective in the second step of the Cellular automata algorithm, where tracklets spanning on consecutive layers and with one cluster in common and compatible directions are considered to be subsequent and are combined into *cells* (3 points seeds).

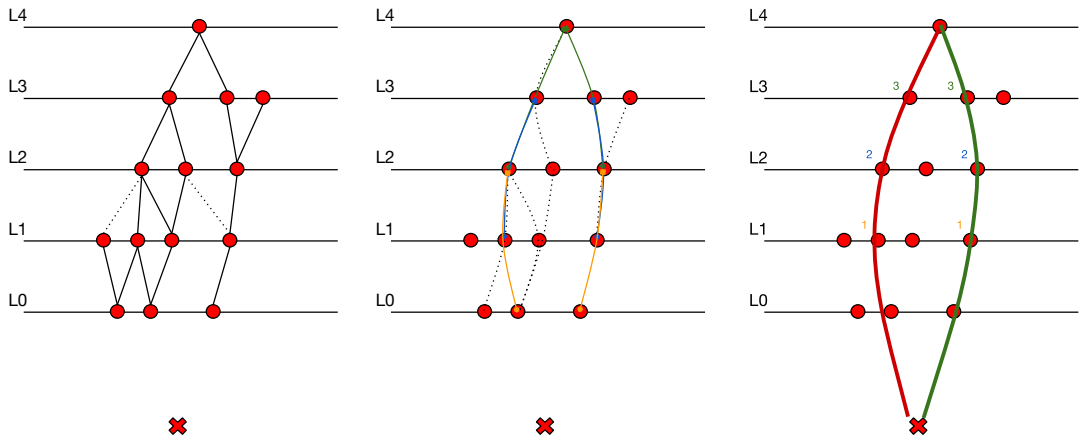

(a) Tracklet finding (b) Cell finding (c) Candidate finding

Figure 4.7: Simplified sketch of the reconstruction steps on the xy transverse plane of the Cellular Automata pattern recognition used for the ITS Upgrade tracking. The red cross represent the reconstructed position of the primary collision while the red dots are the reconstructed hits on the ITS Upgrade layers.

Since the charged particles in the transverse plane bend because of the ALICE magnetic field, the three hits of the seeds lay approximately on a circle, under the hypothesis that the effects of multiple scattering are small. As described in [81], circle finding in 2 dimensions can be mapped to plane finding in the space using the following parametrisation for the hits:

$$\vec{s_i} = \{x_i, y_i, w_i = R_i^2\} \quad i = 0\ldots2$$

where R_i is the distance of the hit i from the beam axis. This is equivalent to map the hits on a paraboloid with minimum point in the origin of the coordinate system and axial symmetry

along the w direction. The hits should lay on a circle in the transverse plane:

$$(x-x_c)^2+(y-y_c)^2=\rho^2 \rightarrow w-2xx_c-2yy_c+w_c-\rho^2=0$$

where $\{x_c, y_c, w_c\}$ are the coordinates of the centre of the circle and ρ is its radius. As anticipated, in terms of the new coordinates the circle equation resembles the equation of a plane in the space. A plane in the space can be defined by the unit vector $\vec{n}$ normal to the plane and by the distance c of the plane from the origin of the coordinate space. Three points in the space define uniquely a plane and the vectors connecting them lay on it. From this observation it follows that $\vec{n}$ can be defined as the external product between the vectors connecting the hits and c is defined[4] as the projection of one of the hits on $\vec{n}$:

$$\vec{n}=\frac{(\vec{s_1}-\vec{s_0})\wedge(\vec{s_2}-\vec{s_0})}{||(\vec{s_1}-\vec{s_0})\wedge(\vec{s_2}-\vec{s_0})||} \quad \text{and} \quad c=-\vec{n}\cdot\vec{s_0}=-\vec{n}\cdot\vec{s_1}=-\vec{n}\cdot\vec{s_2}.$$

By comparing the circle equation and the plane expression the following relations between the radius and the centre of the circle with c and $\vec{n}$ are obtained:

$$\{x_c, y_c\}=-\frac{1}{2}\left\{\frac{n_0}{n_2}, \frac{n_1}{n_2}\right\} \quad \text{and} \quad \rho=\sqrt{\frac{1-n_2^2-4cn_2}{4n_2^2}}.$$

where n_0, n_1 and n_2 are the components of the vector $\vec{n}$. For each cell the mean $\tan\lambda$ is then computed from the constituting tracklets and it is used to extrapolate it to the primary vertex. A cut on the DCA_z is applied to reduce the number of fake cells. The circle parameters are then used to compute the DCA_{xy} and a further selection is applied on it. In the third and last step of the current implementation of the algorithm (Figure 4.7c), the Cellular Automata rules are applied. If the normal vectors $\vec{n}$ and the radii ρ are compatible within a predefined tolerance, two cells spanning on four contiguous layers are considered to be neighbours. An index equal to 1 is given to all the cells without any neighbours (e.g. all the cells spanning over the innermost three layers have index 1). All the cells with one or more neighbours acquire an index equal to the highest index among the neighbours plus one. The continuous sequences of indices represent the track candidates that have to be fitted with the Kalman Filter [82]. If one hit is shared among more track candidates, only the longest one with the lowest χ^2 is kept and stored as reconstructed track, like shown in Figure 4.7c.

Appendix A shows the distribution of all the variables used to cut the combinatorial background during the tracking.

4.4.2 Tracking performance

A series of Monte Carlo simulations has been carried on in order to evaluate the track reconstruction efficiency for the ITS Upgrade and to benchmark the Cellular Automata algorithm.

[4] Using the distributive property of the external product and the rule of the circular shifts in the triple product it can be easily proven that $\vec{n}\cdot\vec{s_i}$ is the same for any $i\in\{0,1,2\}$.

The events were simulated using the HIJING event generator [83] with the addition of the beam induced QED electrons background. The transport of the generated particle through the detector material, as well as the detector response itself, have been simulated using the GEANT3 transport code [84].

When developing a tracking algorithm there are three interesting quantities to monitor: the tracking efficiency, the fraction of fake tracks reconstructed and the number of duplicated tracks. In this context the tracking efficiency computation does not keep into account the cluster finding and the detector inefficiencies and only charged pions with at least one cluster per ITS layer are considered and are called *trackable particles*. Thus the efficiency is computed as the ratio between the correctly reconstructed tracks and the *trackable particles*. A track is considered to be *fake* if at least one attached cluster is not belonging to the tracked particle. A track is considered to be *duplicated* (or *cloned*) if there are more tracks corresponding to the same particle. For the CA algorithm, and also for the CM algorithm, the fraction of duplicated tracks is less than 1% as we require at least 4 clusters for a track (out of a maximum of 7) and the fraction of reconstructed *split clusters*[5] is less than 1% [70].

The tracking efficiency for tracks with different number of clusters attached is shown in Figure 4.8a while Figure 4.8b shows the corresponding fake track fraction. In this case the CA tracking has been used with a set of tight cuts in the tracklet finding (*trackleting*) and in the cell finding such that the tracking efficiency for tracks with 7 clusters drops rapidly for $p_{\mathrm{T}} \leq 0.8$ GeV/c. On the other hand, for the same class of tracks the fake fraction is well below 5%. Looking at shorter tracks it is possible to see that the efficiency is recovered at low p_{T}: for tracks with 4 clusters attached (out of 7 belonging to the particles) the efficiency start dropping significantly only for $p_{\mathrm{T}} \leq 0.3$ GeV/c. The CPU time budget required to reconstruct a central Pb–Pb event with this configuration is 0.7 s on a laptop equipped with a Intel Core i7 5557U processor.

While the tight cut set allows to reach a very good performance in terms of CPU time with a tracking efficiency that is sufficiently high for the online calibration of the TPC, the efficiency estimations provided by the Fast Monte Carlo Tool (FMCT) used in the ITS Upgrade TDR [70] show that the tracking efficiency for 7 cluster tracks in the ITS Upgrade should be much higher at low transverse momentum ($\sim 70\%$ at $p_{\mathrm{T}} = 0.1$ GeV/c). In order to recover the tracking efficiency at low transverse momentum a second tracking iteration has been added. In the first iteration with tight cuts, only tracks with 7 clusters are stored as reconstructed tracks and all their clusters are marked as used. The second iteration then profits from a reduced combinatorial background, running the tracklet and the triplet finding algorithms with a set of loose cuts. This kind of approach leads to a dramatic improvement of the tracking efficiency at low p_{T} for tracks with 7 clusters that start dropping rapidly for $p_{\mathrm{T}} = 0.3$ GeV/c. The integral efficiency with this configuration reaches about 90%. The tracking efficiency for tracks with at least 5 and 6 clusters does not change much with respect to the 7 cluster requirement while for $p_{\mathrm{T}} < 0.1$ GeV/c the efficiency is significantly higher for tracks with at least 4 clusters. On the other hand also the fraction of fake tracks increases significantly at low p_{T} for short tracks

[5] When a particle hitting a sensor creates two clusters these are called *split clusters*.

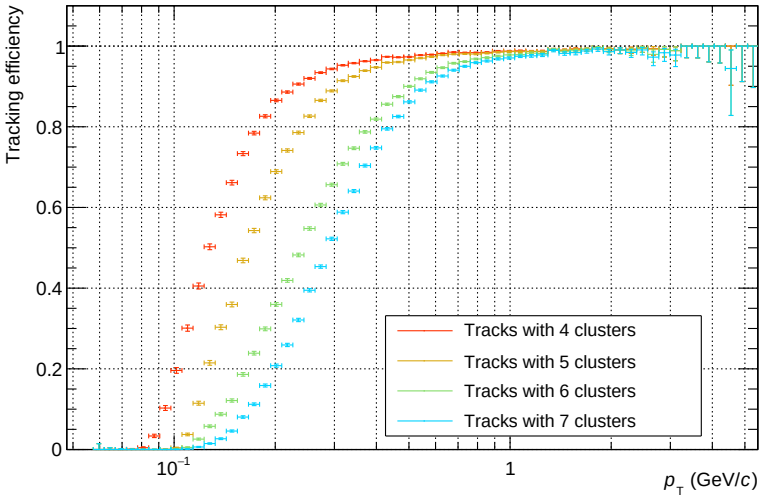

(a)

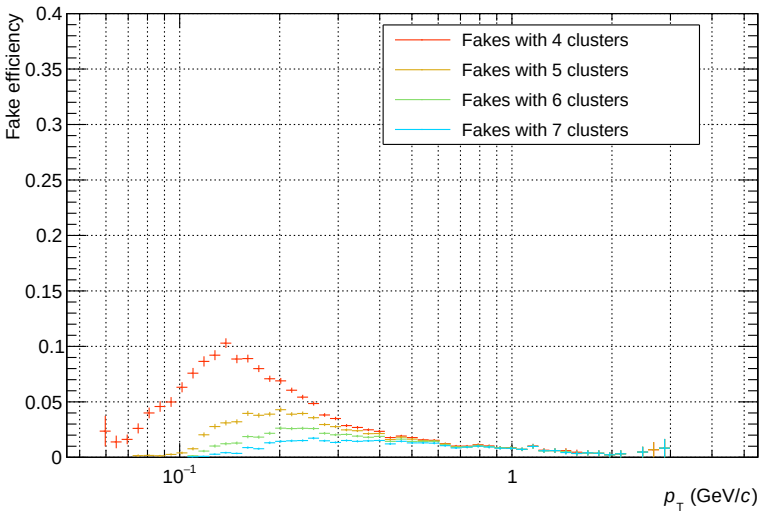

(b)

Figure 4.8: Tracking efficiency (on the top) and fake tracks fraction (on the bottom) in central Pb–Pb events reconstructed with the CA tracking algorithm using tight cuts in the tracklet and cell finding. The efficiency and the fake fractions are shown as a function of the transverse momentum and as a function of the number of attached clusters.

going up to 30% for $p_T < 0.1$ GeV/c. For 7 clusters tracks the fraction of fake tracks stays below 15% for $p_T \leq 10$ GeV/c and on average is below 10%. Running a second iteration of the CA algorithm with looser cuts increases also the CPU time required to run the tracking in a central Pb–Pb event to approximately 1.8 s on a laptop equipped with a Intel Core i7 5557U processor.

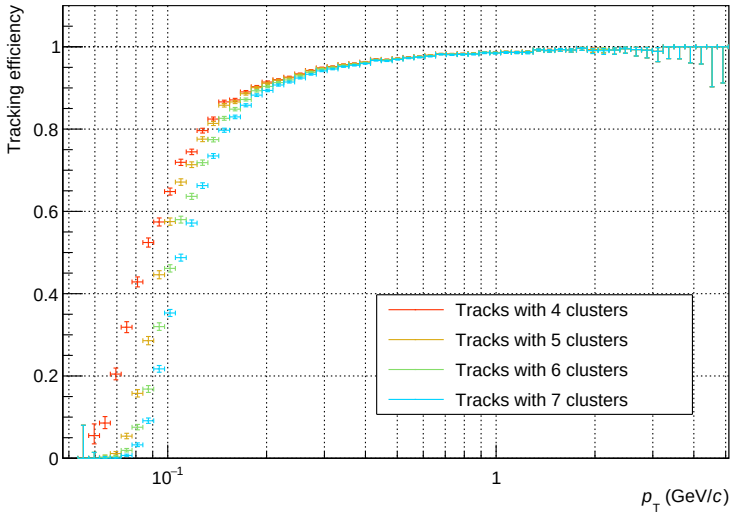

(a)

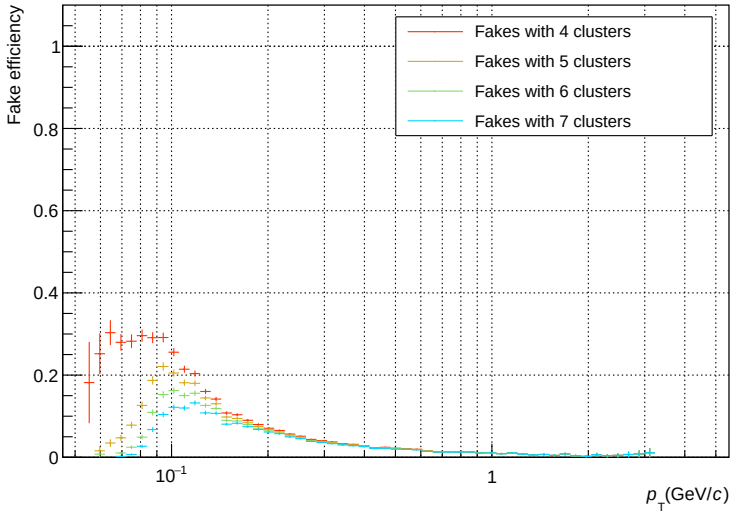

(b)

Figure 4.9: Tracking efficiency (top) and fake tracks fraction (bottom) in central Pb–Pb events reconstructed with the CA tracking algorithm using two iterations: the first with tight cuts and the second with loose cuts. The efficiency and the fake fractions are shown as a function of the transverse momentum and as a function of the number of attached clusters.

The cluster distribution over the layers of the ITS Upgrade for reconstructed tracks (Figure 4.10) indicates that most of the missed clusters are in the outermost layers. Going back to the efficiency plot as a function of the number of clusters attached to the tracks, this effect can be understood as most of the short tracks correspond to low momentum particles. At low momentum, the particle trajectories are heavily affected by the multiple scattering in the

detector material. While missing clusters in the outermost layers of the ITS deteriorate the matching efficiency with the TPC tracks and/or clusters, most of the tracked particles in the ITS with less than 7 clusters have $p_{\mathrm{T}} \leq 0.15$ GeV/c (Figure 4.9a) and they are anyway difficult to track in the TPC. On the other hand, these short tracks spanning on the innermost layer have similar pointing resolution (especially on the z direction) of the tracks with 7 clusters.

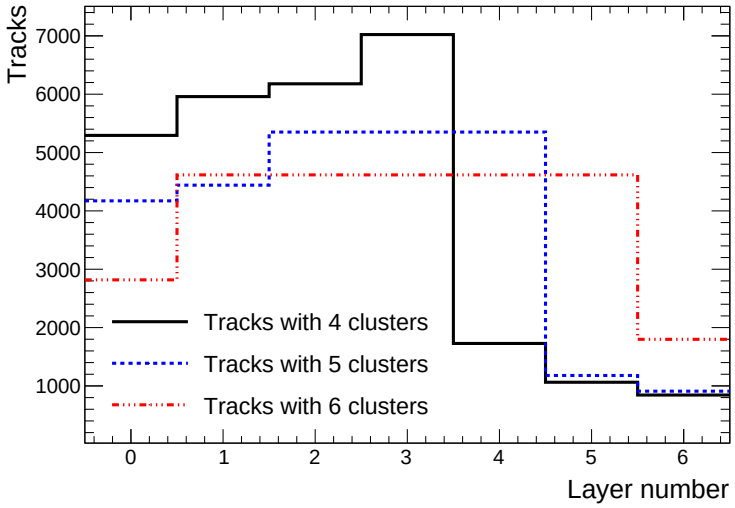

Figure 4.10: Distribution of the clusters on the ITS Upgrade layers for tracks with 4, 5 and 6 clusters attached.

The tracking efficiency and the fake fraction obtained with two iterations of the CA tracker (Figures 4.9a and 4.9b) have been compared to the ones obtained with the Cooked Matrix (CM) tracker. Figure 4.11a shows how the two trackers compare in terms of tracking efficiency. It is possible to notice that the tracking efficiency for pions with 7 clusters on the ITS upgrade is systematically lower for the CM tracker with respect to what is obtained for the CA tracker with two iterations. On the other hand, the fake tracks fractions, represented as shaded areas in Figure 4.11a, are similar for both tracking codes. The efficiency obtained with the CM tracker resembles more the result obtained with the CA tracker with only one tracking iteration, with the exception that the latter reaches the full efficiency for $p_{\mathrm{T}} \sim 1$ GeV/c while the CM tracker efficiency reaches unity only asymptotically at very high p_{T}. The difference is understood by looking at the distribution of the reconstructed track χ^2 for the two different tracking algorithms (Figure 4.11b). The CM tracker is a Kalman Filter based algorithm that applies stringent χ^2 cuts during the pattern recognition phase of the tracking. As a result, the obtained tracks have a very small χ^2. For the CA tracker the pattern recognitions and the fitting procedure, where the track χ^2 is evaluated, are disconnected and therefore also good tracks with bad χ^2 are not rejected during the pattern recognition step. The severe χ^2 cut applied in the pattern recognition of the CM tracker reduces the tracking efficiency especially at low transverse momentum where multiple scattering strongly affects the trajectory of the

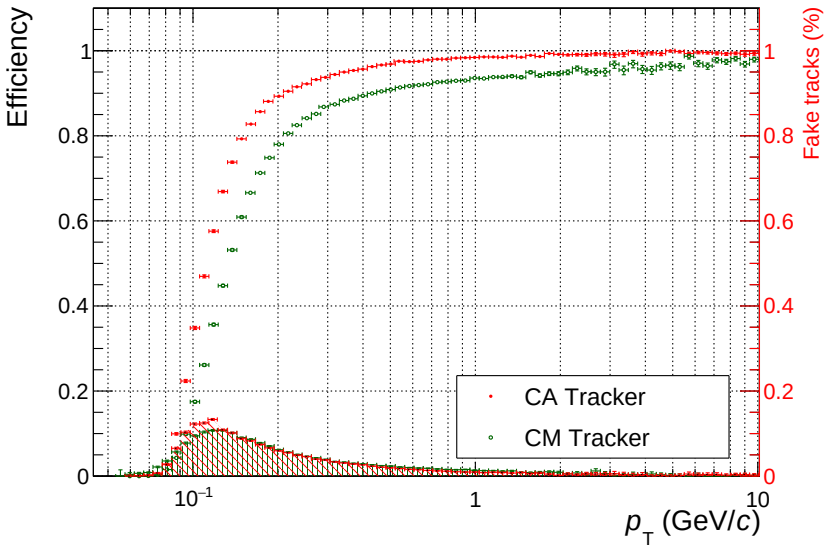

(a)

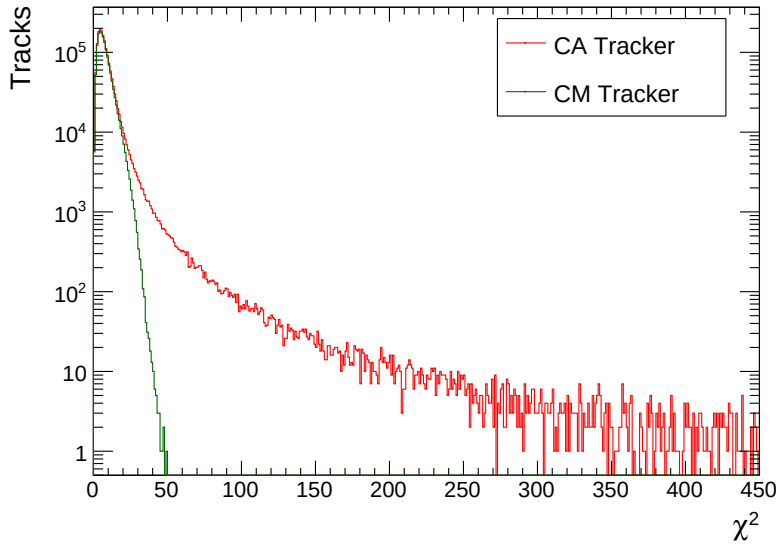

(b)

Figure 4.11: Comparison between the performance of the Cellular Automata and the Cooked Matrix trackers. On the top panel the tracking efficiency (points) and the fake tracks fraction (shaded area) are compared. On the bottom the distribution of the track χ^2 are compared.

particles.

The computing time required by the Cooked Matrix approach is ~ 40% more than the CPU time required by the Cellular Automata tracker using one iteration (approximately 1 second),

having comparable tracking efficiency. On the other hand the CM tracker results faster than the CA with 2 tracking iterations, that outperforms the CM tracker in terms of tracking efficiency at both low and high p_{T}.

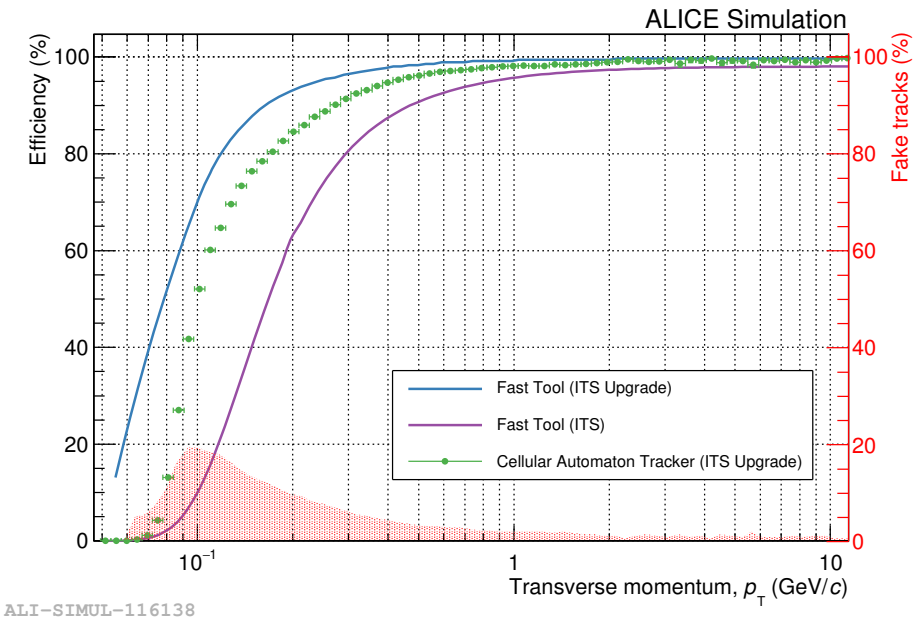

Figure 4.12: Tracking efficiency for pions with 7 clusters with the ITS upgrade detector in central Pb–Pb events. The green points represent the efficiency with the Cellular Automata algorithm while the continuous blue and purple lines represent the efficiency foreseen by the FMCT for the ITS Upgrade and the current ITS respectively. The red shaded area corresponds to the fake track rate for the CA tracker.

Figure 4.12 shows the comparison between the reconstruction efficiency for pions using the Cellular Automata algorithm and the prediction for the same quantity by the Fast Monte Carlo Tool (FMCT) used in the ITS Upgrade TDR [70]. Only tracks with 7 clusters have been considered here and the cluster finding efficiency is not included. It is possible to observe that the FMCT overestimates the efficiency reached by the CA tracker at low p_{T} as it does not keep into account the fluctuations of the energy loss of low energy particles in the ITS material. In addition, the FMCT considers the usage of the Kalman smoothing technique, useful to correct for the wrong cluster associations, which is not used currently in the full track reconstruction.

The foreseen improvement of the ITS Upgrade over the current ITS in terms of pointing resolution will be actually achieved according to the Monte Carlo simulations (Figure 4.13). In this case the FMCT estimation and the full reconstruction using the CA algorithm agree in the case of tracks with 7 clusters and a total χ^2 less than 20. The resolution quoted in the plots is the sigma of the gaussian fits to the distributions of the Distance of Closest Approach (DCA) in the transverse plane and in the z direction. The non gaussian residuals between the hit position and the cluster centre of gravity in the full Monte Carlo simulation and reconstruction

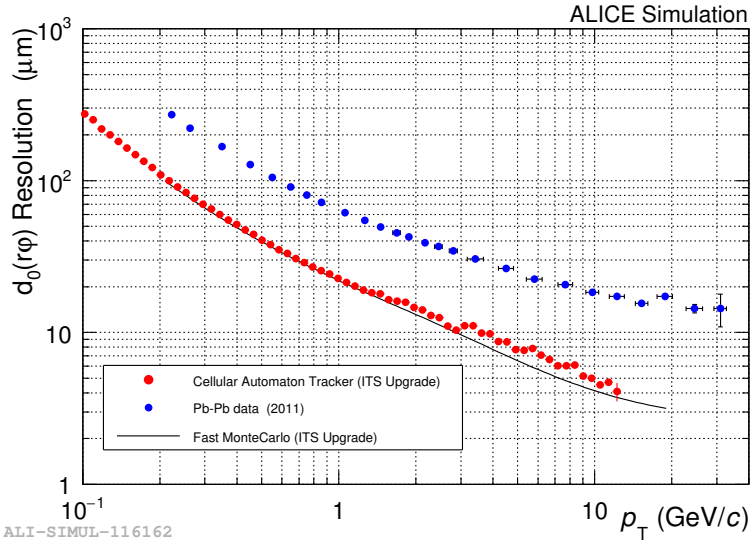

(a) Pointing resolution in the $r\phi$ plane

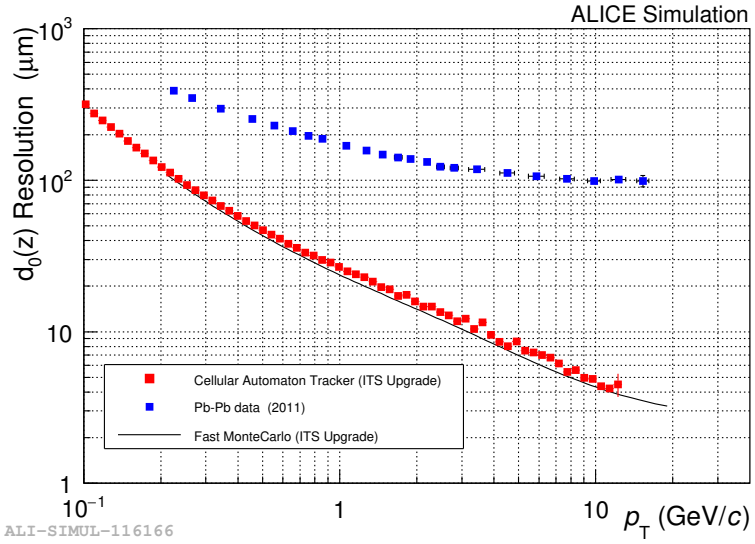

(b) Pointing resolution along z

Figure 4.13: Pointing resolution of the ITS Upgrade in the transverse plane (top) and in the longitudinal direction (bottom). The blue points represent the resolutions extracted with the data of the 2011 Pb–Pb run, the red points are the results obtained with the CA tracker with the aforementioned simulations whereas the black solid lines are the predictions of the FMCT.

are able to explain the slight deviation of the DCA resolutions from the FMCT predictions at high p_T: for high momentum particles the extrapolation error to the primary vertex is negligible and the DCA resolution is more affected by the non–gaussian resolution on the hit

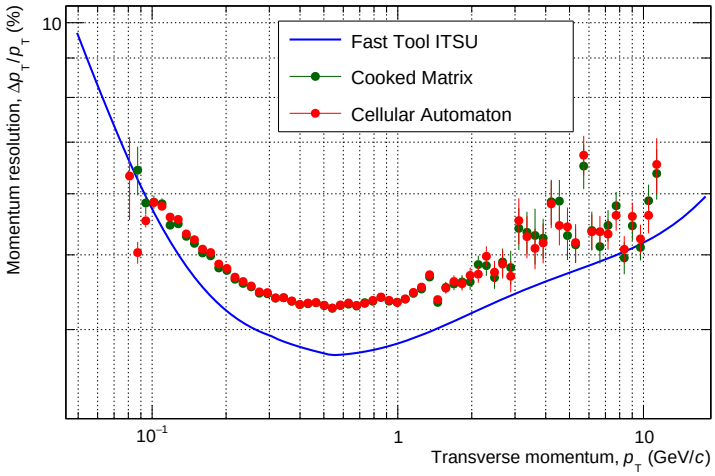

Figure 4.14: Relative momentum resolution as a function of the transverse momentum for ITS standalone tracks with 7 clusters attached. A $\chi^2 \leq 20$ quality cut has been applied in the case of the CA and CM trackers (red and green points respectively). The blue line represents the prediction of the FMCT.

points. Remembering that the momentum resolution has the following dependencies

$$\frac{\sigma_p}{p} \propto p\frac{\sigma_s}{BL^2},$$

where B is the magnetic field and L the lever arm of the tracking detectors, the non–gaussian resolution on the hits is also able to explain the observed deviation between the momentum resolution evaluated in the full simulation and the one estimated by the FMCT. Figure 4.14 shows how the FMCT overestimates the momentum resolution for the tracked particles whereas CM and CA trackers have the same relative resolution: less than 6% for particles with p_{T} between 0.1 GeV/c and 10 GeV/c. The relative resolution on the transverse momentum has been obtained by fitting the $1/p_{\mathrm{T}}^{\mathrm{rec}} - 1/pt^{\mathrm{true}}$ distribution, where $p_{\mathrm{T}}^{\mathrm{rec}}$ is the reconstructed momentum and $p_{\mathrm{T}}^{\mathrm{true}}$ is the one from the tracked Monte Carlo particle, for each p_{T} interval. The relative momentum resolution is then evaluated by applying the error propagation, thus

$$\frac{\sigma_{p_{\mathrm{T}}}}{p_{\mathrm{T}}} = \frac{\sigma_{1/p_{\mathrm{T}}}}{1/p_{\mathrm{T}}}.$$

4.5 Outlook

The vertex finding and tracking algorithms shown in this work satisfy the physics performance requirements of the ALICE experiment for the LHC Run3. However a careful optimisation of the working parameters has to be performed in order to maximise the efficiency of the

algorithms. Moreover some particular cases in the tracking code are still to be covered, for instance:

- the case in which one hit of a particle is missing from one layer of the ITS Upgrade will require a special treatment whereas the trajectory is currently reconstructed only partially (short tracks);
- a proper handling of readout frames for the ITS continuous readout mode should be implemented: this will add the time information to the track finding algorithm that will have to cope with hits from the same collision spanning on different readout frames;
- an optimised handling of the pile–up should be implemented, The current strategy foresees running the track finding algorithm for each vertex found in the event: this has the overhead of repeating the trackleting and the cell finding an unnecessary number of times.

Finally there is an ongoing effort for the parallelisation of the vertex finding and tracking algorithm in order to optimise the CPU usage and fully exploit the heterogeneous architecture that will be available with the O^2 facility. Since both the CA tracker and the primary vertex finder are based on the tracklet finding procedure, a first step towards the parallelisation of these algorithms is implementing the trackleting step using parallel programming. Two preliminary tests have been performed using the OpenMP [85] and the OpenCL [86] technologies on CPU. Starting from the data structures developed for the CA tracker (Figure 4.6), two different approaches have been evaluated:

- finding tracklets in parallel on different layers: as each set of tracklets is independent (e.g. tracklets between Layer 0 and Layer 1 are independent from tracklets between Layer 1 and 2), the procedure of finding tracklets between different couples of layers can be performed in parallel. This kind of approach is extremely easy to implement but it offers only a small degree of parallelism and can be hardly adapted to highly parallel architectures such as Graphics Processing Units (GPU);
- finding tracklets in parallel on different azimuthal regions: as shown in Figure 4.6, for each region in ϕ on Layer 0 it is possible to define a region of interest on Layer 1 where tracklets are defined. In the case of the primary vertex finder the region of interest on Layer 1 cannot be constrained in the z direction but it can be still defined using the azimuthal angle as only constraint. Each of these searches are independent and can be performed in parallel. The main advantage of this approach is the good granularity of the achieved parallelism but it requires some change in the code to avoid *data races*[6].

[6] A data race is, for instance, when two or more independent threads or processes try to write concurrently at the same portion of memory leading to inconsistent results

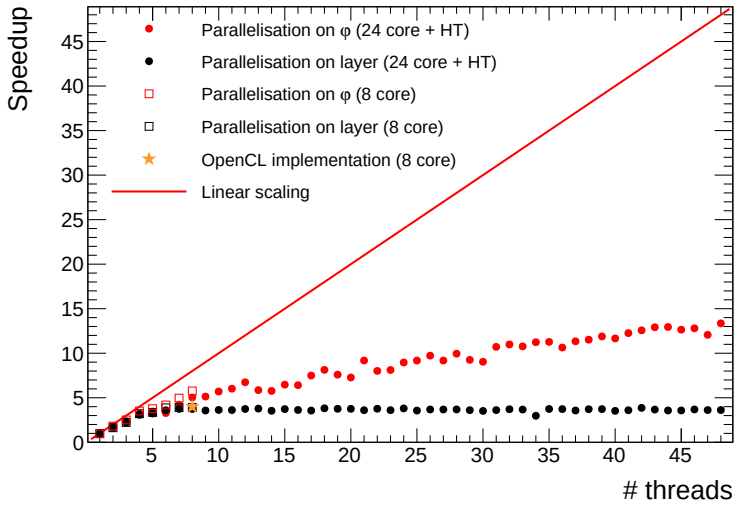

Figure 4.15: Speedup factor as a function of the available number of threads for the two different algorithms in use. The solid red line represents the ideal case of linear speedup. The OpenCL implementation of the algorithm with the parallelisation on ϕ is represented with a green star.

The first method has been implemented only with OpenMP while the second one has been evaluated using also the OpenCL framework. The scalability of the two implementations has been tested on two different setups: one with a Dual CPU configuration without HyperThreading (HT) technology with 8 hardware threads in total and one with a Dual CPU configuration with HT and 48 hardware threads. Figure 4.15 shows the results of this first benchmark: the speedup, defined as the ratio between the computing time required for the parallel processing and time required for the serial processing, is higher for parallelisation on the azimuthal regions even though it does not follow the ideal linear trend with the number of available threads.

A large margin of improvement is feasible with a further optimisation of the code and of the parallelisation strategy. There is an ongoing effort to address the issue of providing primary vertex reconstruction and ITS Upgrade standalone tracking within the time and CPU constraints of the O^2project.

5 Nuclei and anti–nuclei in Pb–Pb collisions: analysis technique

This chapter describes the analysis steps required to measure the production spectra of light (anti-)nuclei in Pb–Pb collisions with the ALICE experiment. The analyses of the (anti–)deuteron production and of the (anti–)^{3}He production spectra have been carried out only in Pb–Pb collision at $\sqrt{s_{\rm NN}}$ =5.02 TeV. While the light nuclei production spectra in Pb–Pb collisions at $\sqrt{s_{\rm NN}}$ =2.76 TeV has been already published by the ALICE collaboration [87], an analysis of the (anti-)deuteron spectra in the Pb–Pb collisions data sample, collected in 2011 at the same energy but with a different trigger menu, is presented here. It will be shown that the study of the (anti–)deuteron production in the unexplored $p_{\rm T}$ region between 4.4 and 6 GeV/c is now possible.

5.1 Data and Monte Carlo samples

The analyses presented in this thesis are based on the data sets of Pb–Pb collisions collected in 2011 ($\sqrt{s_{\rm NN}}$ =2.76 TeV) and in 2015 ($\sqrt{s_{\rm NN}}$ =5.02 TeV). In both data samples the events were collected whenever a coincidence of signals for both sides of the V0 detector was found. On top of this trigger logic, in 2011 a further online selection on the sum of the V0 detectors amplitudes was used to enhance the number of central (0-10%) and semi–central (10-50%) events. Moreover, the timing information of the V0 scintillator arrays paired with the timing information from the ZDC is used as further offline rejection of events triggered by the interactions of the beams with the residual gas in the LHC vacuum pipe. After the offline event selection, the data samples consist of nearly 40 million Pb–Pb collisions at $\sqrt{s_{\rm NN}}$ =2.76 TeV and of about 90 million Pb–Pb collisions at $\sqrt{s_{\rm NN}}$ =5.02 TeV. Figure 5.1 shows the distribution of the event centrality percentile for both data sets. The enhancement of central and semi–central events thanks to the online trigger strategy adopted in 2011 is visible in the distribution for the 2011 sample (Figure 5.1a). Conversely the centrality percentile distribution for the 2015 data (Figure 5.1b), that were collected with a minimum bias trigger, is clearly flat. With the available number of events, the analysis of the (anti-)deuteron production is possible in the centrality ranges 0-50% and 0-90% in the 2011 and 2015 samples respectively.

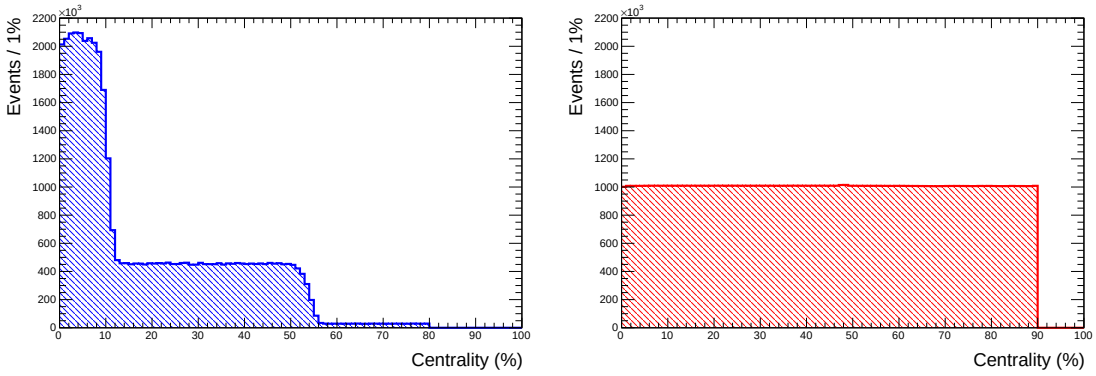

(a) 2011 data sample

(b) 2015 data sample

Figure 5.1: V0M centrality percentile distribution for the 2011 data sample (on the left) and the 2015 data sample (on the right) for events satisfying the event selection criteria. Increasing centrality percentile correspond to decreasing centrality of the collisions studied. The centrality estimation, as well as the definition of the V0M estimator, were briefly discussed in Section 3.6.

The Monte Carlo (MC) samples used to compute the efficiency, acceptance and momentum shift corrections were generated using the HIJING event generator [83]. The conditions of data taking are accounted in the MC by reproducing the actual configuration of the different detectors in the runs used for the analysis. Since the HIJING event generator used to simulate Pb–Pb collisions does not provide light (anti–)nuclei, an *ad–hoc* generator that injects particles on top of a HIJING event was used. The kinematics of the injected nuclei is chosen randomly by picking their transverse momentum from a flat distribution in the range between 0 and 10 GeV/c, their azimuthal angle from a distribution between 0 and 2π radians, and their rapidity from a flat distribution in the range $|y| < 1$. The MC simulation of a full Pb–Pb event, from the generation of the kinematics of the different particles and their transport in the

Table 5.1: Details about the MC productions used in this analysis. For all of them, the particles are injected on top of an HIJING Pb–Pb event. The impact parameter (b) of the HIJING event is extracted from a flat distribution with the limits reported in the table. Each MC sample is simulated using the database of the detector conditions of the data taking period of interest, the *anchor period*. The number of injected particles reported in the third column has to be multiplied by 2 for the injection of the respective charge conjugate states.

Anchor period	b (fm)	Injected particles per event (+cc)	Events
Pb–Pb $\sqrt{s_{\rm NN}}$ =2.76 TeV	0–13.97	10× ^{2}H,^{3}H,^{3}He,^{4}He,Λnn,Ξ^0p	310745
Pb–Pb $\sqrt{s_{\rm NN}}$ =5.02 TeV	0–5	10× ^{2}H,^{3}H,^{3}He,^{4}He, 40×$^3_\Lambda$H, 20×$^4_\Lambda$H,$^4_\Lambda$He	112112
	5–11		439760
	11–15		355740

detector volumes, is expensive in terms of computing resources (approximately one hour per one central Pb–Pb on the ALICE GRID). For this reason only a fraction of the total collected statistics is generated in the MC samples. The centrality of the simulated events is steered by setting the impact parameter (b) of the HIC simulated by HIJING. In the MC samples discussed here, b was picked randomly from a flat distribution for each event. The b_{min} and b_{max} of the distribution were chosen to match the 0-80% V0 centrality interval for the MC anchored to the 2011 data sample. In order to optimise the use of the computing resources, three different MC samples anchored to the 2015 Pb–Pb data sample and using different b intervals were produced. These three MC productions correspond to the 0-10%, 10-50% and 50-90% V0 centrality intervals. The b intervals used as well as the details about the number of different species injected in each MC event and the number of available events are presented in Table 5.1.

5.1.1 Event selection

A further selection of the events to be analysed is performed offline to reduce possible biases from particular conditions of the data taking (e.g. high interaction rate, parts of detectors switched off). The typical selection used in Pb–Pb collision to obtain a symmetric acceptance is the rejection of events with the primary vertex outside the fiducial region of ±10 cm in the beam direction from the nominal collision point ($|V_z| \leq 10$ cm).

The centrality region of interest for the 2011 analysis is between 0 and 50% (Figure 5.1a). Moreover, it is interesting to study the production separately in the central events (from 0 to 10%) and in semi–central events (from 10 to 50%) to observe the centrality dependence of deuteron production and to reproduce and extend the results obtained in [87]. Unfortunately, the centrality distribution shows a non–flat behaviour around 10% centrality, where the transition between the central and the semi–central triggers occurs. In order to avoid biases coming from a non flat centrality distribution in central and semi–central events, a *flattening* procedure was adopted to smooth the centrality distribution. The flattening procedure consists of a first step in which a probability distribution is created from the raw centrality distribution (Figure 5.1a). The probability P_i is computed for each bin of 1% centrality as

$$P_i = \frac{C_{ref}}{C_i} \tag{5.1}$$

where C_{ref} is the target flat value and C_i is the number of counts in the bin corresponding to i% of centrality. In the second step of the flattening procedure, each event with i% centrality has a probability P_i to be kept for the analysis. This step is implemented using a pseudo-random number generator initialised with a seed computed from the date and time at which the analysis job started. Thanks to this two–steps procedure it is possible to select a sample of events with flat centrality distribution in the centrality ranges relevant for the analysis (Figure 5.2), rejecting about 3 millions of events in the centrality range between 0 and 14%. This flattening procedure, developed for the case of the 2011 sample where two different trigger

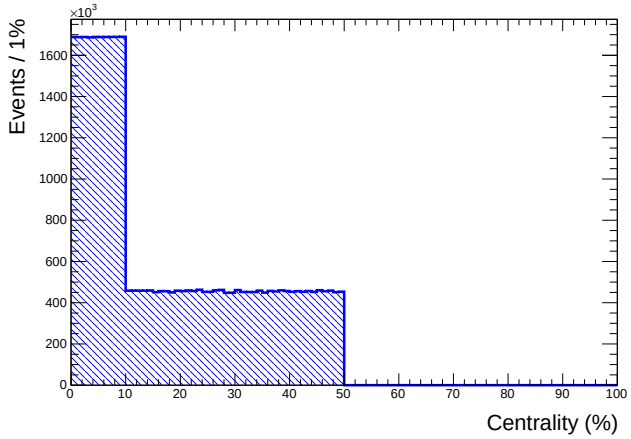

Figure 5.2: V0M centrality percentile distribution for events selected for the analysis on the 2011 data sample after the flattening procedure.

configurations have been used to collect the data, is not necessary for the 2015 data as the V0M centrality distribution is uniform in that sample.

On the other hand, due to the high interaction rate available in the 2015 data taking, a fraction of the triggered events contains data corresponding to more than one collision (pile–up). The first selection criterion applied to remove the pile–up is on the number of primary vertices reconstructed with SPD with more than n contributors, where n is a parameter of the selection.[1] From previous analyses, looking at the multiplicity dependence of the false positive pile–up tagging, the n parameter was set to 5 for events with more than 50 tracklets, to 3 for events with less than 20 tracklets and it was set to 4 for the remaining events. This method removes only the pile–up of collisions occurring either during the same bunch crossing[2] or out of bunch pile–up within the SPD readout time (300 ns). The pile–up tagging method based on the SPD vertex finding is not able to resolve collisions spaced along the beam axis coordinate by less than 8 mm. In this case the pile–up is not detected and the two collisions are merged. Other selections that help reducing the effect of the pile–up background are based on the correlation of different centrality estimators. For instance, the outliers in the correlation between the centrality estimator V0M, based on the V0 detector (whose readout window is 25 ns), and CL0, based on the SPD clusters, are interpreted as events with residual pile–up. Some outliers can be spotted also in the correlation between the V0M centrality estimator and the SPD tracklets. In order to suppress such outliers, a 5 σ selection has been applied on the aforementioned correlations. Figures 5.3a and 5.3b show the correlation between the V0M and CL0 centrality

[1] The number of contributors is the number of SPD tracklets (defined in Chapter 4) used to estimate the vertex position. A tracklet is built by matching two hits, one in the first SPD layer and the other in the second. If a vertex is built with few tracklets, it is possibly a fake.

[2] The bunch crossing is defined as the instant when the two LHC beams cross at the ALICE interaction point. The time windows separating two bunch crossings are always multiple of 25 ns, that is the period of the LHC clock.

Table 5.2: Summary of the event selection applied for the different data samples analysed in this work. See the text for the description of the used variables.

Data sample	Selection
Pb–Pb 2011	Centrality flattening
Pb–Pb 2011 and 2015	$\|V_z\| \leq 10$cm
	$\|\text{V0M} - \text{CL0}\| \leq 5\sigma$
Pb–Pb 2015	$\|\text{V0M} - n_{\text{tracklets}}\| \leq 5\sigma$
	Reject multiple SPD vertices with more than 5 contributors
	$\|\Delta V_z\| \leq 20\ \sigma_{\text{track}}$, $\|\Delta V_z\| \leq 10\ \sigma_{\text{SPD}}$ and $\|\Delta V_z\| \leq 0.2$ cm

estimators before and after the event selection[3] respectively and it is possible to see how the applied selections clean the correlation between these variables. At the same time, the applied selections clean the correlation between tracklets and the V0M estimator (Figure 5.3c and Figure 5.3d). Another visible effect due to the very high multiplicity events, for instance those containing two piled up central collisions, is in the distribution of the z coordinate of the primary vertices. In such conditions the vertex finding algorithm using the reconstructed tracks fails to find the correct primary vertex[4]. As a consequence, the distribution of the primary vertex position along the z axis shows some spikes (Figure 5.4a) before the event selection and a large difference is seen between the reconstructed vertex position obtained with the SPD based method and the track based vertex finding algorithm ΔV_z (Figure 5.4c). These discrepancies are filtered at the level of the event selection, picking only events where ΔV_z is less than $20\ \sigma_{\text{track}}$ and $10\ \sigma_{\text{SPD}}$, where σ_{track} and σ_{SPD} are the resolutions of the primary vertex computed with the track based and the SPD only vertex finding algorithms respectively. In addition the ΔV_z is required to be less than 0.2 cm. Figure 5.4b and Figure 5.4d show how the selections applied cure the distribution of the primary vertex position and of ΔV_z respectively. These additional selections for the pile–up rejection turn out to have a negligible effect on the final analysis results.

The above–mentioned selections are summarised in Table 5.2 together with the dataset to which they are applied. Based on the available number of events and the necessity of comparing and extending the published data [87], the 2011 data sample has been sliced in three centrality intervals on which the analysis is performed: 0-10%, 10-20% and 20-40%. For the 2015 sample the main rationale behind the choice of centrality classes is the necessity of comparing the deuteron production with that of other light flavoured particles, in particular with protons. Therefore in the 2015 data sample, 10 slices in centrality have been used to perform the analysis on deuteron production: 0-5%, 5-10%, 10-20%, 20-30%, 30-40%, 40-50%, 50-60%, 60-70%, 70-80% and finally 80-90%. The study of the production spectra of ^{3}He is more limited by the available amount of events. For this reason the analysis for the ^{3}He is carried out only

[3] Here and in the following, the plots show the difference before and after the complete event selection, including the selection on the trigger scheme and all the selections reported in Table 5.2

[4] One possible explanation of this behaviour is that the analytical minimisation procedure used in this algorithm fails to find the global minimum in the extreme condition of pile-up of two central Pb–Pb events.

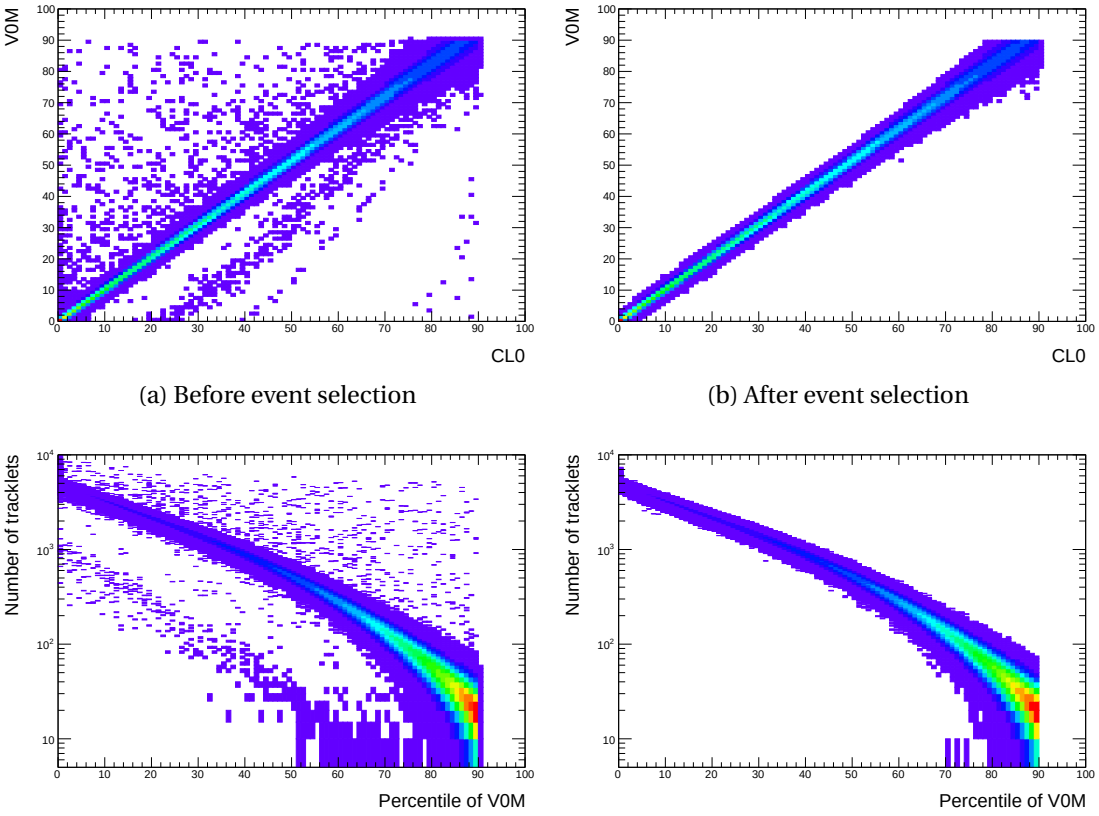

(a) Before event selection

(b) After event selection

(c) Before event selection

(d) After event selection

Figure 5.3: Correlation plot between SPD related quantities and V0M centrality estimator. The top plots show the correlation between the CL0 centrality estimator (proxy for the number of cluster in the innermost layer of SPD) and the V0M estimator before (on the left) and after (on the right) the event selection. Similarly the bottom plots show the correlation between the number of tracklets reconstructed with the SPD and the V0M estimator.

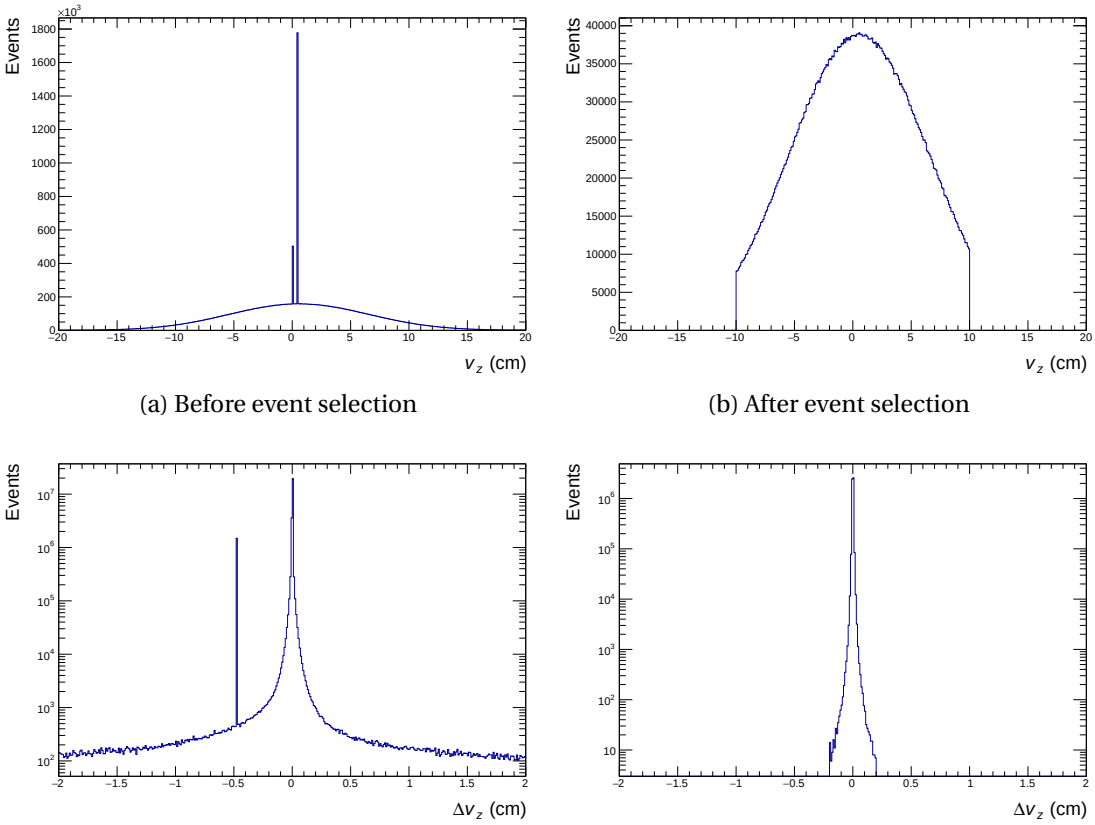

(a) Before event selection

(b) After event selection

(c) Before event selection

(d) After event selection

Figure 5.4: Distribution of the z vertex position (top row) and of the distance between the vertex reconstructed with the track based and the SPD only vertex finding algorithms (bottom row). The left column show the distribution before the event selection while the right column show the effect of the selections on these variables.

in three centrality intervals: 0-10%, 10-40% and 40-90%. In the context of setting up the event selection for this work, I developed a general tool for applying standard event selections in ALICE analyses and it is now adopted by many other analyses in the collaboration.

5.1.2 Track selection

The aim of the analyses presented in this thesis is to measure the primary light (anti–)nuclei production in the mid–rapidity region ($|y| < 0.5$). Primary nuclei are only those produced in the collision or in the evolution stages of the system created in a HIC.

In order to use only the geometrical region in which the ALICE experiment is able to perform full tracking and to provide the best possible PID information, only tracks in the pseudorapidity region $|\eta| < 0.8$ are used in these analyses. Moreover, to guarantee a track momentum resolution of 2% in the relevant p_{T} range and a $\mathrm{d}E/\mathrm{d}x$ resolution of about 6%, the selected tracks are required to have at least 70 clusters in the TPC and two points in the ITS (out of which at least one is in the SPD). The requirement of at least one point in the SPD assures a resolution better than 300 μm [60] on the distance of closest approach to the primary vertex in the plane perpendicular (DCA_{xy}) and parallel (DCA_z) to the beam axis for the selected tracks.

In order to suppress the contribution of secondary particles only tracks with $|\mathrm{DCA}_z| \leq 1$ cm are selected. The main secondary deuteron contribution comes from the knock-out deuterons produced by the interaction of primary particles with the material of the beam-pipe and of the apparatus and it is relevant for the production spectra and the elliptic flow measurements for $p_{\mathrm{T}} \leq 1.4$ GeV/c. The only known contribution to secondary deuterons and anti-deuterons from weak decays comes from the charged three-body decay of the hypertriton (${}^{3}_{\Lambda}\mathrm{H} \rightarrow \mathrm{d+p+}\pi^{-}$) and of the anti-hypertriton (${}^{3}_{\bar{\Lambda}}\overline{\mathrm{H}} \rightarrow \overline{\mathrm{d}} + \bar{\mathrm{p}} + \pi^{+}$). From the measurement of the hypertriton production into charged two-body decay [88] we know that this contribution is negligible. Moreover, the χ^2 per TPC cluster is required to be less than 4 and the χ^2 per ITS cluster is required to be less than 36. Finally tracks of weak-decay products (kink topologies) are rejected as the deuteron is a stable nucleus. When the TOF PID is required, a hit matched to the track extrapolation in the TOF sensitive area is required.

Table 5.3: Summary of the track selections applied in the analyses on the 2011 and 2015 data sample.

Track selections
$\|\eta\| \leq 0.8$ and $\|y\| \leq 0.5$
$n_{\mathrm{TPCclusters}} > 69$, $n_{\mathrm{ITSclusters}} > 1$ and $n_{\mathrm{SPDclusters}} > 0$
$\|\mathrm{DCA}_z\| \leq 1$ cm and $\|\mathrm{DCA}_{xy}\| \leq 0.1$ cm
$\chi^2_{\mathrm{TPC}} / n_{\mathrm{TPCclusters}} \leq 4$
$\chi^2_{\mathrm{ITS}} / n_{\mathrm{ITSclusters}} \leq 36$
Reject kink topologies

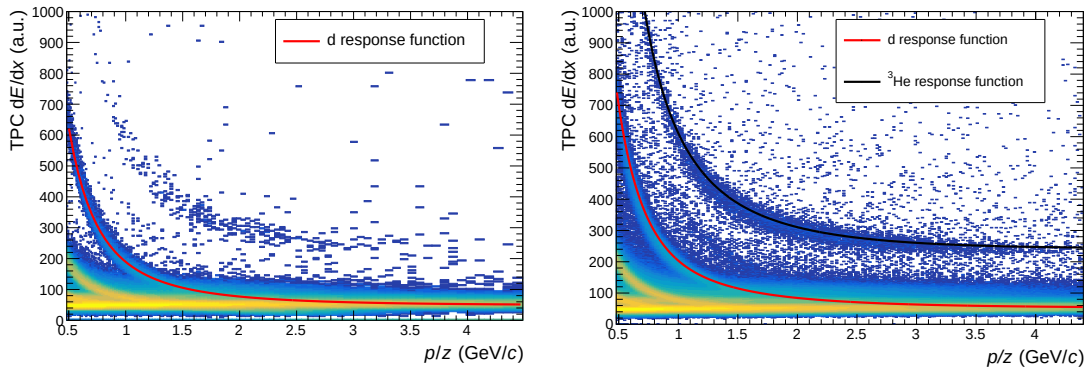

(a) 2011 data sample

(b) 2015 data sample

Figure 5.5: Specific energy loss in the TPC active volume for negative particles as a function of the particle rigidity in Pb–Pb collisions for the 2011 data sample (left) and the 2015 data sample (right). The solid lines represent the expected TPC response for deuterons (red) and ^{3}He (black).

The aforementioned track selection criteria are common to the analyses on the two different data samples and Table 5.3 summarises them.

5.2 Raw spectra extraction

The identification of (anti-)deuteron and (anti-)^{3}He is performed in the analyses reported here using a combination of the particle identification tools provided by the TPC and the TOF for the deuteron, and using the TPC information alone for the (anti–)^{3}He. In the following sections the details about the identification and signal extraction for the light nuclei will be presented.

5.2.1 Deuteron and ^{3}He identification using TPC

As already discussed in Section 3.5.2, the specific energy loss of particles inside the active volume of the TPC can be used to determine their identity.

Figure 5.5a and Figure 5.5b show the specific energy loss for negative particles in the TPC active volume and the expected signal for deuterons and ^{3}He for the 2011 and 2015 data sample respectively. Because of the usage of a different gas in the TPC and the change of its readout electronics between 2011 and 2015, the response functions are slightly different in the two samples.

Since the deuteron is twice as massive than the proton, it reaches the minimum of ionisation at $p \sim 1.8$ GeV/c. Due to the finite resolution on the specific energy loss measured by the TPC

($\approx$ 6% for the selected tracks) and due to the contamination from electrons and positrons, a track–by–track identification of deuterons can be performed using exclusively a fiducial selection on the TPC dE/dx information only up to $p \sim 1$. GeV/c. At higher momenta the identification of deuterons becomes less trivial and the statistical unfolding of the deuteron signal from the minimum ionising particles signal and the electron/positron contamination has to be performed. For sake of simplicity, the identification of the deuteron is achieved in this work by using the combined TPC and TOF information.

Conversely, for the ^{3}He, that has charge $z = 2e$, the sole TPC information provide a clean identification. This can be evicted remembering that the Bethe–Bloch formula for the specific energy loss depends on the square of z, thus the ^{3}He is well separated from all the particle species with $z = 1e$ in a large momentum region.[5] The only known species that might contaminate the identification of the ^{3}He in the TPC is the ^{4}He, but since its expected production rate is approximately 300 times smaller than the expected production of ^{3}He, it can be neglected in this analysis. In the low momentum region, the specific energy loss of ^{3}He becomes similar to the one of the ^{3}H and therefore this contamination has to be subtracted in the signal extraction.

In order to extract the number of produced ^{3}He in a particular transverse momentum interval, the number of entries in the nσ distribution is counted. The nσ distributions are filled with the difference between the specific energy loss associated to all the selected tracks and the expected (anti–)^{3}He dE/dx, normalised on the TPC dE/dx resolution on the specific energy loss σ. The signal of the ^{3}He is expected around 0σ but as it is shown in Figure 5.5b the parametrisation of the expected response for ^{3}He is not perfectly centred around zero even if the trend is rather well reproduced. The maximum shift observed is of 0.5 σ on the negative side. For the purpose of the spectra analysis the centring of the nσ distributions is not fundamental, as the entries can be computed starting from the mean of the observed distribution within a 3σ interval. Figure 5.6a and Figure 5.6c show an example of the nσ distribution for ^{3}He for the 0-10% and 10-40% centrality ranges respectively: these particular distributions correspond to a p_{T} interval between 1.95 and 2.45 GeV/c. In this p_{T} interval the contamination from the ^{3}H is visible on the left of the peak of the ^{3}He distribution. A fit with an exponential function is performed on the tail of the ^{3}H contamination, where no ^{3}He signal is expected. The resulting exponential function is then subtracted to the data histogram to obtain the distribution of the ^{3}He candidates without any significant residual background (Figure 5.6b and Figure 5.6d). The contamination from ^{3}H is present only when analysing at the production of ^{3}He and it is due to secondary ^{3}H nuclei from knock–out interactions of other primary particles with the experiment material. For this reason, such a contamination it is not present in the nσ distributions for the $^3\overline{\mathrm{He}}$.

[5] On top on the z^2 dependence, the Bethe–Bloch formula depends also on the particle Lorentz factors, β and γ:

$$\left\langle \frac{\mathrm{d}E}{\mathrm{d}x} \right\rangle \propto \frac{z^2}{\beta^2} \log\left(\frac{2\gamma^2\beta^2 m_e}{I_0} \right). \tag{5.2}$$

In the formula m_e is the electron mass and I_0 is the minimum energy loss

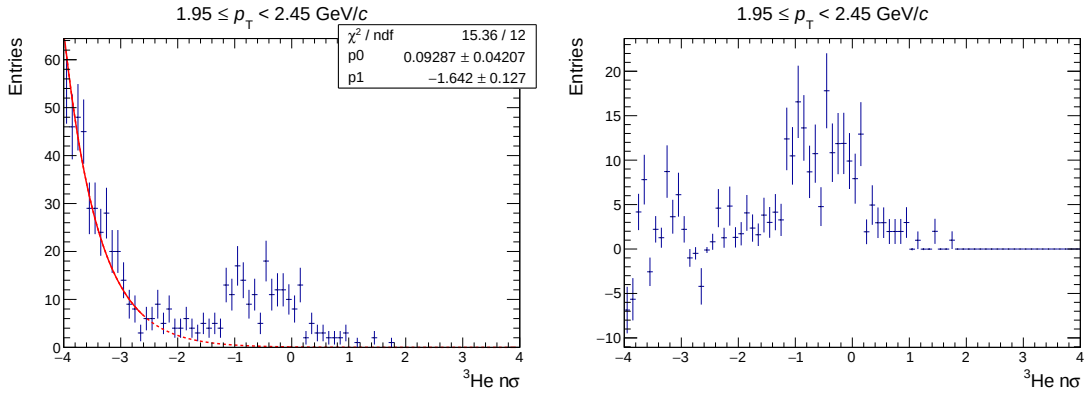

(a) 0-10%

(b) 0-10% contamination subtracted

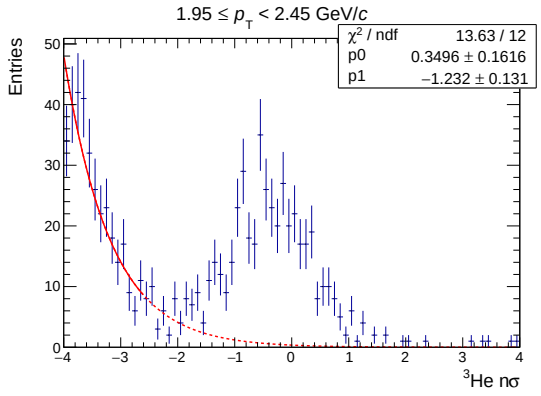

(c) 10-40%

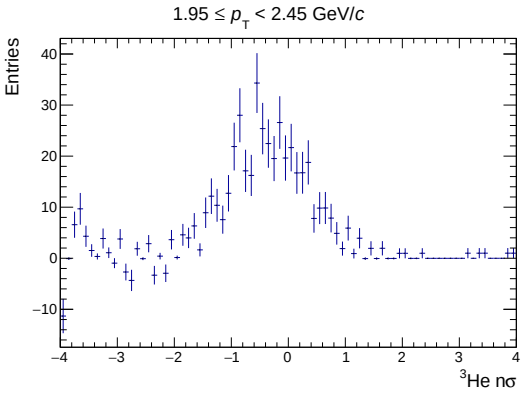

(d) 10-40% contamination subtracted

Figure 5.6: nσ distributions for ^{3}He in the $1.95 \leq p_T < 2.45$ GeV/c bin before (on the left) and after (on the right) the subtraction of the contamination from ^{3}H. The red lines show the fitted function, represented as a solid line in the fit range.

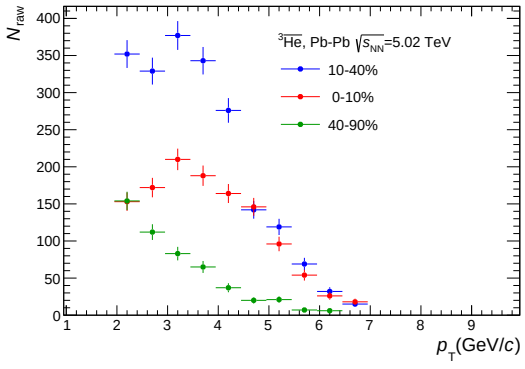

(a) $^3\overline{\text{He}}$

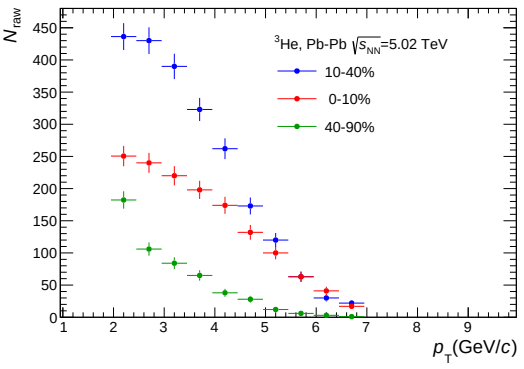

(b) ^{3}He

Figure 5.7: Raw counts for ^{3}He and $^3\overline{\text{He}}$ in the p_T range where the procedure for the signal extraction described in the text was feasible.

Finally, Figure 5.7a and Figure 5.7b show the raw counts extracted with the procedure mentioned above.

5.2.2 Signal extraction for deuterons using TPC+TOF

The signal extraction for (anti–)deuterons is performed combining the information of the specific energy loss measured by the TPC with that of the time of flight measured by the TOF. For this reason an additional track requirement is set for the deuteron analysis: a hit matched in the TOF detector that provides, as its name suggests, an accurate measurement of the time of flight t_{TOF} of a particle. The Lorentz β of the particle can be measured using in addition the track length L measured in the tracking procedure:

$$\beta = \frac{L}{t_{\mathrm{TOF}} c}, \tag{5.3}$$

where c is the speed of light. Combining this piece of information with the measured particle momentum p, the particle mass can be estimated as:

$$m = \frac{\sqrt{1-\beta^2}}{\beta} p. \tag{5.4}$$

(Anti–)deuterons can be separated from lighter species over a wide momentum range thanks to the excellent TOF timing resolution ($\approx$ 80 ps in Pb–Pb collisions). Nevertheless, a clean identification without background it is not possible in Pb–Pb events because of the background from mismatched TOF hits: in high multiplicity events the TOF occupancy is such that, within the track extrapolation resolution in the TOF active volume, it is possible to match more than one hit. When more than one hit can be associated, the closest to the track extrapolation is chosen. Nevertheless, the probability of associating a hit corresponding to another particle is not negligible ($\sim$ 20% for pions at 1 GeV/c in the most central Pb–Pb collisions [89]) and it is higher for low momentum particles. The presence of mismatched hits can be seen in the PID plots as hits not corresponding to any particle species expected signal. In this analysis to remove effectively this background a 3σ track selection criterion around the expected energy loss of (anti–)deuterons in the TPC volume is used. This selection criterion helps to reduce the background from mismatched TOF hits in the p_{T} region where the TPC provides a good separation of deuteron from the lighter species (up to $p_{\mathrm{T}} \sim 1.8$ GeV/c).

Figure 5.8 and Figure 5.9 show two examples each, one at low p_{T} and the other at higher p_{T}, of the distribution of the measured mass squared m^2 shifted by the squared nominal mass of the (anti–)deuteron m^2_{PDG} in the 2011 and 2015 dataset, respectively. The 2015 dataset distributions (Figure 5.9a and Figure 5.9b) show a deviation of m^2 at low p_{T} from the nominal mass of the (anti–)deuteron that was not present in the 2011 sample (Figure 5.8a and Figure 5.8b). This difference could be symptom of some issues in the measurement of masses corresponding to long times of flight (i.e. small β). Such a discrepancy is anyway not affecting the signal extraction for the (anti–)deuterons. Indeed the signal extraction is performed using a

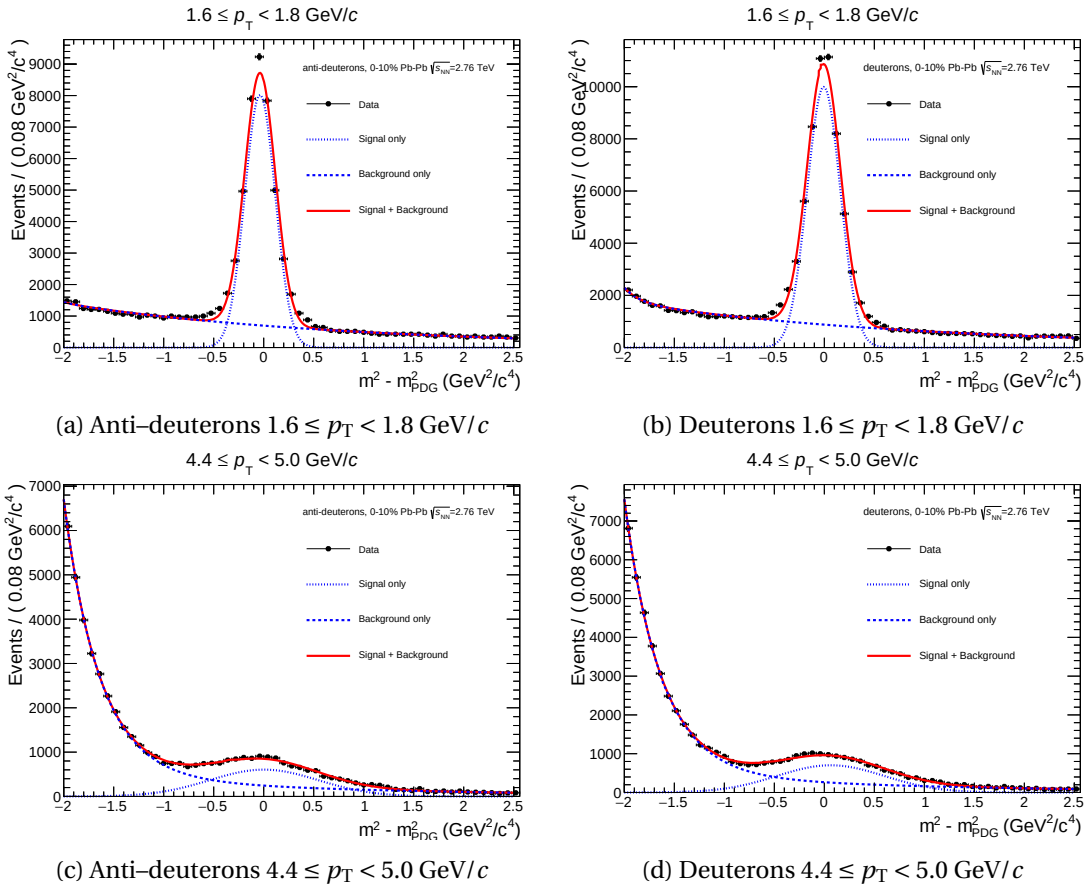

(a) Anti–deuterons $1.6 \leq p_{\mathrm{T}} < 1.8$ GeV/c

(b) Deuterons $1.6 \leq p_{\mathrm{T}} < 1.8$ GeV/c

(c) Anti–deuterons $4.4 \leq p_{\mathrm{T}} < 5.0$ GeV/c

(d) Deuterons $4.4 \leq p_{\mathrm{T}} < 5.0$ GeV/c

Figure 5.8: $m^2 - m^2_{\mathrm{PDG}}$ distributions for anti–deuterons (left) and deuterons (right) in two p_{T} bins (top and bottom) extracted in the 0-10% centrality interval of the 2011 dataset. The dashed line and the dotted line are the background and signal components of the model respectively. The red line represents the total fit to the distributions.

two component fit to the mass spectra in order to unfold the background component from the (anti–)deuteron signal. The (anti–)deuteron signal S is modelled using a Gaussian distribution with an exponential tail:

$$S(x; N_{\mathrm{raw}}, \mu, \sigma, n) \propto N_{\mathrm{raw}} \begin{cases} \exp\left[-\frac{1}{2}\left(\frac{x-\mu}{\sigma}\right)^2\right] & \text{for } x \leq \mu + n\sigma \\ \exp\left[-n\left(\frac{x-\mu}{\sigma} - \frac{n}{2}\right)\right] & \text{for } x > \mu + n\sigma \end{cases} \tag{5.5}$$

where N_{raw} is the number of signal counts, μ and σ are the mean and the standard deviation of the gaussian respectively, while n is the number of σs at which S becomes an exponential function[6]. All these parameters are free to vary in the fitting procedure, thus the shift in the $m^2 - m^2_{\mathrm{PDG}}$ distribution can be easily recovered by the determination of the μ parameter in the fit. The slope of the exponential is defined such that the S function and all its derivatives

[6] My code implementing this function, as well as its proper normalisation are reported in [90].

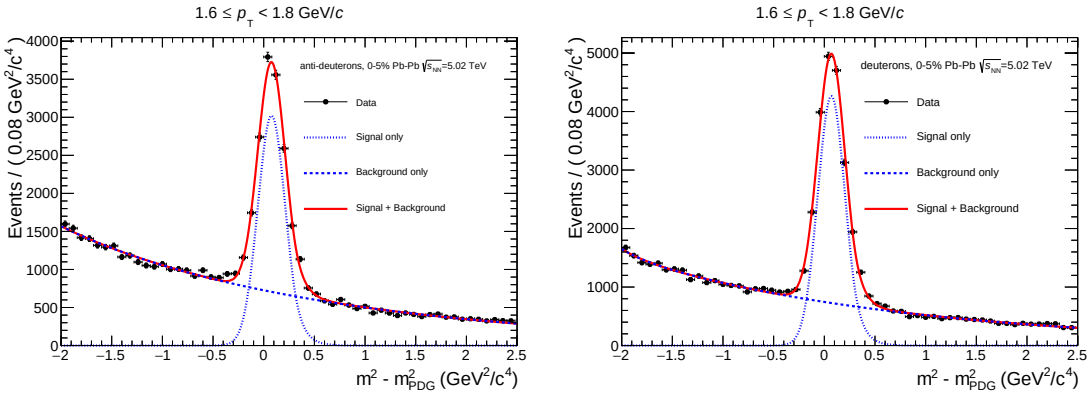

(a) Anti–deuterons $1.6 \leq p_{\mathrm{T}} < 1.8$ GeV/c

(b) Deuterons $1.6 \leq p_{\mathrm{T}} < 1.8$ GeV/c

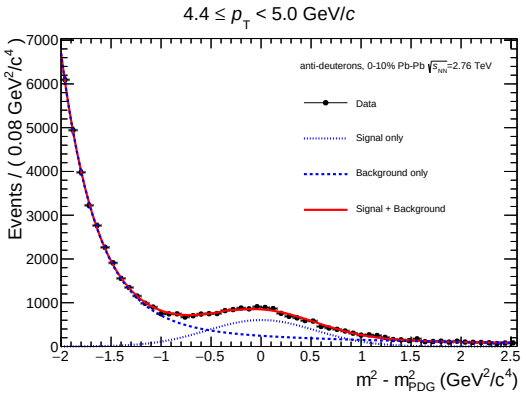

(c) Anti–deuterons $4.4 \leq p_{\mathrm{T}} < 5.0$ GeV/c

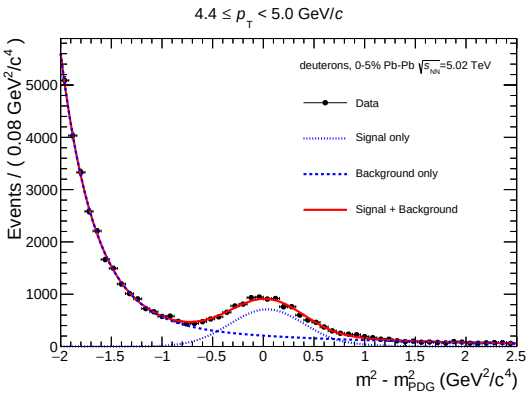

(d) Deuterons $4.4 \leq p_{\mathrm{T}} < 5.0$ GeV/c

Figure 5.9: $m^2 - m^2_{\mathrm{PDG}}$ distributions for anti–deuterons (left) and deuterons (right) in two p_{T} bins (top and bottom) extracted in the 0-5% centrality interval of the 2015 dataset. The dashed line and the dotted line are the background and signal components of the model respectively. The red line represents the total fit to the distributions.

are continuous and differentiable. The function used for modelling the background is the sum of two exponentials: one exponential is used to model the background from mismatched TOF hits shape around the signal peak while the second one is used to model the tail of the proton distribution at high p_{T} (e.g. Figure 5.9c). Since N_{raw} is one of the fit parameters its uncertainty is directly taken by the output of the fitting procedure. Figure 5.10 show the raw yield spectra for deuterons and anti–deuterons in the different centrality classes studied in both the 2011 and 2015 data samples. Only the range in which the signal extraction could be performed is shown. The main factor that limits the p_{T} region of the raw yield extraction is the available amount of events and the stability of the corrections applied to the raw spectra.

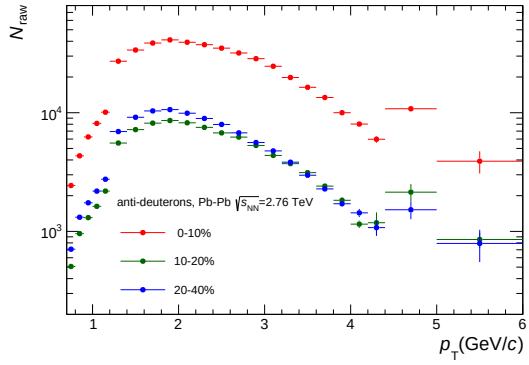

(a) Anti–deuterons Pb–Pb $\sqrt{s_{\mathrm{NN}}}$ = 2.76 TeV

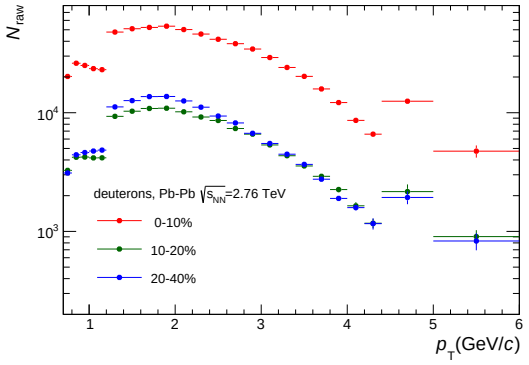

(b) Deuterons Pb–Pb $\sqrt{s_{\mathrm{NN}}}$ = 2.76 TeV

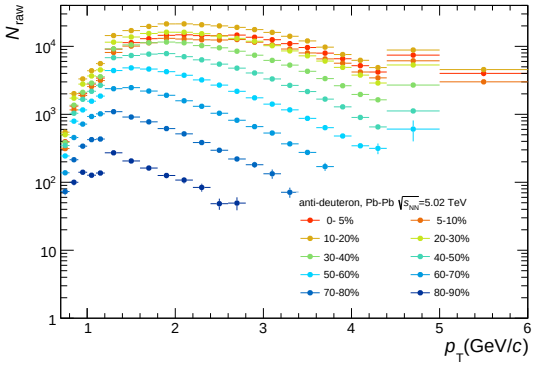

(c) Anti–deuterons Pb–Pb $\sqrt{s_{\mathrm{NN}}}$ = 5.02 TeV

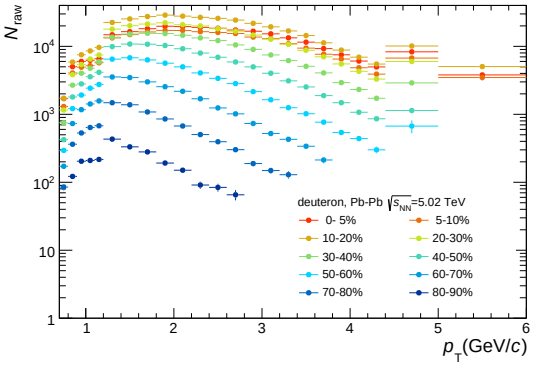

(d) Deuterons Pb–Pb $\sqrt{s_{\mathrm{NN}}}$ = 5.02 TeV

Figure 5.10: Raw yields for anti–deuterons (left) and deuterons (right) represented with different colours for the different centrality classes studied in the 2011 (top) and 2015 (bottom) datasets.

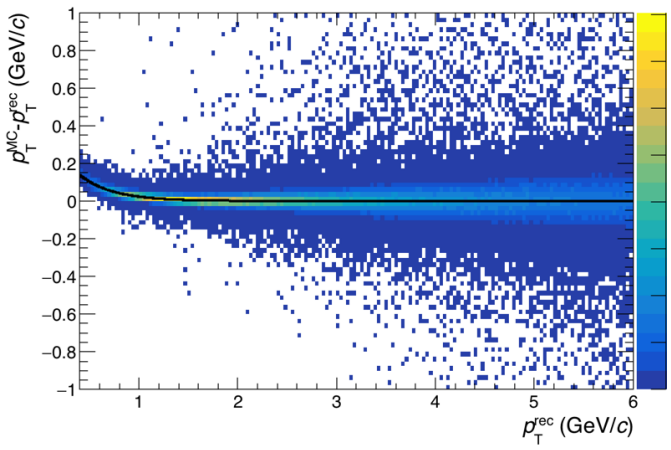

Figure 5.11: Difference between the true p_T of the (anti-)deuteron and the reconstructed one as a function of the reconstructed momentum in the 2011 dataset. The black line represents a fit to this distribution used to correct the measured momentum at the analysis level track-by-track.

5.3 Corrections to the raw spectra

The raw yields extracted in the previous section must be corrected to obtain the real production spectra. There are four major effects to be corrected for the nuclei production spectra: the tracking efficiency, the detector acceptance, the momentum reconstruction imperfections and the contamination from secondary particles. In this section the strategies adopted to correct for these effects are described.

5.3.1 Momentum shift correction

During the track fitting step of the track reconstruction algorithm, the mass hypothesis of the tracked particle is used to properly keep into account the energy loss of the particle when it traverses the detector material. This mass hypothesis is computed after a first fitting pass, using the information about the energy loss of the particle in the TPC and a first rough estimation of the momentum of the particle. A mass hypothesis for nuclei was not available in the tracking algorithm when the 2011 sample was reconstructed, thus they were reconstructed using the mass hypothesis of the pion. The assumption of such a lighter mass biases the momentum estimation at low p_T, where the difference between the energy loss of a pion and the one of a nucleus matters mostly.

This discrepancy can be checked using a MC simulation where the true momentum of the particle being reconstructed is known. Figure 5.11 shows the difference between the true and the reconstructed p_T as a function of the reconstructed p_T. It is possible to see that at low transverse momentum (i.e. $p_T \leq 1$ GeV/c) the reconstructed p_T is underestimated. To recover

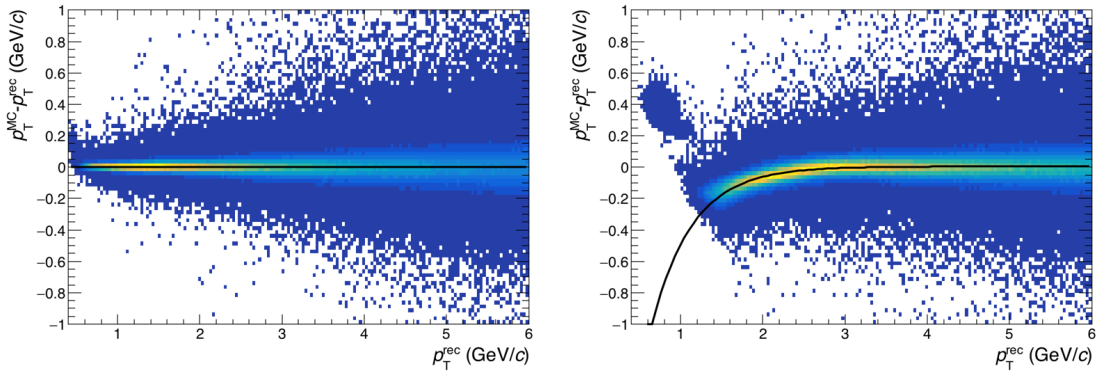

(a) (anti–)deuterons (b) (anti–)^{3}He

Figure 5.12: Difference between the true p_T of (anti–)light nuclei (deuterons on the left, ^{3}He on the right) and the reconstructed one as a function of the reconstructed momentum in the 2015 dataset. The black line represents a fit to this distribution used to correct the measured momentum at the analysis level track-by-track.

the missed momentum fraction, a fit to that distribution has been performed using the *ad-hoc* function

$$f(p_T^{rec}) = a + \exp(b p_T^{rec} + c), \tag{5.6}$$

and the resulting parametrisation has been used to correct track-by-track the reconstructed momentum of the (anti–)deuteron candidates. As already anticipated, the p_T range of the analysis of the 2011 data sample starts at 1 GeV/c, thus the only relevant term of the correction is the constant one (a) that is in the order of 2 MeV/c. This value makes the correction negligible with respect to the p_T bin size of the order of 100 MeV/c used in the analysis. Since from the beginning of the Run 2 of the LHC, the track reconstruction has been changed to use also the nuclei mass hypothesis in the track fitting when relevant. This can be easily spotted in a similar study carried out on the 2015 data samples for both (anti–)deuterons and (anti–)^{3}He (Figure 5.12). The reconstructed p_T for the (anti–)deuterons reproduces accurately the true momentum of the generated particle, with a mean deviation of less than 2 MeV/c.

On the other hand, the true (anti–)^{3}He momentum is not reconstructed accurately for $p_T \leq 2$ GeV/c, where a deviation can be spotted (Figure 5.12b). This time the observed deviation points to an overestimation of the reconstructed momentum, due to the use of the ^{4}He mass hypothesis in the track fitting. The mass hypothesis is chosen among the particles whose expected dE/dx is compatible with the one observed with the track. For ^{3}He and ^{4}He this specific energy loss is very close for $p_T \leq 2$ GeV/c. This, summed with the fact that the expected response available in the central framework of ALICE are not perfectly tuned for light–nuclei and that the mass hypothesis is chosen at a stage where only rough estimates of the track parameters and dE/dx in the TPC are available, makes the ^{4}He the default choice for ^{3}He in

that p_{T} region. Nevertheless, the true momentum for the (anti–)^{3}He is reconstructed correctly in the region of interest of the analysis presented here ($p_{\mathrm{T}} > 2\mathrm{GeV}/c$).

5.3.2 Efficiency×Acceptance correction

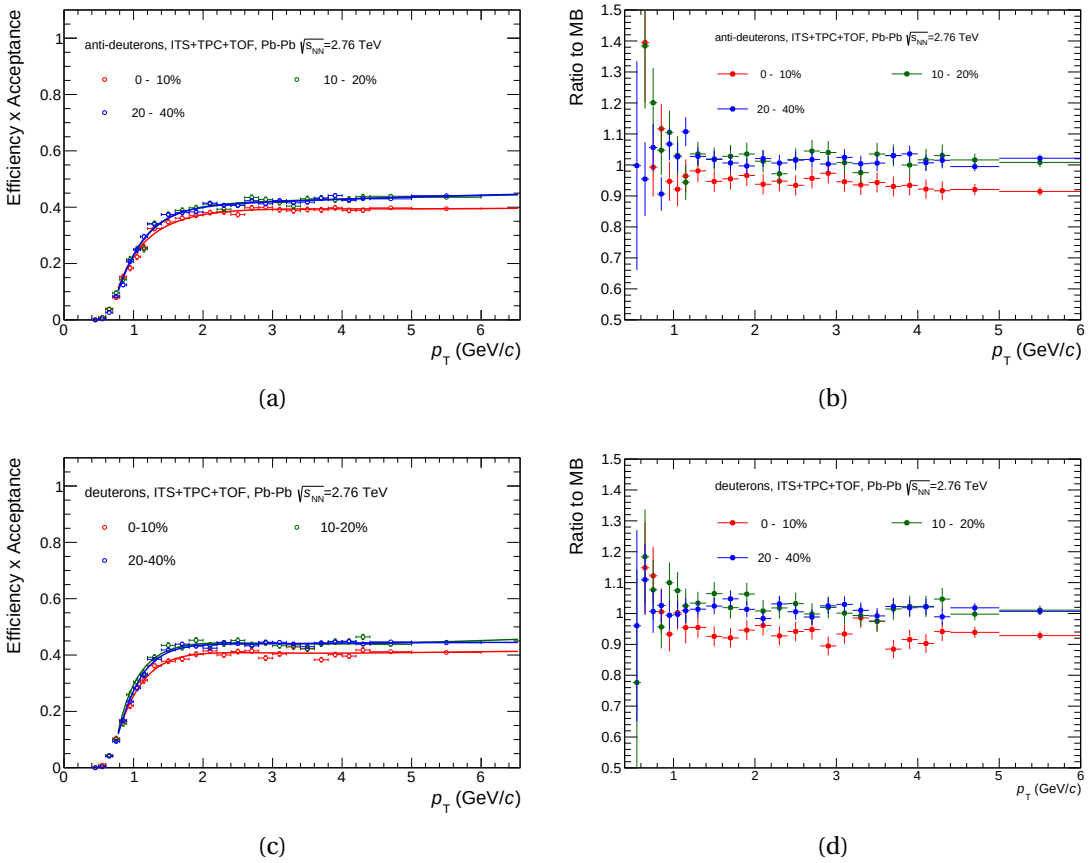

Figure 5.13: On the left: anti–deuteron (top) and deuteron (bottom) efficiency times acceptance computed as a function of the centrality for the 2011 datasets. On the right: ratio between the efficiency times acceptance computed in centrality bins and the one computed without any centrality selection for (anti–)deuterons (top) and deuterons (bottom).

As already shown in Chapter 4, tracking algorithms, even if optimised, are not fully efficient in the reconstruction of particle trajectories. Even if they would be fully efficient, other inefficiency sources would affect the reconstruction. For instance, the active area of the experiment is not hermetic by design (e.g. the sector edges of the TPC) and, sometimes, parts of the detectors might be switched off because of data taking constraints (e.g. some modules excluded from the data acquisition in the SDD because they lack of stability during the data taking).

It is possible to correct for the finite efficiency and acceptance using a MC simulation where

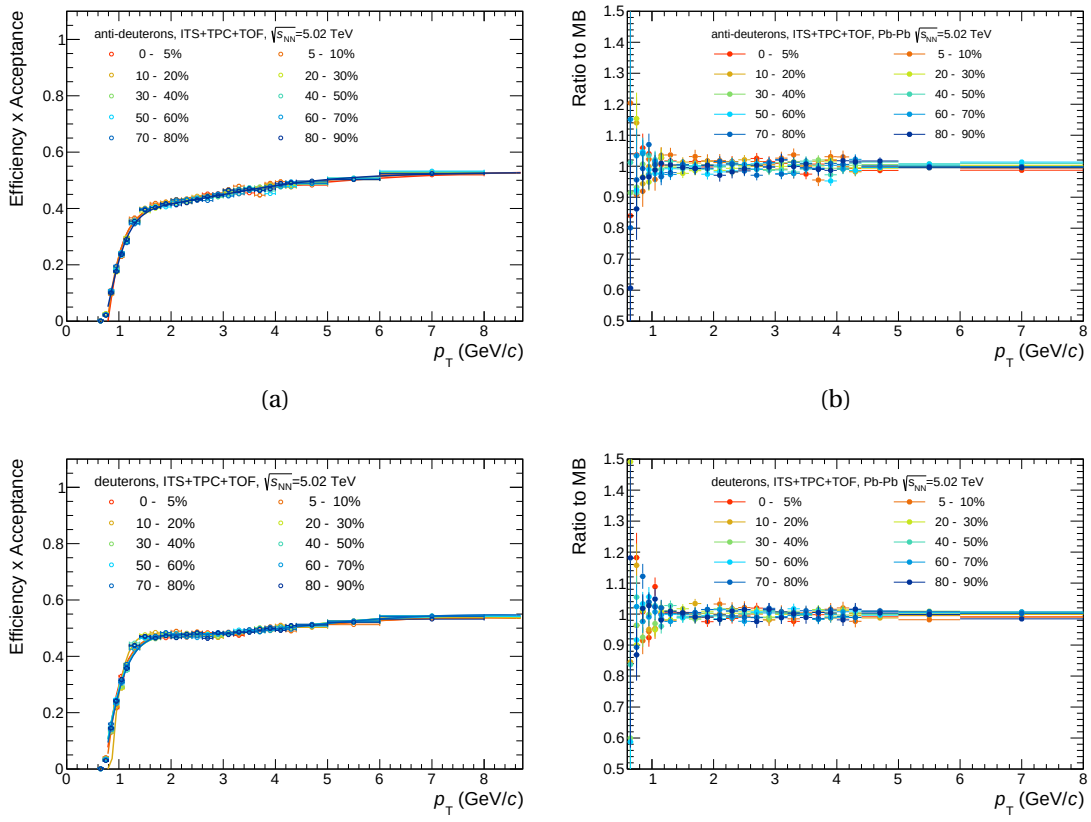

Figure 5.14: On the left: anti–deuteron (top) and deuteron (bottom) efficiency times acceptance computed as a function of the centrality for the 2015 datasets. On the right: ratio between the efficiency times acceptance computed in centrality bins and the one computed without any centrality selection for (anti–)deuterons (top) and deuterons (bottom).

the full geometry and data taking conditions are reproduced. The number of particles crossing the detector is known when using a MC simulation and the efficiency can be defined as:

$$\text{Efficiency} \times \text{Acceptance}\,(p_{\mathrm{T}}^{\mathrm{rec}}) = \frac{N_{\mathrm{rec}}(p_{\mathrm{T}}^{\mathrm{rec}})}{N_{\mathrm{gen}}(p_{\mathrm{T}}^{\mathrm{gen}})}, \tag{5.7}$$

where $p_{\mathrm{T}}^{\mathrm{gen}}$ and $p_{\mathrm{T}}^{\mathrm{rec}}$ are the p_{T} generated by the event generator and the p_{T} measured by the tracking algorithm respectively; N_{gen} is the number of particles generated in the azimuthal region $0 \leq \varphi < 2\pi$ and in the rapidity region $|y| < 0.5$. N_{rec} is the number of tracks corresponding to one of the particle species of interest satisfying the selection criteria summarised in Table 5.3. On top of those criteria, a hit matched in the TOF detector is required for (anti–)deuterons, since the identification strategy for them is based on the TOF PID capabilities. The reconstructed p_{T} and the generated one are used in the numerator and denominator respectively to keep into account the possible shift between p_{T} intervals due to the residual mismatch

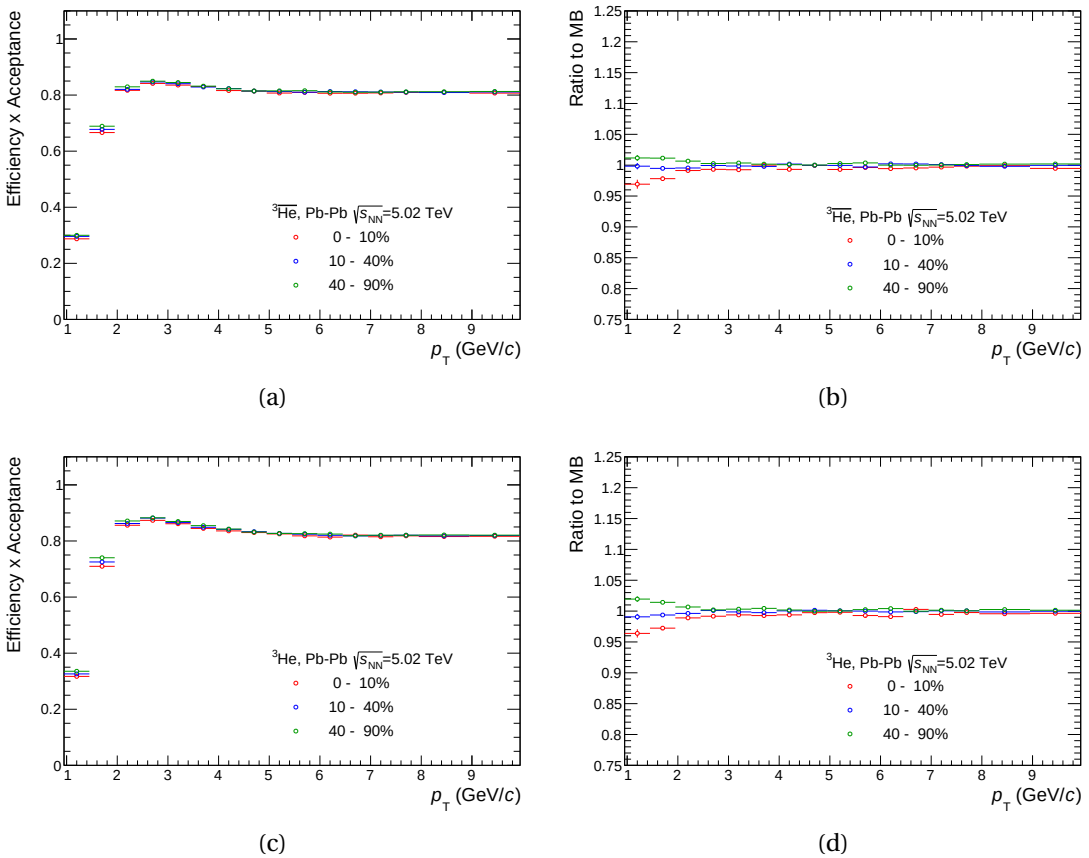

Figure 5.15: On the left: anti–^{3}He (top) and ^{3}He (bottom) efficiency times acceptance computed as a function of the centrality for the 2015 datasets. On the right: ratio between the efficiency times acceptance computed in centrality bins and the one computed without any centrality selection for (anti–)^{3}He (top) and ^{3}He (bottom).

between the reconstructed momentum and the generated one (see the previous Section). This correction is usually evaluated in the various centrality classes used in the analysis, to check if different occupancies of the detector plays a role in the tracking efficiency. Figure 5.13a and Figure 5.13c show the efficiency×acceptance correction for anti–deuterons and deuterons in Pb–Pb collision at $\sqrt{s_{\text{NN}}}$ =2.76 TeV respectively. This correction shows a mild dependence on the centrality, having the most central class (0 – 10%) separated from the others. This can be also observe quantitatively by computing the ratios between the centrality dependent corrections shown in Figure 5.13a and Figure 5.13c and the Minimum Bias (MB, i.e. without any centrality selection) correction. From these ratios, shown in Figure 5.13b for anti–deuterons and in Figure 5.13d for deuterons, it is possible to see a separation of the order of 5% between the correction computed in the 0-10% centrality bin and the MB one. For this reason, in the analysis of the 2011 data sample, the correction has been computed as a function of centrality.

Conversely, this centrality dependence is not visible for (anti–)deuterons in the Pb–Pb at $\sqrt{s_{\rm NN}}$ =5.02 TeV sample. Already from the plot of the efficiency×acceptance as a function of the $p_{\rm T}$ in the centrality classes used for the analysis (Figure 5.14a and Figure 5.14c) it is possible to see that the curves corresponding to different centrality bins are not distinguishable. Following the same approach used for the 2011 data sample, Figure 5.14b and Figure 5.14d show the ratios to the MB correction for anti–deuterons and deuterons respectively. From these ratios it is possible to conclude that there is no clear trend with centrality of the acceptance×efficiency for (anti–)deuterons in the 2015 dataset. For this reason the MB efficiency×acceptance is used to correct the raw spectra in all the centrality classes in order to profit from better statistical uncertainties in the determination of the correction. This is not possible for (anti–)^{3}He in the 2015 samples, since the acceptance×efficiency for these particles shows a trend with centrality (Figure 5.15 and its subfigures).

The acceptance×efficiency correction is fitted with an ad-hoc function

$$f(p_{\rm T}) = a_0 + a_1 e^{a_2 * p_{\rm T}} + a_3/p_{\rm T} + a_4/(p_{\rm T})^2, \tag{5.8}$$

to check if some statistical fluctuations in the efficiency×acceptance correction could affect the final result. The raw spectra are then corrected using both the fit function and the binned correction to evaluate possible differences in the two approaches: the difference between the two cases is found to be less than 1%, and thus negligible, in the $p_{\rm T}$ range of interest of the analyses here presented. Examples of these fits can be found in Figure 5.13a and Figure 5.13c.

5.3.3 Secondary particle background rejection

One of the main source of background in the analysis of the nuclei production spectra is the detection and reconstruction of nuclei coming from secondary interactions. These secondary nuclei come mostly from the interactions of other primary particles with the detector material. In some of these interactions, a light nucleus can be produced by means of knock–out processes. The typical momentum of, for instance, deuterons produced with such processes is less than 1.4 GeV/c. While for the deuteron production spectra it is important to correct for the knock–out production, the $p_{\rm T}$ region in which the ^{3}He productions is studied is unaffected by this source of background. The baryon number conservation sets a very high energy threshold for the production of secondary anti–nuclei with similar processes, thus in the following only the case of nuclei will be discussed. Other processes, such as the decay of (anti–)hypernuclei, represent a negligible fraction of the observed (anti–)deuterons. On the contrary, the decay of (anti–)hypernuclei represents a significant systematic uncertainty for the (anti–)^{3}He production as no effective correction can be put in place in this case, as it will be discussed in the next Section.

To remove the contamination from secondary deuterons it is possible to study the Distance–Of–Closest approach distributions on the transverse plane (DCA$_{xy}$) of the deuteron candidates. Primary particles are expected to have a distribution with a clear peak at DCA$_{xy}$ = 0 cm, that is

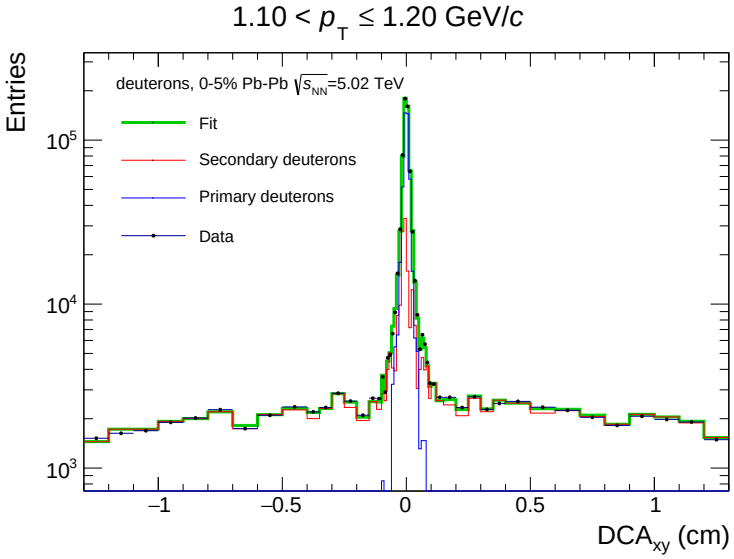

Figure 5.16: Fit to the DCA_{xy} distribution (black points) of deuteron candidates. The green line is the fit result and it represents the sum of the primary particle component (blue line) and secondary particle one (red line).

the expected value for particles coming from the primary vertex. On the other hand, secondary particles are expected to have a flat DCA_{xy} distribution at the first order. Unfortunately this is not the case: sometimes [7] the tracks corresponding to secondary particles are associated to a wrong cluster in the SPD. If this SPD cluster belongs to a primary particle, the extrapolation of the track corresponding to the secondary particle will anyway point to the primary vertex, as the track pointing is given mostly by the SPD clusters. For this reason, a fit to the observed DCA_{xy} distribution is done to extract the primary fraction of observed deuterons using histogram templates for the primary particles and secondary particles component. The histogram templates used for the fit are filled from MC production, where both the identity and the origin of each particle are known. An example of a fit to the DCA_{xy} distribution is shown in Figure 5.16, where it is possible to see that the secondary particle component has, as anticipated, a peak structure at $DCA_{xy} = 0$ cm. The fit is done in a range of DCA_{xy} wider than the actual track selection criterium to better constrain the fit of the secondary particles component, that populates mostly the tails of the DCA_{xy} distribution. Then to obtain the fraction of primary deuterons in the region allowed by the track selection criterium, the fitted primary particles component and the total fit are integrated in that region and the primary fraction is computed from those integrals. The fit has been done using the algorithm implemented in the ROOT TFractionFitter class [91]. This algorithm enables the possibility of fitting of an experimental distribution using MC generated samples, keeping into account the statistical uncertainties on the MC histograms in the likelihood maximisation. This is attained by considering the true value of each bin of the MC samples as one fit parameter. As

[7] in less than the 10% of the cases in the most central Pb–Pb collisions

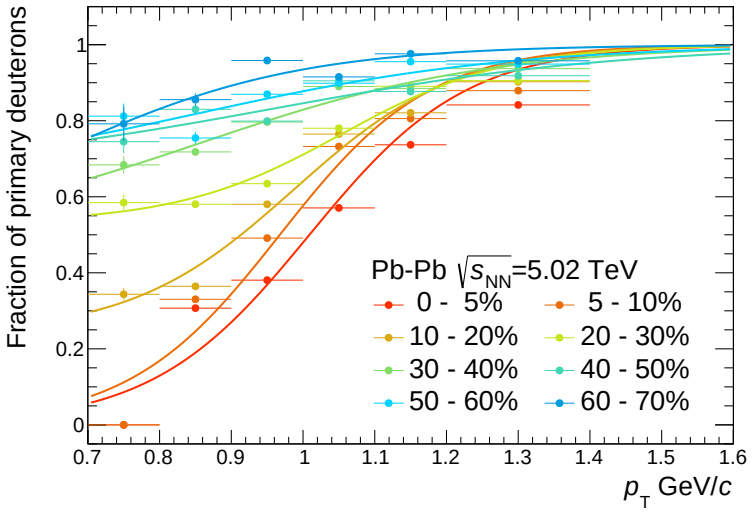

Figure 5.17: Primary fraction of selected deuterons as a function of the transverse momentum. The different colours correspond to different centrality classes. The solid lines represent the fits to the distributions.

a result, the MC components fitted to the data will not have exactly the same shape they had before being fed to the fitting algorithm. [8] The fraction of primary particles as a function of the transverse momentum, has been computed in all the centrality bins covered by this analysis and it is shown in Figure 5.17. From this Figure it is possible to see a clear dependence of the fraction of primary deuterons with centrality: in peripheral events (i.e. low multiplicity events) the fraction of primary deuterons is higher than in central events (i.e. high multiplicity events). This can be easily understood as the higher is the flux of particles in the detector material, the higher is fraction of secondary particles observed in the detector. Since the obtained distribution of primary fraction shows some statistical fluctuations, the final correction $f_p(p_T)$ is obtained by fitting the distribution with the function:

$$f(p_T) = a + \frac{1-a}{1+be^{cp_T}}, \tag{5.9}$$

with $0 \leq a < 1$, $b > 0$ and $c < 0$. The resulting fits are shown as solid lines in Figure 5.17. A large MC sample has been used to create the template histograms for the secondary particles but it was not sufficient to have stable templates in the most peripheral events (from 70% to 90% of centrality). Nevertheless, the corrections in those bins are expected to be small and the systematic contribution of secondary particles to these centrality classes is evaluated by

[8] For this reason this method is potentially dangerous: if the statistical uncertainties of the MC samples are big, the likelihood maximisation can almost adapt any input shape to the data. In general this method is safe only if the user checks carefully that the input MC shapes are well defined and not affected by large statistical fluctuations. The statistical uncertainty of the MC templates used in this analysis were properly checked and were suitable for the use of the TFractionFitter.

varying the DCA_z track selection, that is particularly sensitive to the presence of secondary deuterons, as it will be shown in the next Section.

5.4 Systematic checks

A set of checks is performed to evaluate if and how much the results presented in this work are affected by systematic uncertainties. The checks performed in this context can be classified in three groups:

1. checks on the efficiency×acceptance correction, done by varying the material budget used in the MC simulation of the ALICE apparatus and by changing the transport code used to simulate the passage of particles through the detector material;
2. checks on the track selection criteria, carried out by varying the selection parameters and studying how they affect the final results;
3. finally the checks on the raw yield extraction.

When one of these checks leads to a discrepancy with the obtained results, this discrepancy is kept into account to quantify the systematic uncertainty.

The systematic uncertainty quoted for each of the aforementioned checks is estimated as the standard deviation of the distribution of each possible systematic uncertainty source.

The checks on the efficiency corrections required the simulation of additional MC samples to inquire into possible discrepancies in the evaluated reconstruction efficiency when changing the material budget estimation of the experimental apparatus. The material budget variation has been chosen taking into account the uncertainty on its determination. This last point has been driven by the results obtained from the photon conversion analyses performed in ALICE[9]. Two additional MC samples were then produced, one with the material budget increased by 4.5% and one with the material budget decreased by the same amount. The efficiency× acceptance evaluated in this way are shown in Figure 5.18 for the 2015 data sample. It is possible to see at a first glance a clear trend with the material budget in each p_{T} interval, with a more pronounced difference in the efficiency×acceptance estimation at low p_{T}, as it was expected since low momentum particles lose more energy in the traversed material and the efficiency is rapidly changing in there. For each momentum bin analysed, the variations of the efficiency×acceptance induced by the change of the material budget in the simulation are supposed to follow a uniform distribution around the efficiency× acceptance evaluated with the nominal material budget conditions. For this reason the systematic uncertainty due to the material budget is estimated as:

$$\sigma_{\mathrm{Mat.budget}}(p_{\mathrm{T}}) = \frac{\epsilon_{\mathrm{max}}(p_{\mathrm{T}}) - \epsilon_{\mathrm{min}}(p_{\mathrm{T}})}{\sqrt{12}}, \tag{5.10}$$

[9] ALICE collaboration work in progress.

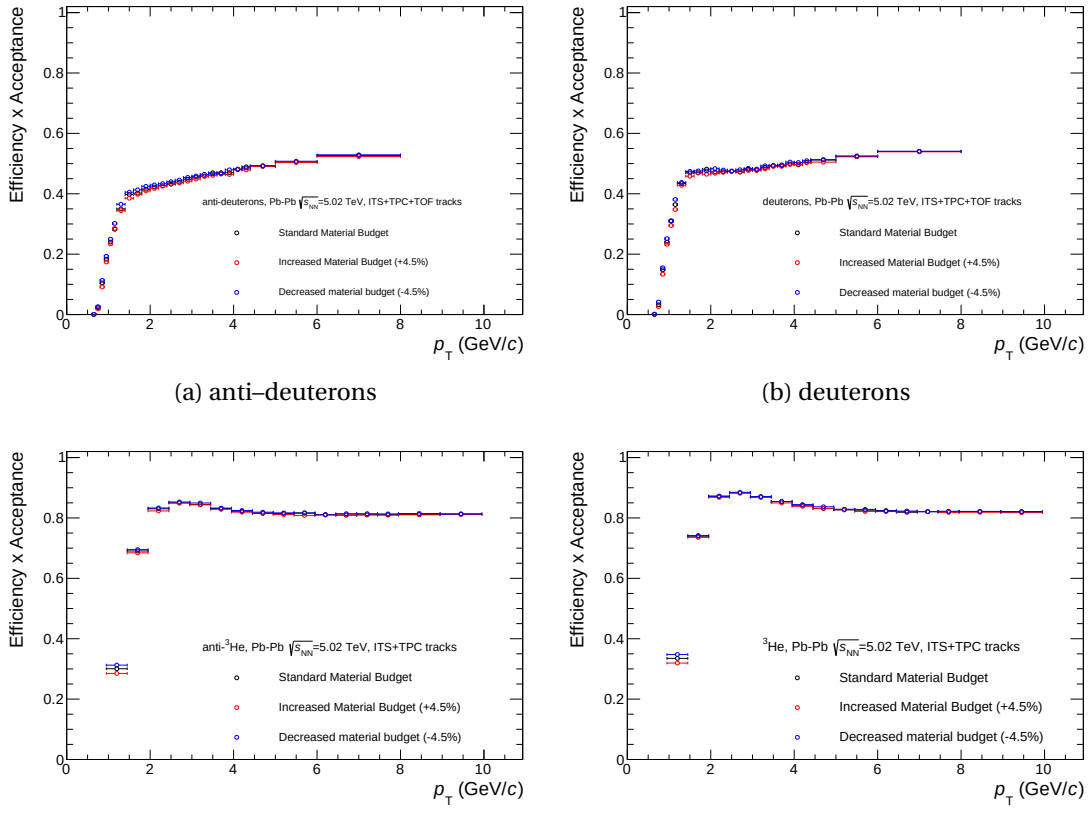

(a) anti–deuterons

(b) deuterons

(c) anti–^{3}He

(d) ^{3}He

Figure 5.18: Study of the effect of the material budget variation on the acceptance×efficiency for (anti–)deuterons (top) and (anti–)^{3}He (bottom).

where $\epsilon_{\max}(p_T)$ and $\epsilon_{\min}(p_T)$ are the maximum and the minimum efficiency×acceptance evaluated in each p_T interval. This formula represents the standard deviation of a uniform distribution assuming that $\epsilon_{\max}$ and $\epsilon_{\min}$ are its edges. This uncertainty estimation for the (anti–)deuteron analysis in the 2011 sample was already adopted in other analyses[10] and it is 3% of the efficiency×acceptance in the whole p_T region covered by the analysis described in this work. A similar result has been obtained for p_T = 1 GeV/c in the (anti–)deuteron analysis of the 2015 dataset but a strong trend is visible as a function of p_T (see the summary Figures 5.22 and 5.23). In the p_T region studied with the (anti–)^{3}He analysis, instead, the variation of the material budget shows an uncertainty of the 3‰ and 2‰ of the estimated efficiency×acceptance for the (anti–)^{3}He and the ^{3}He respectively. This result is expected, as in that p_T region the detector acceptance for (anti–)^{3}He in the rapidity region $|y| < 0.5$ is at its maximum and at the same time the (anti–)^{3}He already reached its minimum of ionisation. Another important check for the (anti–)nuclei analyses is the transport code adopted for the

[10] The estimation was performed for the ALICE deuteron production analysis in p–Pb collisions, that will be published soon.

MC simulations. For the nuclei and especially the anti–nuclei under investigation in this work, the interaction cross sections have been measured in energy ranges far from the typical energies of light nuclei produced and measured in HIC [92–95]. Therefore, the transport code has to interpolate between the measurements at lower and higher energies to get an estimation of the cross sections to be used in the propagation of the (anti–)nuclei in the material. The ALICE simulation framework supports the GEANT3 [96] and the GEANT4 [97] transport codes, with GEANT3 used as the default transport code for simulations. Therefore an additional simulation using the GEANT4 transport code has been performed to check how much the efficiency×acceptance varies. Figure 5.19 shows the efficiency×acceptance corrections evaluated for (anti–)deuterons and (anti–)^{3}He with GEANT3 and GEANT4. The MC production available at the time of this thesis are reproducing the detector configuration and running condition during the 2011 data taking. Since one could opt for either of the two and there is no guidance on which transport code is right in the determination of the efficiency×acceptance, the systematic uncertainty evaluated with this check is the difference between the results obtained with the two transport codes divided by two. This uncertainty accounts for the 8% and 10% of the estimated efficiency×acceptance for nuclei and anti–nuclei respectively in the 2011 data sample. Since the detector configuration was changed before the start of the LHC Run 2 (e.g. the TRD installation was completed during the LHC shutdown) and no GEANT4 Monte Carlo is available for the Pb–Pb at $\sqrt{s_{\rm NN}}$ =5.02 TeV, the systematic uncertainty used in the 2015 analysis is increased by 4% for both nuclei and anti–nuclei to cover the expected increase of this uncertainty with increasing material budget.

The track selection criteria variation is a way to inquire into all the effects that are either not properly described in the Monte Carlo sample (e.g. efficiency as a function of the number of selected clusters in the TPC) or not fully corrected in the analysis, like the secondary particle production from material contamination at low $p_{\rm T}$ for deuterons. The selections shown in Table 5.3 are varied as described in the last column of Table 5.4. For each of these selection variations the analyses are repeated *ab initio*. As changing the selection criteria varies the sample of (anti–)nuclei candidates analysed, only the statistically significant variations of the final results are kept into account in the systematic uncertainty variation. For the systematic uncertainties estimation the results obtained by changing the track selections is then compared with the result attained with the nominal selections: only if the difference is more than 1σ the track selection variation is considered among the systematic uncertainties sources. [11] For each selection criterion, the systematic uncertainty is evaluated as the standard deviation of the significant variations. The total systematic uncertainty due to the track selection variation is then the sum in quadrature of each of these contributions. One interesting feature that can be observed in the systematic uncertainty due to track variation (see the summary Figures 5.20 and 5.22) is the rise of the uncertainty at low $p_{\rm T}$ for deuteron. This rise comes from the variation of the DCA$_z$ track selection: this particular selection is extremely sensitive to the contamination from secondary particles (see also [87]) and shows that the procedure to

[11] This is a general prescription in ALICE, going under the name of *Barlow criterion* from the paper by Roger Barlow [98].

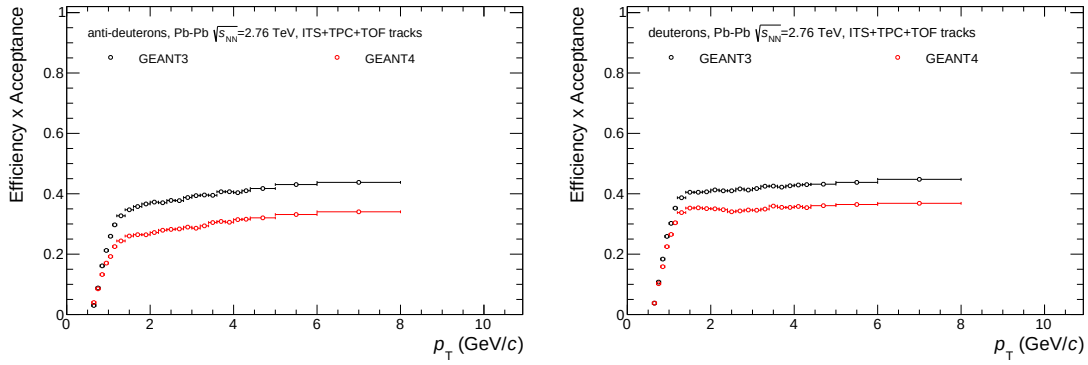

(a) anti–deuterons

(b) deuterons

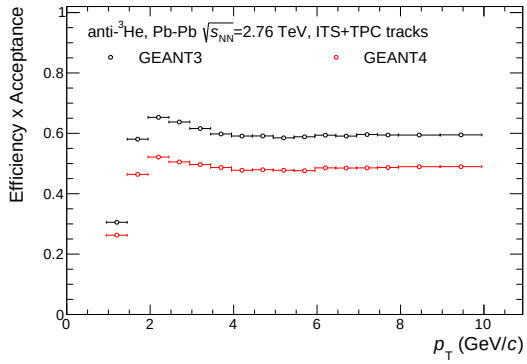

(c) anti–^{3}He

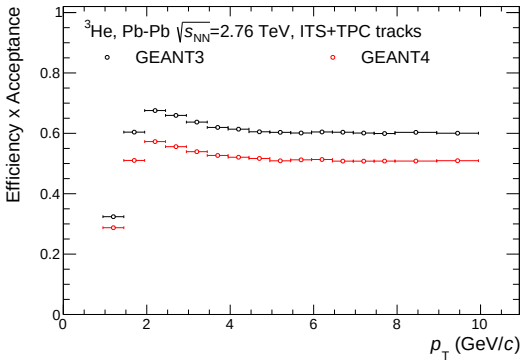

(d) ^{3}He

Figure 5.19: Study of the effect of the transport code variation on the efficiency×acceptance for (anti–)deuterons (top) and (anti–)^{3}He (bottom). The MC simulations used were anchored to the 2011 data sample.

subtract them is not fully efficient when the contamination is more than approximately 85% (i.e. loose DCA$_z$ track selection). The statistical uncertainty of the (anti–)^{3}He is such that none of the track selection variation resulted in a significant variation of the final result, thus no systematic effect can be appreciated for the analysed data sample.

The last systematic checks were done on the signal extraction for (anti–)deuterons and (anti–)^{3}He. For (anti–)deuterons the systematic checks consisted in:

1. changing the fitting range using the same fit functions, having care that the fitting range was sufficiently wide not to cut any significant part of the signal. This has been attained by avoiding variations of the range in the region of 4σ from the mean of the signal, where σ is evaluated in the first fit;

2. changing the signal function to a simple Gaussian and keeping the same background shape;

Table 5.4: Track selection variations with respect to the standard selections quoted in Table 5.3 (replicated here in the column of the default values).

Description	Default values	Other values
# TPC clusters	70	60,65,75,80
$\chi^2/n_{\rm cl}^{\rm TPC}$	4	3.5,4.5,5,5.5,6
DCA$_z$ (cm)	1	0.5,0.75,1.5,2
PID ($\sigma_{\rm TPC}$), only for (anti–)d	3	2.5,3.5

3. changing the background function to the sum of an exponential and a polynomial of the first order.

The systematic uncertainty due to these variations is evaluated by computing their standard deviation. The summary Figures 5.20, 5.21, 5.22 and 5.23 show the trend of the evaluated fit systematic uncertainty in the 2011 and 2015 data samples and in both cases the uncertainty rises with increasing $p_{\rm T}$. This can be explained by the fact that also the signal over background ratio decreases with $p_{\rm T}$ making the signal extraction more challenging at the highest $p_{\rm T}$ interval. For (anti–)^{3}He the systematic checks on the signal extraction have been performed by varying the range in which the bin counting procedure is performed. While the standard range is between -3σ and 3σ, all the possible ranges between -3.5σ and 3.5σ have been checked. The tighter range used in this procedure is from -2.5σ to 2.5σ. The standard deviation of all these checks is taken as the systematic uncertainty of the signal extraction for (anti–)^{3}He. Using this procedure the systematic uncertainty evaluated for (anti-)^{3}He is less than the 3‰, while for ^{3}He, mainly because of the triton contamination subtraction at low $p_{\rm T}$ it is as high as 2% (Table 5.5). Finally, the total systematic uncertainty has been computed summing in quadrature the contributions from all the checks mentioned above. For anti–^{3}He the only significant contribution to the systematic uncertainty is coming from the transport codes and Table 5.5 summarises the outcome of the systematic checks for this species and for the ^{3}He. For the other species studied here, Figures 5.22 and Figure 5.23 show the trend of the total systematic uncertainty, as well as of its components, as a function of $p_{\rm T}$. In general, thanks to the improved tracking performance of the ALICE experiment in the Run2 and a refined analysis strategy, the 2015 analysis shows smaller systematic uncertainties except for the difference between the transport code that needs a dedicated MC sample to be evaluated punctually.

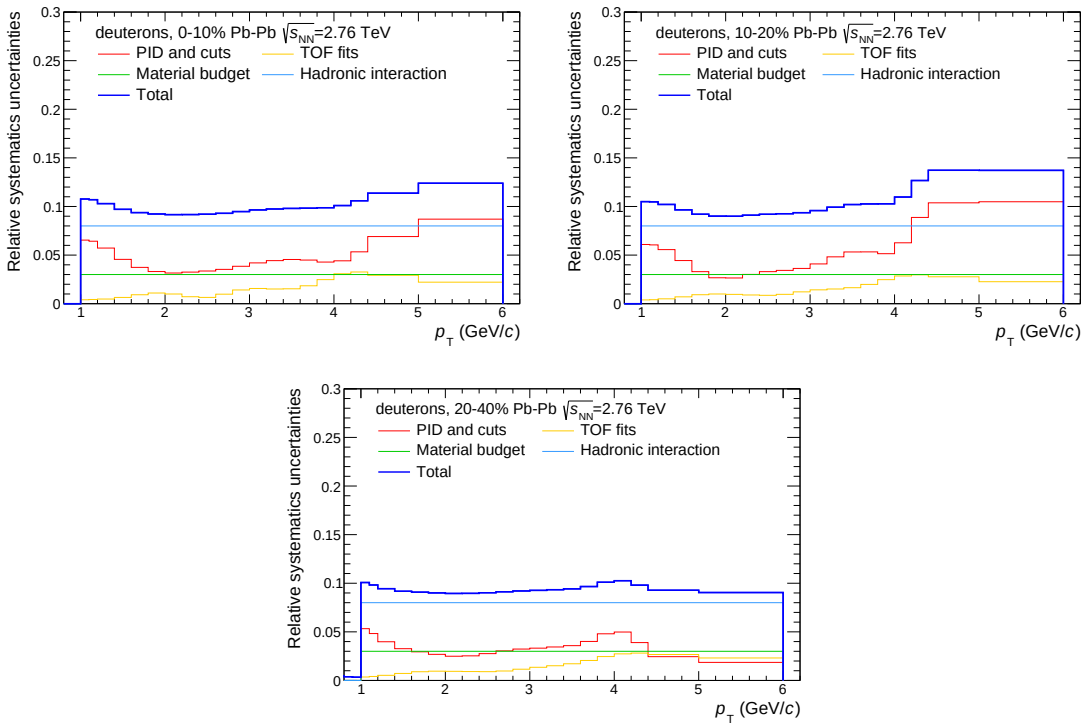

Figure 5.20: Summary of the systematic uncertainties evaluated for the deuteron spectra in the different centrality classes of Pb–Pb at $\sqrt{s_{\rm NN}}$ =2.76 TeV. The thick blue line represents the sum in quadrature of the systematic uncertainties contributions. The dominant uncertainty is the difference between the GEANT3 and GEANT4 transport code (light blue line, called hadronic interaction), the TOF fits uncertainty (yellow line) follows. The PID and track selection variations (red line) show a pronounced peak at low $p_{\rm T}$, because of the contamination from secondary particles. In the 2011 sample the material budget contribution (green line) is flat at 2%.

Table 5.5: Summary of the systematic uncertainties contribution for the (anti-)^{3}He analysis in the Pb–Pb at $\sqrt{s_{\rm NN}}$ =5.02 TeV data sample. This table refers to all the centrality classes analysed in this thesis. The dominant contribution is the difference between the transport codes and for the anti-^{3}He there are no other significant contributions. For the ^{3}He analysis, instead, the track selection and the signal extraction contribute marginally at low $p_{\rm T}$, mainly due to the triton contamination in the TPC PID.

Contribution	anti-^{3}He	^{3}He	
		$p_{\rm T}$ = 2 GeV/c	$p_{\rm T} \geq$ 4 GeV/c
Geant3/Geant4	14%	12%	
Track selections	≤3‰	≈5‰	≤1‰
Signal extraction	≤2‰	2%	≤5‰
Material budget	≤4‰	≤2‰	
Feed-down from (anti-)$^3_\Lambda$H	5%	5%	

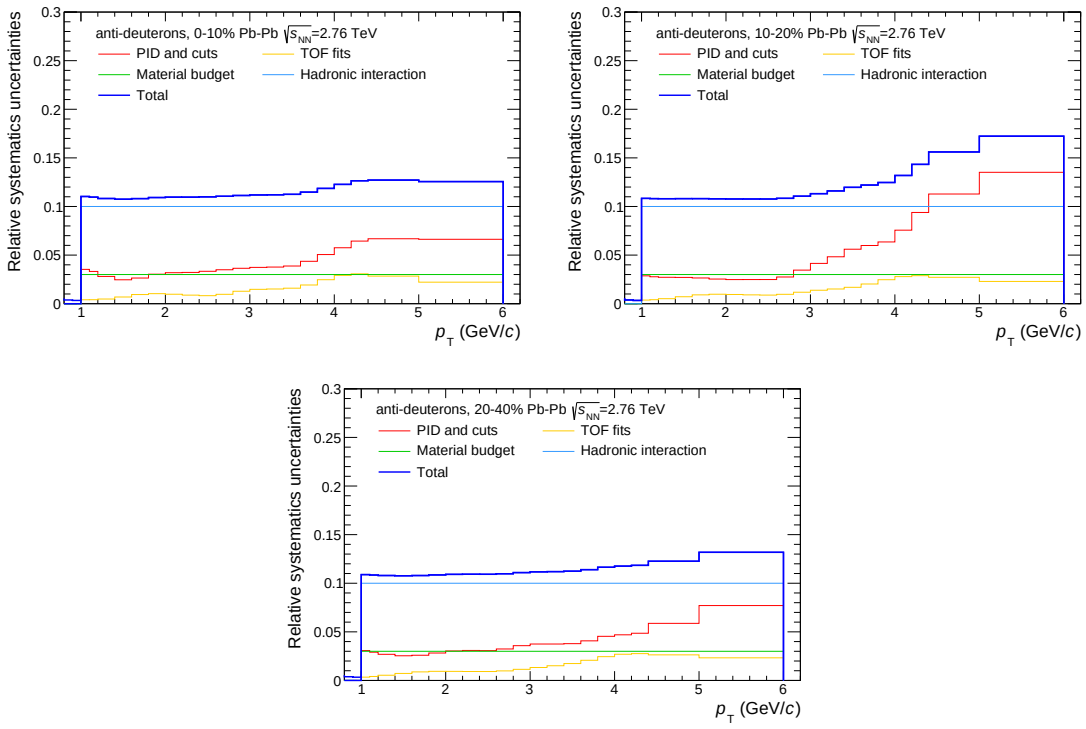

Figure 5.21: Summary of the systematic uncertainties evaluated for the anti–deuteron spectra in the different centrality classes of Pb–Pb at $\sqrt{s_{\rm NN}}$ 2.76 TeV. The thick blue line represents the sum in quadrature of the systematic uncertainties contributions. The dominant uncertainty is the difference between the GEANT3 and GEANT4 transport code (light blue line, called hadronic interaction), the TOF fits uncertainty (yellow line) follows at high $p_{\rm T}$. In the 2011 sample the material budget contribution (green line) is flat at 2%. The PID and track selection variations (red line) do not lead to a pronounced peak at low $p_{\rm T}$, because of the lack of contamination from secondary particles for anti–deuterons.

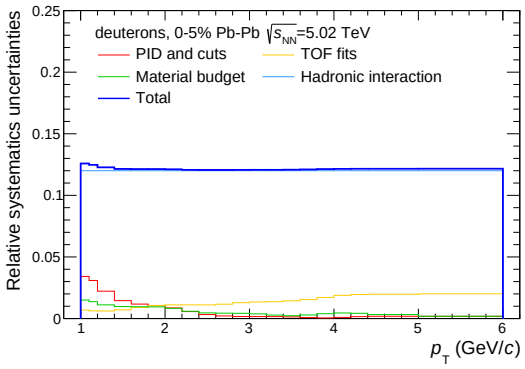
deuterons, 0-5% Pb-Pb $\sqrt{s_{NN}}$=5.02 TeV
PID and cuts
TOF fits
Material budget
Hadronic interaction
Total
Relative systematics uncertainties
p_T (GeV/c)

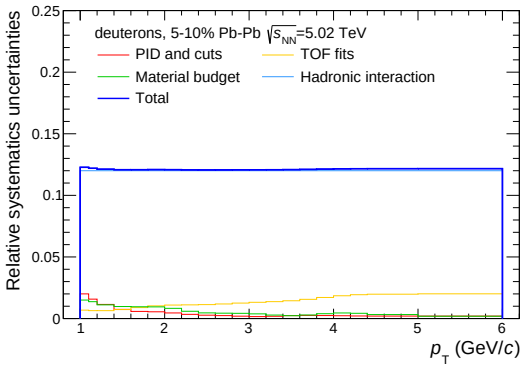
deuterons, 5-10% Pb-Pb $\sqrt{s_{NN}}$=5.02 TeV
PID and cuts
TOF fits
Material budget
Hadronic interaction
Total
Relative systematics uncertainties
p_T (GeV/c)

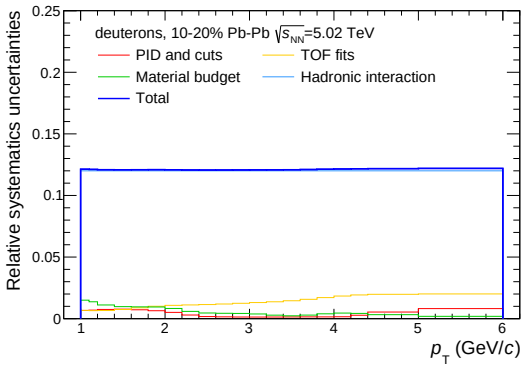
deuterons, 10-20% Pb-Pb $\sqrt{s_{NN}}$=5.02 TeV
PID and cuts
TOF fits
Material budget
Hadronic interaction
Total
Relative systematics uncertainties
p_T (GeV/c)

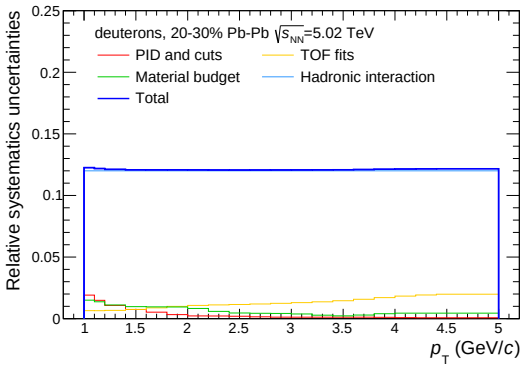
deuterons, 20-30% Pb-Pb $\sqrt{s_{NN}}$=5.02 TeV
PID and cuts
TOF fits
Material budget
Hadronic interaction
Total
Relative systematics uncertainties
p_T (GeV/c)

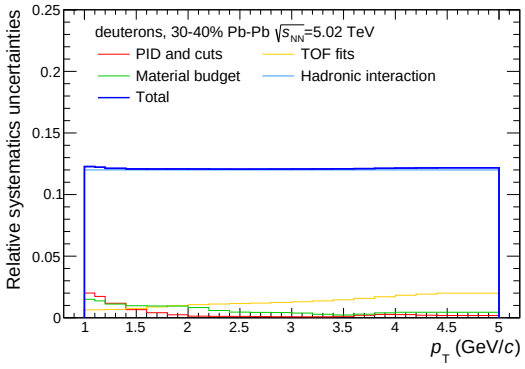
deuterons, 30-40% Pb-Pb $\sqrt{s_{NN}}$=5.02 TeV
PID and cuts
TOF fits
Material budget
Hadronic interaction
Total
Relative systematics uncertainties
p_T (GeV/c)

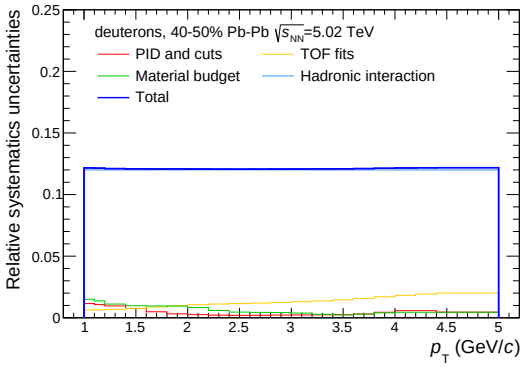
deuterons, 40-50% Pb-Pb $\sqrt{s_{NN}}$=5.02 TeV
PID and cuts
TOF fits
Material budget
Hadronic interaction
Total
Relative systematics uncertainties
p_T (GeV/c)

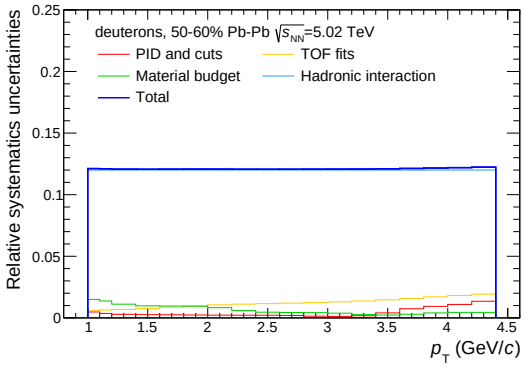
deuterons, 50-60% Pb-Pb $\sqrt{s_{NN}}$=5.02 TeV
PID and cuts
TOF fits
Material budget
Hadronic interaction
Total
Relative systematics uncertainties
p_T (GeV/c)

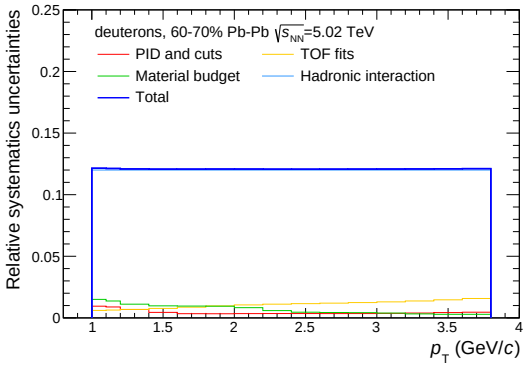
deuterons, 60-70% Pb-Pb $\sqrt{s_{NN}}$=5.02 TeV
PID and cuts
TOF fits
Material budget
Hadronic interaction
Total
Relative systematics uncertainties
p_T (GeV/c)

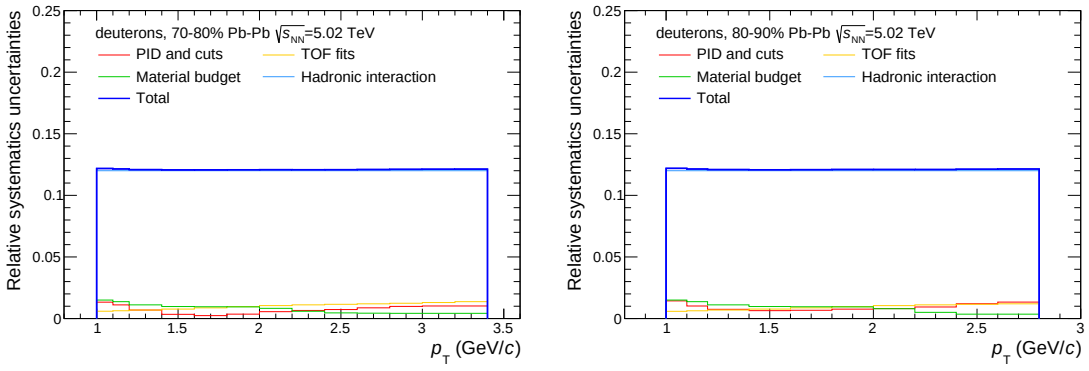

Figure 5.22: Summary of the systematic uncertainties evaluated for the deuteron spectra in the different centrality classes of Pb–Pb at $\sqrt{s_{\rm NN}}$ =5.02 TeV. The thick blue line represents the sum in quadrature of the systematic uncertainties contributions. The dominant uncertainty is the difference between the GEANT3 and GEANT4 transport codes (light blue line, called hadronic interaction), the TOF fits uncertainty (yellow line) follows. The PID and track selection variations (red line) show a pronounced peak at low $p_{\rm T}$, because of the contamination from secondary particles. Also for the material budget variation (green line) the contribution is peaked at low $p_{\rm T}$ where the energy loss of the nuclei is higher.

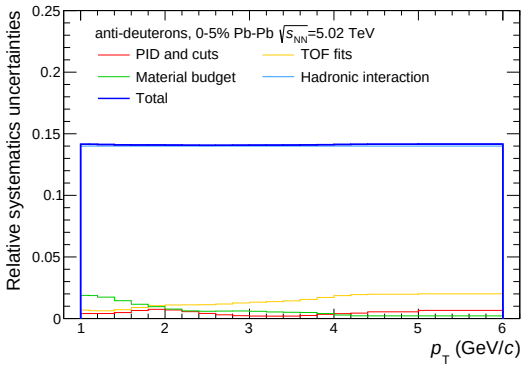
anti-deuterons, 0-5% Pb-Pb $\sqrt{s_{NN}}$=5.02 TeV
PID and cuts
TOF fits
Material budget
Hadronic interaction
Total
Relative systematics uncertainties
p_T (GeV/c)

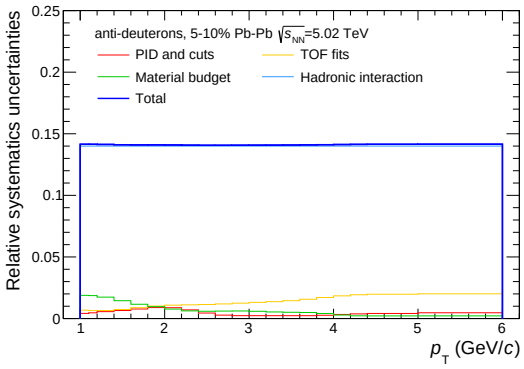
anti-deuterons, 5-10% Pb-Pb $\sqrt{s_{NN}}$=5.02 TeV
PID and cuts
TOF fits
Material budget
Hadronic interaction
Total
Relative systematics uncertainties
p_T (GeV/c)

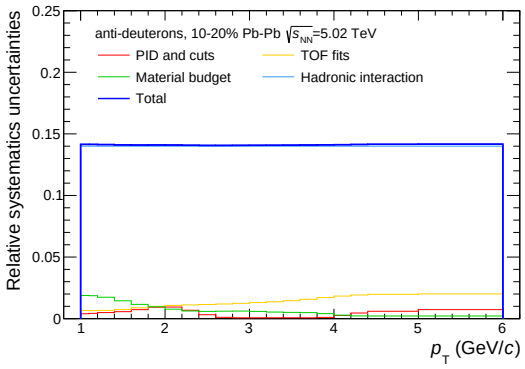
anti-deuterons, 10-20% Pb-Pb $\sqrt{s_{NN}}$=5.02 TeV
PID and cuts
TOF fits
Material budget
Hadronic interaction
Total
Relative systematics uncertainties
p_T (GeV/c)

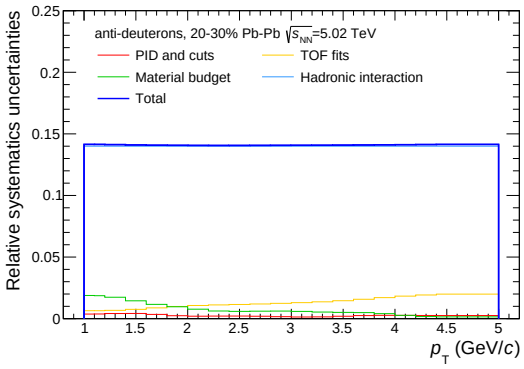
anti-deuterons, 20-30% Pb-Pb $\sqrt{s_{NN}}$=5.02 TeV
PID and cuts
TOF fits
Material budget
Hadronic interaction
Total
Relative systematics uncertainties
p_T (GeV/c)

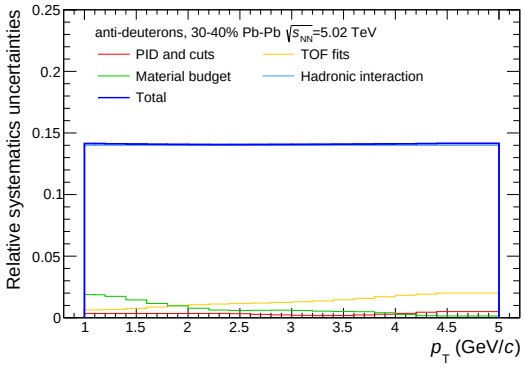
anti-deuterons, 30-40% Pb-Pb $\sqrt{s_{NN}}$=5.02 TeV
PID and cuts
TOF fits
Material budget
Hadronic interaction
Total
Relative systematics uncertainties
p_T (GeV/c)

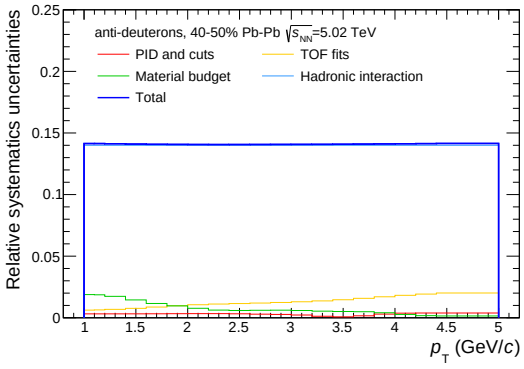
anti-deuterons, 40-50% Pb-Pb $\sqrt{s_{NN}}$=5.02 TeV
PID and cuts
TOF fits
Material budget
Hadronic interaction
Total
Relative systematics uncertainties
p_T (GeV/c)

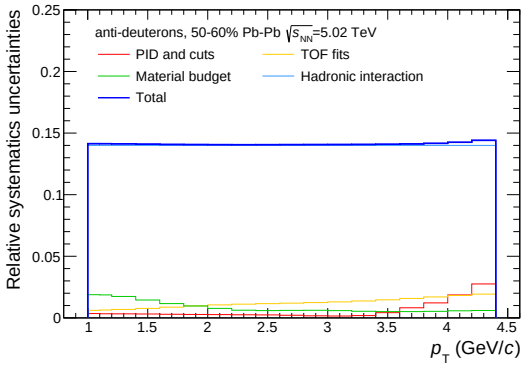
anti-deuterons, 50-60% Pb-Pb $\sqrt{s_{NN}}$=5.02 TeV
PID and cuts
TOF fits
Material budget
Hadronic interaction
Total
Relative systematics uncertainties
p_T (GeV/c)

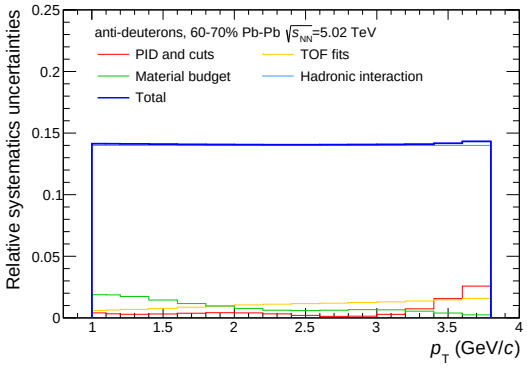
anti-deuterons, 60-70% Pb-Pb $\sqrt{s_{NN}}$=5.02 TeV
PID and cuts
TOF fits
Material budget
Hadronic interaction
Total
Relative systematics uncertainties
p_T (GeV/c)

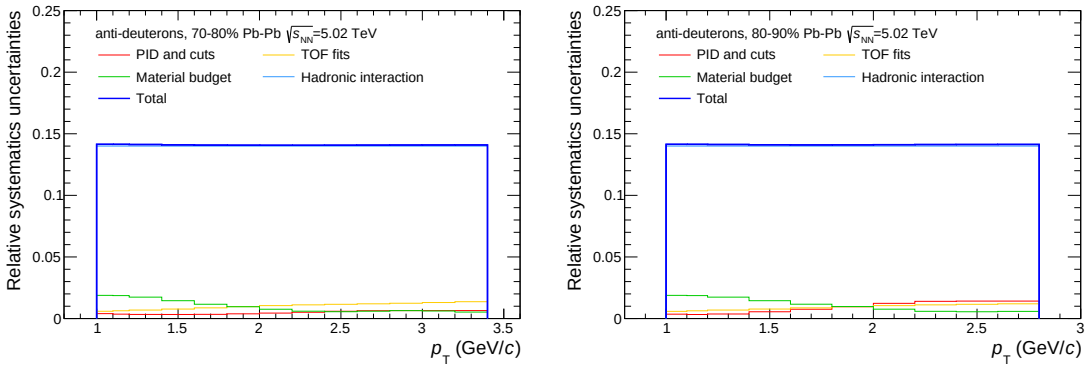

Figure 5.23: Summary of the systematic uncertainties evaluated for the anti–deuteron spectra in the different centrality classes of Pb–Pb at $\sqrt{s_{\rm NN}}$ =5.02 TeV. The thick blue line represents the sum in quadrature of the systematic uncertainties contributions. The dominant uncertainty is the difference between the GEANT3 and GEANT4 transport codes (light blue line, called hadronic interaction), the TOF fits uncertainty (yellow line) follows at high $p_{\rm T}$. The material budget variation (green line) is peaked at low $p_{\rm T}$ where the energy loss of the nuclei is higher. Conversely the PID and track selection variations (red line) do not lead to a pronounced peak at low $p_{\rm T}$, because of the lack of contamination from secondary particles for anti–deuterons, instead an enhancement of this contribution is visible around around $p_{\rm T}$ =2 GeV/c where the TPC nσ selection looses its effectiveness in rejecting the contamination from lighter particles.

6 Final results

In this chapter the measurements of the (anti-)deuteron and (anti-)^{3}He spectra in the Pb–Pb collision data sample collected by ALICE will be shown and discussed. The results obtained in the Pb–Pb sample at $\sqrt{s_{\rm NN}}$ =2.76 TeV will be compared with those published in [87] to corroborate the validity of the adopted analysis method and to show how the results obtained in this thesis extend the $p_{\rm T}$ of the published measurements. The measurements of the (anti-)deuteron and (anti-)^{3}He production spectra in Pb–Pb at $\sqrt{s_{\rm NN}}$ =5.02 TeV will follow in this Chapter, together with an analysis of the integrated yields and mean transverse momentum of the spectra. Finally the results will be compared with the production of protons to inquire into the production mechanism of light nuclei in HIC.

6.1 Production spectra

Combining the information of the signal extraction and the corrections illustrated in the previous Chapter, the production spectra of light nuclei is evaluated as:

$$\frac{1}{N_{\rm ev}}\frac{{\rm d}^2N}{{\rm d}y{\rm d}p_{\rm T}} = \frac{1}{N_{\rm ev}}\frac{f_{\rm primary}}{\epsilon\cdot\epsilon_{\rm G4/G3}}\frac{{\rm d}N_{\rm raw}}{{\rm d}p_{\rm T}}, \tag{6.1}$$

where $N_{\rm ev}$ is the total number of events analysed for the measurement, ε is the acceptance×efficiency correction, $f_{\rm primary}$ is the estimated fraction of primary particles and $\epsilon_{\rm G4/G3}$ is the correction due to the difference between GEANT3 and GEANT4 in the evaluation of the tracking efficiency.

Figure 6.1 show the spectra computed with this experimental technique for deuterons in the Pb–Pb at $\sqrt{s_{\rm NN}}$ =2.76 TeV data sample. The spectra are presented in three centrality classes (0–10% , 10–20% and 20-40%) in order to assess their dependence on the centrality of the collision. The slope of the spectrum becomes steeper and steeper going from central collisions to the peripheral ones. This is one indication of the presence of a radial flow component of the spectra that modifies the slope proportionally to the strength of the pressure gradients existing in the expanding source. Using the experimental techniques highlighted

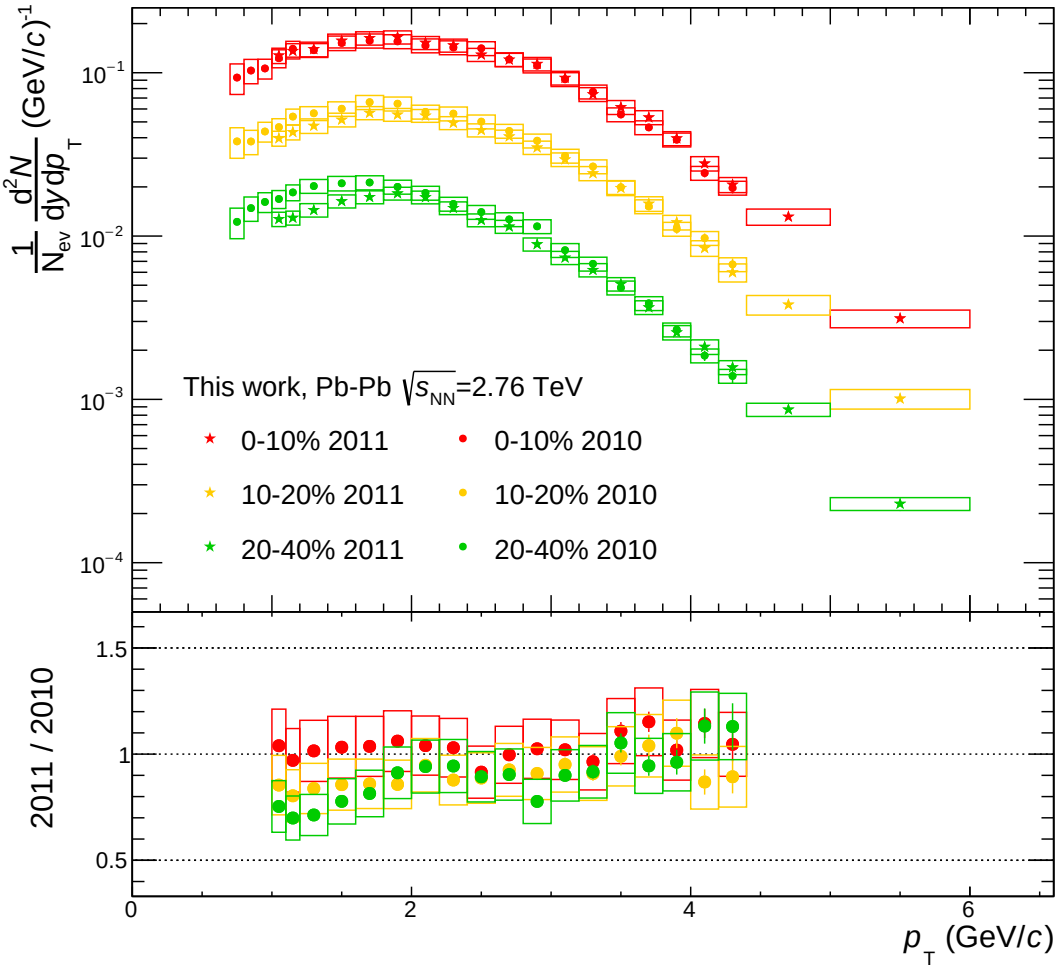

Figure 6.1: Deuteron spectra measured in this work on the Pb–Pb data at $\sqrt{s_{\rm NN}}$ =2.76 TeV collected in 2011 compared with the published results [87], concerning the 2010 data sample. Systematic uncertainties are represented with boxes, while the vertical lines are the statistical ones. Both spectra are in fair agreement. At $p_{\rm T}$ lower than 1.4 GeV/c the agreement is limited by the different correction for secondary particles.

in the previous Chapter, the published measurement of ALICE [87] was extended to the unexplored transverse momentum region between 4.4 and 6 GeV/c. The obtained spectra at lower $p_{\rm T}$ are in fair agreement with the ones published by the ALICE collaboration within the systematic uncertainties of the measurements. For $p_{\rm T} \leq 1.4$ GeV/c (Figure 6.1, bottom panel) the agreement is limited by the different correction for secondary particles. In a forthcoming publication the obtained results are combined with the published ones to obtain the widest $p_{\rm T}$ reach ever measured in the study of (anti–)deuteron production. Since the 2010 data

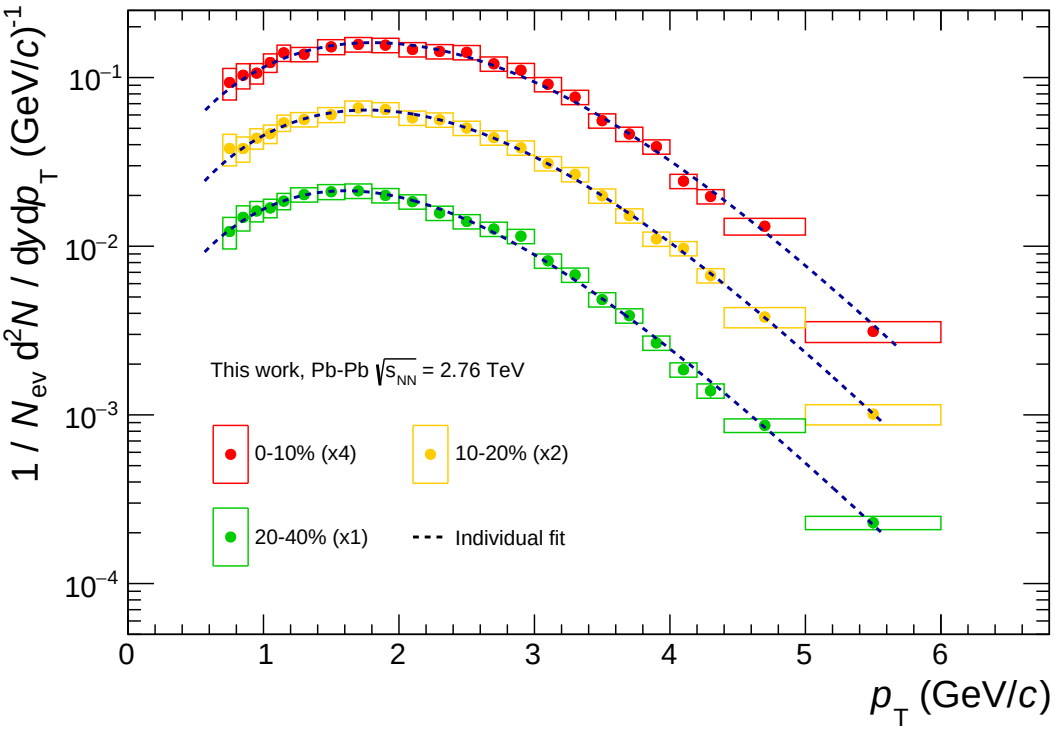

Figure 6.2: Compilation of deuteron spectra measured in this work on the Pb–Pb at $\sqrt{s_{\rm NN}}$ =2.76 TeV data collected in 2011 and the published results [87], concerning the 2010 data sample. Systematic uncertainties are represented with boxes, while the vertical lines are the statistical ones. The dashed lines represent the individual Blast Wave fit to the spectra.

sample is less affected by the differences between the transport codes in the determination of the efficiency due to a lower material budget in front of the TOF detector (less TRD super-modules were installed in 2010), the combination is performed using the published results at $p_{\rm T} \leq 4.4$ GeV/c and the new results for the higher $p_{\rm T}$ region. The obtained spectra are shown in Figure 6.2. This extension at high transverse momenta can be used as an input for models to investigate the possible analogies between the X, Y and Z hadronic states and loosely bound nuclear clusters [99] as deuterons. The main limitation of the current studies is the upper $p_{\rm T}$ value reached by the light nuclei spectra with the present sample size which limits the accuracy of the extrapolation to the high $p_{\rm T}$ region (between 10 and 30 GeV/c) where the X state has been measured.

Using the same experimental techniques, the production spectra of (anti–)deuterons in Pb–Pb were measured at the unprecedented energy of $\sqrt{s_{\rm NN}}$ = 5.02 TeV. The final spectra are shown in Figure 6.3. Thanks to the high number of events analysed in this new data sample, it has been possible to measure the spectra in finer centrality classes with respect to the published results [87] keeping, for the most central events, the same $p_{\rm T}$ reach obtained in the re-analysis

Table 6.1: Ratio between matter and anti-matter for deuterons and ^{3}He in the Pb–Pb data sample at $\sqrt{s_{\rm NN}}$ =5.02 TeV. The values were estimated by a weighted average of the ratios between anti–matter and matter production spectra. The first uncertainty is the statistical one, whereas the second is the systematic. All the measured ratios are reported in the Appendix B.

Species	Centrality	Ratio
$\overline{\rm d}$/d	0-5%	$0.99 \pm 0.00 \pm 0.04$
	5-10%	$0.98 \pm 0.00 \pm 0.04$
	10-20%	$0.97 \pm 0.00 \pm 0.04$
	20-30%	$0.98 \pm 0.00 \pm 0.04$
	30-40%	$1.00 \pm 0.00 \pm 0.04$
	40-50%	$1.03 \pm 0.00 \pm 0.04$
	50-60%	$1.00 \pm 0.01 \pm 0.05$
	60-70%	$0.99 \pm 0.01 \pm 0.05$
	70-80%	$0.99 \pm 0.02 \pm 0.05$
	80-90%	$0.89 \pm 0.04 \pm 0.07$
$^3\overline{\rm He}/^3$He	0-10%	$0.89 \pm 0.04 \pm 0.08$
	10-40%	$0.97 \pm 0.03 \pm 0.08$
	40-90%	$1.02 \pm 0.06 \pm 0.10$

of the Pb–Pb at $\sqrt{s_{\rm NN}}$ =2.76 TeV presented in this thesis. The change of shape with the centrality of the spectra can be appreciated thanks to the finer centrality classes. This change indicates a modification of the properties of the expanding source as a function of the impact parameter. The same kind of qualitative observation applies to the (anti–)^{3}He spectra measured on the new data sample and shown in Figure 6.4. The centrality classes definition in this case is statistically constrained by the low production yield of the ^{3}He and the number of collected events in 2015. Nevertheless, the measurements published in [87] are extended, adding one more centrality class: the new centrality classes allow us to inquire into the differences among central (0-10%), semi-central (10-40%) and peripheral (40-90%) collisions in the (anti-)^{3}He production.

The anti–deuteron production spectra are compatible within the systematic and the statistical uncertainties with those of deuteron, as can be evicted from Table 6.1. The $\bar{d}/d$ and $^3\overline{\rm He}/^3$He ratios were estimated by a weighted average of the ratios between anti–matter and matter production spectra (see Appendix B). The statistical uncertainty is the error on the average of the $p_{\rm T}$ dependent ratio weighted with its statistical uncertainties. Similarly the systematic uncertainty has been evaluated with the same procedure but using as weights the systematic uncertainties of the $p_{\rm T}$ dependent ratio. In both coalescence and thermal model frameworks, the obtained ratios are compatible with the expectation of a system with vanishing baryon chemical potential. If the μ_B of the system is null or close to zero, the number of nucleons and anti–nucleons in the system is the same and in the coalescence model there is no difference between the probability of producing a nucleus or an anti–nucleus. At the same time, in the thermal model approach the fugacity of a particle species $\lambda_i \propto e^{B_i \mu_B / T}$ (with B_i indicating the

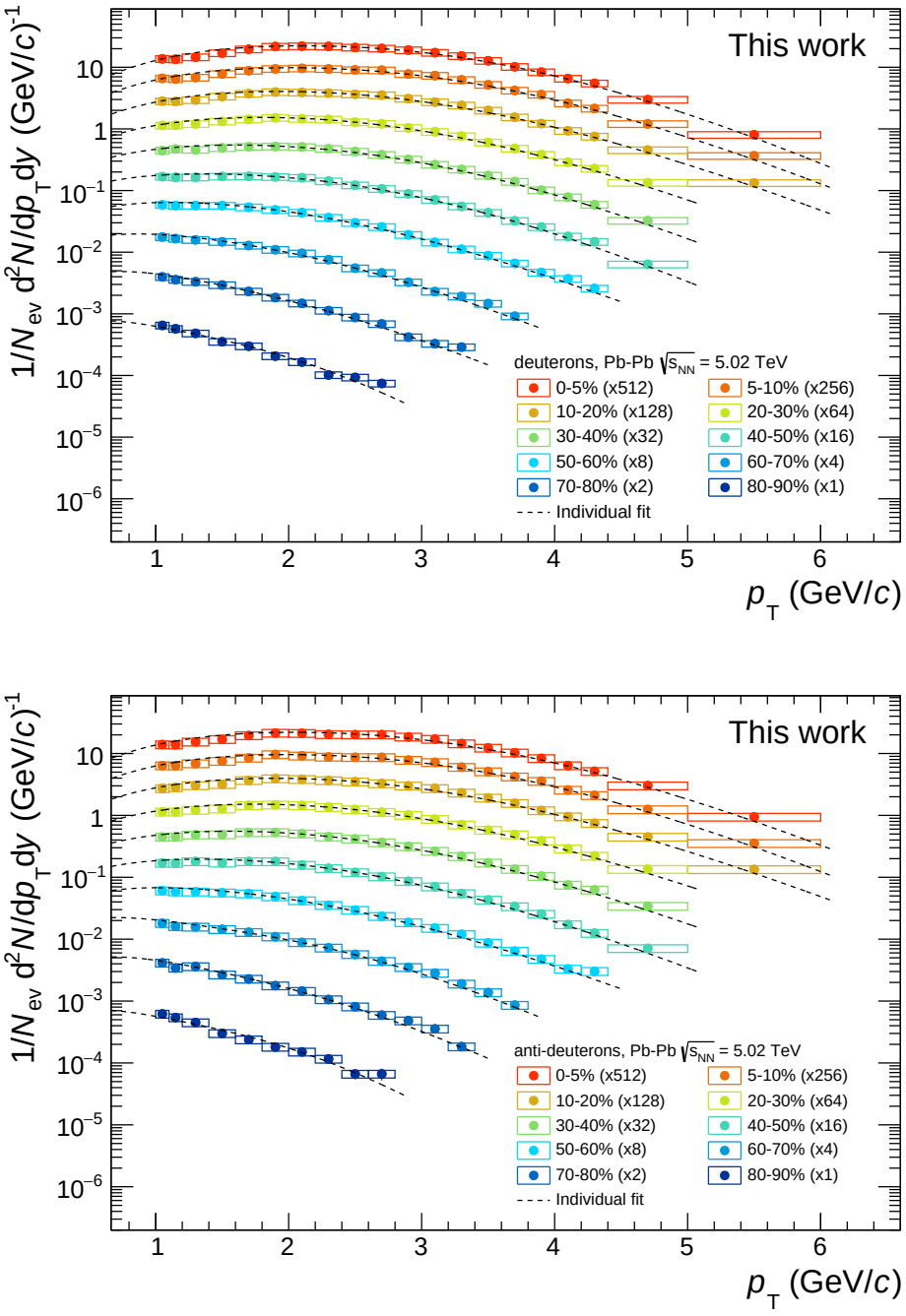

Figure 6.3: Deuteron (top) and anti–deuteron (bottom) spectra measured in this analysis on the Pb–Pb at $\sqrt{s_{\rm NN}}$ =5.02 TeV data sample. The boxes represent the systematic uncertainties while the vertical lines are the statistical ones. The dashed lines represent the individual Blast Wave fit to the spectra.

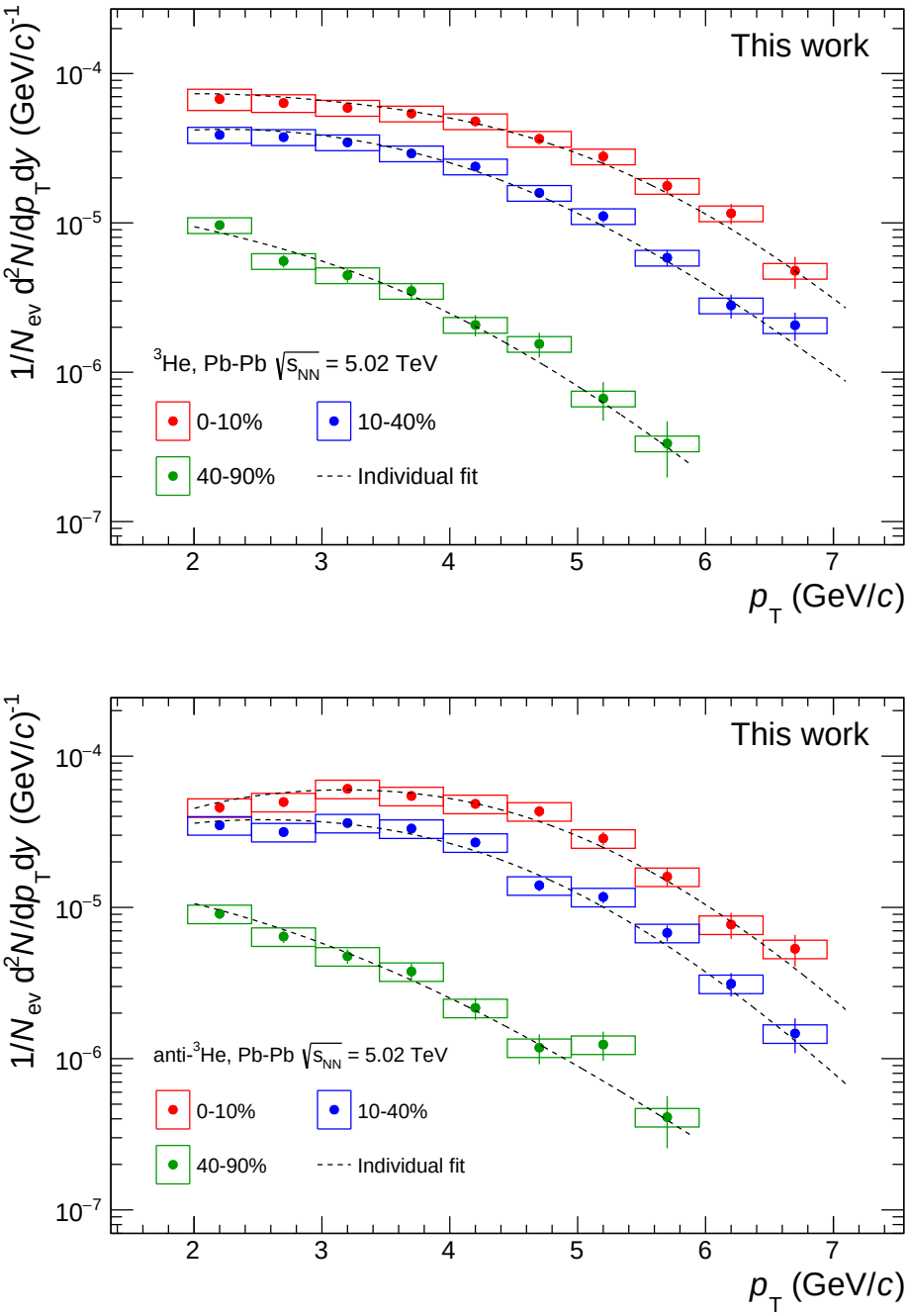

Figure 6.4: ^{3}He (top) and anti–^{3}He (bottom) spectra measured in this analysis on the Pb–Pb at $\sqrt{s_{NN}}$ =5.02 TeV data sample. The boxes represent the systematic uncertainties while the vertical lines are the statistical ones. The dashed lines represent the individual Blast Wave fit to the spectra.

Table 6.2: Summary of the measured $\mathrm{d}N/\mathrm{d}y$ and $\langle p_{\mathrm{T}} \rangle$ for deuterons and ^{3}He in the centrality classes analysed in the Pb–Pb at $\sqrt{s_{\mathrm{NN}}}$ =5.02 TeV data sample. The last column reports the χ^2/ndf for the Blast Wave fits to the spectra.

Species	Centrality	$\mathrm{d}N/\mathrm{d}y$	$\langle p_{\mathrm{T}} \rangle$ (GeV/c)	χ^2/ndf
d	0-5%	$(1.19 \pm 0.00 \pm 0.21) \times 10^{-1}$	$2.45 \pm 0.00 \pm 0.09$	0.14
d	5-10%	$(1.04 \pm 0.00 \pm 0.19) \times 10^{-1}$	$2.41 \pm 0.01 \pm 0.10$	0.17
d	10-20%	$(8.42 \pm 0.02 \pm 1.50) \times 10^{-2}$	$2.34 \pm 0.00 \pm 0.11$	0.15
d	20-30%	$(6.16 \pm 0.02 \pm 1.10) \times 10^{-2}$	$2.21 \pm 0.00 \pm 0.12$	0.08
d	30-40%	$(4.25 \pm 0.01 \pm 0.75) \times 10^{-2}$	$2.05 \pm 0.00 \pm 0.12$	0.07
d	40-50%	$(2.73 \pm 0.01 \pm 0.48) \times 10^{-2}$	$1.88 \pm 0.01 \pm 0.12$	0.09
d	50-60%	$(1.62 \pm 0.01 \pm 0.28) \times 10^{-2}$	$1.70 \pm 0.01 \pm 0.11$	0.06
d	60-70%	$(8.35 \pm 0.14 \pm 1.43) \times 10^{-3}$	$1.46 \pm 0.01 \pm 0.12$	0.16
d	70-80%	$(3.52 \pm 0.06 \pm 0.63) \times 10^{-3}$	$1.27 \pm 0.02 \pm 0.11$	0.30
d	80-90%	$(1.13 \pm 0.03 \pm 0.23) \times 10^{-3}$	$1.09 \pm 0.02 \pm 0.40$	0.39
^{3}He	0-10%	$(2.70 \pm 0.13 \pm 0.59) \times 10^{-4}$	$3.06 \pm 0.09 \pm 0.34$	0.41
^{3}He	10-40%	$(1.45 \pm 0.07 \pm 0.28) \times 10^{-4}$	$2.84 \pm 0.09 \pm 0.28$	0.69
^{3}He	40-90%	$(3.18 \pm 0.30 \pm 0.59) \times 10^{-5}$	$1.99 \pm 0.12 \pm 0.11$	1.92

baryon number of the particle species) is the only different term in the expected total yields of baryons and anti–baryons. For vanishing chemical potential, the fugacities of nuclei and anti–nuclei coincide and their yields are the same according to the Statistical Hadronisation Models [26]. Quantitatively, both the statistical hadronization and the coalescence models predict that $\bar{d}/d = (\bar{p}/p)^2$ and $^3\overline{\mathrm{He}}/^3\mathrm{He} = (\bar{p}/p)^3$: this prediction is confirmed by the results of the present work when comparing them with the published $\bar{p}/p$ measurements [100].

6.2 Yield and mean p_{T}

In order to measure the total yield per rapidity unit ($\mathrm{d}N/\mathrm{d}y$) of (anti–)deuterons and (anti–)^{3}He and their average transverse momentum ($\langle p_{\mathrm{T}} \rangle$), their spectra were fit with the Blast Wave function [101]. This function describes the measured spectra features assuming a thermal production of particles from an expanding source:

$$\frac{1}{p_{\mathrm{T}}}\frac{\mathrm{d}N}{\mathrm{d}p_{\mathrm{T}}} \propto \int_0^R r\, m_{\mathrm{T}} I_0\left(\frac{p_{\mathrm{T}} \sinh\rho}{T_{\mathrm{kin}}}\right) K_1\left(\frac{m_{\mathrm{T}} \cosh\rho}{T_{\mathrm{kin}}}\right) \mathrm{d}r, \tag{6.2}$$

where I_0 and K_1 are the modified Bessel functions, r is the distance from the centre of the expanding system, R is the limiting radius of the system expansion, T_{kin} is the temperature of the kinetic freeze–out and ρ is the velocity profile. The velocity profile can be expressed in terms of the transverse expansion velocity at the system surface, β_S, and an exponent n:

$$\rho = \tanh^{-1}\left[\beta_S (r/R)^n\right]. \tag{6.3}$$

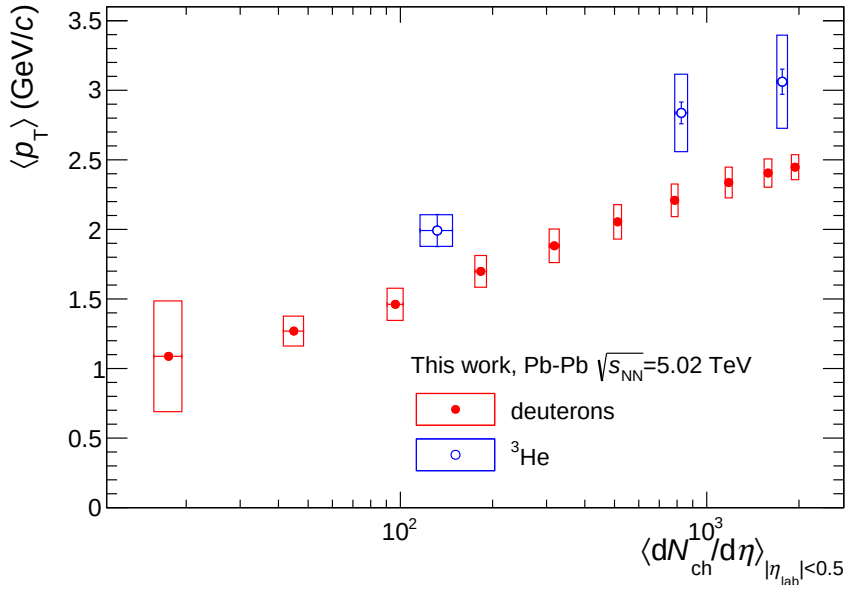

Figure 6.5: Mean transverse momentum for deuterons (red) and ^{3}He (blue) as a function of the measured charged particle multiplicity in the pseudorapidity region $|\eta| < 0.5$. The vertical lines and the boxes represent the statistical and systematic uncertainties respectively.

Since the production spectra of nuclei and anti–nuclei are compatible and the anti–nuclei spectra are affected by larger systematic uncertainties, the measurement of the yield is performed using the nuclei spectra only. The Blast-Wave function was used to extract the central value and the statistical uncertainties of the $\mathrm{d}N/\mathrm{d}y$ and $\langle p_{\mathrm{T}} \rangle$, but the systematic uncertainty due to the extrapolation in the unmeasured region at high and low transverse momenta was evaluated by fitting the spectrum using three additional functions:

1. an m_{T} exponential function

$$\frac{\mathrm{d}N}{\mathrm{d}p_{\mathrm{T}}\mathrm{d}y} = Ae^{-m_{\mathrm{T}}/T}, \tag{6.4}$$

with A and T as fit parameters;

2. a Levy–Tsallis model [102]

$$\frac{1}{p_{\mathrm{T}}}\frac{\mathrm{d}N}{\mathrm{d}p_{\mathrm{T}}\mathrm{d}y} = \frac{\mathrm{d}N}{\mathrm{d}y}\frac{(n-1)(n-2)}{nC[nC+m(n-2)]}\left(1+\frac{m_{\mathrm{T}}-m}{nC}\right)^{-n}, \tag{6.5}$$

with C, n and the $\mathrm{d}N/\mathrm{d}y$ as fit parameters and m the mass of the particle under study;

3. a Boltzmann distribution

$$\frac{\mathrm{d}N}{\mathrm{d}p_{\mathrm{T}}\mathrm{d}y} = Ap_{\mathrm{T}}m_{\mathrm{T}}e^{-m_{\mathrm{T}}/T}, \tag{6.6}$$

with A and T as fit parameters.

Half of the difference between the maximum and the minimum $\mathrm{d}N/\mathrm{d}y$ and p_{T} computed with the different functions was added in quadrature to the systematic uncertainty. The latter was evaluated by fitting the Blast Wave function to the spectrum shifted up and down by a factor equal to its systematic uncertainty. The difference between the different fit functions is the dominant contribution to the systematic uncertainty in the case of the ^{3}He spectra and the spectra of deuterons in peripheral events (from 70% to 90%) because of the limited p_{T} coverage of the analysis. The measured $\langle p_{\mathrm{T}}\rangle$ and $\mathrm{d}N/\mathrm{d}y$ with their statistical and systematic uncertainties are shown in Table 6.2.

Figure 6.5 shows the evolution of the $\langle p_{\mathrm{T}}\rangle$ with the average charged particles density in the pseudorapidity region $|\eta| < 0.5$, that is a proxy for the centrality of the collision. The centrality classes adopted in the extraction of the spectra were translated in $\langle \mathrm{d}N/\mathrm{d}\eta\rangle$ using the values tabulated in [103]. The rise of the mean transverse momentum with the centrality confirms the trend observed for the other particle species because of the presence of stronger pressure gradients in the system created in HIC generating a stronger *radial flow*. The relevance of radial flow is also often highlighted by the presence of a mass ordering of the $\langle p_{\mathrm{T}}\rangle$: this phenomenology is visible also in the case of the light nuclei where the ^{3}He (i.e. the heavier between ^{3}He and deuterons) has the highest mean transverse momentum when comparing similar centralities (Figure 6.5).

6.3 Comparisons to the theoretical expectations

As already highlighted in the previous section, the fugacity of a particle species is steering its production yield. Since the ratio between the baryons and the anti–baryons production is compatible with unity in HIC at the LHC, the fugacity is (very close to) 1 for nucleons and light nuclei. In a simplistic approach within the SHM framework, the production yield of protons, deuterons and ^{3}He should follow

$$\left(\frac{\mathrm{d}N}{\mathrm{d}y}\right)_{\mathrm{nucl.}} \propto e^{-m/T_{\mathrm{chem}}}, \tag{6.7}$$

where m is the mass of the nucleon(us) and T_{chem} is the temperature of the chemical freeze–out.[1] Figure 6.6 shows the $\mathrm{d}N/\mathrm{d}y$ of protons[2] , deuterons and ^{3}He in the 0-10% centrality class of the Pb–Pb at $\sqrt{s_{\mathrm{NN}}}$ =5.02 TeV data sample as a function of their mass. The exponential

[1] This approach neglects many caveats of the statistical hadronisation model, for instance the different eigen–volume correction for different particle species and the resonance feed-down.

[2] The $\mathrm{d}N/\mathrm{d}y$ of protons, as well as the spectra that will be used later, were taken by the recently released preliminary analysis of the ALICE experiment [89, 104].

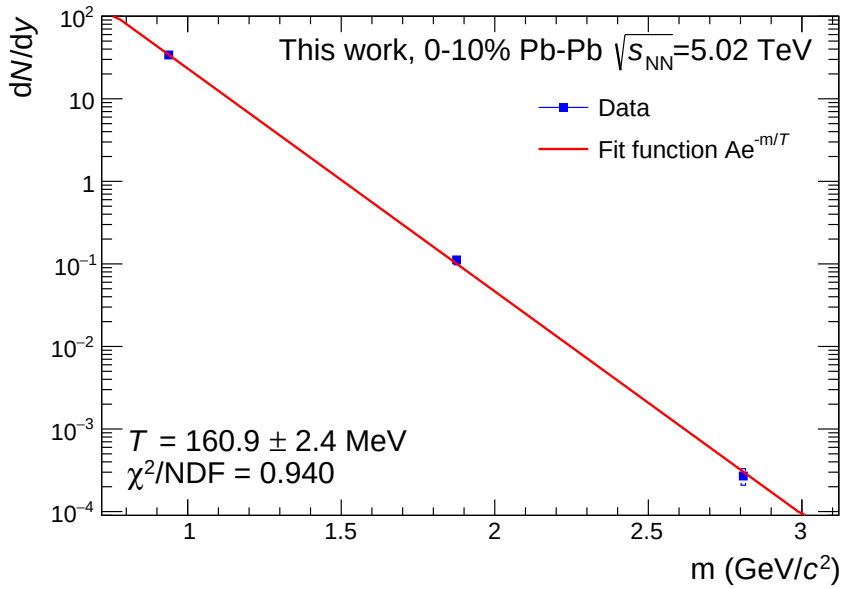

Figure 6.6: Distribution of the $\mathrm{d}N/\mathrm{d}y$ of protons, deuterons and ^{3}He as a function of their mass for the Pb–Pb data sample at $\sqrt{s_{\mathrm{NN}}}$ =5.02 TeV. The red line shows the fit to this distribution with the exponential law expected by a simplified approach to the thermal model.

function 6.7 fits the data with a good reduced χ^2 and with parameters compatible with those shown in [87]. Thanks to the result of this exponential fit, the expected $\mathrm{d}N/\mathrm{d}y$ of heavier nuclei is predicted knowing that adding an additional nucleon to a nucleus will cost a penalty factor of approximately 300 to its $\mathrm{d}N/\mathrm{d}y$.

In the thermal model framework, the yield of a particle species i, $\langle N_i \rangle$, is proportional to the volume of the system V. The dependence on the system volume is eliminated when studying the ratio between the yield of different particle species. The chemical freeze-out temperature of the system can be investigated directly in this way. Figure 6.7 shows the comparison between the measured ^{3}He over deuteron (blue line) and ^{3}He over proton ratios (red line) and the prediction from two different implementation of the SHM [26, 105, 106] as a function of the chemical freeze–out momentum. The range of chemical freeze-out temperatures compatible within 1σ with the measurements is between 150 and 158 MeV, that is very close to the temperature attained with the simplistic approach used in Figure 6.6.

The other class of models for the production of (anti–)nuclei in HIC can be investigated by computing the coalescence parameters B_2 and B_3 for deuterons and ^{3}He respectively:

$$B_A = E_i \frac{\mathrm{d}^3 N_i}{\mathrm{d}p_i^3} \left(E_p \frac{\mathrm{d}^3 N_\mathrm{p}}{\mathrm{d}p_\mathrm{p}^3} \right)^{-A}. \tag{6.8}$$

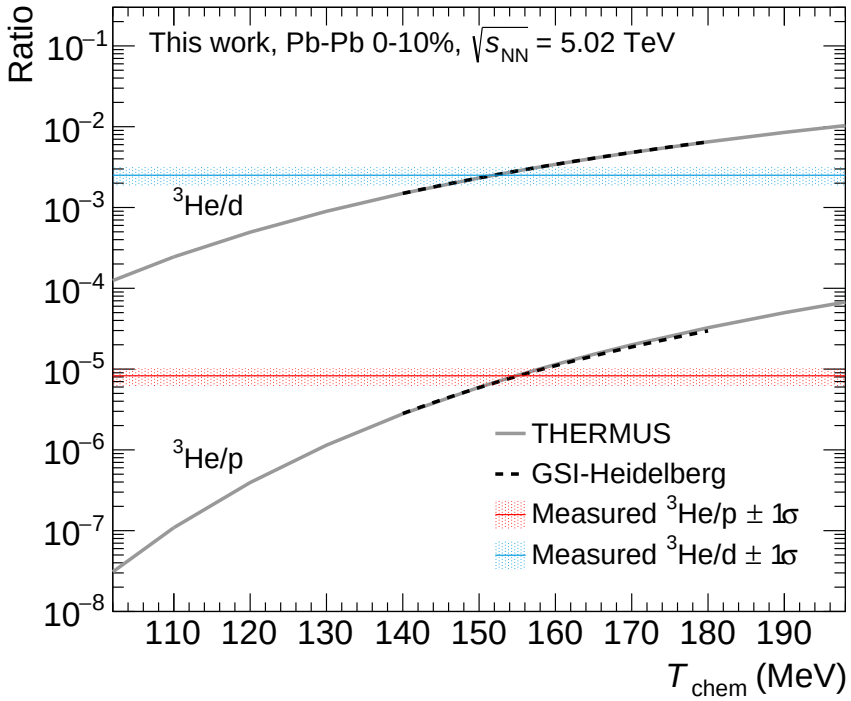

Figure 6.7: Measured ^{3}He over deuteron ratio (blue line) and ^{3}He over proton ratio (red line) compared with the predictions of the THERMUS (grey line, [105]) and GSI-Heidelberg (dashed line, [26]) SHM models. The shaded areas correspond to the 1σ uncertainty (statistical + systematic) interval from the measurements.

The definition adopted in the models uses the proton spectra before the formation of the nuclei. The experimental computation of the coalescence parameters relies on the fact that the production of nuclei with mass number A is suppressed by a factor of $(300)^A$ with respect to the proton yield. Therefore, the proton spectrum used in the coalescence model can be replaced by the measured proton spectrum. Figure 6.8 shows the measured coalescence parameters B_2 and B_3 as a function of the transverse momentum scaled by the mass number A for Pb–Pb collisions at $\sqrt{s_{NN}}$ = 5.02 TeV. This Figure show an ordering of the coalescence parameters with the centrality, going from higher B_A values in peripheral collisions to lower B_A values in the central ones. As illustrated in the introduction Chapter, this trend with centrality is explained in the coalescence model framework as an increasing volume $V_{\rm eff}$ of the source going from peripheral to central events. If the $V_{\rm eff}$ is bigger, the probability of having two nucleons close enough in the phase space to form a bound state is lower, thus the coalescence parameters are smaller. In addition, the measured coalescence parameters show a significant increase with the transverse momentum that is not explained by the simplest formulation of the coalescence models. One possible extension to the model, briefly described in the introduction Chapter and in [28], explains the observed trend by assuming a smaller emission radius, thus a smaller $V_{\rm eff}$, for particles with higher and higher momentum. Alternatively, as

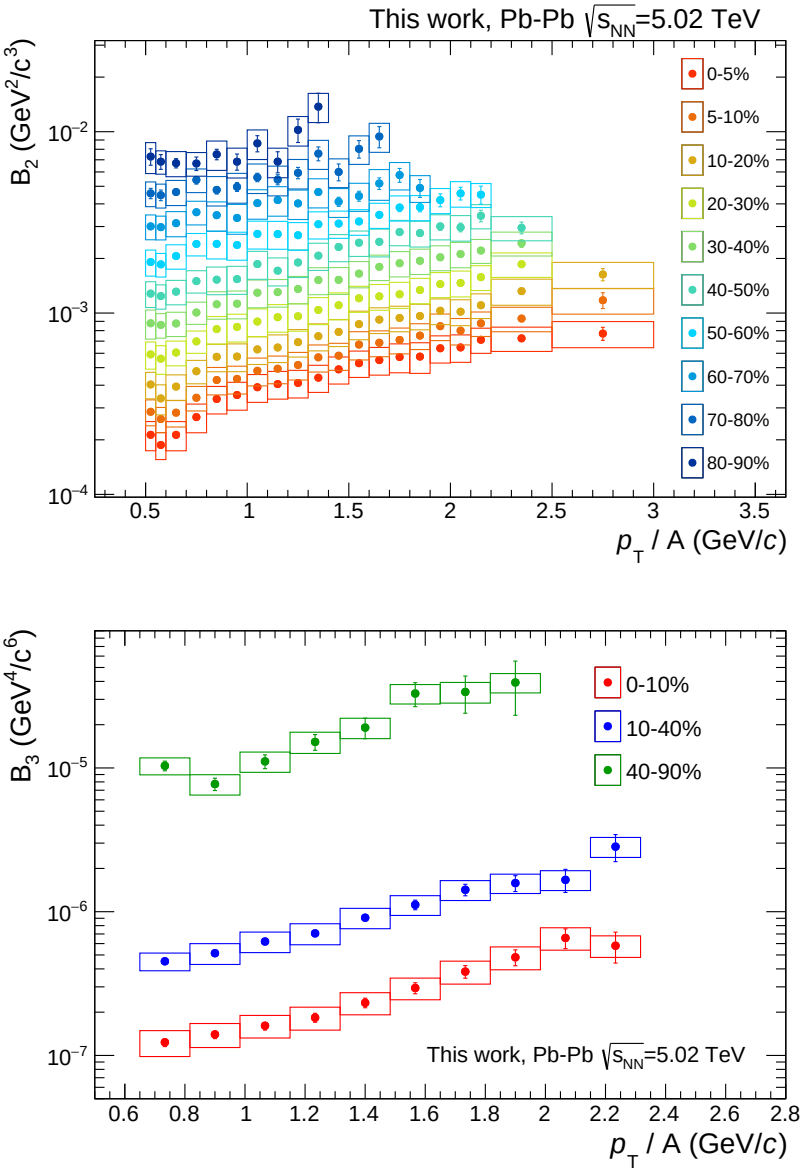

Figure 6.8: Coalescence parameters B_2 (top) and B_3 (bottom) measured in Pb–Pb collisions at $\sqrt{s_{NN}}$ =5.02 TeV as a function of the transverse momentum scaled by the mass number of the nucleus. Each colour corresponds to a different centrality class. See the text for details.

outlined in [87], a qualitative explanation for this trend can be found by taking into account the position–momentum correlation induced by an expanding thermal source [107]. Nevertheless, at the time of this thesis there are no quantitative predictions in the coalescence model framework that can be compared with the results obtained in this work.

6.4 Nucleus over proton ratio

In the HIC, the evolution with centrality, and in general with the charged particle multiplicity, of the ratio between nuclei and protons $\mathrm{d}N/\mathrm{d}y$ defined as

$$R(A) = \frac{\left(\mathrm{d}N/\mathrm{d}y\right)_A}{\left(\mathrm{d}N/\mathrm{d}y\right)_p} \tag{6.9}$$

it is a benchmark for the models of the nuclei production mechanism. According to the thermal model interpretation, $R(A)$ is fixed by the temperature of the source, thus it has to stay constant with the charged particle multiplicity evolution. On the other hand, in a naive coalescence picture $R(A)$ should increase with the multiplicity of nucleons produced in the collision. The $R(A)$ ratio as a function of multiplicity published in [87] was found to be independent of the charged particle multiplicity. The published ratio was compatible with the thermal model prediction with a chemical freeze–out temperature between 150 and 160 MeV [87]. Figure 6.9 shows $R(2)$ for deuterons (top panel) and $R(3)$ ^{3}He (bottom panel). In both cases the measurement presented in this work represents a substantial extension of the multiplicity range covered in this kind of analysis. In the case of the ^{3}He over proton ratio, the result obtained in this work is compatible, within uncertainties, with that shown in [87]. This ratio does not exhibit any evident trend with the multiplicity, confirming the picture sketched by the thermal model predictions. Conversely the deuteron over proton ratio shows a deviation from the constant behaviour. In the region of overlap with the results shown in [87], the ratio computed in this thesis is compatible with that obtained in Pb–Pb collisions at $\sqrt{s_{\mathrm{NN}}}$ =2.76 TeV. Furthermore an important point is that, thanks to the analysis carried out in the present work, a quantitative comparison with preliminary results in p–Pb collisions was done. Indeed, at low charged particle multiplicity the ratio for Pb–Pb starts to decrease and it overlaps with the p–Pb results. Similarly, at high multiplicity a hint of suppression of the deuteron production with respect to protons is visible. One possible explanation of the observed pattern can be found in [108], where the similar trend observed in the Ξ over pion ratio is explained as a consequence of the different rescattering conditions after the chemical freeze–out. In that context, the depletion for very central collision is interpreted as an increased number of interactions in the rescattering phase, moving the observed yield away from the chemical equilibrium. While at low multiplicity, *corona* effects [109] lead to a depletion of the deuteron over proton ratio going toward the value observed in pp collisions.

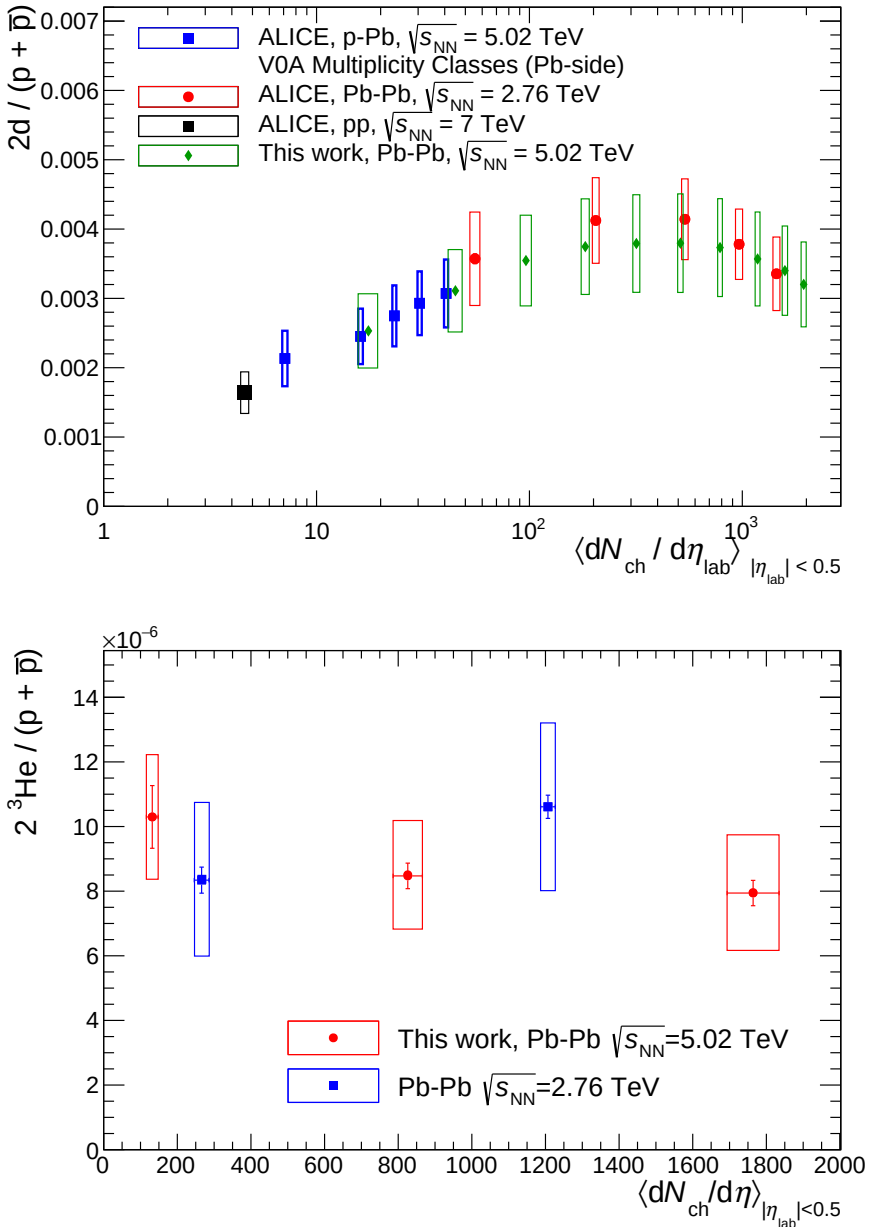

Figure 6.9: Ratio between the measured $\mathrm{d}N/\mathrm{d}y$ of nuclei and proton as a function of the charged particle multiplicity. The vertical lines represent the statistical uncertainties while the boxes represent the systematic ones. The top panel shows the results for d/p ratio obtained in this thesis (green points) compared with those published in [87] (red points for Pb–Pb and black dot for pp) and the preliminary results of ALICE in p–Pb collisions [106] (blue points). The bottom panel shows the ^{3}He$/p$ ratio measured in this thesis (red points) compared with those published (blue dots).

7 Conclusions

The aim of this thesis project was twofold: developing new software instruments for the future ALICE experiment and the analysis of the current data in the quest for the determination of the production mechanism of light (anti–)nuclei in heavy ion collisions. The highlights of the work described in details in the past chapters related to these two objectives can be summarised in two plots.

The first plot, Figure 7.1, shows the tracking efficiency obtained with the Cellular Automata (CA) tracking algorithm developed for the new Inner Tracking System that is under construction

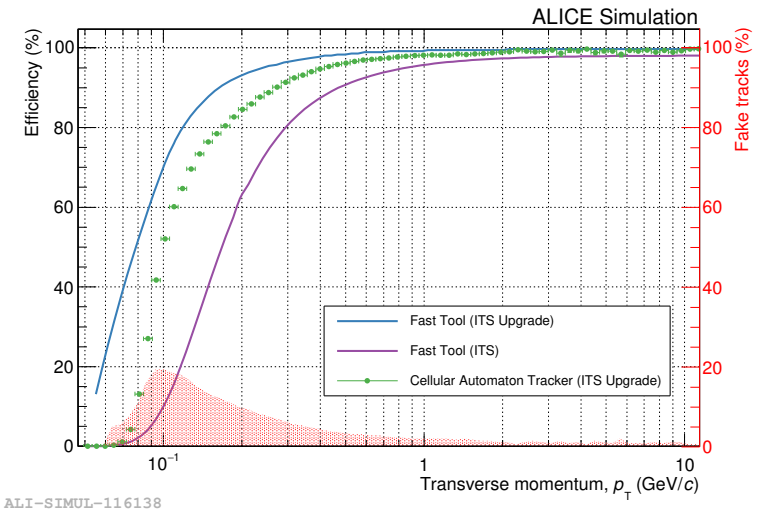

Figure 7.1: ITS Upgrade tracking efficiency in central Pb–Pb events for pions with a cluster in each layer of the detector. The green points show the efficiency with the Cellular Automata algorithm while the continuous blue and purple lines represent the efficiency obtained using the Fast Monte Carlo Tool for the ITS Upgrade and the current ITS respectively. The red shaded area corresponds to the fake track rate for the CA algorithm.

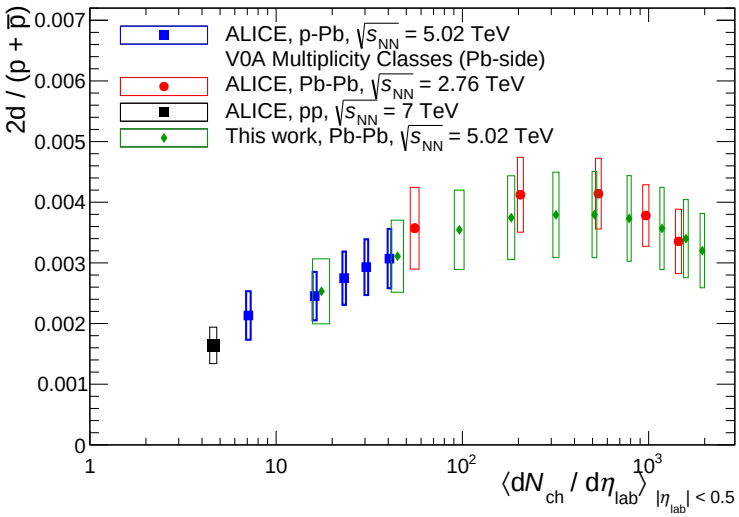

Figure 7.2: Ratio between the measured $\mathrm{d}N/\mathrm{d}y$ of deuteron and proton as a function of the charged particle multiplicity. The vertical lines represent the statistical uncertainties while the boxes represent the systematic ones. The panel shows the results obtained in this thesis (green diamonds) compared with those published in [87] (red points for Pb–Pb and black square symbols for pp) and the preliminary results of ALICE in p–Pb collisions [106] (blue squares).

and it will be commissioned for the LHC Run 3 scheduled for 2020. The CA algorithm satisfies the requirements of the ITS Upgrade project in terms of tracking efficiency and track quality, for what concerns pointing resolution, transverse momentum resolution and low rate of misidentified particle trajectories (fake tracks). Furthermore it sets a new standard in terms of reduction of the required CPU time, since, for the reconstruction of a central Pb–Pb collision at top energy, it is faster by about one order of magnitude than the present tracker.

For the nuclei production in HIC, the evolution of the deuteron over proton ratio as a function of the charged particle multiplicity is one of the most intriguing results obtained in this work (Figure 7.2). While the almost linear increase of this ratio from the pp multiplicity to the top p–Pb one is understood in terms of the naive coalescence models, the saturation reached in Pb–Pb collisions requires additional conditions to fit the measured values in the coalescence picture. In addition, the observed trend in the ratio measured in this thesis, confirms a slight suppression of deuterons with respect to protons in the most central Pb–Pb collisions and the same kind of behaviour is observed in the most peripheral ones. This observation challenges the picture of a constant deuteron over proton ratio depicted by thermal models. However, models including baryon annihilation in a long rescattering phase after the hadronisation and *corona* effects in peripheral HIC reproduce a similar deviation from the expected thermal behaviour for the Ξ/π ratio. The results presented here on the deuteron production at high transverse momentum in Pb–Pb collisions at $\sqrt{s_{\mathrm{NN}}}$ =2.76 TeV are a part of a forthcoming paper while the results at the new energy will be presented in the summer conferences after the

approval of the ALICE collaboration.

While concluding the Ph.D. course and setting some important milestones for both the new ITS software and the study of the nuclei production in HIC, the results shown in this thesis open the stage for new developments in both fields. In the era of the Big Data and the exascale computing, the usage of heterogenous hardware, such as GPUs and FPGAs, is a possible way to further improve the performance of the ITS upgrade algorithms to cope with the 50 kHz Pb–Pb collisions interaction rate expected for the LHC Run 3. A first rough implementation of the *trackleting* algorithms in a language, OpenCL, that enables the possibility of running it on heterogeneous hardware, was already implemented in this work and the idea will be further developed in the next future.

On the other hand, the analysis results presented in this work challenge theoretical models for the (anti–)nuclei production and suggest additional experimental effort for reducing the uncertainties affecting the measurements with the aim of constraining models. Moreover an analysis campaign to study the nuclei production as a function of multiplicity in pp collisions is required to see whether the observed multiplicity trend is a general feature across different systems, similarly to what has been observed for the strange particle production [110].

A List of selections used in the CA tracker

This appendix is devoted to the illustration of the selection criteria used in the CA tracker to reject the combinatorial background in the early stages of the track reconstruction in the ITS Upgrade. The full code of the CA algorithm is available under the GPL licence and it can be downloaded from the GitHub repository of AliRoot. The code consists of five files:

- AliITSUCACell.h, containing the basic data structures for tracklets, cells and roads;
- AliITSUCATracker.{h,cxx}, containing the implementation of the tracking code;
- AliITSUCATrackingStation.{h,cxx}, the container for the clusters of one layer.

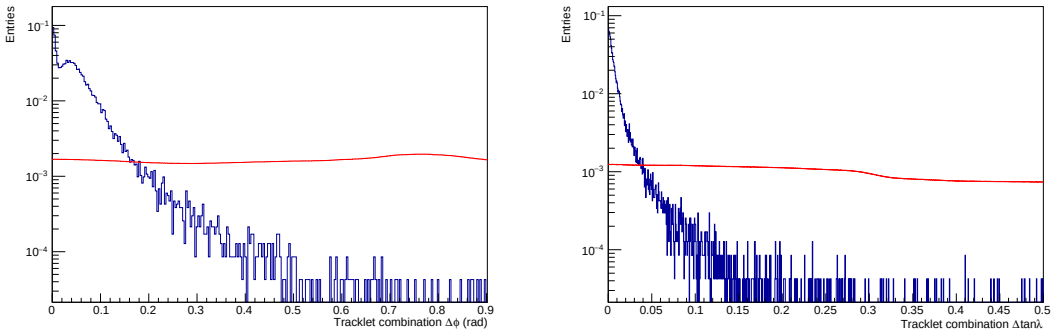

(a) $\Delta\varphi$ (b) $\Delta \tan\lambda$

Figure A.1: Selection variables used during the tracklet combination. The red histogram represents the case of two tracklets belonging to the same particle while the red histogram represents the case of two tracklets coming from different particles (or one of the two fake). On the left, the difference between the azimuthal inclination of the tracklets is shown. On the right the difference between the $\tan\lambda$ of the two tracklets is illustrated. All the distributions are normalised to the visible range.

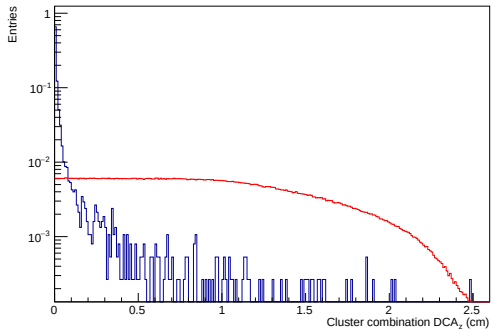

(a) Combinations L0-L1

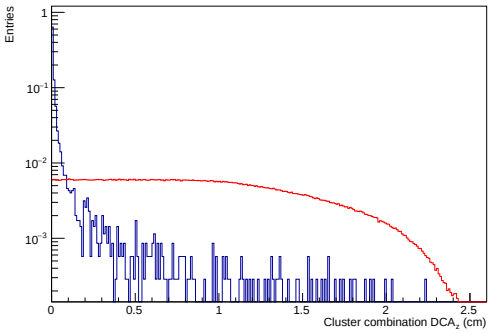

(b) Combinations L1-L2

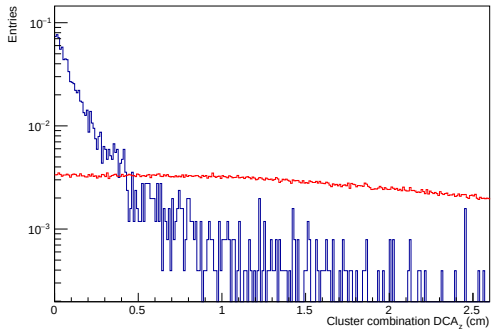

(c) Combinations L2-L3

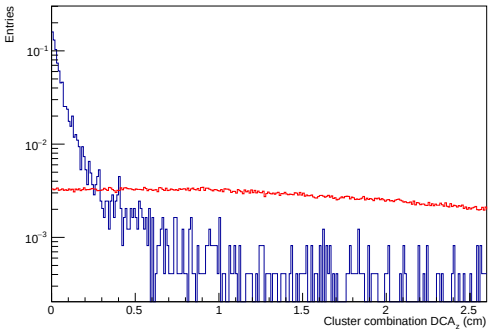

(d) Combinations L3-L4

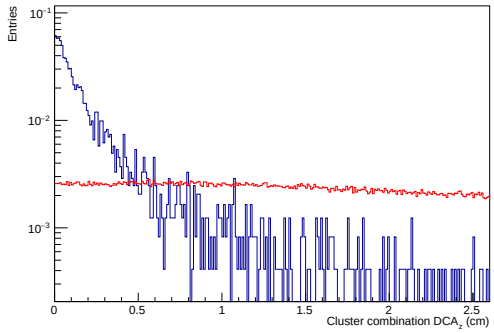

(e) Combinations L4-L5

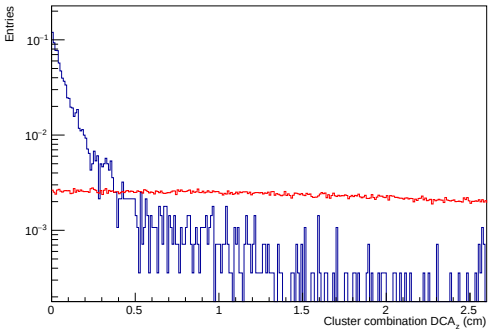

(f) Combinations L5-L6

Figure A.2: Distributions for different layer combinations (Ln-L$n+1$) of the distance along the z direction between the primary vertex and the extrapolation to the beamline of a tracklet candidate. The blue histogram represents the case of two cells belonging to the same particle while the red histogramblue histogram represents the case of two cells coming from different particles (or one of the two fake). In this case the distributions are normalised to the visible range.

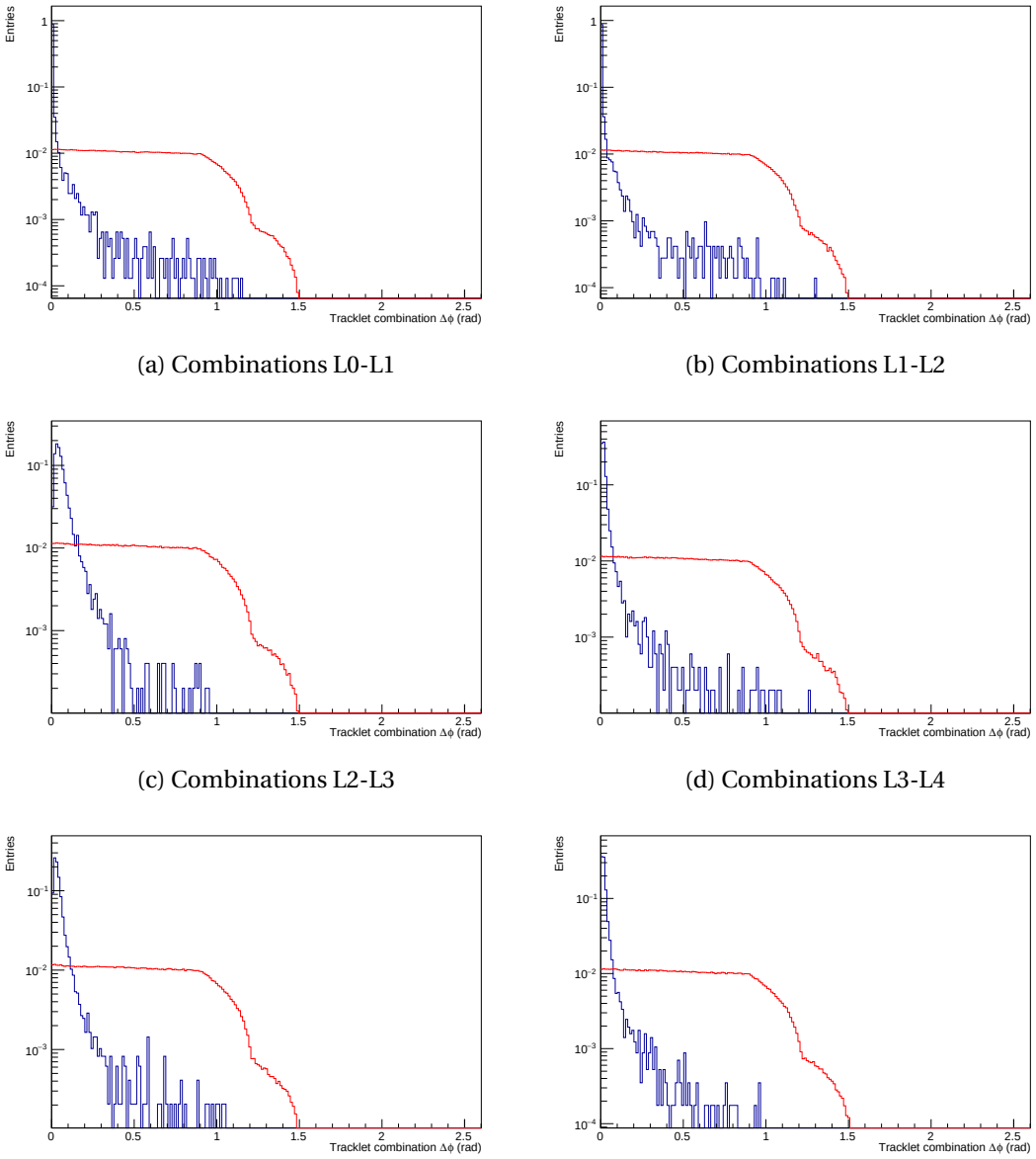

(a) Combinations L0-L1

(b) Combinations L1-L2

(c) Combinations L2-L3

(d) Combinations L3-L4

(e) Combinations L4-L5

(f) Combinations L5-L6

Figure A.3: Cut on the azimuthal angle difference between clusters of subsequent layers (Ln-L$n+1$) used during the tracklets combination. The blue histogram represents the case of two cells belonging to the same particle while the red histogram represents the case of two cells coming from different particles (or one of the two fake). The distributions are normalised to the visible range.

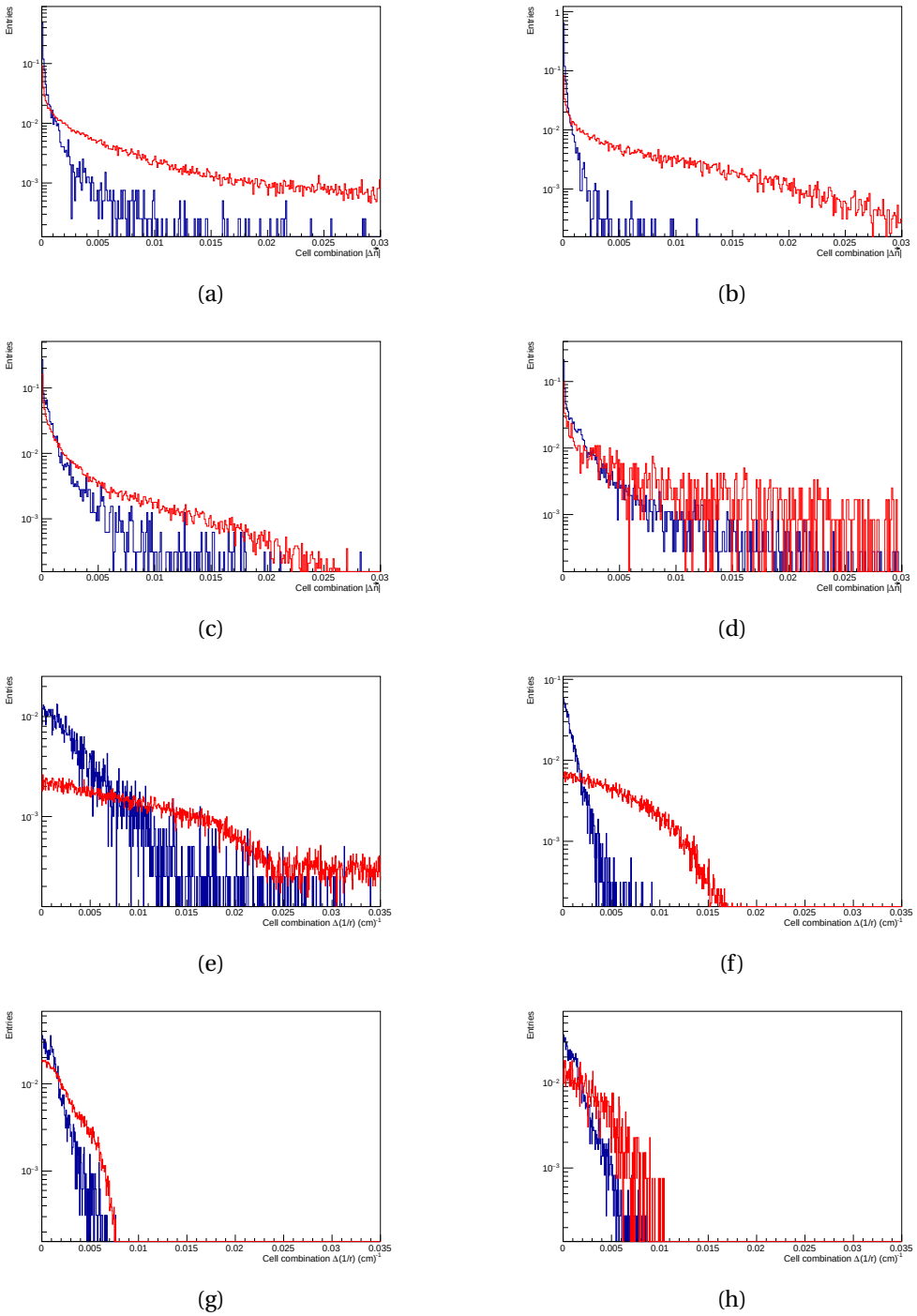

Figure A.4: Selection variables used during the cell combination. The blue histogram represents the case of two cells belonging to the same particle while the red histogram represents the case of two cells coming from different particles (or one of the two fake). The top four figures show the modulo of the difference between the normal vectors of the cells. The remaining figures show the difference between the curvatures of the cells being combined. All the distributions are normalised to the visible range.

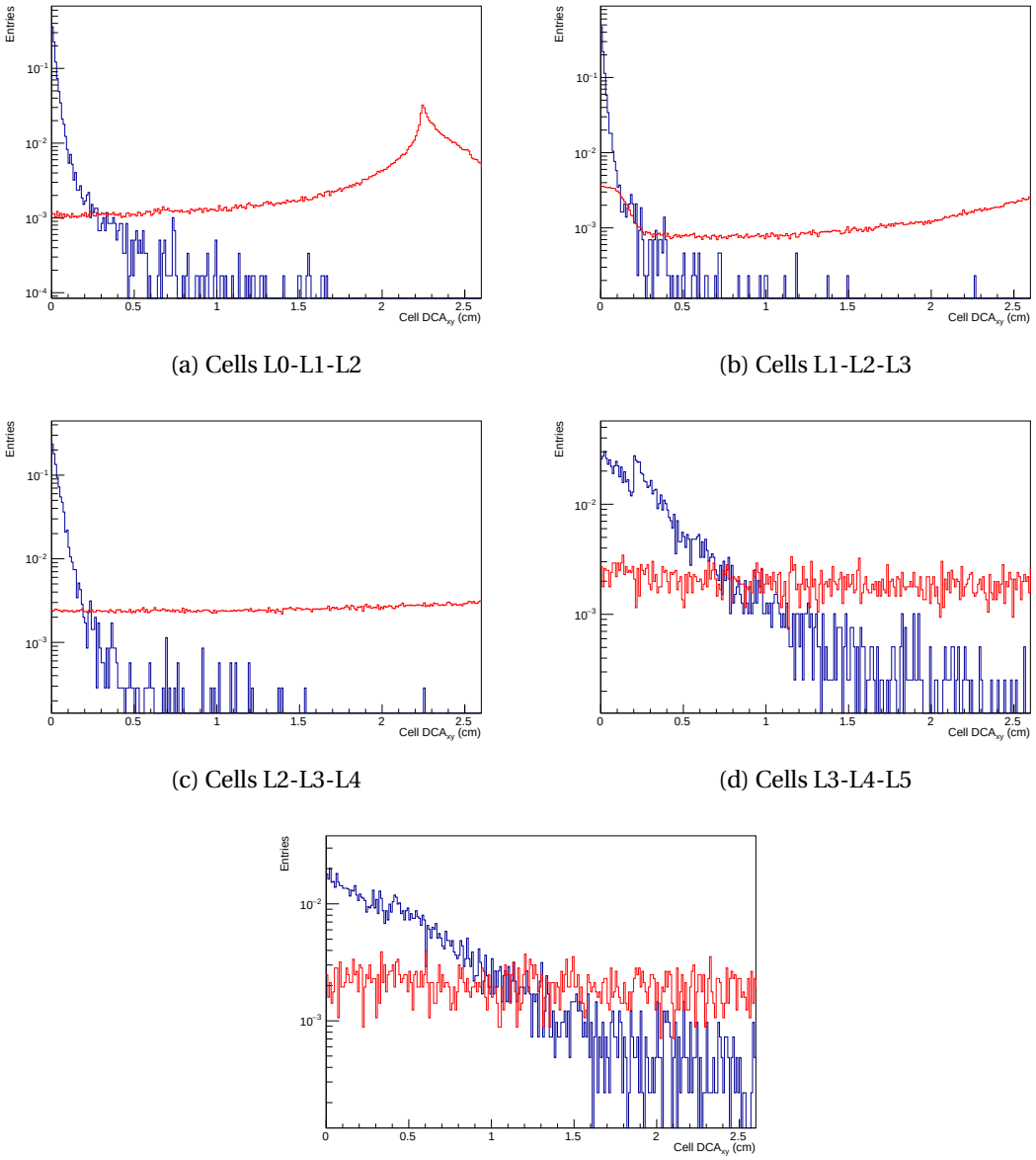

(a) Cells L0-L1-L2

(b) Cells L1-L2-L3

(c) Cells L2-L3-L4

(d) Cells L3-L4-L5

(e) Cells L4-L5-L6

Figure A.5: Distribution of the Distance of Closest Approach on the transverse plane (DCA$_{xy}$) computed for by prolonging the cell to the beam line position. The blue histogram represents the case of good cells while the red histogram represents the fake ones. All the distributions are normalised to the visible range.

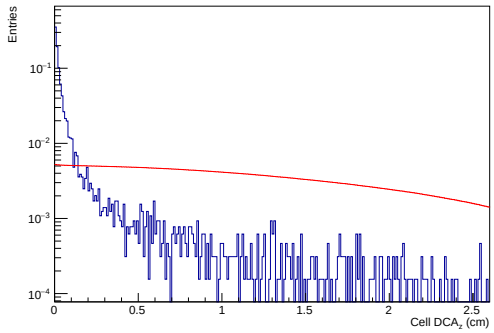

(a) Cells L0-L1-L2

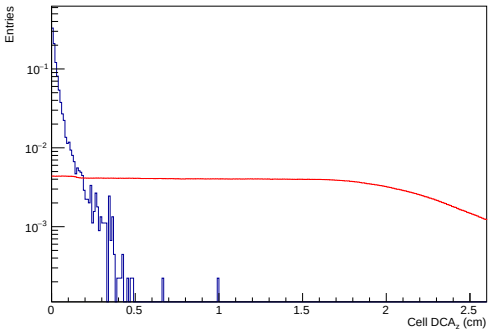

(b) Cells L1-L2-L3

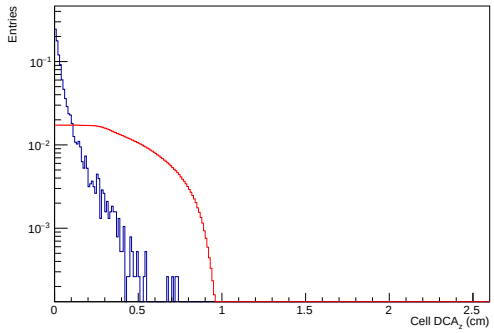

(c) Cells L2-L3-L4

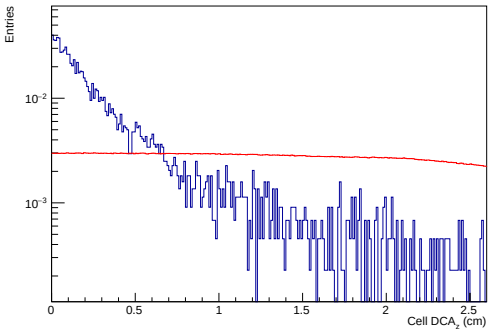

(d) Cells L3-L4-L5

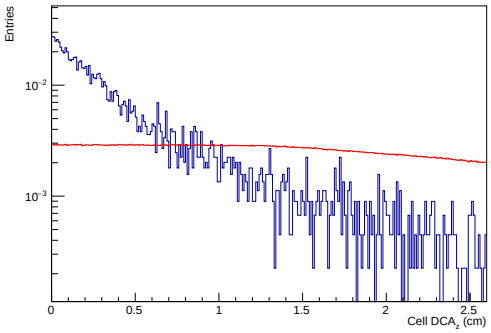

(e) Cells L4-L5-L6

Figure A.6: Distribution of the Distance of Closest Approach on the longitudinal direction (DCA_z) computed for by prolonging the cell to the beam line position. The blue histogram represents the case of good cells while the red histogram represents the case of the fake ones. All the distributions are normalised to the visible range.

B Ratios anti–nuclei over nuclei

In this appendix the ratios between the anti–nuclei and the nuclei spectra are shown as a function of the transverse momentum and in all the centrality classes analysed in this work.

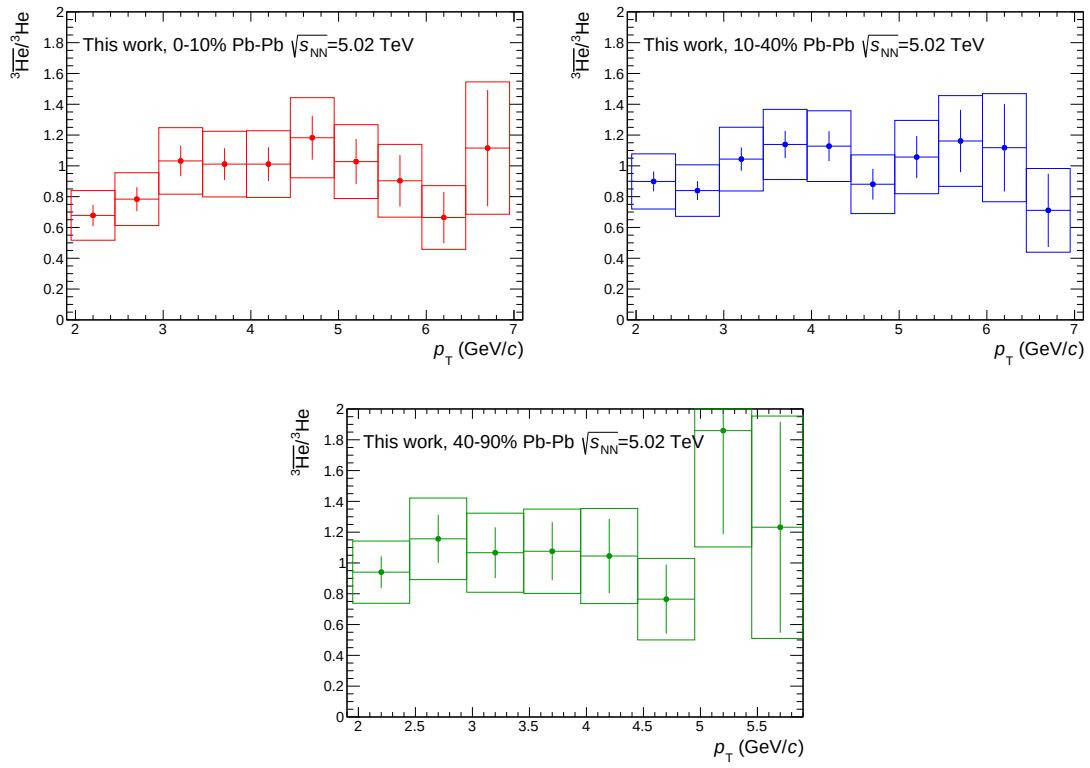

Figure B.1: Ratio between the $^3\overline{\mathrm{He}}$ and the ^{3}He spectra for all the centrality classes covered in this work for the Pb–Pb at $\sqrt{s_{\mathrm{NN}}}$ =5.02 TeV data sample.

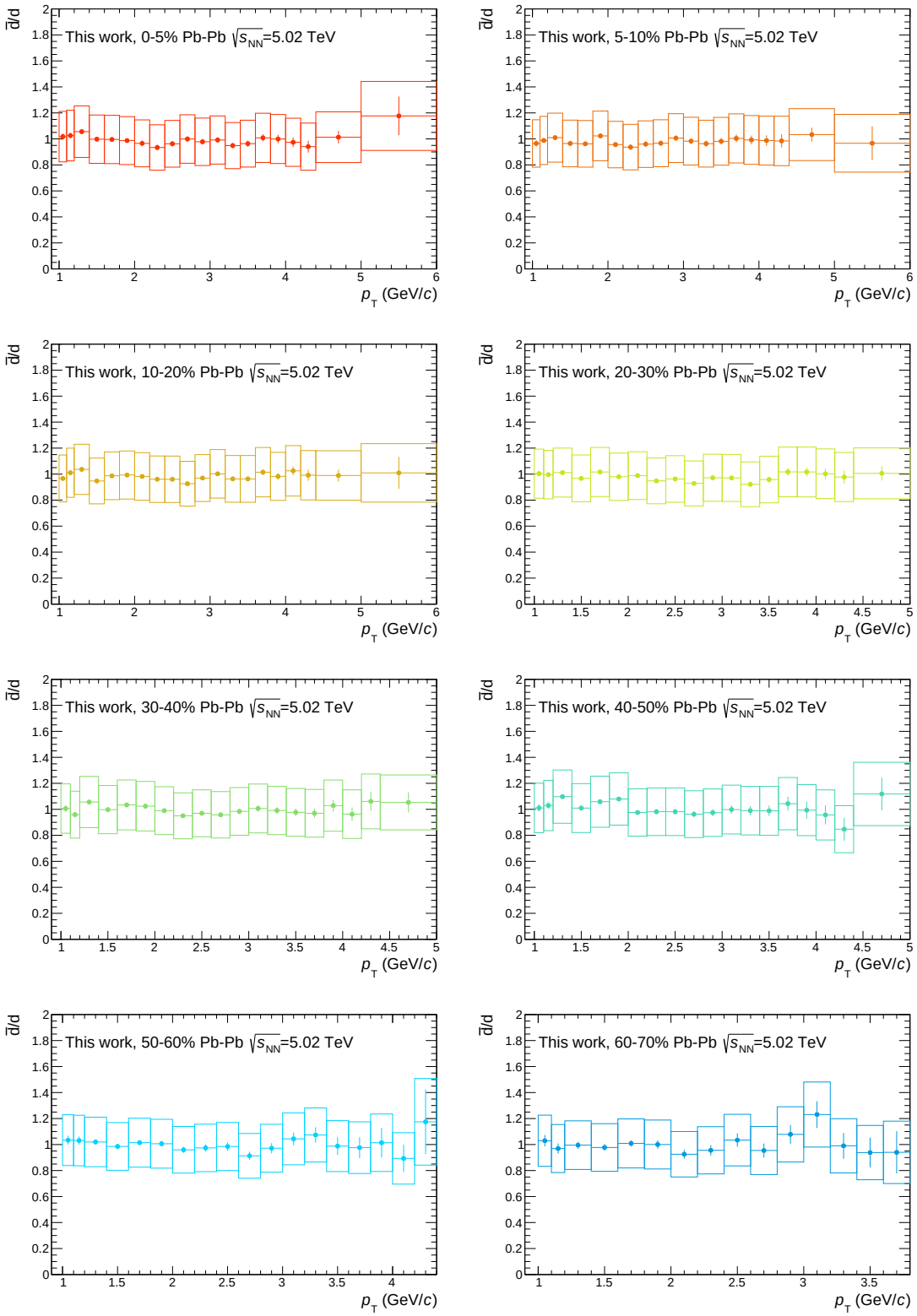
This work, 0-5% Pb-Pb $\sqrt{s_{NN}}$=5.02 TeV
This work, 5-10% Pb-Pb $\sqrt{s_{NN}}$=5.02 TeV
This work, 10-20% Pb-Pb $\sqrt{s_{NN}}$=5.02 TeV
This work, 20-30% Pb-Pb $\sqrt{s_{NN}}$=5.02 TeV
This work, 30-40% Pb-Pb $\sqrt{s_{NN}}$=5.02 TeV
This work, 40-50% Pb-Pb $\sqrt{s_{NN}}$=5.02 TeV
This work, 50-60% Pb-Pb $\sqrt{s_{NN}}$=5.02 TeV
This work, 60-70% Pb-Pb $\sqrt{s_{NN}}$=5.02 TeV
$\bar{d}/d$
p_T (GeV/c)

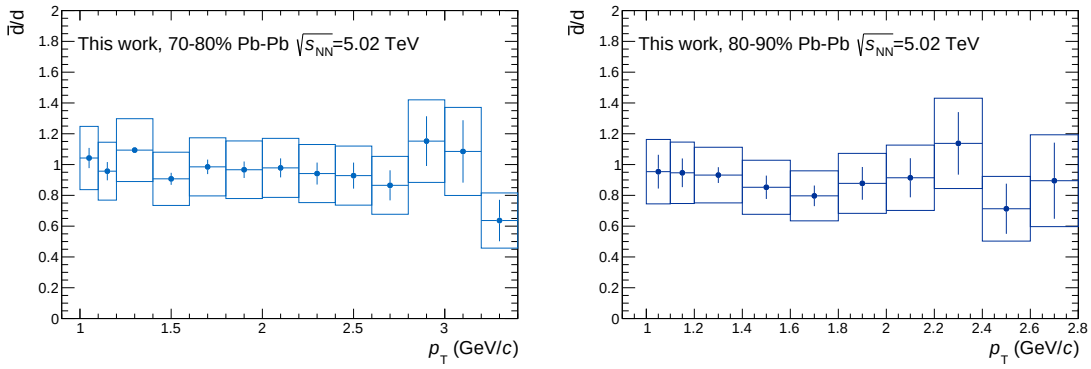

Figure B.2: Ratio between the anti–deuteron and the deuteron spectra for all the centrality classes covered in this work for the Pb–Pb at $\sqrt{s_{\rm NN}}$ =5.02 TeV data sample.

Bibliography

[1] M. Gell-Mann, (1961).

[2] Y. Ne'eman, Nucl. Phys. **26**, 222 (1961).

[3] M. Gell-Mann, Phys. Lett. **8**, 214 (1964).

[4] G. Zweig, An SU(3) model for strong interaction symmetry and its breaking. Version 2, in *DEVELOPMENTS IN THE QUARK THEORY OF HADRONS. VOL. 1. 1964 - 1978*, edited by D. Lichtenberg and S. P. Rosen, pp. 22–101, 1964.

[5] H. Fritzsch and M. Gell-Mann, eConf **C720906V2**, 135 (1972), hep-ph/0208010.

[6] Particle Data Group, K. A. Olive *et al.*, Chin. Phys. **C38**, 090001 (2014 and 2015 update).

[7] H. Fritzsch, M. Gell-Mann, and H. Leutwyler, Phys. Lett. **B47**, 365 (1973).

[8] H. D. Politzer, Phys. Rev. Lett. **30**, 1346 (1973).

[9] D. J. Gross and F. Wilczek, Phys. Rev. Lett. **30**, 1343 (1973).

[10] K. G. Wilson, Phys. Rev. **D10**, 2445 (1974), [45(1974)].

[11] S. Durr *et al.*, Science **322**, 1224 (2008), 0906.3599.

[12] P. Braun-Munzinger, V. Koch, T. Schäfer, and J. Stachel, Phys. Rep. **621**, 76 (2016), 1510.00442.

[13] M. G. Alford, A. Schmitt, K. Rajagopal, and T. Schäfer, Rev. Mod. Phys. **80**, 1455 (2008), 0709.4635.

[14] A. Chodos, R. L. Jaffe, K. Johnson, C. B. Thorn, and V. F. Weisskopf, Phys. Rev. **D9**, 3471 (1974).

[15] F. Becattini, An Introduction to the Statistical Hadronization Model, in *International School on Quark-Gluon Plasma and Heavy Ion Collisions: past, present, future Villa Gualino, Torino, Italy, December 8-14, 2008*, 2009, 0901.3643.

[16] HotQCD, A. Bazavov *et al.*, Phys. Rev. **D90**, 094503 (2014), 1407.6387.

[17] S. Borsányi *et al.*, JHEP **04**, 138 (2015), 1501.02173.

[18] Y. Aoki *et al.*, JHEP **06**, 088 (2009), 0903.4155.

[19] M. L. Miller, K. Reygers, S. J. Sanders, and P. Steinberg, Ann. Rev. Nucl. Part. Sci. **57**, 205 (2007), nucl-ex/0701025.

[20] U. W. Heinz, Concepts of heavy ion physics, in *2002 European School of high-energy physics, Pylos, Greece, 25 Aug-7 Sep 2002: Proceedings*, pp. 165–238, 2004, hep-ph/0407360.

[21] C. Gale, S. Jeon, and B. Schenke, Int. J. Mod. Phys. **A28**, 1340011 (2013), 1301.5893.

[22] J. I. Kapusta, Phys. Rev. **C21**, 1301 (1980).

[23] P. Braun-Munzinger, K. Redlich, and J. Stachel, (2003), nucl-th/0304013.

[24] V. Vovchenko and H. Stoecker, J. Phys. Conf. Ser. **779**, 012078 (2017), 1610.02346.

[25] G. Torrieri *et al.*, Comput. Phys. Commun. **167**, 229 (2005), nucl-th/0404083.

[26] A. Andronic, P. Braun-Munzinger, J. Stachel, and H. Stocker, Phys. Lett. **B697**, 203 (2011), 1010.2995.

[27] A. Mekjian, Phys. Rev. Lett. **38**, 640 (1977).

[28] R. Scheibl and U. W. Heinz, Phys. Rev. **C59**, 1585 (1999), nucl-th/9809092.

[29] ALICE, B. Abelev *et al.*, Phys. Rev. Lett. **109**, 252301 (2012), 1208.1974.

[30] STAR, B. I. Abelev *et al.*, Phys. Rev. **C79**, 034909 (2009), 0808.2041.

[31] PHENIX, S. S. Adler *et al.*, Phys. Rev. **C69**, 034909 (2004), nucl-ex/0307022.

[32] Yu. A. Karpenko and Yu. M. Sinyukov, J. Phys. **G38**, 124059 (2011), 1107.3745.

[33] P. Bozek, Phys. Rev. **C85**, 034901 (2012), 1110.6742.

[34] STAR, L. Adamczyk *et al.*, Phys. Rev. Lett. **113**, 052302 (2014), 1404.1433.

[35] ALICE, E. Abbas *et al.*, JINST **8**, P10016 (2013), 1306.3130.

[36] ALICE, J. Adam *et al.*, Phys. Rev. Lett. **116**, 132302 (2016), 1602.01119.

[37] J. W. Cronin *et al.*, Phys. Rev. **D11**, 3105 (1975).

[38] CMS, V. Khachatryan *et al.*, JHEP **04**, 039 (2017), 1611.01664.

[39] ALICE, J. Adam *et al.*, Phys. Rev. **C93**, 034913 (2016), 1506.07287.

[40] CMS, S. Chatrchyan *et al.*, Phys. Rev. **C84**, 024906 (2011), 1102.1957.

[41] CMS, S. Chatrchyan *et al.*, Phys. Rev. Lett. **109**, 222301 (2012), 1208.2826.

[42] ALICE, B. Abelev *et al.*, Phys. Rev. Lett. **109**, 072301 (2012), 1202.1383.

[43] M. Winn, Few Body Syst. **58**, 53 (2017), 1609.01135.

[44] R. L. Thews, M. Schroedter, and J. Rafelski, Phys. Rev. **C63**, 054905 (2001), hep-ph/0007323.

[45] P. Braun-Munzinger and J. Stachel, Phys. Lett. **B490**, 196 (2000), nucl-th/0007059.

[46] CMS, S. Chatrchyan *et al.*, Phys. Rev. Lett. **106**, 212301 (2011), 1102.5435.

[47] ALICE, J. Adam *et al.*, Phys. Lett. **B754**, 235 (2016), 1509.07324.

[48] ATLAS, G. Aad *et al.*, Phys. Lett. **B716**, 1 (2012), 1207.7214.

[49] CMS, S. Chatrchyan *et al.*, Phys. Lett. **B716**, 30 (2012), 1207.7235.

[50] LHCb, R. Aaij *et al.*, Phys. Rev. Lett. **115**, 072001 (2015), 1507.03414.

[51] The CERN accelerator complex, https://cds.cern.ch/record/1997193, 2012.

[52] W. Fischer and J. M. Jowett, Rev. Accel. Sci. Tech. **7**, 49 (2014).

[53] S. van der Meer, (1968).

[54] L. Evans and P. Bryant, JINST **3**, S08001 (2008).

[55] L. Evans, The Large Hadron Collider, in *Lecture Notes, Les Houches Summer School, 97th Session: Theoretical Physics to Face the Challenge of LHC: Les Houches, France, August 1-26, 2011*, pp. 1–33, 2015.

[56] M. Giovannozzi, The LHC machine: from beam commissioning to operation and future upgrades, in *Lecture Notes, Les Houches Summer School, 97th Session: Theoretical Physics to Face the Challenge of LHC: Les Houches, France, August 1-26, 2011*, pp. 35–55, 2015.

[57] ALICE, P. Cortese *et al.*, J. Phys. **G30**, 1517 (2004).

[58] ALICE, P. Cortese *et al.*, J. Phys. **G32**, 1295 (2006).

[59] ALICE, K. Aamodt *et al.*, JINST **3**, S08002 (2008).

[60] ALICE, B. Abelev *et al.*, Int. J. Mod. Phys. **A29**, 1430044 (2014), 1402.4476.

[61] ALICE, J. Adam *et al.*, Eur. Phys. J. **C75**, 226 (2015), 1504.00024.

[62] ALICE, J. Adam *et al.*, JCAP **1601**, 032 (2016), 1507.07577.

[63] ALICE, J. Adam *et al.*, (2016), 1610.03055.

[64] ALICE, B. Abelev *et al.,* Phys. Rev. **C88**, 044909 (2013), 1301.4361.

[65] ALICE, B. Abelev *et al.,* Phys. Rev. Lett. **111**, 232302 (2013), 1306.4145.

[66] ALICE, F. Carena *et al.,* Nucl. Instrum. Meth. **A741**, 130 (2014).

[67] M. Krzewicki *et al.,* J. Phys. Conf. Ser. **664**, 082023 (2015).

[68] G. Agakishiev *et al.,* Nucl. Instrum. Meth. **A394**, 225 (1997).

[69] W. Blum, L. Rolandi, and W. Riegler, *Particle detection with drift chambers* (, 2008).

[70] ALICE, B. Abelev *et al.,* J. Phys. **G41**, 087002 (2014).

[71] ALICE, Report No. CERN-LHCC-2015-001. ALICE-TDR-018, 2015 (unpublished).

[72] ALICE, Report No. CERN-LHCC-2013-020. ALICE-TDR-016, 2013 (unpublished).

[73] ALICE, Report No. CERN-LHCC-2013-019. ALICE-TDR-015, 2013 (unpublished).

[74] ALICE, Report No. CERN-LHCC-2015-006. ALICE-TDR-019, 2015 (unpublished).

[75] F. Reidt, JINST **11**, C12038 (2016).

[76] D. Rohr, Tracking performance in high multiplicities environment at ALICE , https://indico.cern.ch/event/517784/contributions/2496892/, 2017.

[77] M. Puccio, Vertex reconstruction in p-p and Pb-Pb collisions at LHC with the upgraded tracker of the ALICE experiment, Master's thesis, Università degli studi di Torino, 2013.

[78] D. Rohr *et al.,* J. Phys. Conf. Ser. **664**, 082047 (2015).

[79] V. Akishina and I. Kisel, EPJ Web Conf. **127**, 00003 (2016).

[80] D. Funke *et al.,* J. Phys. Conf. Ser. **513**, 052010 (2014).

[81] R. Frühwirth, A. Strandlie, and W. Waltenberger, Nucl. Instrum. Meth. **A490**, 366 (2002).

[82] R. Fruhwirth, Nucl. Instrum. Meth. **A262**, 444 (1987).

[83] X.-N. Wang and M. Gyulassy, Phys. Rev. **D44**, 3501 (1991).

[84] R. Brun, F. Bruyant, M. Maire, A. C. McPherson, and P. Zanarini, *GEANT 3: user's guide Geant 3.10, Geant 3.11; rev. version* (CERN, Geneva, 1987).

[85] L. Dagum and R. Menon, Computational Science & Engineering, IEEE **5**, 46 (1998).

[86] J. E. Stone, D. Gohara, and G. Shi, IEEE Des. Test **12**, 66 (2010).

[87] ALICE, J. Adam *et al.,* Phys. Rev. **C93**, 024917 (2016), 1506.08951.

[88] ALICE, J. Adam *et al.,* Phys. Lett. **B754**, 360 (2016), 1506.08453.

[89] N. Jacazio, Private communication.

[90] M. Puccio, RooCustomPdfs, https://github.com/mpuccio/RooCustomPdfs, 2016.

[91] R. J. Barlow and C. Beeston, Comput. Phys. Commun. **77**, 219 (1993).

[92] A. Auce *et al.*, Phys. Rev. **C53**, 2919 (1996).

[93] F. G. Binon *et al.*, Phys. Lett. **31B**, 230 (1970).

[94] J. Jaros *et al.*, Phys. Rev. **C18**, 2273 (1978).

[95] S. P. Denisov *et al.*, Nucl. Phys. **B31**, 253 (1971).

[96] R. Brun, R. Hagelberg, M. Hansroul, and J. C. Lassalle, *Simulation program for particle physics experiments, GEANT: user guide and reference manual* (CERN, Geneva, 1978).

[97] GEANT4, S. Agostinelli *et al.*, Nucl. Instrum. Meth. **A506**, 250 (2003).

[98] R. Barlow, Systematic errors: Facts and fictions, in *Advanced Statistical Techniques in Particle Physics. Proceedings, Conference, Durham, UK, March 18-22, 2002*, pp. 134–144, 2002, hep-ex/0207026.

[99] A. Esposito *et al.*, Phys. Rev. **D92**, 034028 (2015), 1508.00295.

[100] ALICE, B. Abelev *et al.*, Phys. Rev. **C88**, 044910 (2013), 1303.0737.

[101] E. Schnedermann, J. Sollfrank, and U. W. Heinz, Phys. Rev. **C48**, 2462 (1993), nucl-th/9307020.

[102] C. Tsallis, J. Statist. Phys. **52**, 479 (1988).

[103] ALICE, J. Adam *et al.*, Phys. Rev. Lett. **116**, 222302 (2016), 1512.06104.

[104] ALICE, N. Jacazio, (2017), 1704.06030.

[105] S. Wheaton and J. Cleymans, Comput. Phys. Commun. **180**, 84 (2009), hep-ph/0407174.

[106] B. Dönigus, Private communication.

[107] A. Polleri, J. P. Bondorf, and I. N. Mishustin, Phys. Lett. **B419**, 19 (1998), nucl-th/9711011.

[108] F. Becattini, E. Grossi, M. Bleicher, J. Steinheimer, and R. Stock, Phys. Rev. **C90**, 054907 (2014), 1405.0710.

[109] F. Becattini and J. Manninen, Phys. Lett. **B673**, 19 (2009), 0811.3766.

[110] ALICE, J. Adam *et al.*, Nature Phys. (2017), 1606.07424.

Acknowledgements

I would like to thank all the people that contributed in my education in the last three years and first of all Massimo Masera and Stefania Bufalino, who provided always useful suggestions and an extraordinary support in all my activities. I want to thank Francesco Prino, who always provided insights on tracking, handling of uncertainties and analysis techniques in general, and Alexander Kalweit, who solved my doubts and gave me insights about the nuclei and light flavour analyses in many dinners at R1.

All my colleagues in Torino deserve a place in this acknowledgements as well: Elena Bruna, Yasser Corrales, Mario Sitta, Luciano Ramello, Stefania Beolè, Stefano Trogolo, Bruno Alessandro, Anastasia Barbano, Fabrizio Grosa, Luca Barioglio, Matteo Concas, Ivan Ravasenga, Nicolò Jacazio ... thanks for all the discussions and the time spent together!

Finally I would like to thank my parents, my friends and Giulia for supporting me and being so patient in the last three years.

Torino, 2017, May M. P.